THE UNIVERSITY OF QUEENSLAND

AUSTRALIA

Development of a multiphase lattice Boltzmann model for high-density and viscosity ratio flows in unconventional gas wells

Travis Mitchell

B.Eng. (Mechanical, Hons 1)

B.Sc. (Mathematics)

A thesis submitted for the degree of Doctor of Philosophy at

The University of Queensland in 2019

School of Mechanical and Mining Engineering

Abstract

The confined flow of multiphase fluids is relevant in a range of applications in both science and engineering. For example, the two-phase flow of gas and liquid can commonly be observed in boilers used for power production, nuclear reactors (particularly in a *loss-of-coolant accident*) as well as in the transportation of hydrocarbons in the oil and gas industry. The optimal design and operation of these systems relies on an understanding of how the phases interact and the behaviour emergent from these interactions.

This thesis studies multiphase flows in the field of natural gas extraction from unconventional reservoirs, with a focus on coal seam gas (CSG). In this context, the bottom hole pressure (BHP) in a natural gas well is an important parameter in the effective design of well completions and artificial lifting systems. Poor estimation of this can lead to liquid loading in the wellbore and reduced efficiency of the extraction process. The complex interaction of production gas and the associated water can increase the uncertainty in pressure gradients and ultimately impact the BHP estimation. A significant body of research has explored pressure gradients in the co-current multiphase flows found in conventional gas extraction, but these are not expected to hold for the counter-current regimes present in CSG production. Therefore, this research aimed to develop a fully resolved-numerical model for the simulation of simultaneous gas and liquid transport in scenarios applicable to CSG extraction.

When two-phases flow in a confined environment such as a pipe or conduit, the topology of the interface is described by commonly observed flow regimes. When the pipe is in a vertical configuration, the typical regimes include bubble, slug, churn and annular flow. The models that describe the liquid-gas interactions are typically dependent on the flow regime and can significantly impact the accuracy of pressure predictions. As a result, knowledge of the flow regime is required *a priori* to predicting the pressure gradient. Once this has been determined, the uncertainty associated with the phase interaction models can still deteriorate the practical use of predictive tools. The rise velocity of elongated bubbles in the slug flow regime has recently been identified in the literature as impacting greatly on the estimation of liquid hold up and pressure gradients in a piping system. Understanding the behaviour of these bubbles, termed Taylor bubbles, allows operators to reduce pressure oscillations in the wellbore and more accurately forecast production over the life of the well. This work seeks to capture the behaviour of these bubbles in flow configurations applicable to CSG extraction. This involves modelling annular pipe systems at a range of inclinations as well as with fluids propagating in co- and counter-current directions.

This thesis presents the development, verification and validation of a phase-field lattice Boltzmann method (PFLBM) that allows for the simulation of dynamic liquid-gas flows with density ratios on the order of 1000. The PFLBM proposed was able to enhance the locality of numerical operations within the algorithm and, consequently, improve the efficiency of parallel computations. Additionally, during the verification and validation process, the robustness of the model was shown through the simulation of high density ratio flows at Reynolds numbers in excess of previously reported results. From here, the research investigated the flow of gas in annular piping systems applicable to CSG extraction.

Initially, the work proposes a two-dimensional, velocity-based lattice Boltzmann model (LBM) to resolve the hydrodynamics coupled with the conservative phase-field model to capture the interfacial dynamics of a liquid-gas system. The model was verified and evaluated against previous PFLBMs using a layered Poiseuille flow test. This indicated that the local flow behaviour about the interface could be resolved using isotropic differences, removing the need for directional-derivatives found in other models. The well-studied, Rayleigh-Taylor instability provided verification in a scenario involving high levels of interfacial curvature, where the robustness of the PFLBM was highlighted with simulations at a high Reynolds number. With the model verified, the dynamics of planar Taylor bubbles was investigated. Here, the model was able to recover expected rise velocity correlations in stagnant liquid. The introduction of liquid motion allowed the investigation of counter-current flow. From this, the value of the empirical distribution parameter, used to describe the liquid contribution to the gas velocity, was found to be approximately equal to the co-current value present in the literature.

With promising results in two-dimensions, the PFLBM was extended into three-dimensions. In order to retain the robustness observed in two-dimensions, the implementation employed a *weighted*-multiple-relaxation time in the collision process of the velocity-based LBM. After verification, the model was compared with experimental measurements of a gas bubble rising through a tube of olive oil. This allowed validation, not only of the macroscopic dynamics such as the bubble rise velocity, but also the local flow field through particle-image velocimetry. This study was extended to include pipe inclinations and liquid motion as required to capture scenarios relevant to the oil and gas industry. In this study it was found that existing correlations perform poorly at intermediary pipe inclination angles. However, a methodology was presented through which the accuracy of a unified model could be improved.

To complete the research, the three-dimensional PFLBM was applied to study the dynamics of Taylor bubbles in annular pipes. This is directly applicable to the slug flow regime that may occur in CSG wellbores. The first component of this section recreated air-water experiments reported in the literature with the PFLBM. This validated the model's ability to capture quantitative parameters relating to the bubble rise as well as the asymmetric shape experimentally observed with the introduction of a central tube. From here, inclination effects were studied and it was found that the most accurate correlation required the coupling of tubular and vertical annular bubble rise models from the literature. Incorporating liquid motion into the system indicated that the distribution parameter, similar to the two-dimensional case, remained approximately constant between co- and counter-current flow. This agreed with some experimental work from the 1970s, but differed substantially from tubular relations that can be found in existing annular mechanistic models.

This thesis has outlined the development and practical application of a fully-resolved model of liquid-gas flows. It provided insight into the dynamics of Taylor bubbles in a range of configurations and proposed a methodology for which a unified bubble rise correlation could be formulated in future work. Additional avenues of research were identified for both model improvement, such as adaptive mesh refinement, and model application, including the extension to porous media flow to capture reservoir dynamics.

Declaration by author

This thesis is composed of my original work, and contains no material previously published or written by another person except where due reference has been made in the text. I have clearly stated the contribution by others to jointly-authored works that I have included in my thesis.

I have clearly stated the contribution of others to my thesis as a whole, including statistical assistance, survey design, data analysis, significant technical procedures, professional editorial advice, financial support and any other original research work used or reported in my thesis. The content of my thesis is the result of work I have carried out since the commencement of my higher degree by research candidature and does not include a substantial part of work that has been submitted to qualify for the award of any other degree or diploma in any university or other tertiary institution. I have clearly stated which parts of my thesis, if any, have been submitted to qualify for another award.

I acknowledge that an electronic copy of my thesis must be lodged with the University Library and, subject to the policy and procedures of The University of Queensland, the thesis be made available for research and study in accordance with the Copyright Act 1968 unless a period of embargo has been approved by the Dean of the Graduate School.

I acknowledge that copyright of all material contained in my thesis resides with the copyright holder(s) of that material. Where appropriate I have obtained copyright permission from the copyright holder to reproduce material in this thesis and have sought permission from co-authors for any jointly authored works included in the thesis.

Publications included in this thesis

1. [1] Gruszczyński, G, **Mitchell, T.**, Leonardi, C., Łaniewski-Wołłk, Ł., Barber, T., A cascaded phase-field lattice Boltzmann model for the simulation of incompressible, immiscible fluids with high density contrast, *Computers and Mathematics with Applications*, In Press, 2019.

2. [2] **Mitchell, T.**, Leonardi, C., Firouzi, M., and Towler, B., Towards closure relations for the rise velocity of Taylor bubbles in annular piping using phase-field lattice Boltzmann techniques, *21st Australasian Fluid Mechanics Conference* (AFMC 2018), Adelaide (Australia), 10–13 December 2018.

3. [3] **Mitchell, T.**, Leonardi, C. and Fakhari, A., Development of a three-dimensional phase-field lattice Boltzmann method for the study of immiscible fluids at high density ratios, *International Journal of Multiphase Flow*, 107, 1–15, 2018

4. [4] Fakhari, A., **Mitchell, T.**, Leonardi, C., and Bolster, D., Improved locality of the phase-field lattice-Boltzmann model for immiscible fluids at high density ratios, *Physical Review E*, 96, 053301, 2017

5. [5] Wu, B., Firouzi, M., **Mitchell, T.**, Rufford, T., Leonardi, C., and Towler, B., A critical review of flow maps for gas-liquid flows in vertical pipes and annuli, *Chemical Engineering Journal*, 326, 350–377, 2017

Other publications during candidature

Peer-reviewed papers

1. **Mitchell, T.**, Hill, B., Firouzi, M. and Leonardi, C., Development and Evaluation of Multiphase Closure Models used in the Simulation of Unconventional Wellbore Dynamics, *SPE/AAPG/SEG Asia Pacific Unconventional Resources*, URTEC-198239-MS, 18–19 November, 2019.

2. Leonardi, C., Regulski, W., McCullough, J. W. S., Wang, D., **Mitchell, T. R.**, Jones, B. D., and Williams, J. R., Characterising the Behaviour of Hydraulic Fracturing Fluids via Direct Numerical Simulation, *SPE Asia Pacific Oil & Gas Conference and Exhibition*, SPE-182458-MS, 25–27 October, 2016

3. **Mitchell, T.**, Leonardi, C., Micromechanical investigation of fines liberation and transport during coal seam dewatering, *Journal of Natural Gas Science and Engineering*, 35A, 1101–1120, 2016

Conference abstracts

1. **Mitchell, T.**, Hill, B., Leonardi, C., Firouzi, M., Upscaling direct numerical simulation of multiphase flow to wellbore flow in CSG wells, *SPE/AAPG/SEG Asia Pacific Unconventional Resources Technology Conference* (URTeC 2019), Brisbane (Australia), 18–19 November 2019.

2. **Mitchell, T.**, Leonardi, C., Firouzi, M., Multiphase lattice Boltzmann modelling of elongated bubbles in annular piping: Applications in the extraction of natural gas, *28th International Conference on Discrete Simulation of Fluid Dynamics*, Bangalore (India), 22–26 July 2019.

3. **Mitchell, T.**, Leonardi, C., Firouzi, M., and Towler, B., Towards closure relations for the rise velocity of Taylor bubbles in annular piping using phase-field lattice Boltzmann techniques, *21st Australasian Fluid Mechanics Conference* (AFMC 2018), Adelaide (Australia), 10–13 December 2018.

4. **Mitchell, T.**, Leonardi, C., Towler, B., Firouzi, M., Phase-field lattice Boltzmann modelling and its application in the oil & gas sector, *15th International Conference for Mesoscopic Methods in Engineering and Science* (ICMMES 2018), Newark, Delaware (USA), 9–13 July 2018.

5. **Mitchell, T.**, leonardi, C., Towler, B., Towards the development of a unified closure relation for Taylor bubble rise velocity in annular pipes, *27th International Conference on Discrete Simulation of Fluid Dynamics*, Worcester, MA (USA), 25–29 June 2018.

6. **Mitchell, T.**, Lattice Boltzmann modelling of two-phase flows: Applications in the oil & gas sector, *10th Engineering, Architecture and Information Technology Postgraduate Conference*, Brisbane (Australia), 6 June 2018.

7. **Mitchell, T.**, Leonardi, C., Fakhari, A., Towler, B., A multiple-relaxation-time lattice Boltzmann model for simulating high-density-ratio fluids using phase-field theory, *14th International Conference for Mesoscopic Methods in Engineering and Science* (ICMMES 2017), Nantes (France), 17–21 July 2017.

8. **Mitchell, T.**, Leonardi, C., Fakhari, A., Towler, B., Phase-field based simulation of Taylor bubbles using lattice Boltzmann techniques, *26th International Conference on Discrete Simulation of Fluid Dynamics* (DSFD 2017), Erlangen (Germany), 10-14 July 2017.

9. **Mitchell, T.**, Leonardi, C., Towler, B., Lattice Boltzmann modelling of counter-current multiphase flow in annular piping, *9th Engineering, Architecture and Information Technology Postgraduate Conference*, Brisbane (Australia), 6 June 2017.

10. **Mitchell, T.**, Computational modelling of counter-current multiphase flows, *8th Engineering, Architecture and Information Technology Postgraduate Conference*, Brisbane (Australia), 6 June 2016.

Contributions by others to the thesis

- Dr Christopher Leonardi - Provided initial research directions, assisted to refine the scope of project works and revised written content as the Principal Advisor of the dissertation.
- Dr Abbas Fakhari - Provided assistance in familiarising with phase-field theory and guidance in the choice of numerical algorithms. Provided the initial development of the two-dimensional phase-field model. Additionally, revised content written into Included Publications 1 and 2.
- Dr Łukasz Łaniewski-Wołłk - Developed the open-source lattice Boltzmann framework, TCLB. This framework provided the development location for models developed and implemented in this dissertation.
- Dr Mashid Firouzi - Provided initial input into the direction and objectives of the research. Gave information regarding the problems faced by the industry from a larger perspective highlighting certain motivations behind the work.

Statement of parts of the thesis submitted to qualify for the award of another degree

No works submitted towards another degree have been included in this thesis.

Research involving human or animal subjects

No animal or human subjects were involved in this research.

Acknowledgments

The completion of this work would not have been possibly without the support of many people that not only supported me during this time, but helped me develop as a person. For the lessons they taught me, I will be forever grateful.

I would like to first thank my principal advisor, Dr. Christopher Leonardi, and my associate advisor, Dr. Mahshid Firouzi. For your academic guidance throughout the course of my study, I am sincerely thankful. In particular, I would like to thank Dr. Leonardi for his generosity and continuous encouragement. The many opportunities I had during my candidature, from studying abroad to attending conferences and working on the development of grants, would not have been possible without your support. I have truly enjoyed working with you, and look forward to doing so again in the future.

To the office crew, Dr. Jon McCullough, Dr. Ed Hay, Dr. Amin Kamyar and Dr. Duo Wang as well as Nathan Di Vaira and Bryce Hill, the hours at the university would have been nowhere near as enjoyable without you - it is hard to play office cricket on one's own. In all seriousness, your support and assistance, no matter how big or small, has been very much appreciated.

I would like to thank Prof. Jens Harting from the Helmholtz Institute Erlangen-Nüremberg for Renewable Energy in Germany for allowing me to visit for three months in 2017. In particular, thanks to David Jung and Stefan Zitz for sharing their office with me and the rest of the team (Manuel Zellhöfer and Dr's Othmane Aouane, Alexander Sukhov, Daniel Berger, Simon Bogner and Nicolas Rivas) for insightful discussions and making me feel like part of the group.

In 2018, I was fortunate enough to spend two months on the east coast of America visiting universities and attending conferences. I would like to thank Prof. Emilio Baglietto for allowing me to present my work to his group at the School of Nuclear Science & Engineering at MIT, and to Sam Raymond, Justin Montgomery and Dixia Fan for showing me around the research labs and Boston city. I also sincerely thank Dr. Abbas Fakhari for hosting me during my visit at the University of Pennsylvania. Having the chance to work with you in person after two years of emails was very rewarding.

I would like to thank the Society of Petroleum Engineers Queensland section for awarding me a post-graduate scholarship in 2018 which supported my travel and conference registration in America. Furthermore, I would like to thank the Australasian Fluid Mechanics Society for providing me with a Student Award to cover my registration at the 21st Australasian Fluid Mechanics Conference, where I was lucky enough to be awarded the David Wilkinson prize.

Acknowledgement and my sincerest gratitude must also be given to Dr. Łukasz Łaniewski-Wołłk. Thank you for welcoming me into your home during my visit to the Politechnika Warszawska and showing me your city. The work you have done in developing the open-source framework, TCLB, allowed my study to progress at a much more rapid rate than it otherwise would have. I thoroughly enjoyed working beside you during your stay at UQ, and hope it is not too long until we can work together again.

Finally, I would like to thank the support of my friends and family. A particular mention must be given to Climb Club and the larger climbing community for providing the main distraction from my work. To my parents, Mark and Helene, and brothers, Braden and Damon, I feel like you are never too far away and always there if I need a hand, for that, I cannot thank you enough.

Financial support

This research was supported by an Autralian Government Research Training Program Scholarship.

This research was supported by the School of Mechanical and Mining Engineering, The University of Queensland.

This research was supported by a Candidate Development Award provided by the Graduate School of The University of Queensland.

This research was supported by facilities provided by The Pawsey Supercomputing Centre with funding from the Australian Government and the Government of Western Australia.

This research was supported by the Queensland Section of the Society of Petroleum Engineers.

These sources of funding and access to computational facilities is gratefully acknowledged for the contribution they provided to this research.

Research classifications

Keywords

Multiphase lattice Boltzmann methods, counter-current flow, Taylor bubble dynamics, phase-field modelling, wellbore flow, annular piping, natural gas extraction

Australian and New Zealand Standard Research Classifications (ANZSRC)

ANZSRC code: 091501, Computational Fluid Dynamics, 50%
ANZSRC code: 090407, Process Control and Simulation, 25%
ANZSRC code: 091406, Petroleum and Reservoir Engineering, 25%

Fields of Research (FoR) Classification

FoR code: 0915, Interdisciplinary Engineering, 50%
FoR code: 0904, Chemical Engineering, 25%
FoR code: 0914, Resources Engineering and Extractive Metallurgy, 25%

Contents

List of figures

List of tables

List of abbreviations and symbols

Abbreviations	
2D	Two-dimensional
3D	Three-dimensional
BC	Boundary conditions
bcf	Billion cubic feet
BGK	Bhatnagar, Gross, Krook
BHP	Bottom hole pressure
CFD	Computational fluid dynamics
CGM	Colour-gradient method
CMFD	Computational multi-fluid dynamics
CPU	Central processing unit
CSF	Continuum surface force
CSG	Coal seam gas
DNS	Direct numerical simulation
FEM	Finite element method
GPU	Graphical processing unit
ID	Inner diameter
IFE	Institute for Energy Technology
IPR	Inflow performance ratio
ITM	Interface tracking method
LBM	Lattice Boltzmann method
LNG	Liquified natural gas
LS	Level set
MAC	Marker-and-Cell
MRT	Multiple relaxation time
MUSIG	Multiple size group model
NSE	Navier-Stokes equations
PDE	Partial differential equation
PF	Phase field
SRT	Single relaxation time
TFM	Two-fluid model
VOF	Volume-of-fluid

Unless otherwise stated in the text, a number of commonly used symbols in this dissertation include:

Symbols	
α	Void fraction
β	Chemical potential parameter (1)
κ	Chemical potential parameter (2)
μ	Dynamic viscosity
μ_ϕ	Chemical potential
ν	Kinematic viscosity
ϕ	Order parameter
ρ	Density
σ	Surface tension coefficient
τ_N	Newtonian viscous stress tensor
D	Characteristic diameter
f	Friction factor
f_i	Density based distribution functions
g_i	Pressure or velocity based distribution functions
h_i	Phase field based distribution functions
H_L	Liquid hold-up
p	Hydrodynamic pressure
S	Surface
t	Time
V	Volume
W	Interface thickness
Vectors	
$\mathbf{F}$	Force
$\mathbf{g}$	Gravitational acceleration
$\mathbf{u}$	Velocity (u, v, w)
$\mathbf{x}$	Positional coordinate (x, y, z)
Dimensionless numbers	
Ca	Capillary number
Cn	Cahn number
Eo	Eötvös number
Fr	Froude number
Mo	Morton number
N_f	Inverse viscosity number
Re	Reynolds number
We	Weber number

Chapter 1

Introduction

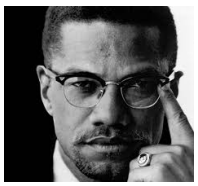

"Education is the passport to the future, for tomorrow belongs to those who prepare for it today."
Malcolm X

Hydrocarbon fuels derived from oil and gas reserves were one of the key products that enabled the continuation of the industrial revolution in the late half of the 20th century. With great change in terms of construction materials and inter-connectivity within countries, along with the exhaustion of a number of coal mines in Western Europe, the supply of fuel became critically important. The dependence on oil and gas is still evident today with significant use in industries ranging from electricity generation and transportation through to the production of everyday plastics. In order for developing and developed nations to continue progressing with this reliance, there is a need for access to such commodities, at least in the medium-term future. This is particularly evident in the energy sector when one considers the environmental impact of alternative, low-cost, continuous supply sources currently in use (e.g. coal). A 2015 report from APGA, APPEA and ENA [7], documented that natural gas was delivering electricity at one-quarter to one-sixth of the carbon intensity when compared to typical forms of mains supply.

The transition towards environmentally sustainable energy has brought further focus onto the natural gas industry. A prevailing mitigation philosophy, termed *Carbon Stabilising Wedges*, for reducing CO_2 emissions was introduced by two professors from Princeton, Robert Socolow and Stephen Pacala, and identified "*Fuel-Switching for Electricity*" as one of their 15 currently available offset technologies [8]. Here, the recommendation to move from a base load supply of predominately coal to gas is predicted to halve the emissions in this sector by 2060.

In the year 2015-16, natural gas-fired generation contributed 20% of Australia's total electricity production compared with 63% from coal-fired plants. However, high gas prices saw a reduction to 18% supply by the end of 2016 while coal remained stationary [9]. The fixed generation from coal could be considered surprising with the uptake of renewable technologies in Australia, but perhaps current cost, intermittency and government policies limit the renewables penetration into grid-scale

main supply. Although the domestic electricity generation from gas as a percentage declined through 2015-16, the international export significantly increased (by 46%) as a result of liquefied natural gas (LNG) projects reaching export capability in both Queensland and Western Australia [9]. If one looks outside of electricity generation, to energy consumption as a whole, oil and gas activities supply over 60% of Australia's requirement. The ability to access natural gas domestically with the increased international interest while upholding the need for low-cost, low-emission energy is one of the driving motivations for the work in this dissertation.

In the Australian market there has been large growth in onshore resources, particularly in Queensland with coal seam gas (CSG) developments in the Surat and Bowen basins. This is looking to fill the market gap created from the depletion of more easily accessible resources. Typically these are termed '*conventional*' due to the method of extraction, in which, the natural permeability of the reservoir and pressure difference between the subsurface and surface is sufficient for extraction. Contrary to this, '*unconventional*' is used to describe storage sites such as coal seams, shale rock and tight sandstone where the system requires artificial manipulation for feasible production. In coal seams, the initial dewatering phase is an example of this, while tight reservoirs, like shale and deep sandstone, may require induced fractures to enhance permeability and ultimately create connection pathways to the wellbore. Figure 1.1 provides an example of how a conventional reservoir may be formed with permeable sandstone beneath a cap-rock or other form of low permeability seal. The unconventional resource depicted in this figure can be seen to have a more complex well trajectory with induced fractures into the source rock to access previously inhibited gas reserves.

Figure 1.2 shows the depletion of conventional reserves in South East Queensland and the CSG developments that are providing for this deficit [11]. Here, one can observe rapid growth in both the Surat and Bowen basins after CSG production initiated. This additional production has allowed the trend of gas extraction to continue on an upward curve after the depletion of the conventional Cooper and Eromanga basins. For resources such as CSG from Queensland to continue to compete in the global market it is essential that production occurs efficiently. To this end, the development of accurate prediction and modelling tools specifically designed for the extraction of this unconventional resource are required.

A particular area of note, is the need to accurately assess the bottom hole pressure (BHP) of CSG wells in the field. The ability to monitor and calculate this pressure provides essential information with regards to the effective design of well completions and artificial lift systems as well as providing a key boundary condition in reservoir and surface process simulations [12–14]. Poor estimations of this can lead to early onset of liquid loading in the wellbore, reduced efficiency of the extraction process and potential damage to the reservoir if managed incorrectly [14, 15].

The pressure gradient along the wellbore is dependent on a number of factors and becomes complicated based on the fluids and phases present, the flow regime and the direction of flow. Dissimilar to more conventional gas resources, CSG extraction techniques create a counter-current flow phenomena in the wellbore. The cause of this lies in the annular construction of the well in which a central casing is used to pump brine from the subsurface environment allowing for gas desorption and extraction

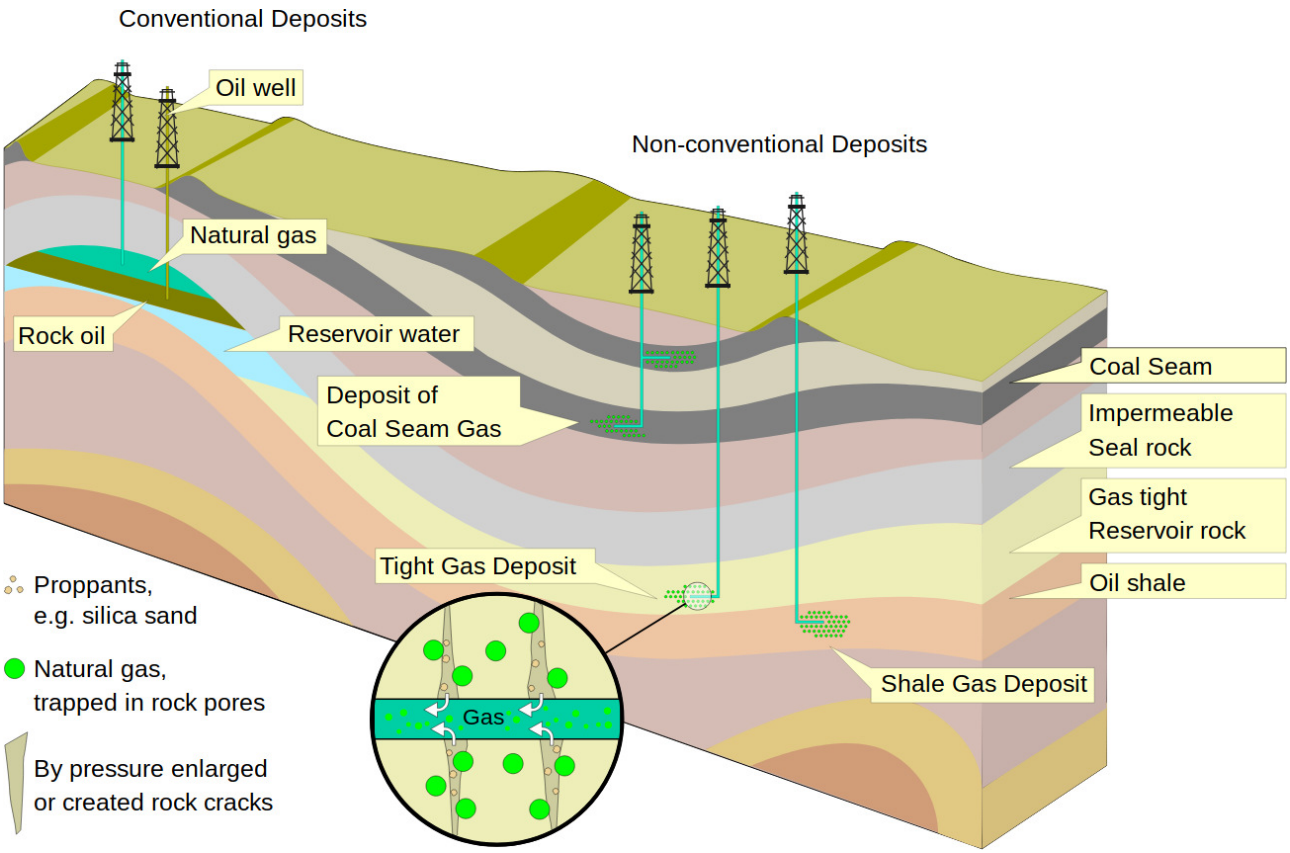

Figure 1.1: Schematic indicating the form in which conventional gas is typically captured within a reservoir in comparison to unconventional gas. Reproduced from [10] under the Creative Commons Attribution-Share Alike 4.0 International license.

through the outer annuli. This forms a downward flow of liquid and a countering upward flow of natural gas in the annulus tubing [16].

Typically when two phases flow together in a tubular pipe, the interface between them can be observed to form characteristic topological patterns called flow regimes. Experimental works indicate that at low gas flow rates, small bubbles can be observed to propagate through a liquid-continuous system in a regime termed bubbly flow. With a continued increase in gas flow, the coalescence of bubbles is promoted and *Taylor bubbles* form which occupy almost the full cross-section of the pipe. Characteristically, these bubbles are surrounded by a thin liquid film in contact with the wall and are followed by a liquid slug giving it the name slug or intermittent flow. With higher flow rates still, these large bubbles breakdown and a churn-type transitional regime occurs. From here the gas eventually forces the liquid into a film about the pipe wall known as annular flow. This covers the general terminology of flow regimes seen in vertical co- and counter-current flow. However, a phenomenon unique to counter-current flow is observed with a further increase in gas flow where the liquid film is reversed and moves in a co-current direction, presenting the flooding-limit at which counter-current flow can exist.

In order to further understand these confined systems containing multiple fluids, the study of multiphase flows is required. Predicting how multiphase systems behave has intrigued the scientific community with applications observed in both industrial and natural processes. It is studied by

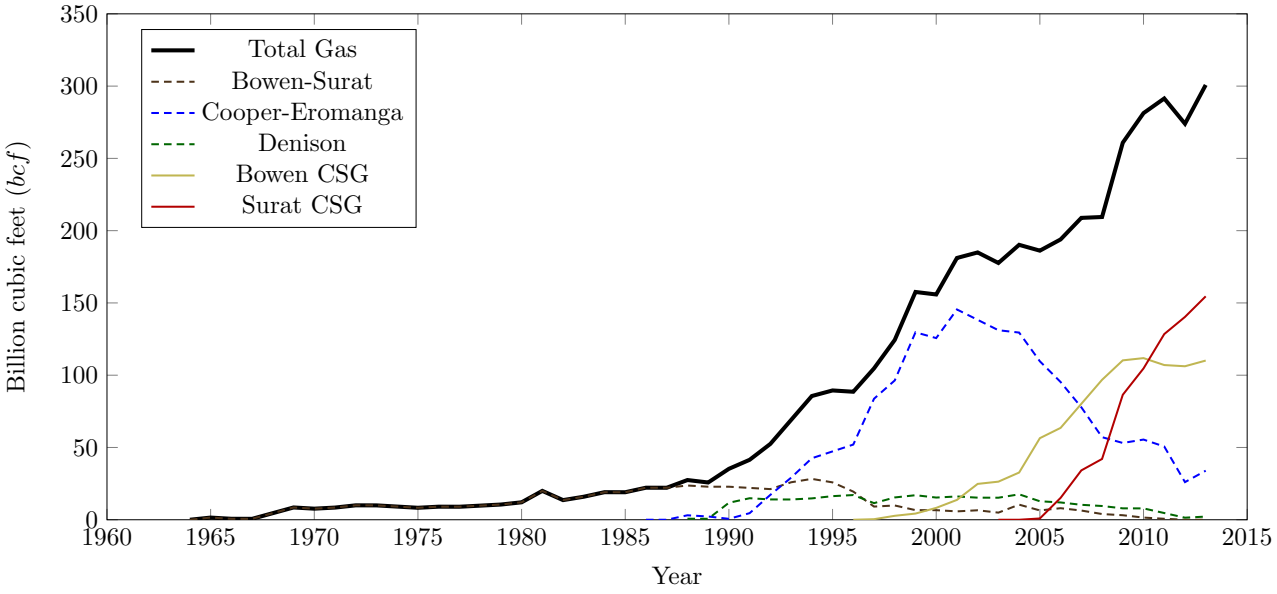

Figure 1.2: The development of fields in Queensland, Australia comparing conventional reserves to coal seam gas production. Recreated from Towler *et al.* [11].

physicists and applied mathematicians looking to further their knowledge of fundamental interactions. Additionally, engineers are dependent on the analysis of these systems to optimise designs and improve operational performance in practice. Currently, the oil and gas industry extensively use one-dimensional (1D) computational models that are reliant on averaging and correlated closure relations to simplify the three-dimensional (3D) system [17]. This may work well for large-scale, homogeneous pipelines stretching hundreds of kilometres, but limits the applicability when looking at a system that experiences a varied flow configuration, whether this is due to complex fluid types, piping geometry and or flow directions, for which the derived correlations may not be valid. More recently, the use of two-dimensional (2D) and 3D computational fluid dynamics (CFD) has been used for the analysis of multiphase pipe flow. It has allowed for improved accuracy of 1D models by investigating closure relations over ranges of flow parameters that would be infeasible to investigate experimentally [18].

The use of CFD simulations has become a core aspect of scientific modelling giving detailed insights into complex and transient systems. However, the extension from single phase to multiphase flows comes with a number of key distinctions that can be problematic for numerical evaluation. Namely, it is typical of such systems to consist of at least two fluids that may differ substantially in properties such as density and viscosity over an infinitesimally thin interface. This interface is preserved as the equilibrium between the thermodynamic pressure imbalance due to molecular interactions and the surface tension forces [19, 20]. In order to deal with these problems numerically this discontinuity is often approximated as a smoothly changing function over a finite number of computational cells that is advected with the flow. Careful treatment of the sharp gradients within this diffused interface is often necessary in the form of highly resolved grids or additional stabilisation techniques.

The discretised solutions to the Navier-Stokes equations (NSE) have long been a common approach to CFD. These methods (such as finite difference, element or volume) provide a high degree of accuracy and have been used extensively in both research and industry applications. However, it has been

noted that these solvers can face "operational complications when applied to multiphase flows of real scales" [21]. One reason for this is the non-linearity and high degree of coupling between the NS equations, and this along with discontinuities at phase interfaces can limit the applicability of these methods. On the other hand, kinetic based techniques such as the lattice Boltzmann method (LBM) have proven themselves as a promising alternative for the problem of computational multi-fluid dynamics (CMFD), these will be discussed in detail in Chapter 3 [22–28].

1.1 Industrial context

The industrial problem that this research will look to address is often referred to as a production technology issue in the oil and gas sector. Here, one is concerned with the transport of natural resources from the subsurface environment in a safe, efficient and economical manner. To do this, production engineers must have a detailed understanding of the wellbore dynamics as this impacts greatly on optimal pump rates and predictions of the fluid quantity to be processed through the surface network. The interest in unconventional gas has grown with the depletion of conventional reserves, and with this comes the requirement of new techniques for extraction. This is evident in CSG where counter-current flow is observed down-hole in pumped wells. Work from Firouzi *et al.* [29] has highlighted the level of error present in naively applying co-current flow correlations to predict the pressure drop through such a system. With recent work in the literature still improving flow correlations [18], it is clear that there is still a lack of fundamental knowledge not only in the unconventional space, but in general multiphase transport. This fact is discussed and reviewed in Chapter 2.

Figure 1.3a shows an example configuration for a conventional well, in this an annular packer is typically used to isolate the central production string through which all fluids are produced. In comparison, Figure 1.3b shows a pumped CSG well which produces gas through the annulus while lowering reservoir pressure through the extraction of water in the tubing string. In both of these diagrams, it is evident that the wellbore provides the critical link between two well developed areas of engineering, namely reservoir and production. Reservoir or subsurface engineering deals with upstream issues surrounding the drainage of fluids through the reservoir. Downstream of the well, process engineers take over surface operations, controlling the flow of produced materials from the wellhead to delivery points. Understanding the flow within the wellbore itself provides key boundary conditions for both of these areas, without which there is inherent error down-hole and on the surface prior to even considering which predictive tools are to be used.

In addition to providing accurate boundary conditions for reservoir and surface operations, the design of completions is also dependent on the wellbore flow dynamics. The pressure drop along the well impacts the inflow performance ratio (IPR) which is used in determining parameters such as optimal pipe geometries and requirements for down-hole lifting equipment. The selection of pump capacity is critical for efficient production, especially if one wishes to maintain a particular flow regime in the well. Therefore, due to the associated impacts throughout the life of a well, from design through

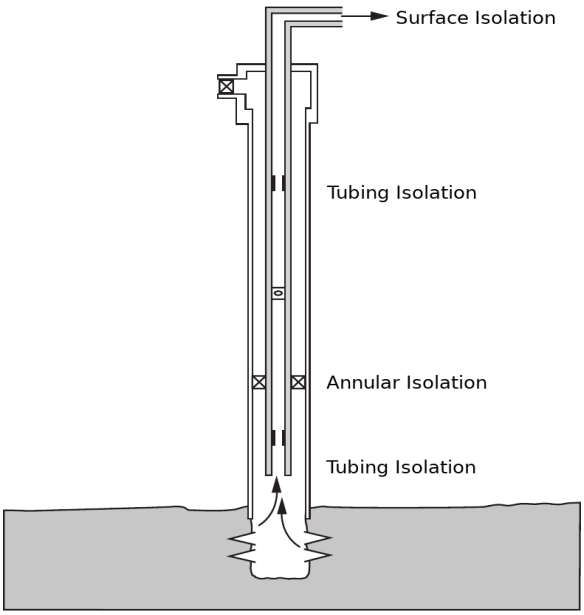

(a) Conventional well completion

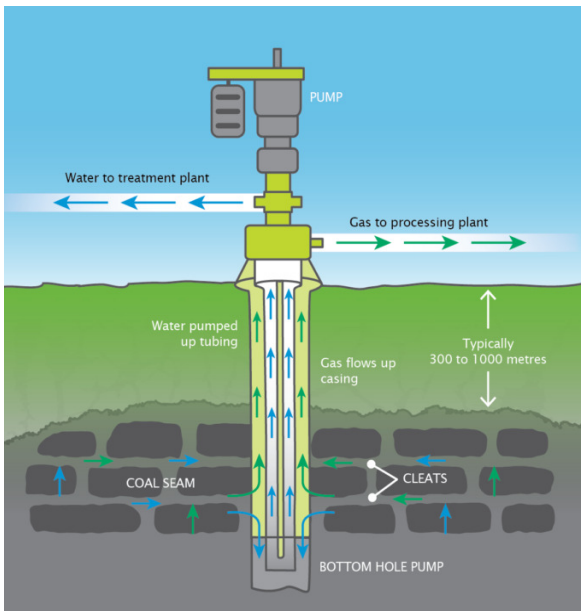

(b) Coal seam gas well completion

Figure 1.3: A conceptual schematic of completions indicating the difference in flow configurations between a conventional and unconventional well. Of particular note here is the flow directions from the reservoir in each case, (a) co-current (Recreated from [30]) vs. (b) counter-current (Image from [31]).

to deliverance, it is understanding the interaction of liquids and gases in this critical link between the reservoir and surface that this dissertation develops.

1.1.1 Industrial modelling strategies

With the universal existence of multiphase flows in the extraction of oil and or gas from subsurface environments, various *multi-fluid* modelling and simulation techniques as well as software packages have been developed. These tools were initially based on purely empirical correlations before developing into phenomenological or otherwise termed *mechanistic* models. Mechanistic models incorporate physical descriptions of the flow in an attempt to close the set of governing equations. This improves the ability for models to predict both pressure gradients and phase fractions along the wellbore in the absence of sufficient experimental data. For co-current flows, researchers have attempted to homogenise the system by considering two separate phases as a '*mixture-phase*' with averaged fluid properties. A slip-velocity based on empirical parameters is often introduced to cater for varying phase velocities and the formulations are generally classified as *drift-flux* models [32, 33]. With the development of computational capabilities, the *two-fluid* model has also seen widespread use for predicting multiphase system behaviours. These methods will be reviewed in detail in Chapter 2. Here, two predominant industry codes are highlighted as examples of commonly used software packages:

- the simulator OLGA®, originally designed by Dag Malnes and Kjell Bendiksen at the Institute for Energy Technology (IFE) in Norway, with rights currently held by Schlumberger after the acquisition of SPT Group; AND

- the simulator LedaFlow®, that was developed in Norway by Sintef in collaboration with Total and Conoco Phillips.

In-built in these software packages generally exist a series of checks to predict an expected flow regime at certain locations in the system before using this to discern between appropriately tuned flow correlations. From this, key flow features such as pressure drop, liquid hold up and flow rates along pipelines can be predicted. This is required as the flow correlations are regime-dependent and as such, the regime must be known *apriori*. This can prove problematic when new fields or extraction techniques are developed as both the correlations for predicting the regime and flow behaviours thereafter have been developed from significant experimental tuning.

In more recent years, the advent of interface tracking methods (ITM) along with the computational ability to make use of them, has allowed for multiphase simulations to be conducted independent of flow regime predictions. In this family of methods, a governing partial differential equation (PDE) is introduced to describe the evolution of fluid-fluid interfaces. These formulations are typically referred to as *one-fluid* models and were introduced as early as the 60s with the Marker-and-Cell method of Harlow and Welch at Los Alamos [34]. Here, the interface is tracked such that fluid properties on either side are known and resultantly, the exchange of mass, momentum and energy between phases can be accurately determined. In order for this to be successful, sufficient resolution surrounding an interface is required and numerical techniques to resolve sharp gradients that can occur due to varying fluid properties must be implemented.

1.1.2 A brief history on interface modelling techniques

With the associated difficulty of multiphase experiments, the need for numerical modelling has long been realised resulting in significant research efforts. Here, a few of the major developments are presented to give the reader a brief history and more fundamental motivation for certain sections of work in this thesis. Initial efforts looked to simplify the problem by considering either *Stokes flows*, in which a large viscosity dominates inertial forces or *inviscid flows*, where one neglects viscous effects. Birkhoff [35] presented one of the first attempts to predict the dynamics between two fluids by assuming inviscid, irrotational flow. Here, a heavy fluid was modelled over the top of a lighter fluid within a gravitational field resulting in the now, well-known Rayleigh-Taylor instability. This paper is highlighted here in particular as this flow configuration was one used to analyse the solver presented in the chapters to follow. The techniques used to solve inviscid and Stokes flow systems are typically approached with boundary integral or element methods.

To bridge the gap between zero and infinite Reynolds number flows, the Marker-and-Cell (MAC) method was formulated in the Los Alamos labs [34]. This method was tested against the Rayleigh-Taylor instability and numerous other configurations in the years to follow. A shortcoming of the method was the potential inaccuracies of placing marker particles through the domain, from which the idea of a marker function was born. Hirt and Nichols [36] coined the name volume-of-fluid (VOF) to this effect, and so began the development of one of the most active streams of one-fluid simulations

conducted today. One difficulty associated with this progression is the numerical diffusion associated with advecting a marker function through the domain that has been averaged within computational cells. This produces a need for reconstruction schemes to define the shape of the interface, restricting its advection to a new cell to be physically consistent.

Connecting the philosophies of the MAC and VOF method, Unverdi and Tryggvason [37] used a series of linked marker points to identify the fluid-fluid interfaces and advect material properties. However, the domain was still updated with a fixed grid, which is in line with the computations of the VOF method. Moving away from these discontinuous or sharp-interface approaches, the level-set (LS) [38] and phase-field methods [39] used a diffuse interface and an average contour to identify the interface location. These two methods share a number of similarities, but are formulated from a fundamentally different point of view. The LS method uses a smoothed interfacial zone for numerical purposes only, whereas the phase-field approach is conducted so that this region is thermodynamically consistent. Phase field methods present one of the key techniques used in this thesis and will be thoroughly examined throughout.

Moving away from explicitly tracking the interfacial dynamics of the multiphase system, early LBM methods were able to recover fluid separation from incorporating intermolecular interactions. The colour-gradient method (CGM) [40] and pseudo-potential model [22, 41] were amongst the first to use this idea. Since the introduction of multiphase LBMs, there has been significant development including those that make use of interface tracking methods like VOF, LS and phase-field models.

1.2 Research question

This thesis aims to answer questions that are related both to the industrial application of fluid flow in a CSG well and those posed from the theoretical basis of the LBM and multiphase simulations. However, the overarching research question motivating this work is:

What are the key factors influencing the pressure drop from the bottom of an unconventional (CSG) well to the surface and how can this be accurately predicted?

The initial phase of the project was focused on the development of a numerical technique capable of modelling the range of flow regimes expected in a CSG wellbore. Here, the applicability of LBM to liquid and gas flows within pipes of real scales was investigated. The model developed and proposed for this is highlighted in Chapter 4 and provides a possible solution for how the pressure drop may be more accurately predicted.

From here, the developed LBM was applied to analyse current assumptions used by 1D mechanistic-type models, relating in particular to the slug flow regime. This was conducted to assess the accuracy of closure correlations for counter-current annular flow as well as to present a methodology for which new correlations can be formed. The value of CMFD in the oil and gas industry is highlighted in this work, with the potential to save cost and time through reduced experimental testing and development of fundamental knowledge.

1.3 Project aims and objectives

This thesis looks to address limitations currently existing in the simulation of multiphase flows. Developments in this area could lead to numerous engineering advances in areas such as nuclear reactor design, chemical processing and subsurface resource extraction as well as in the understanding of natural phenomena including rain drop formation and coastal wave dynamics. In this dissertation a particular focus has been placed on the extraction of unconventional resources where efficient transport of hydrocarbons is essential for feasible production. As such, this research has two primary aims:

(1) develop a fully resolved computational model capable of simulating two phase flows with high density and viscosity ratios, and
(2) use this modelling capability to gain key insights into the counter-current flow that occurs in the process of extracting natural gas from coal seams.

In order to achieve these aims and answer the overarching research question, a number of interim objectives have been constructed:

1. Define the state-of-the-art in CMFD modelling;
2. Develop, verify and validate a numerical model against base-case multiphase flow scenarios;
3. Demonstrate the capability of the model to replicate liquid-gas flows in dynamic scenarios, as well as to capture the fundamental behaviours expected in flow regimes applicable to a CSG well;
4. Investigate the effect of annular pipe configurations on the slug flow regime;
5. Investigate the effect of various system configurations including liquid velocities, piping geometries and inclination angles;
6. Propose a methodology for which improved closure relations can be formulated for mechanistic models applicable in the natural gas industry.

1.4 Methodology and scope of works

In this research, resolved simulations of liquid-gas flows were required to develop understanding of how separate fluid phases interact within a confined environment, namely piping configurations for the extraction of natural gas. Here, the objective was to move away from models that imitate momentum exchange between phases and directly resolve the interfacial dynamics. This was conducted to assist in determining whether existing models were applicable in a counter-current flow environment as well as to provide a cost and time effective methodology for the development of such closure models.

In order to accurately describe the interfacial dynamics, a partial differential equation (PDE) was introduced in the form of the Allen-Cahn equation [42, 43]. This is in addition to resolving the

hydrodynamics of the system through the Navier-Stokes equations. In order to solve the governing dynamics, the LBM provided a mature alternative to discretisation techniques such as the finite difference, finite element and finite volume methods. For this particular case, the LBM provides a mesoscopic level in which to build surface force interactions. This has been shown to provide favourable outcomes in terms of interface reconstruction, achieving results that require hybrid methods in certain finite volume frameworks [3]. Additionally, the LBM is intrinsically dynamic allowing transient simulations, a requirement to analyse flow regime transition in which the time-dependent scenarios of coalescence, break-up and instability growth are of key interest.

The lattice Boltzmann algorithm lends itself to efficient implementation on parallel architectures, which is discussed in Chapter 3. Here, the '*open-source*' framework, TCLB[1], within which the models developed and tested in this thesis are available. This framework was designed by Dr. Ł. Łaniewski-Wołłk for rapid model development and deployment on multi-GPU and CPU systems [44]. The computational advantages gained from the locality of the algorithm, in particular on GPU-architectures, was one of the inspirations behind the model proposed in Chapter 4.

It is important to identify the limitations placed on the scope of this dissertation, so as to have a complete description of the project. In simulations, fluids are assumed to be immiscible, isothermal and Newtonian unless otherwise stated. The scope of works starts with the presentation of a phase-field LBM specifically designed for systems exhibiting high density and viscosity contrasts as well as moderate Reynolds numbers. Verification of the model through well established benchmarks is conducted prior to validation with relevant experimental findings. Following this, the model is applied to analyse certain closure models and the methodology to improve these is established, however, the development of new closure relations themselves is placed beyond the scope and remains for future investigations.

1.5 Thesis structure

This dissertation contains eight chapters that articulate how the work conducted during this project addresses the aims and objectives outlined. To start with they give an overview of prior knowledge in both the area of multiphase flow modelling and lattice Boltzmann theory. Following this, a model designed for liquid-gas flows along with its verification, validation and application to scenarios relevant to the natural gas industry is presented. Chapter 2 introduces the reader into the fundamentals of multiphase flow in general as well as in confined environments, such as a wellbore or pipeline. The fundamentals of LBM are described in Chapter 3 starting from single phase flow and progressing into multiphase methods. These are extended in Chapter 4 where an LBM capable of solving multiphase flows with large density and viscosity contrasts is formulated in a 2D setting. Chapter 5 builds on this theory to stabilise the formulation in 3D and presents a detailed validation study of a Taylor bubble propagating within a vertical tube. Investigation studies are then conducted in Chapters 6 and 7 to analyse the behaviour of Taylor bubbles over a range of fluid parameters, pipe configurations and flow

[1] `https://github.com/CFD-GO/TCLB`

directions. The outcomes of the thesis, the major contributions and directions for future work are summarised in Chapter 8.

Part of the following publication has been incorporated as Chapter 2 - Fundamentals of Multiphase Flow.

1. [5] Benjamin Wu, Mahshid Firouzi, **Travis Mitchell**, Thomas Rufford, Christopher Leonardi and Brian Towler, A critical review of flow maps for gas-liquid flows in vertical pipes and annuli, *Chemical Engineering Journal* 326, 350-377, 2017.

Contributor	Statement of contribution	%
Travis Mitchell	writing of text	15
	proof-reading	20
	theoretical derivations	10
	numerical calculations	75
	preparation of figures	60
	initial concept	15

This paper was a group effort to review experimental, mechanistic and simulation techniques related to multiphase pipe flow. Additionally, a large body of data was collected from flow loop experiments in the literature in order to compare existing models of regime prediction. The main contributions from the author of this dissertation were around the review of simulation approaches and the data analysis for flow regime prediction. The paper itself is not directly included in this chapter, but parts of work here contributed towards the above referenced manuscript.

Chapter 2

Fundamentals of Multiphase Flow

"Mathematics is just another way of predicting the future."
Ralph Abraham

This thesis is primarily focused on the LBM, which is a kinetic approach to fluid mechanics. However, a detailed understanding of the macroscale hydrodynamics is crucial as it is this behaviour that one looks to mimic in simulations. In this chapter, a mathematical description of the NSE is first presented before a set of useful dimensionless numbers for multiphase flow are introduced. From here, the scope of review is focused on multiphase pipeline flows and the fundamental work conducted in this area. Moving more towards direct modelling of multiphase flows, the chapter analyses potential techniques for simulating the dynamics of fluid-fluid interfaces and the developments to date in the field of LBM.

2.1 Governing equations

To solve a subset of fluid flow problems, one can start by considering three fundamental laws of physics. In the case of isothermal fluids, this reduces to the conservation of mass and Newton's second law as the conservation of energy can be omitted,

$$\partial_t \rho = 0, \tag{2.1}$$

$$\rho \frac{d\mathbf{u}_i}{dt} = \sum \mathbf{F}_i. \tag{2.2}$$

There is work, for example by the likes of Michaelides [45], that require up to six principles to resolve the desired level of physics in the flow of heat and mass. This includes the conservation of mass, linear momentum, angular momentum, energy, space and "from the second law of thermodynamics, the principle of entropy increase of an isolated system" [45]. However, for the purposes of this explanation, Equations 2.1 and 2.2 are sufficient. In these, ρ, $\mathbf{u}_i$ and t are a fluid particles density, the velocity of particle, i, and a measure of time, respectively. The force acting on a particle, i, is given by $\mathbf{F}_i$ and is

the net contribution from all external forces and attractions. Similar descriptions for the NSE can be found in numerous texts in the literature [20,46,47], but here it is presented to give the reader sufficient knowledge of multiphase flows for the following chapters. Equations 2.1 and 2.2 take a *Lagrangian* perspective that accounts for the movement of each fluid particle within the simulated system. When one considers the quantity of fluid molecules that may be present in a simulation, it is not hard to see that this may quickly approach the current limit of computational capability. Fortunately, for practical fluids relating to this work, an *Eulerian* perspective can be used where the fluid is viewed as a continuum, here the analysis is of a fixed volume in space rather than individual molecules.

To extend the equations above to the new reference frame, an integration over the volume (V) is required. The translation of Equations 2.1 and 2.2 require one to equate the change of a parameter in the volume with the fluxes in and out. For the conservation of mass, the change in the integral of density over the volume with time is equated with the mass in and out of the volume in that time,

$$\partial_t \int_V \rho dV = -\int_S (\rho \mathbf{u}) \cdot \mathbf{n} dS. \tag{2.3}$$

A similar methodology can be applied to Newton's second law, but in this case the momentum flux is used in place of mass and surface and volumetric forces (F_s, F_v respectively) are separated,

$$\partial_t \int_V (\rho \mathbf{u}) dV = -\int_S (\rho \mathbf{u}\mathbf{u}) \cdot \mathbf{n} dS + \int_V F_v dV - \int_S F_s \cdot \mathbf{n} dS. \tag{2.4}$$

To achieve the well known NS equations, the divergence theorem is applied to the surface integrals and the volume of analysis is taken towards zero,

$$\partial_t \rho + \nabla \cdot (\rho \mathbf{u}) = 0, \tag{2.5}$$

$$\partial_t (\rho \mathbf{u}) + \nabla \cdot (\rho \mathbf{u}\mathbf{u}) - \nabla \cdot (-p\mathbf{I} + \tau_N) - \rho \mathbf{g} = 0. \tag{2.6}$$

In Equation 2.6, the surface force has been evaluated into components of stress, namely the viscous, τ_N, and normal stress as a result of the pressure, p, while the volumetric force is equated as a gravitational acceleration, $\mathbf{g}$. To solve this set of PDEs, often simplifying assumptions are made both for ease of implementation and computational efficiency. Some common assumptions include the incompressibility of the fluid, such that Equation 2.5 reduces to describing a divergence-free velocity field, as well as the proportionality between the viscous stress and strain tensor, in this case, a *Newtonian fluid* [21],

$$\tau_N = \mu(\nabla \mathbf{u} + \nabla \mathbf{u}^T), \tag{2.7}$$

where μ is the dynamic viscosity. As a result, Equation 2.5 and 2.6 can be written as,

$$\nabla \cdot \mathbf{u} = 0, \tag{2.8}$$

$$\rho \partial_t \mathbf{u} + \rho(\mathbf{u} \cdot \nabla)\mathbf{u} + \nabla p - \nabla \cdot (\mu(\nabla \mathbf{u} + \nabla \mathbf{u}^T)) - \rho \mathbf{g} = 0. \tag{2.9}$$

One approach used to extend Equations 2.8 and 2.9 to incorporate an interface between phases can be thought of as the addition of boundary conditions (BCs) along a surface (S) within the domain.

These BCs need to be constructed in such a way that surface tension balances the pressure and velocity gradients, and in the case of immiscible fluids, there must be no mass flux through S. To do this, one simply equates the surface force previously discussed with the surface tension and looks at a restriction of the velocity through the interface,

$$F_s = (-p\mathbf{I} + \mu(\nabla\mathbf{u} + \nabla\mathbf{u}^T)) \cdot \mathbf{n}, \tag{2.10}$$

$$\mathbf{u} \cdot \mathbf{n} = 0. \tag{2.11}$$

Therefore, if conventional boundary conditions are applied at the extents of the domain, a general set of governing equations for a multiphase system can be described by Equations 2.8 to 2.11. However, in order to implement these a number of questions still need to be resolved, specifically how to handle the discontinuous jumps in density and viscosity from a numerical point of view as well as the introduction of surface tension forces. One such method to assist with the discontinuous jump, without the imposition of internal boundary conditions is to approximate the change with a characteristic or smoothed *Heaviside* function, commonly approached with the use of an order parameter, ϕ [47]. This is a function that for example, equals zero in fluid A and one in fluid B then varies smoothly between these values over a finite interface,

$$\phi(\mathbf{x}) = \begin{cases} 0, & \text{if } \mathbf{x} \in \text{fluid A} \\ I(x), & \text{if } \mathbf{x} \in \text{close proximity to interface} \\ 1, & \text{if } \mathbf{x} \in \text{fluid B.} \end{cases} \tag{2.12}$$

Here, $I(\mathbf{x})$ can take on different forms depending on how one decides to regularise the interface. Typical formulations can include trigonometric functions or higher order polynomials [21]. This is done as a means to interpolate the fluid properties at each node in the computational domain, which can be found as a function of ϕ. For example the density, ρ, and kinematic viscosity, ν, can be found by,

$$\rho(\mathbf{x}) = \rho_A + (\rho_B - \rho_A) \times \phi(\mathbf{x}), \tag{2.13}$$

$$\nu(\mathbf{x}) = \nu_A + (\nu_B - \nu_A) \times \phi(\mathbf{x}). \tag{2.14}$$

With this defined, it is now important to note the principals behind the force of surface tension and how this is employed in the NSE. In this, two perspectives are generally taken, one from a geometry argument [47–49] and the other from a chemical-potential/free-energy view point [28, 42, 43, 50]. Geometrically, one can view the surface tension as a force that acts to minimise the interfacial surface area. From this thinking, a formulation of the surface tension depending on the local curvature, κ_l, the vector normal to the interface, $\mathbf{n}$, and a surface tension coefficient, σ, can be found,

$$\mathbf{F}_s = \sigma\kappa_l\mathbf{n}. \tag{2.15}$$

To apply this as a fixed (Dirichlet) BC along with Equation 2.10 may look simple in its construction; however, the requirement for this would entail knowing the exact interface location at every point

in time. Additionally, careful consideration of the interface when it is not aligned directly with the discretised computational domain would be required and further complicate the implementation. As such, it is common practice to apply $\mathbf{F_s}$ over a certain interface thickness as a volumetric force. This is referred to as the *continuum surface force* (CSF) approach and can be used in both sharp and diffuse interface methods [49].

The second perspective thinks of the interface construction as being the minimisation of the chemical potential, μ_ϕ, of the system. This is often done based on a Cahn-Hilliard [42] or Cahn-Hilliard-like equation such as that proposed by Allen and Cahn [43]. In this sense, the surface tension is dependent on the gradient of the chemical potential and the order parameter,

$$\mathbf{F}_s = -\phi \nabla \mu_\phi, \tag{2.16}$$

$$\mu_\phi = 4\beta\phi(\phi-1)(\phi-0.5) - \kappa\nabla^2\phi. \tag{2.17}$$

This is not the only form that the chemical potential can take, but in this example β and κ are related to the interface width, W, and the surface tension coefficient by,

$$\beta = 12\sigma/W, \tag{2.18}$$

$$\kappa = 3\sigma W/2. \tag{2.19}$$

Jacqmin [39] developed the potential form for the surface tension force as,

$$\mathbf{F}_s = \mu_\phi \nabla \phi. \tag{2.20}$$

This was done in order to avoid calculating gradients of the chemical potential, effectively enhancing the locality of the numerical method as well as avoiding the numerical stiffness present in this calculation. Additionally, Kim [51] proposed a continuum surface tension force that did not require the use of a chemical potential at all,

$$\mathbf{F}_s = -\kappa|\nabla\phi|^2 \mathbf{n} \nabla \cdot \mathbf{n}. \tag{2.21}$$

Independent of the chosen surface tension derivation, the force is incorporated into the conservation of momentum equation. This results in the multiphase NSE to be solved in the form,

$$\rho(\partial_t \mathbf{u} + \mathbf{u}\cdot\nabla\mathbf{u}) = -\nabla p + \nabla\cdot[\mu(\nabla\mathbf{u} + \nabla\mathbf{u}^T)] + \mathbf{F}_s + \rho\mathbf{g}. \tag{2.22}$$

Further details of surface tension formulations will be given on a model-specific basis when discussing methods that are implemented in the progress of this work. At this stage the above is presented to simply give the reader a listing of potential avenues for incorporating interface forces and an idea of the governing hydrodynamic equations.

2.1.1 Dimensionless groups

The use of dimensionless groups in fluid mechanics has long been a standard in analysing systems of scale and generalising solutions to a wider problem set. Multiphase fluids are no different to this, and

although there remains no globally defined set, there are commonly used groups for certain problems. Additionally, equivalence of the various number sets can be shown under particular transformations (for example Archimedes Number (Ar) and the inverse viscosity number (N_f), $Ar = N_f^2$ [52]). The list presented in Table 2.1 has been constructed to support the work in this thesis. However, it is not exhaustive, and for a comprehensive review of this topic the interested reader is pointed to Awad [53].

Arguably the most common set of dimensionless numbers used to describe a two-phase flow problem (at least in pipe flows) consists of the Eötvös (Eo), Morton (Mo), Froude (Fr) and Reynolds (Re) numbers. However, additional dimensionless numbers that frequently appear in the literature include the Weber number (We) as well as N_f or Ar.

Table 2.1: Summary of dimensionless numbers common in multiphase flow problems (formulations from [53]).

Number	Formulation	Physical Meaning
Eo	$(\rho_l - \rho_g)gd^2/\sigma$	Ratio of gravitational to capillary type forces
Mo	$(\rho_l - \rho_g)g\mu_l^4/(\rho_l^2\sigma^3)$	Along with Eo is used to describe bubble shape
Fr	$u/\sqrt{gd}$	Measure of gravitational and inertial forces
Re	$\rho_l u d/\mu_l$	Ratio of inertial to viscous type forces
We	$\rho u^2 d/\sigma$	Measure of inertial to interface forces
N_f	$\sqrt{\rho_l(\rho_l - \rho_g)gd^3}\ /\mu_l$	Ratio of gravitational to viscous type forces
Ca	$\mu_l u/\sigma$	Ratio of viscous drag to surface tension
Cn	W/d	Ratio of interface thickness to pipe diameter

2.2 Multiphase pipe flow

Due to the scale of modelling required for pipeline flows, specifically in the transport of hydrocarbons, it is not always feasible to resolve the interfacial interactions directly. In place of this, it is common practice in the oil and gas industry to approach the problem from an averaged properties perspective and model the interactions between phases. This can involve using historic data to find empirical predictions, finding a solution to the NSE based on mixture properties or resolving the governing dynamics of both phases weighted by the void fraction, α_i. In these methods, closure relations are required to describe the heat, mass and momentum transfer between phases in order to find accurate predictions of the system behaviour. In order to do this, it becomes highly important to understand which flow regime is present in the pipeline as well as how this affects the phase interactions. The definition of flow regimes comes from the characteristic interface topologies that form in confined multiphase flows [54].

The reliance on models to describe interface interactions often means that new correlations are required for variance in the flow configuration which lends itself to the need for extensive experimental testing. Alternatively, multiphase fluid dynamics has been proven as a possible alternative for these

tests, and it is in this area that this thesis will focus. For completeness, the following sections provide background on the various flow regimes expected in vertical piping, in particular that of annular geometry as well as the current mechanistic models available in literature.

Due to the prevalence of two-phase flow in industrial systems, the study of co-current pipe flow has been extensively investigated and numerous models for predicting liquid hold-up and pressure gradients have been proposed [55–62]. On the contrary, there are only a handful of studies in the literature analysing counter-current, two-phase flow, with the majority focusing on the flooding phenomena and even fewer focusing on annular piping geometries [16]. For a detailed history on the development of modelling techniques the interested reader is pointed towards the work of Lizarraga-Garcia [63].

2.2.1 Flow regime maps and transitions

In the modelling of multiphase fluid flow through a pipe or conduit system, the pressure drop and liquid hold-up tend to be the key parameters of interest [29]. These factors are intrinsically linked to the configuration of the flow and how the phases present interact. In order to recognise this fact, it is common practice to refer to flow regime maps describing what characteristic distribution of phases can be expected [5]. Common classifications of flow regimes in vertical piping include bubbly, dispersed, slug and annular flow. Additional transition stages are often given independent names such as churn flow, which is used to describe the instability of Taylor bubbles as one progresses from slug flow towards the annular regime. The naming conventions and appearance hold for co- and counter-current flow in vertical pipes but are expected to appear at different superficial liquid and gas velocities. As previously mentioned, one phenomena that is unique to the counter-current flow configuration is that of flooding. This occurs when the gas has sufficient energy to reverse the flow of the liquid film in the annular regime presenting the limit of counter-current flow. A sketch of the various regimes can be seen in Figure 2.1.

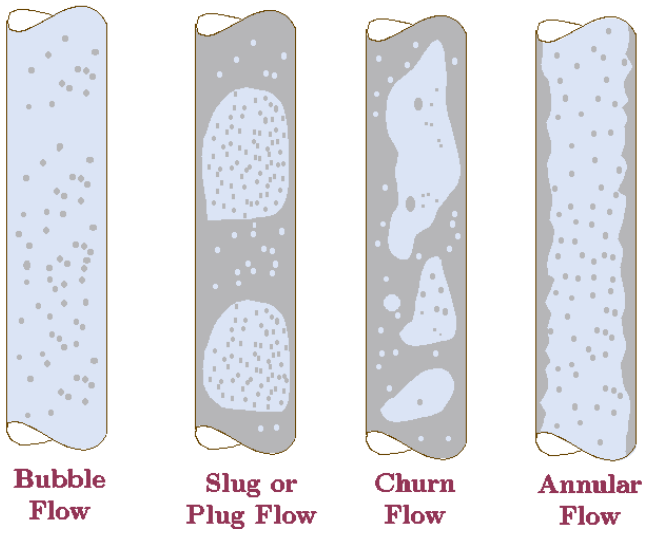

Figure 2.1: Schematic of flow regime topologies showing the generally accepted terminology.

The two-phase flow patterns described are dependent on a number of different parameters, including

the fluid properties (density, viscosity, surface tension) and flow rates as well as geometric restrictions such as pipe diameter and orientation. Flow pattern maps attempt to reduce this problem to a 2-dimensional graph with axes that are dependent on the superficial flow velocities of each phase. An example of a flow pattern map for both co- and counter-current vertical, tubular pipe flow is given in Figure 2.2. The co-current map was produced by Taitel *et al.* [58] and later a counter-current map was presented by Taitel and Barnea [64].

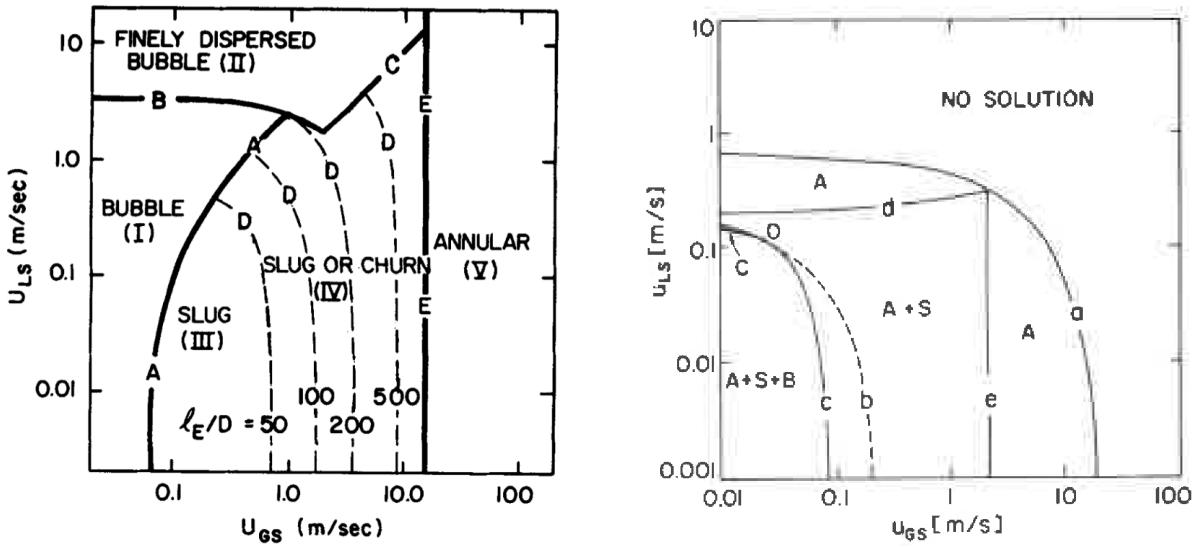

(a) Co-current upward flow map in vertical piping

(b) Counter-current flow map in vertical piping

Figure 2.2: Examples of flow regime maps developed from experiments using air-water in a 5 cm diameter vertical pipe, for (a) co-current [58], and (b) counter-current [64]. Note that in (b) the flow regimes are listed as, A: annular, S: slug, B: bubble and the region of no solution indicates flooding of either the liquid or gas phase.

The first counter-current flow map was presented in 1982 by Yamaguchi and Yamazaki [65] after a series of experimental tests in vertical tubing. Figure 2.3 displays a photograph showing an example of the flow patterns achieved during the study. Yamaguchi and Yamazaki were able to compare the predicted void fraction with the drift flux model and for most regimes, inconsistency of results was observed in comparison with published co-current data. The shortcoming of the correlations to transfer directly to the counter-current regime has been noted by the authors and can significantly impact flow regime, liquid hold-up and pressure gradient predictions.

One of the key benefits of the flow maps is the ability to quickly assess the regime based on superficial velocities. In order to give the reader an idea of how the transition lines are generated, parts of the model presented by Firouzi *et al.* [16] are reviewed here. Starting from the bubble flow region, the progression to slug flow is assumed to occur due to the coalescence of cap bubbles reaching a void fraction of 0.2 at which point a Taylor bubble is postulated to have formed [66]. It should be noted that other models exist which take transition void fractions between a much larger range, for example, Taitel *et al.* [58] assumed the void fraction for which a Taylor bubble would form was dependent on the superficial velocities, ranging from 0.25 to 0.53. Taking the assumption from Caetano [66] along with the correlated rise velocity of a gas bubble in a swarm, the function for the transition line can be

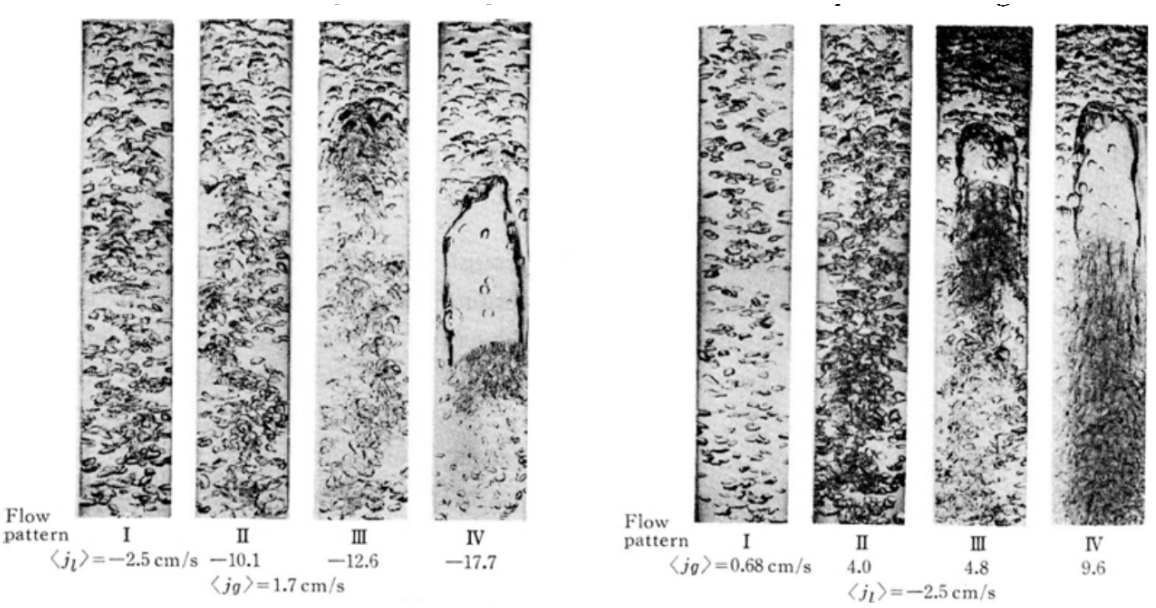

Figure 2.3: Photographic image of the experimental observations of Yamaguchi and Yamazaki (1982) displaying the various flow regimes achieved.

written as,

$$u_{SL} = 0.33u_{\infty} - 4u_{SG}, \tag{2.23}$$

where u_{SL} and u_{SG} are the superficial liquid and gas velocities respectively. The rise velocity for a single bubble, u_{∞}, is defined from the work of Harmathy [67] as,

$$u_{\infty} = 1.53\left[\frac{(\rho_L - \rho_G)g\sigma}{\rho_L^2}\right]^{0.25}. \tag{2.24}$$

Different approaches have been used in the literature to determine the transition from slug to annular flow. Here, the view of Taitel and Barnea [64] is highlighted in which a flooding criterion is applied to the relative velocity of the liquid film and the Taylor bubble. This implies local flooding is the cause of transition, when this condition is met for the superficial gas and liquid flow rates, the flooding line above which "no solution" to the equations can be obtained (as seen in Figure 2.2). The particular flooding criterion used in Taitel and Barnea [64] and Firouzi *et al.* [16] comes from the semi-empirical equation from [68],

$$(\hat{u}_{SG})^{0.5} + m(\hat{u}_{SL})^{0.5} = C, \tag{2.25}$$

where m and C are empirical constants and the hat indicates dimensionless velocities defined as,

$$\hat{u}_{S\alpha} = u_{S\alpha}\sqrt{\frac{\rho_\alpha}{gD(\rho_L - \rho_G)}}, \qquad \alpha \in G, L. \tag{2.26}$$

Other approaches such as that from Mishima and Ishii [69] describe the instability of the Taylor bubbles to be a result of the liquid slug size. In this sense, if the slug length is insufficient to slow the falling liquid film, it may disrupt the subsequent bubble and eventuate into a churn regime.

2.2.2 Mechanistic pressure gradient models

When modelling two-phase pipe flow, the interest generally lies in the void fraction or liquid hold-up profiles and the resultant pressure drop in the system. It is common to express the pressure drop in gradient form, in which it is the summation of hydrostatic pressure, frictional and acceleration losses expressed as,

$$\left(\frac{dp}{dz}\right)_T = \left(\frac{dp}{dz}\right)_G + \left(\frac{dp}{dz}\right)_F + \left(\frac{dp}{dz}\right)_A . \tag{2.27}$$

This is obtained through the addition of momentum equations for each phase, resulting in the steady state mixture equation presented. Lumping the momentum equations together in this sense is the fundamental difference between a two-fluid and some mechanistic or empirical models. Namely, an empirical model will look to determine the flow regime and directly apply an experimentally-tuned expression to solve for the pressure gradients. A mechanistic approach would look to derive the components of Equation 2.27 from first principles in the hope that it can be extrapolated further from the benchmark and or lab conditions. Closure models describing bubble flow velocities and certain features of the expected flow regime are typically required in this process. The two- (or multi-) fluid model writes a NSE for each phase present but includes phase interactions as a source and or forcing term. It is noted that correlations are still required to model the phase interactions but the increased level of physics incorporated has seen both mechanistic and two-fluid techniques gather widespread support, appearing in commercialised codes such as OLGA®.

The two overarching philosophies for existing multiphase flow models can be described as homogeneous, where mixture properties are used, and separated, where contributions from each phase are accounted for. Homogeneous models like that of Hagedorn and Brown [55] were initially used in the design of proper tubing sizes and to predict well performance. Separated models can be either empirically based [56, 57, 70, 71] or come from a mechanistic approach [62, 72, 73]. As the mechanistic models are built from considerations of the basic fluid mechanics, it is argued that they can be extrapolated to new flow conditions with similar levels of confidence. However, these models can be computationally expensive and still yield poor results when applied in the field [74]. In addition to this, the benchmarks for these models do not typically cover flow configurations expected in a CSG well. It was shown by Firouzi *et al.* [16] that extrapolating previous mechanistic models to the counter-current, annular flow expected in a pumped CSG well provided insufficient results and further research was necessary. This may currently be the case, but one could hypothesise that as mechanistic models are based on first principles, perhaps it is the closure relations rather than the governing equations that need to be re-developed.

In order to currently predict the pressure gradient, models first determine the expected flow regime before formulating expressions for the hydrostatic pressure as well as frictional and acceleration losses. For *bubble* flow, where gas is dispersed through a continuous liquid phase, the acceleration losses are typically neglected [56, 70] and the gravitational and frictional losses can be calculated for a vertical

annular pipe as [16],

$$\left(\frac{dp}{dz}\right)_G = g\rho_m, \tag{2.28}$$

$$\left(\frac{dp}{dz}\right)_F = \rho_m u_m^2 \frac{2f}{D_C - D_T}, \tag{2.29}$$

where D_C and D_T are the diameter of the casing and tubing, respectively. The mixture velocity is determined as, $u_m = u_{SL} + u_{SG}$, while the mixture density is given by, $\rho_m = \rho_L H_L + \rho_G(1 - H_L)$, where H_L is the liquid holdup. The friction factor, f, is dependent on wellbore geometry, which is characterised as $D_R = D_T/D_C$, fluid mixture properties and velocity with expressions given by Caetano *et al.* [60]. It is assumed here that the superficial velocities are measured quantities, leaving the liquid holdup as the unknown to be determined. This is done using Equation 2.30, which relates the rising velocity of gas bubbles, u_G, in a swarm to the continuous liquid, u_L,

$$u_\infty H_L^{0.5} = u_G + u_L. \tag{2.30}$$

Now replacing the average velocities with superficial and rearranging Equation 2.30 gives,

$$H_L(U_{LS} - u_{GS}) - U_{LS} + u_\infty H_L^{3/2}(1 - H_L) = 0, \tag{2.31}$$

the solution to which provides the liquid holdup and ultimately the pressure gradient through the system.

The *slug* flow regime is typically analysed as a series of slug units that consist of a leading Taylor bubble and the liquid slug separating it from the trailing Taylor bubble. Figure 2.4 indicates an idealised form of this regime where the length of the Taylor bubble, L_{TB}, liquid slug, L_S, and the full slug unit, L_{SU}, are shown. A number of key characteristics can be gathered from this schematic, with the gas regions consisting of the elongated Taylor bubble occupying the majority of the cross-sectional domain and as dispersed bubbles in the liquid slug. The liquid can be seen present in the slug region, but also in a falling film both on the interior and exterior walls of the annular gap. It is noted here that in an annular piping configuration, the Taylor bubble does not typically occupy the entire cross-sectional area, with a liquid bridge tending to break the symmetry of the system.

In order to analyse the slug unit, the ratio of the Taylor bubble length to the full unit length is defined as, $\beta = L_{TB}/L_{SU}$, and a material balance is made in the two sections; (1) Taylor bubble region, (2) liquid slug region [16],

$$u_{SL} = \beta u_{L_1} H_{L_1} - (1 - \beta) u_{L_2} H_{L_2}, \tag{2.32}$$

$$u_{SG} = \beta u_{G_1}(1 - H_{L_1}) + (1 - \beta) u_{G_2}(1 - H_{L_2}). \tag{2.33}$$

Rearranging Equations 2.32 and 2.33 for the ratio β and equating them results in,

$$\frac{u_{SL} + u_{L_2} H_{L_2}}{u_{L_1} H_{L_1} + u_{L_2} H_{L_2}} = \frac{u_{SG} - u_{G_2}(1 - H_{L_2})}{u_{G_1}(1 - H_{L_1}) - u_{G_2}(1 - H_{L_2})}. \tag{2.34}$$

In addition to this, a mass balance between region (2) and the Taylor bubble for the fluids results in,

$$(u_{TB} - u_{G_2})(1 - H_{L_2}) = (u_{TB} - u_{G_1})(1 - H_{L_1}), \tag{2.35}$$

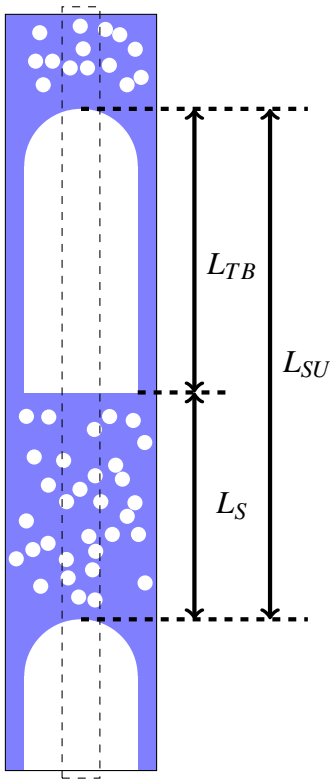

Figure 2.4: The schematic of a slug unit indicating the Taylor bubble trailed by a liquid slug.

$$(u_{TB} - u_{L_2})H_{L_2} = (u_{TB} + u_{L_1})H_{L_1}. \tag{2.36}$$

The rise velocity of the Taylor bubble, u_{TB}, is then assumed as per Caetano *et al.* [61],

$$u_{TB} = 0.345\sqrt{g(D_C + D_T)} + C(u_{SG} - u_{SL}), \tag{2.37}$$

where C is typically taken as unity for co-current downward flows, and the first term on the right hand side represents the Taylor bubble propagation in a stagnant fluid. Keeping in mind Equation 2.34, the mass balance expressions can be re-written to match the denominators as,

$$u_{L_1}H_{L_1} + u_{L_2}H_{L_2} = u_{TB}(H_{L_2} - H_{L_1}), \tag{2.38}$$

$$u_{G_1}(1 - H_{L_1}) - u_{G_2}(1 - H_{L_2}) = u_{TB}(H_{L_2} - H_{L_1}). \tag{2.39}$$

Substituting these into Equation 2.34 and rearranging gives,

$$u_{SL} - u_{SG} + H_{L_2}(u_{L_2} - u_{G_2}) + u_{G_2} = 0, \tag{2.40}$$

where one can now seek expressions for H_{L_2}, u_{L_2} and u_{G_2}.

As depicted in Figure 2.4, there exist gas bubbles within the liquid slug, the velocity of which can be described by assuming a slip velocity between the liquid and gas phases,

$$u_{G_2} - u_{L_2} = u_\infty H_{L_2}^{0.5}. \tag{2.41}$$

The difference between velocities is thus equated to the rise of a single bubble, u_∞, corrected by a swarm factor that is related to the liquid holdup in the slug.

Substituting Equation 2.41 into 2.40 allows the gas velocity in the slug to be removed,

$$u_{SL} - u_{SG} - H_{L_2}(u_\infty H_{L_2}^{0.5}) + u_{L_2} + u_\infty H_{L_2}^{0.5} = 0. \tag{2.42}$$

From here, Equation 2.35 can be used to relate the liquid velocity in the slug to that in the liquid film, which can be analysed to close the set of equations,

$$u_{SL} - u_{SG} - H_{L_2}(u_\infty H_{L_2}^{0.5}) + \left[\frac{u_{TB}(H_{L_2} - H_{L_1}) - u_{L_1} H_{L_1}}{H_{L_2}}\right] + u_\infty H_{L_2}^{0.5} = 0. \tag{2.43}$$

From here, the effect of the liquid film can be analysed by first relating the liquid film velocity, u_{L_1}, to the film thickness, δ. The thickness of the film is taken as constant for bubbles of sufficient length due to a balance between gravity and wall shear forces [58, 61, 64],

$$u_{L_1} = \frac{\mu_l}{4\rho_l}\left[\frac{\delta^{1-C_M}}{C_K\left(\frac{\mu_l^2}{g(\rho_l-\rho_g)}\right)^{1/3}}\right]^{1/C_M}, \tag{2.44}$$

where C_M and C_K are analytically determined for laminar flow as $1/3$ and 0.9086 respectively. For turbulent flow, recommended values in the literature are $2/3$ and 0.0682, respectively. For the film thickness, the correlation presented by Caetano *et al.* [61] is commonly used,

$$H_{L_1} = \frac{4\delta(D_C - \delta)}{D_C^2 - D_T^2}. \tag{2.45}$$

Substituting Equations 2.44 and 2.45 into Equation 2.43 gives an expression where the unknowns are the liquid hold up in both the Taylor bubble and slug region,

$$u_{SL} - u_{SG} + (1 - \frac{H_{L_1}}{H_{L_2}}) - \frac{\mu_l H_{L_1}}{4\rho_l H_{L_2}}\left[\frac{\delta^{1-C_M}}{C_K\left(\frac{\mu_l^2}{g(\rho_l-\rho_g)}\right)^{1/3}}\right]^{1/C_M} + u_\infty H_{L_2}^{0.5}(1 - H_{L_2}) = 0. \tag{2.46}$$

To solve this equation, one can follow the work of Barnea and Brauner [75], where the liquid holdup in the slug zone is assumed constant and equal to the bubble-slug transition point, $H_{L_2} = 0.8$ as measured by Caetano *et al.* [61]. Thus, the liquid holdup in the film can be found and back-substituted to find the other unknown parameters with the exception of the length of the liquid unit. The ratio, β, between the Taylor bubble and slug region can now be found so to close the system of unknowns Taitel *et al.* [58,64] took the slug zone to be a constant length equal to $L_S = 16D$ for vertical co- and counter-current pipes. Firouzi *et al.* [16] followed on from the work of Caetano *et al.* [61], and used this same correlation with the hydraulic diameter as the characteristic length.

To complete the pressure gradient analysis for the slug flow regime, the final assumption is that in comparison to the liquid slug, the pressure drop over the Taylor bubble region is negligible. Therefore, the gradient is determined over the slug length, L_S, and averaged over the entire slug unit, L_{SU} [16, 61, 76], for which the pressure gradient contributions are,

$$\left(\frac{dp}{dz}\right)_G = (\rho_l H_{L_2} + \rho_g(1 - H_{L_2}))\, g(1 - \beta), \tag{2.47}$$

$$\left(\frac{dp}{dz}\right)_F = (\rho_l H_{L_2} + \rho_g(1-H_{L_2}))\, u_m^2(1-\beta)\frac{2f}{D_C - D_T}, \tag{2.48}$$

and the pressure gradient associated with the acceleration was determined to be negligible by Firouzi *et al.* [16].

For the *annular* flow regime, Hasan and Kabir [77] were able to show that a homogeneous flow model produced reasonable results in which the mixture velocity and density is simply given by,

$$u_m = u_{SG} + u_{SL} \tag{2.49}$$

$$\rho_m = \frac{1}{u_m}(\rho_g u_{SG} + \rho_l u_{SL}). \tag{2.50}$$

Taking this model, the thickness of the liquid film is assumed to be negligible resulting in the pressure gradients predicted by,

$$\left(\frac{dp}{dz}\right)_G = \rho_m g, \tag{2.51}$$

$$\left(\frac{dp}{dz}\right)_F = \rho_m u_m^2 \frac{2f}{D_C - D_T}. \tag{2.52}$$

From the pressure gradient models presented here, it is clear that the slug regime is the most complicated from a numerical standpoint. It also relies on a significant number of assumptions and correlations. After proposing a model for the simulation of multiphase flow, this work looks to analyse in detail the behaviour of Taylor bubbles to give key insights into this regime.

2.3 Multiphase simulation techniques

This Chapter has demonstrated so far that multiphase flow in pipes and annuli is sensitive to a large number of parameters whether material, geometrical or operational. This makes comprehensive experimental investigation of the relevant phenomena difficult. Further, many of the experimental studies that have been reviewed exhibit incongruent or contradictory findings. In spite of these challenges, a range of criteria has been developed for the description of the various multiphase flow regimes and their transitions, but these are constrained by their empirical basis.

Simulation methods represent one possibility for improving the description of the various regimes of multiphase flow in industrial-scale pipes and annuli. These techniques are typically founded in the discretisation of widely-accepted analytical systems of equations, which are then solved using computers. Prominent examples in engineering include the finite element method (FEM) for structural mechanics and CFD for vehicle aerodynamics. Some of the major benefits of such numerical methods is that they are deterministic, readily able to explore a wide range of problem parameters, and relatively inexpensive to use once developed.

As an extension to CFD, the use of computational multiphase fluid dynamics (CMFD) has become common practice in a number of industrial sectors such as nuclear, thermal-hydraulics, and petrochemical [78]. This first started with the introduction and development of the two-fluid model

(TFM) in the 1970-80s, which acted as a key driver in the removal of limitations associated with the use of empirically determined parameters for 1D modelling [79–81]. The use of high resolution 3D simulation has allowed for more accurate closure relations in 1D models and insights into transition mechanisms which had previously not been possible. Additionally, the development of interface tracking methods (ITM) provides researchers with the ability to further reduce modelling assumptions, particularly those associated with flow topology and momentum interactions between phases [82].

This section describes and presents examples of how numerous simulation methods have been applied to capture multiphase flow regimes and their development. A detailed description of the governing equations and their discretisation is not attempted here. For more information the interested reader is pointed towards texts such as those by Prosperetti [83] and Martin [46]. Instead, it is the intention that this section elucidates the potential for numerical methods to contribute to the state of knowledge in multiphase flows and highlights the aspects in need of further research.

2.3.1 Numerical methods

The TFM has seen extensive use in commercial codes including OLGA® in the oil and gas industry or the more recent PeTra, as well as in general simulation software such as ANSYS Fluent and CFX. The method relies on phases being treated as interpenetrating continua, and in this sense, continuity equations for each phase are solved throughout a fixed, or Eulerian numerical domain [83]. This can be expressed by weighted continuity equations [131],

$$\partial_t \alpha_i \rho_i + \nabla \cdot (\alpha_i \rho_i \mathbf{u}_i) = 0, \tag{2.53}$$

$$\partial_t (\alpha_i \rho_i \mathbf{u}_i) + \nabla \cdot (\alpha_i \rho_i \mathbf{u}_i \times \mathbf{u}_i) = -\alpha_i \nabla p + \nabla \cdot (\alpha_i \mathbf{T}_i) + \alpha_i \rho_i \mathbf{g} + \mathbf{F}_i^{inter} \tag{2.54}$$

where, the subscript i indicates the phase (gas/liquid/oil) present in the system, α_i, is the void fraction of phase i with $\sum_i \alpha_i = 1$, and $\mathbf{F}_i^{inter}$ represents the interfacial forces that are used to couple interactions between phases. Additionally, $\mathbf{T}_i$ represents the viscous stress tensor while $\mathbf{u}_i$, ρ_i, p and g represent the fluid velocity, density, pressure and gravitational acceleration, respectively. It is noted that closure relations need to be incorporated to account for the phase interactions including drag, lift, wall lubrication, virtual mass and turbulent dispersion forces within $\mathbf{F}_i^{inter}$. For a detailed description of the available correlations for these forces, the reader is referred to the literature [46, 84–86].

The ITMs discussed here are generally implemented on an Eulerian grid, however, these methods only solve one set of continuity equations. The ITMs can be divided further into volume-tracking or front-tracking methods. The volume-tracking methods were developed from the marker-and-cell approach proposed by Harlow [34]. In these methods, for example volume-of-fluid (VoF) [36], level-set (LS) [38] or Phase Field (PF) [42], an order parameter is advected through the flow field to track the location of each phase present in the system. Thus, the volume of each phase is effectively being tracked and the interface can be re-constructed from this information. These methods typically solve a single set of continuity equations weighted by the phase fraction or order parameter, which is tracked by a marker function of the form,

$$\partial_t \alpha + \mathbf{u} \cdot \nabla \alpha = 0, \tag{2.55}$$

The implementation of interfacial interactions, such as surface tension, on an Eulerian grid is performed via a volumetric force in the momentum equation to account for the likelihood of the interface location to be 'off-grid. In this sense the force is applied to a regularised region about the interface, rather than as a force at the interface point only. There are two ways in which the surface tension force can be derived. Firstly, one can consider a geometric argument, in which the force acts to minimise the interfacial area. Alternatively, one can also look at the system from a chemical potential perspective in which the force acts to minimise the free energy functional of the system [42].

In addition to the previously mentioned TFM (also referred to as the Euler-Euler approach or multifluid model if more than two phases are present) and interface tracking techniques, another important class of two-phase solvers is the Euler-Lagrange method. Here, the dispersed phase is no longer captured on an Eulerian grid, but the position of each particle or bubble is tracked and propagated using Newtons laws of motion. The behaviour of the individual bubbles is then coupled to the bulk media, which is solved through the Reynolds-averaged Navier Stokes (RANS) equations. The bulk media can be resolved with varying techniques including the finite volume and lattice Boltzmann methods [87].

In multiphase pipe flows, various flow regimes are observed in which the gas-liquid interface acquires characteristic topologies that affect the phase interactions. As such, the traditional form of methods such as the one-, two- or three-dimensional TFM require correlations to describe the phase interactions, creating a dependence on the flow regime. This means that *a priori* knowledge is required to describe how the flow will manifest before predictions and or simulations are conducted and, therefore, the importance of flow regime maps is realised. Contrary to this, recent works have developed hybrid models that effectively couple the TFM with either a population balance model (PBM) or an ITM in an attempt to eliminate the dependency on prior knowledge of the flow regime. The commercial CFD code, CFX for example has implemented an inhomogenous multiple size group (MUSIG) model [88–90] that has been reported to capture flow regimes consistent with the work of Taitel *et al.* [58] on vertical co-current flow.

One criticism of experimentally generated flow maps is the level of subjectivity that arises in determining the current flow regime. To cater for this, Krepper *et al.* [90] looked to use more objective criteria when analysing co-current vertical flows by measuring the bubble size distributions and radial gas volume fraction profiles. This was performed in both their experimental setup and CFD simulations. They were able to show that their model could quite accurately capture bubble size distributions correlating to the transition from bubble to slug flow.

Parvareh *et al.* [91] used the VOF technique to capture the liquid-gas interface development in co-current flow for both horizontal and upwards vertical flow configurations. Experimental work was performed in small diameter pipes of 2 cm diameter and 4 m length. In the tested cases, the researchers were able to qualitatively match simulation and experimental results for slug, churn and annular flows, but only a limited discussion of the numerics was given.

Dakshinamoorthy *et al.* [92] followed the approach of coupling the TFM with the VOF technique to analyse flow in a large vertical pipe (ID of 189mm) with a superficial liquid velocity of 0.05m/s and

varying superficial gas velocities from 0.1 to 1.0m/s. In this study, the authors were able to qualitatively identify flow regimes consistent with experimental results and without the need for pre-identification. It is noted that slight trouble in identifying a pure bubble regime was observed, with small regions of high void fraction possibly indicating a move to intermittent slug flow, again highlighting the difficulty that can arise in determining specific transition points. Quantitatively the same study compared both pressure drop and void fraction profiles for the slug and annular flow cases that showed reasonable agreement with experimental measurements.

The following sections discuss the aforementioned simulation techniques for simulation of different flow regimes.

Bubbly flow

Modelling of dispersed bubbly flow in pipes is typically approached using either the TFM or an Euler-Lagrangian technique. In order to model this flow regime with an ITM alone, a high-resolution grid is required to fully resolve the bubble motion which leads to excessive computations for practically sized scenarios. However, this approach is often used for direct numerical simulation (DNS) of a finite number of bubbles in order to derive correlations also known as closure models, for the interfacial forcing terms, such as drag and lift. These forces need to be modelled as sub-grid-scale interactions in both the TFM and Euler-Lagrange methods [86, 93, 94].

The TFM was validated by Rzehak and Krepper [95] against experimental void fraction and mean fluid superficial velocities of the bubble flow regime in upward flows through ANSYS CFX. It is noted that extensive validation with experimental data is still required for closure models under a wide range of flow conditions (e.g. counter-current flows) and configurations (e.g. inclined or annular pipe geometry, different pipe sizes). This can potentially limit the TFM, but the possibility of formulating these correlations from CFD experiments is one option to streamline the process.

Slug flow

Capturing the bubble to slug regime transition can be quite complex using the TFM as the bubble size tends to be predefined in order to apply closure models. Therefore, MUSIG solvers along with PBMs have been developed to account for bubble coalescence and break-up. Such models were used by Lucas *et al.* [89] and further developed by Das and Das [96] to simulate the transition from bubbly to slug flow regimes in upwards vertical pipes and annular geometries, respectively. These studies highlighted the importance of capturing the radial position of different sized bubbles in predicting the transition point as a function of pipe length over diameter. The simulation results showed that small bubbles moved closer to the wall, but after coalescence they shifted towards the centre of the pipe.

The application of ITMs such as the VOF, LS and PF techniques have been utilised in the literature to resolve the shape, velocity and liquid film parameters of Taylor bubbles to assist in the understanding of the slug flow regime. Additionally, these techniques have been used to analyse the wake region of the liquid slug in which smaller bubbles are typically found. Taha and Cui [97] used the VOF

technique within the ANSYS CFX platform to analyse all of these parameters. They used a vertical pipe with a 19 mm diameter and concluded ranges of dimensionless numbers for which varying shape profiles, rise velocities and wake behaviour could be expected. In the study, the bubble rise velocity, in the form of the bubble Froude number, was shown to be a function of the surface tension. The results were consistent with experimental data from the literature with Eötvös numbers ranging from five to 500. Additionally, the inverse viscosity number, N_f, was found to be correlated to the length of the bubble wake, with numerical results presented for N_f between 100 and 750. These such relations can be essential to close the system of equations in 1D mechanistic models.

Churn/annular flow

With a continued increase in gas velocity, Taylor bubbles become unstable and the flow within a pipe breaks down into the churn regime. Da Riva and Del Col [98] used the VOF technique and the ANSYS CFX simulation software in order to simulate the churn flow regime and its transition mechanisms in small diameter pipes (ID of 32mm). Deforming bubbles in the churn flow regime introduce a great level of complexity in modelling via the TFM due to the lack of robust closure models for this regime. A DNS approach is also complicated due to the variation in bubble size and the requirement of a finely-resolved solution to capture the break-up of small bubbles. Montoya *et al.* [99] proposed that perhaps a hybrid model would be effective to capture the sub-grid-scale behaviour, however, this required the development of accurate break-up and coalescence models.

Further increase in gas flow leads to the annular flow regime in which gas flows in the core of the pipe carrying entrained liquid droplets and surrounded by a thin liquid film. A simplified view of annular flow tends to be particularly well suited for interface tracking methods with a high level of separation. However, similar to the churn flow regime, there is a range of scales evident in the system and to accurately capture the behaviour of entrained droplets would require a high computational grid resolution using an ITM alone. Such a problem was addressed by Liu *et al.* [100] where a two-phase, two-component numerical model was proposed to analyse vertical upwards annular flow in a small diameter pipe (ID of 31.8mm). This study used a two-fluid-type mixture model in the gas core and a VOF method to differentiate the gas core from the liquid film. Good predictions were found for the pressure gradient, wall shear stress, film thickness and the film flow flux and the parameters associated with the wave-like behaviour in the liquid film. This presents an interesting technique for capturing the various scales present in two-phase flows, however, a complete understanding of deposition and entrainment of liquid droplets is required for varying flow configurations.

Despite the large body of existing literature in the simulation of flow regimes, complete validation of these models across a large range of flow geometries has not yet been achieved. This indicates potential work in the future to develop either robust coupling methods to capture bubble size of varying scales or improved closure relations to model the complex phase interactions. In this work, there is a focus on improved closure relations through high resolution CMFD using lattice Boltzmann techniques.

2.3.2 Multiphase lattice Boltzmann modelling

An alternative method of reconstructing the NS equations that has become prominent in recent literature is the lattice Boltzmann method. Multiphase and multicomponent (MPMC) fluid dynamics is currently an active area of research in the lattice Boltzmann community. The method has many inherent traits that make it a strong candidate for two-phase flow problems. In addition to the discussion of multiphase LBM techniques presented here, Chapter 3 provides the fundamental theory for the interested reader. The LBMs derivation from the Boltzmann equation as a mesoscopic method allows more control over the molecular interactions that lead to macroscopic behaviours seen in multi-fluid flows. Being comparatively new to its use in multiphase dynamics, there still exist a number of model variations in active use around the LBM community. The models can be grouped into four categorise based on the philosophy from which they were derived and the method of implementing inter-particle forcing terms. There is the chromodynamic or colour-gradient method (CGM) [101], pseudo-potential [22, 41], free-energy [102] and mean-field [103] schemes. In this section, an overview of the timeline in which methods were proposed as well as the primary strengths and weaknesses are discussed. A mathematical basis for the models used in this works will be discussed in detail in Chapter 3.

The CGM was proposed by Gunstensen *et al.* [101] based on the work of Rothman and Keller [40] in multiphase lattice gas automata. The method has seen continued development in the LBM community with modifications by the likes of Grunau *et al.* [104], and with successful implementation in areas such as porous media flows [105] and ocean-based carbon capture and storage [106]. However, coming from the lattice gas automata, the method was not originally based on a physical description of the fluid, but rather a heuristic approach. Following on from this, Shan and Chen [22, 41] proposed a pseudo-potential method in which a fluid-fluid interaction force is defined enabling non-ideal equations of state to be obtained. A number of limitations with the original model were observed including large spurious currents, thermodynamic consistencies and limited density/viscosity ratios as well as difficulty in adjusting fluid properties independently (e.g. surface tension) [102, 107, 108]. A number of improvements have been seen over the years with the pseudo-potential technique often being used in bubbly and slug flow simulations [94, 109–111]. Ngachin *et al.* [111] for example, used the pseudo-potential LBM in comparison with a validated level set method in COMSOL Multiphysics. They were able to obtain reasonable qualitative (Figure 2.5) and quantitative agreement between the cases.

In order to obtain these type of results, the critical improvements needed in the pseudo-potential LBM included proper forcing models and implementation schemes as well as techniques for incorporating realistic equations of state. The benefits of improved forcing models tends to act to reduce the spurious currents and improve the general stability of the model. This is particularly important in high density ratio simulations. The currents tend to originate from a lack of isotropy in the discrete gradient term used to drive ‘like’ fluids together and repel dissimilar fluids [112]. Recent work by Kupershtokh *et al.* [113] and Lycett-Brown and Luo [27] have developed new force schemes that not only reduce spurious currents but allow the independent tuning of parameters such as surface tension. In order to model higher density ratios, researchers such as He and Doolen [107], Sankaranarayanan *et al.* [94]

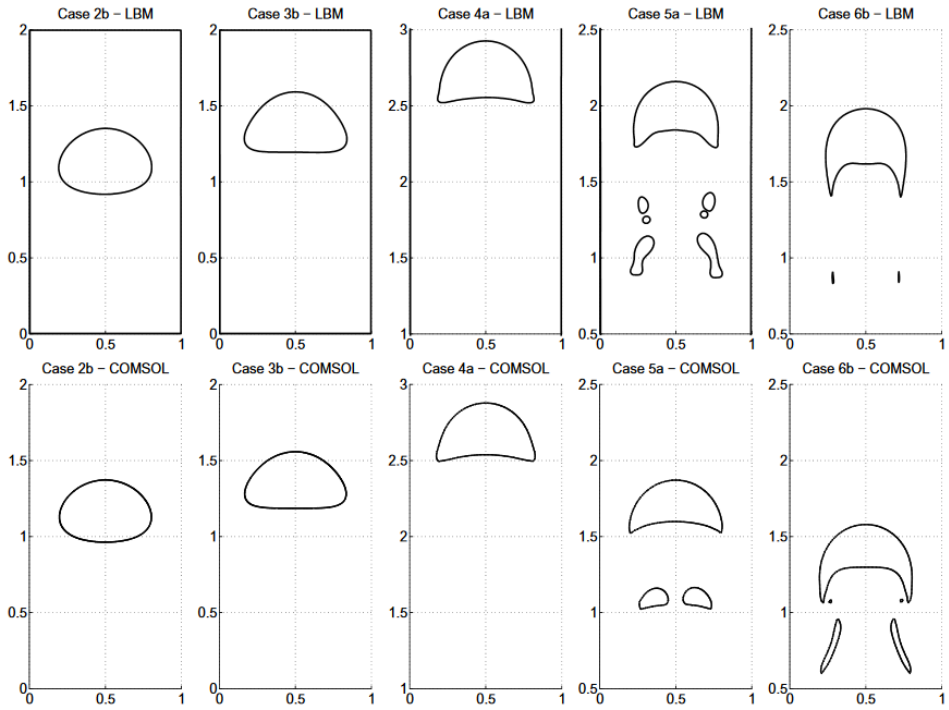

Figure 2.5: Comparison by Ngachin *et al.* [111] using a pseudopotential LBM with benchmark test cases simulated in COMSOL Multiphysics.

and Yuan and Schaefer [26] devised fluid interaction forces that expanded to recover equations of state including the van der Waals, Peng-Robinson or Carnahan-Starling equations. Even with the above improvements, this method still struggles to maintain stability in dynamic simulations at high density ratios. Additionally, there is a disconnect between simulation and physically realisable parameters, namely, interface thickness and surface tension. Here, interface thickness is typically determined by the equation of state parameters and surface tension is found as a result of the inter-particle attractions.

Due to the limitations that initially existed in the psuedo-poential LBM, Swift *et al.* [102, 114] developed a model through formulation of the free energy in the system so as to ensure thermodynamic consistency. An additional benefit with the free energy formulation was that it incorporated physical characteristics such as surface tension and interface thickness allowing them to be directly altered in place of indirectly through model parameters. The method however, was criticised for lacking Galilean invariance and had similar issues of density contrast as the original pseudo-potential LBM. In order to correct the Galilean invariance, Holdych *et al.* [115] proposed corrective forcing terms such that the NS equations would be satisfied in regions of high density gradients. In the same work, the model Swift *et al.* [102] presented on a D2Q7 lattice was extended to a rectangular, D2Q9 lattice. Lattice shapes and constructions will be discussed in Chapter 3.

The free energy LBM has found a wide range of application, from bubble rise cases [116] and multi-component mixing in channels through to complex flow systems such as liquid crystal hydrodynamics [117]. Takada *et al.* [116] verified the model against volume of fluid solutions, but only with a small density ratio applied (see Figure 2.6). A significant breakthrough in free energy models came in 2006 when Zheng *et al.* [118] pointed out that the method could be extended to

correctly solve the Cahn-Hilliard interface tracking equation. This enabled realistic gas-liquid flows with high density ratios and complex interface topologies to be stably captured. However, certain limitations were inherited from the original free-energy model. As a result, the model was unable to correctly recover local density variation in the momentum equations. However, a transformation was recently proposed by Shao *et al.* [119] that allowed the model to resolve this issue. Shao *et al.* [119] performed verification works against a number of benchmark cases including layered Poiseuille flow, Rayleigh-Taylor instability as well as droplet splash and collision.

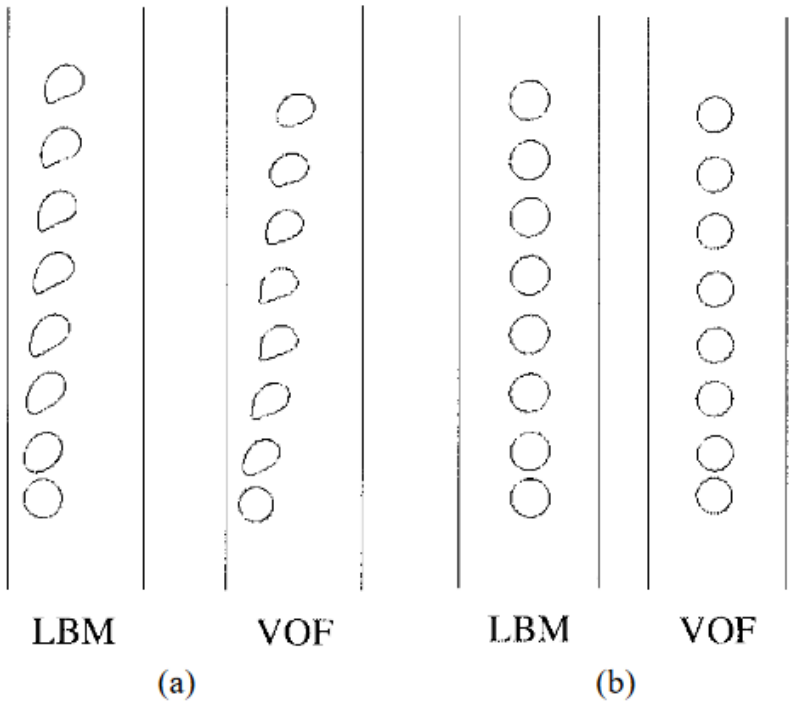

Figure 2.6: Comparison by Takada *et al.* [116] using a free energy LBM with benchmark test cases simulated in using a volume of fluids technique.

During the time that the free energy method was being developed, another stream of researches headed by He, Chen, Zhang and Doolen were investigating an artificial compressibility-like equation [103]. This was extended by Lee and Lin [25] from the perspective of a simplified pressure evolution equation that had no reliance on an equation of state after initialisation. They outlined the update from an equation of state as the cause for pressure fluctuations at phase interfaces, and hence a way to avoid it in the form of a pressure evolution LBM. A downfall of this method was a lack of mass conservation, but recent work [28] has corrected this issue with the incorporation of a conservative phase-field equation. Fakhari *et al.* [28] then continued to showcase the method, coupled with an adaptive mesh refinement scheme in order to simulate bubble rise, fall and splashing phenomena. Certain implementation issues still existed with this model including a lack of locality (lattice update requires information from cells $\pm 2\Delta x$ away) as well as choice in finite difference stencils. Work presented in Chapters 4 and 5 of this dissertation and published by Fakhari *et al.* [120] and Mitchell *et al.* [3] improve the locality of the phase field method and demonstrate its robustness for both high density and viscosity ratio systems.

In addition to the multiphase methods discussed above, LBM has also been coupled with conventional interface tracking techniques such as the VOF and LS methods. Yu *et al.* [121] and Thommes *et al.* [122] for example have looked at coupling the LBM with a LS interface tracking algorithm. These authors used the verification of Young-Laplace's law before applying their methods to problems such as a dam breaking and viscous fingering respectively. The collaborative work from The University of Erlangen-Nueremberg and the System Simulation Group, Erlangen, analysed bubbly flows with specific applications in modelling foams using a coupled LBM-VOF technique [123].

2.4 Chapter summary

This chapter has looked to give a theoretical basis for multiphase flow systems, highlight the current methods employed in day-to-day industry activities as well as introduce available simulation techniques. The reliance of 1D two-fluid, mechanistic models as well as 1D empirical models on closure relations defined from a database of experimental results was discussed. However, with a strong focus on tubular, co-current flows in literature, a gap still exists in relation to the behaviour of counter-current flow, particularly with internals. This not only includes parameters such as spherical and or Taylor bubble rise characteristics which affect the pressure drop once a flow regime is determined, but also in the governing aspects of flow regime transitions. As discussed, a common approach used to determine transition is through flow regime maps, for which no universal counter-current annular piping map currently exists. The lack of studies surrounding counter-current flow has greatly restricted the accuracy of flow predictions in these types of systems.

To study the behaviour of multiphase flows, CMFD was discussed as a potential option in place of experimental works. Here, the use of CMFD can reduce the time and cost required to generate a database of flow characteristics which has historically been done through experimentation in flow loop equipment. Additionally, the high resolution results generated over the full domain from 3D CMFD can provide new insight into flow regime transitions. In comparison, experimental measurements often require intrusive probes that can disrupt the flow and or expensive sensory equipment in order to extract useful information from an apparatus. For these reasons the approach in this work will focus on numerical modelling and simulation results in order to develop understanding. In this, the LBM provides an alternative approach to accurately incorporate the range of scales evident in multiphase flows. The computational cost of conventional methods can be exhaustive, with iterative schemes often required to ensure stability and convergence (e.g. solution of the Poisson equation for the system pressure), in contrast, the inherent parallelism of the LBM can assist take full advantage of available computational resources. This stems from the kinetic roots of the LBM making it ideal for modern computer architectures, including large scale CPU and GPU clusters.

This work looks to exploit the advantages of the LBM to gain detailed insights into the liquid-gas interactions within an unconventional wellbore. As a result of this, the following chapter looks to give the reader a detailed overview of the LBM. This includes both the theory of single phase and multiphase flows, with the limitations discussed where relevant.

Chapter 3

Fundamentals of Multiphase Lattice Boltzmann Methods

$$S = k.\log W$$

"If you are out to describe the truth, leave elegance to the tailor."
Ludwig Boltzmann

The objective of this chapter is to introduce the reader to lattice Boltzmann methods for fluid mechanics. This is done by a discussion of the single phase LBM and the lattice constructions generally used in literature. From here, the connection to the NS equations is discussed. This will outline where some of the key benefits of the method arise. Finally, the numerical details are presented for common multiphase LB schemes. These methods represent the foundation of this work, facilitating the analysis of flow scenarios relating to the extraction of natural gas.

3.1 Single phase lattice Boltzmann techniques

In order to simulate the dynamic fluid interactions present in the wellbore, the LBM provided the primary numerical tool for resolving the governing equations of multiphase flow. Over the past few decades, the LBM has been increasing in popularity and its use in a broad class of complex flow cases is evident. Notable inclusions of LBM applications are that of "thermal flows, reactive transport, turbulent flows, and multiphase flows" [108]. The LBM builds on the observation that macroscale fluid dynamics is a result of the interaction of particles within a system. Therefore, by looking statistically at the interaction of the molecules, the macroscopic behaviour is recovered. As a result of the method's roots in kinetic theory, it is often referred to as a mesoscopic method.

Figure 3.1 from the work of Delbosc [124], gives an overview of three length scales commonly applied to describe fluid flow. At the microscopic scale, the trajectories of molecules in the fluid are

represented. The mesoscale then studies the averaged behaviour of these particles by capturing the evolution of probability or particle distribution functions, $f(\mathbf{x},\xi,t)$. Finally, the macroscale looks at the fluid as a continuum in which flow parameters (velocity, pressure etc.) are defined at each point in space and time [124].

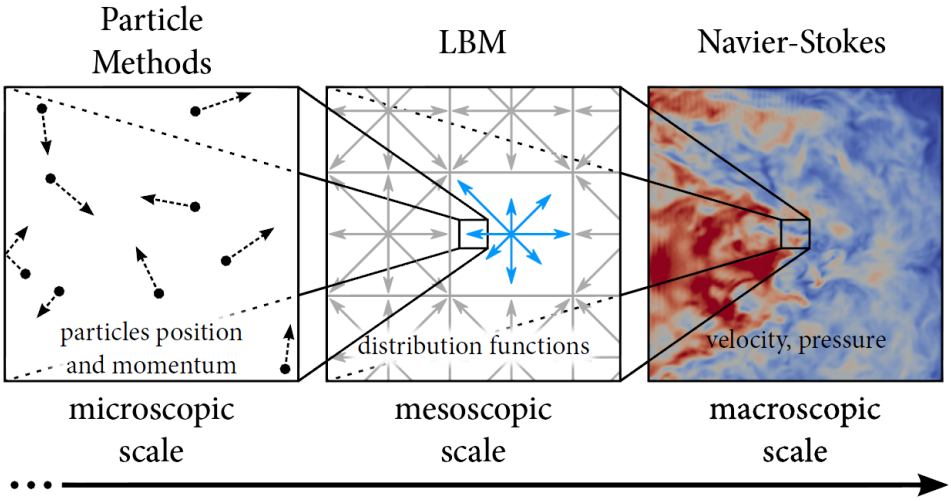

Figure 3.1: Image from Delbosc [124] indicating the various physical scales commonly used in the analysis of fluid flow.

The LBM can be described as the numerical scheme that allows one to solve the discretised Boltzmann equation. This is obtained from the well known continuum Boltzmann equation,

$$\frac{\partial f}{\partial t} + \xi.\nabla f + \mathbf{F}.\frac{\partial f}{\partial \xi} = \Omega, \tag{3.1}$$

where $f = f(\mathbf{x},\xi,t)$ is the probability distribution of finding a fluid particle at a point in space, $\mathbf{x}$, with microscopic velocity, ξ, at time, t. The collision operator, Ω, describes the interaction of molecules and, $\mathbf{F}$, indicates a body force applied to the system (e.g. gravity). For ease and clarity of description, the Bhatnagar Gross Krook (BGK) approximation for the collision operator is used [125],

$$\Omega_{BGK} = \frac{f^{eq} - f}{\tau}, \tag{3.2}$$

where τ is the relaxation parameter linked to kinematic viscosity through the Chapman-Enskog expansion [126],

$$\nu = \frac{\Delta x^2}{3\Delta t}\left[\tau - 0.5\right], \tag{3.3}$$

and f^{eq} is the Maxwell-Boltzmann equilibrium distribution function. The Chapman-Enskog expansion was named after Sydney Chapman and David Enskog who were able to independently show the connection of the lattice Boltzmann method with the Navier-Stokes equations. The method takes on the form of an asymptotic analysis in which the probability distribution functions and temporal variables are expanded by assuming a very small Knudsen number, ε,

$$f = f^{(0)} + \varepsilon f^{(1)} + \varepsilon^2 f^{(2)} + \ldots \tag{3.4}$$

$$\partial_t = \partial_{t0} + \varepsilon\partial_{t1} + \varepsilon^2\partial_{t2} + \ldots. \tag{3.5}$$

This expansion is based on the assumption that the mean free time between particle collisions is sufficiently small in comparison with the time scale of the macroscale flow evolution. In other words, the flow of the fluid changes only slightly over a large number of particle collisions.

The Maxwell-Boltzmann distribution is traditionally adopted for the defining f^{eq},

$$f^{eq} = \frac{\rho}{(2\pi\theta)^{D/2}}.exp\left(\frac{-(\xi-u)^2}{2\theta}\right), \tag{3.6}$$

and indicates the distribution of molecules moving with certain velocities. Here, D is the dimensional space covered by ξ, and $\theta = k_B T/m$ is the normalised temperature with k_B, the Boltzmann constant and T, the temperature. By Taylor expanding the exponential and choosing a discrete velocity set $\xi \rightarrow \mathbf{c}_i$, Gaussian quadrature can be applied to determine the the equilibrium distribution as [127],

$$f_i^{eq}(\rho,\mathbf{u}) = w_i\rho\left[1 + \frac{\mathbf{c}_i\cdot\mathbf{u}}{c_s^2} + \frac{(\mathbf{c}_i\cdot\mathbf{u})^2}{2c_s^4} - \frac{\mathbf{u}\cdot\mathbf{u}}{2c_s^2}\right]. \tag{3.7}$$

Here, w_i is the lattice weights and c_s is the numerical speed of sound, both of which depend on the lattice structure chosen. Integrating Equation 3.1 along the characteristic directions, $\mathbf{c}_i$ from time t to $t+\delta_t$ and assuming ideal collisions such that the collision operator is constant through the process, the lattice Boltzmann equation (with single-relaxation-time BGK collisions) is obtained [127, 128],

$$f_i(\mathbf{x}+\mathbf{c}_i\delta_t, t+\delta_t) = f_i(\mathbf{x},t) - \frac{f_i(\mathbf{x},t) - f_i^{eq}(\mathbf{x},t)}{\tau} + S_i(\mathbf{x},t). \tag{3.8}$$

Here, the subscripts i indicate that the probability distribution function (or forcing term) that is related to the discrete velocity direction i. The forcing term has been incorporated in the source parameter, S_i, in which body forces and intermolecular forces can be applied.

3.1.1 Common lattice constructions

The discretisation of the physical system is an important aspect of the LBM, as it must be performed in a manner that allows recovery of the hydrodynamic moments and fluxes relevant to NS fluid mechanics. As a result of this, lattice constructions need to be symmetric, which helps to ensure isotropy of the second-rank, or second-order velocity tensors. In the LBM literature, the common terminology to describe a lattice is given as $DdQq$, where d is the dimensional space of the system and q is the number of discrete velocities. Frisch et al. [129] were the first to propose a lattice that could successfully recover the NS equations in 1986. This was done with the use of a hexagonal (D2Q6) construction and collisions rules that were able to conserve both mass and momentum. This has since evolved into a D2Q9 structure, which is currently the most commonly seen 2D lattice. With the D2Q9 lattice, it is evident that the lengths between orthogonal, diagonal and rest directions are different, and this tends to be captured in the weightings, w_i. Figure 3.2 shows the links between the lattice nodes in which probability distribution functions, f_i, move from the centre to each node in the direction c_i.

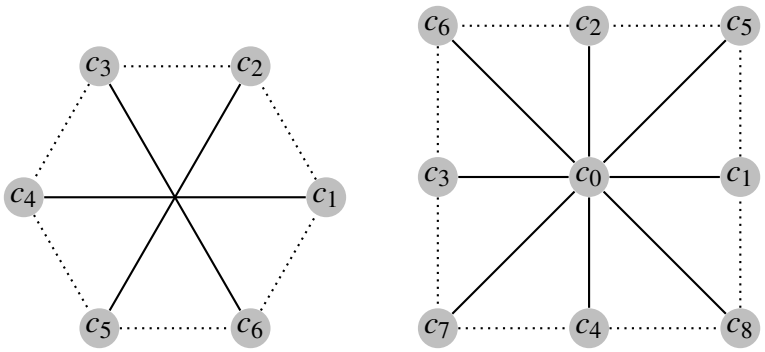

(a) D2Q6 (b) D2Q9

Figure 3.2: The connection between a node and its neighbours showing the discrete velocity space in two dimensions. Solid lines represent the discrete velocity directions from a computational node at the centre of each stencil.

Lattices that can be found in the literature for three dimensions include the $D3Q13$, $D3Q15$, $D3Q19$ and the $D3Q27$ and are displayed in Figure 3.3. Using a higher-order lattice allows the capturing of hydrodynamic moments and can enhance both the stability and accuracy of the LBM. The lattices touched on thus far only include links to *nearest* neighbours. Lattices exist that extend beyond this single stencil layer, but are generally incorporated only if higher order physics is required (e.g. energy conservation) [130]. Extending the stencil causes a loss in locality of the algorithm and can hinder computational efficiency.

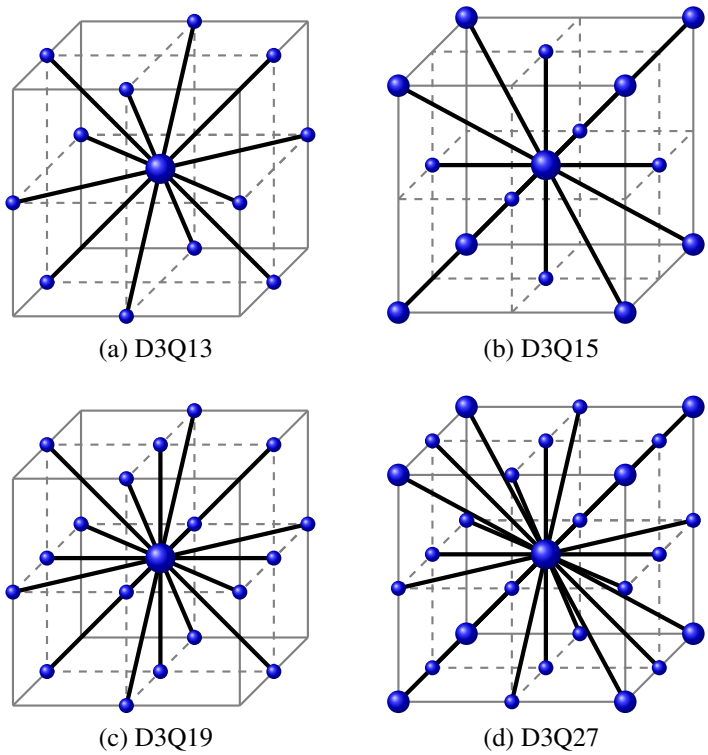

(a) D3Q13 (b) D3Q15

(c) D3Q19 (d) D3Q27

Figure 3.3: The connection between a node and its neighbours showing the discrete velocity space in three dimensions. Here, solid lines represent the discrete velocity directions from a computational node at the centre of each cube.

3.1.2 Stream and collide

The LB algorithm can be broken into two stages, a streaming or communication step and a collision step. This is one of the benefits of the LBM, as the streaming step requires neighbouring node information to be processed, but all operations are linear. Whereas the nonlinear operations involved in the collision step are confined locally to be performed at each node. The order of the stream/collide steps do not affect the accuracy of the algorithm, but can alter the computational efficiency. This is a result of memory location on computing architectures and the fact that an unordered (uncoalesced) read of data followed by an ordered (coalesced) write is typically faster than the reverse. Work by Delbosc [124] found a 10% speed up on a TESLA K40, by simply using this *pull-in* streaming in place of a *push-out* technique. In this sense, the general computer algorithm used for the LBM consists of:

1. Initialise: here the domain is set to an equilibrium distribution
$$f_i = f_i^{eq}(\rho, \mathbf{u}) = w_i \rho \left[1 + \frac{\mathbf{c}_i \cdot \mathbf{u}}{c_s^2} + \frac{(\mathbf{c}_i \cdot \mathbf{u})^2}{2c_s^4} - \frac{\mathbf{u} \cdot \mathbf{u}}{2c_s^2} \right] \tag{3.9}$$
2. pull-in stream: read neighbour populations into update node
$$f_i(\mathbf{x}, t) = f_i(\mathbf{x} - \mathbf{c}_i \delta t, t) \tag{3.10}$$
3. Calculate macroscopic properties from the streamed populations.
$$\rho = \sum_i f_i \tag{3.11}$$
$$\rho \mathbf{u} = \sum_i f_i \mathbf{c}_i \tag{3.12}$$
$$p = c_s^2 \rho. \tag{3.13}$$
4. Collide: perform relaxation and write new state to local update node (alternatively, incorporate boundary conditions to be discussed in Section 3.1.4).
$$f_i(\mathbf{x}, t + \delta t) = f_i(\mathbf{x}, t) - \frac{f_i(\mathbf{x}, t) - f_i^{eq}(\mathbf{x}, t)}{\tau} + S_i. \tag{3.14}$$

Here it is noted, that the collision stage can vary significantly, with various techniques used in the literature to improve stability. The BGK relaxation described above is commonly used due to its simplicity, but a number of limitations exist. The connection of the relaxation parameter, τ, to viscosity puts a lower bound of 0.5 to maintain physical realness. For example, the parameterisation of viscosity shown in Equation 3.3 requires that the relaxation parameter, τ, is always greater than 0.5. Additionally, values far away from 1 can result in larger errors and tend to show a τ-dependency, not seen in physical problems. Therefore, in order to obtain low viscosities, or a range of viscosities (e.g. for a liquid and a gas) it is necessary to employ a more advanced collision kernel. Of particular use in this work is the multiple-relaxation time (MRT) operator.

In addition to the BGK and MRT methods, further work has been undertaken in an attempt to improve accuracy and stability of the LBM with relaxation kernels such as the *entropic* [131], *cascaded* [132] and *cumulant* [133] operators. The scope of this work does not include the development of new operators, but both the MRT and cascaded methods are utilised.

3.1.3 Multiple-relaxation-time collision operators

The MRT operator was proposed by d'Humieres [134] in 1992, and has seen widespread use in the LBM community, especially in multiphase dynamics. The collision operator was tested in detail by Lallemand and Luo [135], where results indicated a significant improvement in stability when compared with the BGK operator. The MRT looks to separate out the hydrodynamic quantities and their fluxes explicitly as moments of the probability distribution functions, f_i. This allows each mode to be relaxed independently and overcomes a number of the deficits present in the BGK simplification.

In order to convert the system to the macroscopic moments relating to hydrodynamic properties, a transformation matrix, M, is defined. In the following, the standard notation is used to represent column vectors, $[f_0, ..., f_i]^T = |f\rangle$. The moments can then be given as,

$$|m(\mathbf{x},t)\rangle = M|f(\mathbf{x},t)\rangle. \tag{3.15}$$

Following the description from Lallemand and Luo [135], $|m(\mathbf{x},t)\rangle$ for the nine-velocity LBM (D2Q9) is chosen as,

$$|m(\mathbf{x},t)\rangle = (\rho, e, \varepsilon, j_x, q_x, j_y, q_y, p_{xx}, p_{xy}), \tag{3.16}$$

such that the rows of the transformation matrix, M, are given by,

$$M_0 = (1,1,1,1,1,1,1,1,1) \tag{3.17a}$$
$$M_1 = (-4,-1,-1,-1,-1,2,2,2,2) \tag{3.17b}$$
$$M_2 = (4,2,2,2,2,1,1,1,1) \tag{3.17c}$$
$$M_3 = (0,1,0,-1,0,1,-1,-1,1) \tag{3.17d}$$
$$M_4 = (0,-2,0,2,0,1,-1,-1,1) \tag{3.17e}$$
$$M_5 = (0,0,1,0,-1,1,1,-1,-1) \tag{3.17f}$$
$$M_6 = (0,0,-2,0,2,1,1,-1,-1) \tag{3.17g}$$
$$M_7 = (0,1,-1,1,-1,0,0,0,0) \tag{3.17h}$$
$$M_8 = (0,0,0,0,0,1,-1,1,-1). \tag{3.17i}$$

Here, the above parameters from ρ to p_{xy} are described as the density and energy modes, energy square, mass and energy fluxes and the diagonal/off-diagonal components of the second order stress tensor. If higher order lattice constructions are considered, it is possible for non-physical modes to occur and their relaxation tuned for stability. Treatment of these is often left to the user, so long as the collision matrix remains invertible. The discretised evolution equation then becomes,

$$|f(\mathbf{x}+\mathbf{c}_i\delta t, t+\delta t)\rangle = |f(\mathbf{x},t)\rangle - M^{-1}\hat{S}(|m(\mathbf{x},t)\rangle - |m^{eq}(\mathbf{x},t)\rangle) \tag{3.18}$$

where $\hat{S}$ is a diagonal matrix corresponding to the relaxation parameters of each mode and M^{-1} transforms the result back to f-space. If the diagonal values of the relaxation matrix are selected to be equal, the MRT method becomes equivalent to the LBGK. However, with the hydrodynamic

properties separated, it is clear that each can be relaxed independently, giving the user the ability to tune parameters such as the bulk and shear viscosity [136]. Particular note is made in numerous studies that pressure oscillations are also reduced with the use of MRT-LBM, which is advantageous in this work, but the primary reason for its implementation is the requirement of viscosity contrast in a liquid-gas system.

3.1.4 Boundary conditions

The specification of boundary conditions in any CFD code is crucial for the accuracy and stability of the method. The effects of a poorly-implemented boundary can result in large errors even in far-field areas. This is no different in the LBM, and can be complicated due to the abstraction of distribution functions from macroscopic parameters. Therefore, when implementing boundaries in the LBM, it is commonplace to map specified macroscopic conditions (pressure, velocity etc.) to the unknown distribution functions found at boundary nodes after the streaming stage. There has been a number of proposed methods to deal with boundary nodes over the development of LBM. This section looks at those boundary conditions applicable in this work. An exhaustive review of all LBM boundary implementations is not given, but the interested reader is pointed to the work of Delbosc [124] and references therein.

Bounce-back

When looking at flow within a pipe, there is an obvious need for solid wall boundaries in order to confine the flow. Achieving this in the LBM framework turns out to be a straightforward exercise, and one that has contributed greatly to its popularity. To achieve the *no-slip* boundary condition the distribution functions entering a boundary node are simply reversed,

$$f_i(\mathbf{x},t) = f_{\bar{i}}(\mathbf{x},t), \tag{3.19}$$

where i and $\bar{i}$ correspond to opposing lattice directions.

There exist two schemes to implement this boundary, namely the *full-way* (FBB) and *half-way* bounce-back (HBB). The primary difference between these methods is the characterisation of the bounding node; in FBB the boundary node is flagged as solid and no collision operation is performed. All distribution functions streamed into the node are reversed and streamed back out in the proceeding time step. This gives a wall location at the halfway point between the bounding solid node and interior fluid node. In comparison, the HBB requires a post (or during)-streaming operation to reverse only the distribution functions moving out of the domain, allowing the bounding node to be treated as a fluid, with normal relaxation procedures applied. The result of the HBB scheme is a wall boundary half a grid spacing outside the computational domain. In this work, the FBB has been applied as it eliminates the need for specifying wall normal directions in order to determine reversed distribution functions.

Periodic domain

Periodicity is arguably the most common (and simple) boundary to be applied in LBM simulations. In this, populations exiting from one side of the domain are simply redirected to the opposing side using modular arithmetic. Here, it is noted that the populations need to be mapped to their true advection position based on the discrete velocity directions, not simply straight across the periodic bound. This allows for steady-state behaviour to be determined by effectively simulating flow through an infinite domain.

Pressure/velocity conditions

In conventional CFD, fixed pressure and velocity boundaries are often selected for inlet and outlet conditions. In the LBM these macroscopic properties are not in themselves streamed through the domain, but can be used to reconstruct the *unknown* populations at an inlet/outlet node. The first to propose this reconstruction process was Zou and He, and as such the method is often referred to as the ZOU-HE boundary condition [137]. To provide an insight to the workings of the ZOU-HE boundary condition, the following demonstrates the reconstruction process for a fixed velocity, left wall using a D2Q9 lattice. At the boundary node, the unknown properties post-streaming include the fluid density as well as f_1, f_5 and f_8 (refer to Figure 3.2b for directions). This gives four unknowns, and using the moments of mass and momentum, we only have three equations,

$$\rho = \sum_i f_i \tag{3.20}$$

$$\rho u_x = \sum_i c_{i,x} f_i \tag{3.21}$$

$$\rho u_y = \sum_i c_{i,y} f_i \tag{3.22}$$

In order to provide the closing equation for the system of unknowns, the bounce-back rule is applied for the non-equilibrium component of the distribution functions normal to the boundary,

$$f_1 + f_1^{eq} = f_3 + f_3^{eq} \tag{3.23}$$

Therefore, one starts by combining Equations 3.20 and 3.21 to obtain the density as,

$$\rho = \frac{1}{1-u_x}\left[f_0 + f_2 + f_4 + 2(f_3 + f_6 + f_7)\right]. \tag{3.24}$$

Expanding Equation 3.23, and using the known density f_1 is given by,

$$\begin{aligned} f_1 &= f_3 - \rho w_3 \left[1 + \frac{-u_x}{c_s^2} + \frac{u_x^2}{2c_s^4} - \frac{u_x^2}{2c_s^2}\right] + \rho w_1 \left[1 + \frac{u_x}{c_s^2} + \frac{u_x^2}{2c_s^4} - \frac{u_x^2}{2c_s^2}\right] \\ &= f_3 + \frac{2}{3}\rho u_x. \end{aligned} \tag{3.25}$$

From here it is simply a matter of rearranging Equations 3.21 and 3.22 to find,

$$f_5 = f_7 + \frac{\rho}{2}\left(\frac{u_x}{3} + u_y\right) + \frac{1}{2}(f_4 - f_2) \tag{3.26}$$

$$f_8 = f_6 + \frac{\rho}{2}\left(\frac{u_x}{3} - u_y\right) - \frac{1}{2}(f_4 - f_2) \tag{3.27}$$

This same logic can be applied to various lattice stencils and holds in 3D. However, Delbosc [124] reported that the method requires significant changes for higher order lattices such as the D3Q19 and D3Q27, that can make it difficult to implement. To get around this, a method proposed by HO-CHEN-LIN [138] looks to write the unknown distribution functions as a summation of the equilibrium distribution and an additional source vector, $Q = (Q_x, Q_y, Q_z)$. This effectively reduces the number of unknowns to three no matter the lattice stencil size. The interested reader is pointed to a detailed description of this work in Ho et al. [138] or a brief overview in Delbosc [124].

3.2 Multiphase models

As discussed in Chapter 2, there are a variety of models within the LB framework that look to solve multiphase (and multicomponent) flow problems. A number of these schemes have been adopted in both commercial and research codes [21], and it is these models as well as extensions to them that will be described in this section. These methods include the colour-gradient model [101], the Shan-Chen *psuedo-potential* model [22], the free energy model [102], and the phase-field coupled pressure evolution LBM presented by Lee and Lin [25]. From these, the Shan-Chen model is particularly well-known, and has been credited as the inspiration for the later two models.

3.2.1 Colour-gradient

As the name suggests, the colour-gradient model assigns each phase in the system a different colour (commonly red and blue). For each colour, a set of distribution functions (referred herein as a *population*) are initialised, $|f_b\rangle$ and $|f_r\rangle$, and the total mixture population is then given as, $|f\rangle = |f_b\rangle + |f_r\rangle$. In this, a perturbation term, Γ_i^p, is included to account for the inter-particle interactions and allow for phenomena such as phase separation [139],

$$f_i(\mathbf{x} + \mathbf{c}_i\delta t, t + \delta t) = f_i(\mathbf{x}, t) + \Omega_i + \Gamma_i^p. \tag{3.28}$$

The macroscopic properties for each fluid phase are then constructed in the normal way from each respective population and mixture properties are simply the summation of the phase density and velocity at each node. In order to determine Γ_i^p an order parameter is first introduced in order to determine the local colour gradient, $\mathbf{G}(\mathbf{x}, t)$, for each node,

$$\psi(\mathbf{x}, t) = \rho_r(\mathbf{x}, t) - \rho_b(\mathbf{x}, t) \tag{3.29}$$

$$\mathbf{G}(\mathbf{x}, t) = \sum_i \mathbf{c}_i \psi(\mathbf{x} + \mathbf{c}_i\delta t, t). \tag{3.30}$$

Following this, the perturbation term is calculated by [139],

$$\Gamma_i^p = A|\mathbf{G}(\mathbf{x}, t)|cos(2\theta_i), \tag{3.31}$$

where θ_i is the angle between $\mathbf{c}_i$ and $\mathbf{G}(\mathbf{x},t)$, while A is a parameter used to control the surface tension.

Having determined the perturbation term the nodal relaxation can be performed according to Equation 3.28, following this a *re-colouring* step is required. This effectively enforces "the direction of the [colour] flux $H = \rho_r u_r - \rho_b u_b$ to match that of the [colour] gradient" [139]. As a result of this, the fluid is forced into regions of its own colour, inducing phase separation. As previously discussed, being an early method of the multiphase LBM family, the colour-gradient models tend not to have a strong physical description of the fluid [124], but advances in this model have seen to a wide range of applications. The interested reader is pointed to the book by Guo and Shu [139] for a detailed description of the theoretical basis of this model.

3.2.2 Pseudo-potential

The model proposed by Shan and Chen [22] looked to improve on the colour-gradient model by replacing the perturbation term with a *pseudo-potential* force between molecules. In a single component system, this could be thought of as an approximation of the Lennard-Jones potential. It is noted here, that the *psuedo-potential* model can be used in either a *single-component multi-phase* (SCMP) or *multi-component multiphase* (MCMP) formulations. In order to extend the SCMP to an MCMP, additional populations must be introduced and the interaction force between components described. In the original model proposed on a D2Q9 lattice, the SCMP inter-particle force is given by [140],

$$\mathbf{F}_{int} = -G\psi(\mathbf{x},t)\sum_i w_i \mathbf{c}_i \psi(\mathbf{x}+\mathbf{c}_i\delta t,t), \tag{3.32}$$

where ψ represents the mean-field potential and G controls the strength of the interaction force. Different potential forms have been used in literature, but it is generally a function of density, $\psi = \psi(\rho)$. Shan and Chen [22] originally proposed,

$$\psi(\rho) = \rho_0(1 - exp(-\rho/\rho_0)), \tag{3.33}$$

where ρ_0 is simply a constant, usually taken as one. This form allowed for density variation, but capped the magnitude of the gradient of ψ over an interface. Further understanding of the force being applied from Equation 3.32 is given by analysing its Taylor expansion for example on a D2Q9 lattice,

$$F_\alpha = -G\frac{\delta t}{6}\partial_\alpha \psi^2 - G\frac{\delta t^3}{18}\psi\partial_\alpha\nabla^2\psi, \tag{3.34}$$

where α refers to the Cartesian coordinates. Combining this with the knowledge that at equilibrium,

$$\nabla p = \nabla(\rho c_s^2) - \mathbf{F}, \tag{3.35}$$

one can find the non-ideal equation of state and rearrange to obtain an expression for ψ,

$$p = \rho c_s^2 + \frac{G c_s^2}{2}\psi(\rho)^2 \tag{3.36}$$

$$\psi = \sqrt{\frac{2(p-\rho c_s^2)}{G c_s^2}}\,. \tag{3.37}$$

Here, it is clear that Equation 3.33 is not equivalent to 3.37. This is the thermodynamic inconsistency that has been criticised extensively in the early pseudo-potential models. The inconsistency is primarily a result of the assumption that a molecule at a computational node interacts only with its nearest neighbours, whereas a Lennard-Jones potential includes both short range repulsion and long range attractions. Therefore, as the errors due to this truncation grow, the model can suffer from non-physical diffusion and spurious currents at the interface [21]. In the original model, these issues caused instabilities for moderate density ratios and provided a serious limitation to the method.

An example of how researchers have circumvented these effects can be seen in the works of Yuan and Schaefer [26]. They improved the *psuedo-potential* model such that generic equations of state could be selected by proposing ψ to align with Equation 3.37, where the pressure is defined by a desired equation of state. This allowed the model to be extended to higher density ratios, but careful selection of initial conditions are required to maintain consistency with thermodynamics (namely the *Maxwell equal area rule*). Lycett-Brown and Lou [27] further extended this method to allow independent tuning of physical parameters including surface tension and interface thickness. Sbragaglia et al. [141] looked to resolve these issues by including two or more layers of nodes in order to improve Equation 3.32. Additional aspects of importance in *pseudo-potential* models include the forcing scheme and the mechanical stability condition. A discussion of these aspects is not presented in this dissertation, but the interested reader is again pointed to books of Guo and Shu [139] and Huang et al. [140] and recent work by Lycett-Brown and Lou [27].

3.2.3 Free-energy

Swift et al. [114] proposed another approach, formulated with the use of a free-energy functional in order to capture interfacial interactions. This allowed the dynamics of the interface to be captured in a "thermodynamically consistent manner" [142]. Similar to the *psuedo-potential* method, the *free-energy* approach has both a SCMP and MCMP formulation. Here, the SCMP is introduced, but the interested reader is pointed to the formulation in Swift et al. [114] and reviewed in Liu et al. [142]. The concept for this model was to incorporate the phase interactions by generalising the equilibrium particle distribution function to include a non-ideal pressure tensor term.

In its simplest form, the Landau free-energy functional for a single component fluid is described as [42, 143],

$$\Psi = \int_V \left[\psi(T,\rho) + \frac{\kappa}{2}(\nabla\rho)^2 \right] dV, \tag{3.38}$$

where ψ describes the bulk free-energy,the second term is used to model the associated free-energy of the interface within which κ is related to the surface tension. Additional terms can be included in Equation 3.38 to account for interactions with solid interfaces, and can be controlled to capture a variety of contact angles at the three-phase interaction point.

The free-energy functional is then related to both the pressure (p) and the thermodynamic pressure

tensor (**P**) through Equations 3.39 and 3.40 (where p_0 is given by an equation of state).

$$\begin{aligned} p(\mathbf{x}) &= \rho \frac{\partial \Psi}{\partial \rho} - \Psi \\ &= p_0 - \kappa \rho \nabla^2 \rho - \frac{\kappa}{2} (\nabla \rho)^2 \end{aligned} \tag{3.39}$$

$$\mathbf{P}_{\alpha\beta} = p \delta_{\alpha\beta} + \kappa \frac{\partial \rho}{\partial x_\alpha} \frac{\partial \rho}{\partial x_\beta} \tag{3.40}$$

In addition to constructing the pressure and pressure tensor, the equilibrium distribution function (given for a single-phase fluid in Equation 3.7) is generalised to,

$$f_i^{eq} = A + B(\mathbf{c}_i \cdot \mathbf{u}) + C(\mathbf{u} \cdot \mathbf{u}) + D(\mathbf{c}_i \cdot \mathbf{u})^2 + \mathbf{G} : \mathbf{c}_i \mathbf{c}_i, \tag{3.41}$$

where A, B, C, D and $\mathbf{G}$ are determined by the requirements for the moments of the equilibrium distribution function. Namely,

$$\sum_i f_i^{eq} = \rho, \tag{3.42}$$

$$\sum_i f_i^{eq} c_{i\alpha} = \rho u_\alpha, \tag{3.43}$$

$$\sum_i f_i^{eq} c_{i\alpha} c_{i\beta} = \mathbf{P}_{\alpha\beta} + \rho u_\alpha u_\beta. \tag{3.44}$$

Therefore, the original formulation was closed by combining the constraints, the generalised equilibrium distribution and the pressure tensor formulated from the Landau free-energy functional. The derivation of the unknown constants is not presented here, but the interested reader is pointed to [143].

3.2.4 Multiphase pressure evolution LBM

The final model introduced from the literature is the interface tracking model proposed by Lee and Lin [25] and further developed by Fakhari et al. [28], as an improvement to the models introduced by He et al. [103]. The major development for these models in capturing the behaviour of high density ratio systems was the decoupling of the LBE from the density variations, such that they would not be present in the collision step. Instead, the LBM is constructed in such a way that the macroscopic velocity and dynamic pressure are recovered as moments of the first lattice population, eliminating the need for the use of an equation of state. To recover the local density, a second lattice population is introduced and typically used to solve an Cahn-Hilliard-like equation. The model presented here was one of the key inspirations for the phase-field LBM developed and presented in Chapter 4.

Lee and Lin [25] extended from the work of He et al. [103] in which the discrete Boltzmann equation was presented as,

$$D_t f_i = \frac{\partial f_i}{\partial t} + \mathbf{c}_i \cdot \nabla f_i = -\Lambda (f_i - f_i^{eq}) + \frac{(\mathbf{c}_i - \mathbf{u}) \cdot \mathbf{F}}{c_s^2} \Gamma_i, \tag{3.45}$$

where,

$$\Gamma_i = w_i \left[1 + \frac{\mathbf{c}_i \cdot \mathbf{u}}{c_s^2} + \frac{(\mathbf{c}_i \cdot \mathbf{u})^2}{2c_s^4} - \frac{\mathbf{u} \cdot \mathbf{u}}{2c_s^2} \right], \tag{3.46}$$

Λ represents the collision type (e.g. BGK, MRT, ...) and $\mathbf{F}$ is a volumetric force. From here, the new pressure evolution distribution function, $g_i = g_i(\mathbf{x}, t)$, is defined as,

$$g_i = f_i c_s^2 + w_i(p - \rho c_s^2) \tag{3.47}$$

$$g_i^{eq} = f_i^{eq} c_s^2 + w_i(p - \rho c_s^2) \tag{3.48}$$

The forcing term is then described as,

$$\mathbf{F} = -\nabla(p - \rho c_s^2) + \mathbf{F}_B + \mathbf{F}_s, \tag{3.49}$$

where $\mathbf{F}_B$ is a body force (e.g. gravity) and $\mathbf{F}_s$ is the resultant force due to the surface tension between fluids and or phases. Here, the continuum surface tension form is taken as [39, 51],

$$\mathbf{F}_s = \mu_\phi \nabla \phi, \tag{3.50}$$

where ϕ is the order parameter (or phase indicator) and the chemical potential, μ_ϕ, is given as,

$$\mu_\phi = 4\beta\phi(\phi - 1)(\phi - 0.5) - \kappa \nabla^2 \phi. \tag{3.51}$$

Here, κ and β are chosen to control both the surface tension (σ) and the interface width (W) . The transformation from f_i to the governing equation for g_i given in Equation 3.52 can be seen in Appendix A.2.

$$D_t g_i = -\Lambda(g_i - g_i^{eq}) + \left[(\Gamma_i - w_i)(\rho_h - \rho_l) c_s^2 + \Gamma_i \mu_\phi \right] (\mathbf{c}_i - \mathbf{u}) \cdot \nabla \phi + \Gamma_i (\mathbf{c}_i - \mathbf{u}) \cdot \mathbf{F}_B. \tag{3.52}$$

To reduce compressibility errors in the low density phase, the order parameter is designed to vary between 0 and 1 rather than -1 and 1. In the model of Fakhari et al. [28], the dynamics of the order parameter is governed by the conservative phase-field equation,

$$\frac{\partial \phi}{\partial t} + \nabla \cdot \phi \mathbf{u} = \nabla \cdot \left[M \left(\nabla \phi - \frac{1 - 4(\phi - 0.5)^2}{W} \mathbf{n} \right) \right], \tag{3.53}$$

where M controls the diffusional arrangement of the phase field about the interface, W is the interface width in lattice units and $\mathbf{n}$ is the vector normal to the interface. The mobility coefficient, M, is not a physical parameter but plays an important role in the interfacial behaviour. Ultimately, it affects the "thickness and perturbation magnitude of the chemical potential boundary layers" [39] which can act to encourage or inhibit coalescence phenomena. It is noted that this equation could also be replaced by a LS or VOF-type equation and the pressure evolution LBM would still remain valid. The solution to Equation 3.53 minimises the free-energy associated with the interface, and is defined at equilibrium to fit a hyperbolic tangent profile in the direction normal to the interface. This is different from the commonly used *Heaviside* function in conventional sharp interface models as the parameter varies over the diffuse interface rather than experiencing a step jump.

With two governing equations to solve, a double-distribution-function approach is required. As such, a second population is introduced to the lattice and evolved through,

$$h_i(\mathbf{x}+\mathbf{c}_i\delta t, t+\delta t) = h_i(\mathbf{x},t) - \frac{h_i - h_i^{eq}}{\tau_\phi + 0.5}, \tag{3.54}$$

$$\text{where } h_i^{eq} = \phi\Gamma_\phi + \frac{M}{c_s^2}\left[\frac{1-4(\phi-0.5)^2}{W}\right] w_i\mathbf{c}_i\cdot\mathbf{n}. \tag{3.55}$$

This equation takes a very similar form to that used to solve the Navier-Stokes equations, and as such, it may not be how this resolves Equation 3.53. One can consider the adaption of the LBM to the advection-diffusion-type equation (ADE) by considering the Navier-Stokes equation as an ADE for the fluid momentum. There are a number of differences that should be highlighted between these, namely that an ADE typically has just one conserved quantity, in the case of Equaton 3.53 it is ϕ. As a result, this is included in the equilibrium distribution while the velocity is imposed from the fluid externally. The single-relaxation or BGK model is used in the collision stage for this population, where the relaxation time τ_ϕ is related to the interface mobility, $M = \tau_\phi c_s^2 \delta t$.

From here, the macroscopic properties obtained are,

$$\phi = \sum_i h_i, \tag{3.56}$$

$$\rho = \rho_l + \phi(\rho_h - \rho_l), \tag{3.57}$$

$$\mu = \mu_l + \phi(\mu_h - \mu_l), \tag{3.58}$$

$$\mathbf{u} = \frac{1}{\rho c_s^2}\sum_i g_i\mathbf{c}_i + \frac{1}{2\rho}(\mathbf{F}_s + \mathbf{F}_B), \tag{3.59}$$

$$p = \sum_i g_i + \frac{1}{2}(\rho_h - \rho_l)c_s^2\mathbf{u}\cdot\nabla\phi. \tag{3.60}$$

This method has been applied to a number of test cases including bubble collision, coalescence, falling and rising [28, 144], however a number of limitations still exist. In order to accurately capture the behaviour at the interface, Lee and Lin [25] had to apply mixed derivatives to determine the gradient of the order parameter, $\nabla\phi$. This causes a loss in the locality of the collision operation and the resultant non-coalesced memory reads can have a severe impact on the algorithm speed on parallel architectures. A further limitation of a diffuse interface method is the requirement for high resolution at liquid-gas boundaries. The mixture of high resolution, non-local memory calls and the need for a double-distribution-function model can lead to excessive computational costs. In order to partially alleviate this issue, authors such as Fakhari *et al.* [28] have looked to use adaptive mesh refinement. This saves memory and required lattice updates per iteration by concentrating the Cartesian mesh around complex zones, while remaining coarse in areas of bulk media.

3.3 Chapter summary

This chapter aimed to introduce the reader to lattice Boltzmann modelling. It started with a description of the single phase formulation, introducing it as a mesoscopic method, in between that of continuum

fluid mechanics and molecular simulations. From here, the common domain deconstructions were discussed along with their respective advantages and disadvantages. In the interest of applying the scheme, a step-by-step breakdown of the algorithm was presented, including the relation between the probability distribution function and macroscopic parameters through moments. As with all solutions to partial differential equations, boundary conditions are essential and as such, the commonly used formulations were introduced and the methodology behind them outlined.

Following on from this, the focus shifted to multiphase lattice Boltzmann models. Four main categories were outlined including the colour-gradient [40], pseudo-potential [22, 41], free-energy [102, 114] and the variant of these that is commonly referred to as phase-field models [103]. The key philosophies behind these methods were discussed as well as a number of their limitations and the progressive developments to alleviate them. From this chapter, the reader should have a base level of understanding as to both lattice Boltzmann modelling of single and multiphase flow. With this, the work of the subsequent chapter formulates an improved phase-field model to enhance the density ratios and Reynolds numbers able to be simulated with multiphase lattice Boltzmann schemes. The purpose of this is to allow for simulations to address a large range of potential well operating conditions in the extraction of coal seam gas.

Part of the following publication has been incorporated as Chapter 4.

1. [4] Abbas Fakhari, **Travis Mitchell**, Christopher Leonardi and Diogo Bolster, Improved locality of the phase-field lattice-Boltzmann model for immiscible fluids at high density ratios, *Physical Review E* 96, 053301, 2017.

Contributor	Statement of contribution	%
Travis Mitchell	writing of text	60
	proof-reading	60
	theoretical derivations	30
	numerical calculations	70
	preparation of figures	75
	initial concept	50

2. [1] Grzegorz Gruszczyński, **Travis Mitchell**, Christopher Leonardi, Łukasz Łaniewski-Wołłk and Tracie Barber A cascaded phase-field lattice Boltzmann model for the simulation of incompressible, immiscible fluids with high density contrast, *Computers and Mathematics with Applications, In Press, 2019*.

Contributor	Statement of contribution	%
Travis Mitchell	writing of text	30
	proof-reading	50
	theoretical derivations	30
	numerical calculations	40
	preparation of figures	40
	initial concept	40

The papers above have not necessarily been included directly in this chapter, and all work presented here was written and tested by the author of this dissertation. It is noted in the case of the Poiseuille flow, the author re-created these tests in the open-source code TCLB while in the paper referenced above, [4], these were completed by Dr. Fakhari.

Chapter 4

Improved Phase-Field Lattice Boltzmann Modelling

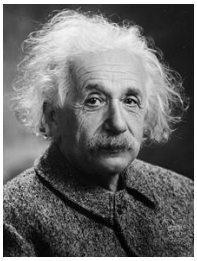

"Logic will get you from A to B.
Imagination will take you everywhere."
Albert Einstein

This chapter develops a robust multiphase lattice Boltzmann model that is capable of accurately simulating systems that exhibit both high density ratios and Reynolds numbers. The work from this chapter was published in the papers referenced on the previous page and resolved issues of non-locality and erroneous interface velocity profiles that had been observed in previous phase-field models. The model is introduced in a two-dimensional setting and benchmark test cases are examined. This includes the layered Poiseuille flow in which the model results are compared with the phase-field model by Fakhari *et al.* [28] and to high resolution finite difference solutions to verify its implementation. The robustness is then tested by examining the Rayleigh-Taylor instability that occurs when a heavy fluid is situated above a lighter one within a gravitational field. With the model verified, the computational benefit of the improved locality is assessed. From here, the dynamics of a Taylor bubble in a duct are investigated for cases where the bulk media is stationary as well as flowing in both a co-current and counter-current configuration. In doing this, the proposed model shows good agreement with the available numerical and experimental data as well as improved capability in relation to alternative phase-field LBMs in terms of the parameter range that can be simulated.

4.1 Lattice Boltzmann equations

The model developed for the simulation of multiphase flows uses a double-distribution-function approach, similar to that described for phase-field methods in Chapter 3. In this, one population is used to recover the NSE and the other for the conservative phase-field equation.

4.1.1 LBE for hydrodynamics

In this study, the velocity-based LB approach used by Zu and He [145] is extended and allows for the governing hydrodynamics to be resolved,

$$\frac{\partial \rho}{\partial t} + \nabla \cdot \rho \mathbf{u} = 0 \tag{4.1}$$

$$\rho \left(\frac{\partial \mathbf{u}}{\partial t} + \mathbf{u} \cdot \nabla \mathbf{u} \right) = -\nabla p + \nabla \cdot (\mu [\nabla \mathbf{u} + (\nabla \mathbf{u})^T]) + \mathbf{F}_s + \mathbf{F}_B. \tag{4.2}$$

The LBE used for this can be given in a general form as,

$$g_i(\mathbf{x} + \mathbf{c_i}\delta t, t + \delta t) = g_i(\mathbf{x}, t) + \Omega_i(\mathbf{x}, t) + F_i(\mathbf{x}, t), \tag{4.3}$$

where $\Omega_i(\mathbf{x}, t)$ represents the collision operator of choice and g_i is the velocity based distribution function with a modified equilibrium distribution given by,

$$\bar{g}_i^{eq} = g_i^{eq} - 0.5 F_i, \tag{4.4}$$

where,

$$g_i^{eq} = w_i \left(p^* + \frac{\mathbf{c}_i \cdot \mathbf{u}}{c_s^2} + \frac{(\mathbf{c}_i \cdot \mathbf{u})^2}{2c_s^4} - \frac{\mathbf{u} \cdot \mathbf{u}}{2c_s^2} \right), \tag{4.5}$$

and $p^* = p/\rho c_s^2$ is the normalised pressure. The collision operator can then be expressed, for example, in the simplest BGK form as,

$$\Omega_i^{BGK} = -\frac{g_i - \bar{g}_i^{eq}}{\tau + 0.5}, \tag{4.6}$$

or the more sophisticated MRT model [135, 146],

$$\Omega_i^{MRT} = -(\mathbf{M}^{-1}\mathbf{S}\mathbf{M})(g_i - \bar{g}_i^{eq}). \tag{4.7}$$

The orthogonal collision matrix, $\mathbf{M}$, transforms the distribution functions from physical to momentum space and the diagonal relaxation matrix is given by,

$$\mathbf{S} = \mathrm{diag}(1, 1, 1, 1, 1, 1, s_\nu, s_\nu), \tag{4.8}$$

where, $s_\nu = (\tau + 0.5)^{-1}$. The hydrodynamic forcing term is incorporated in $F_i(\mathbf{x}, t)$ as,

$$F_i(\mathbf{x}, t) = w_i \frac{\mathbf{c}_i \cdot \mathbf{F}}{\rho c_s^2} \delta t. \tag{4.9}$$

After substituting Equation 4.9 into Equation 4.4, it can be seen that this is consistent with the leading order term in the forcing scheme of Guo *et al.* [147]. It is noted here that the higher order form,

$$F_i(\mathbf{x}, t) = \delta t w_i \left[\frac{\mathbf{c}_i - \mathbf{u}}{\rho c_s^2} + \frac{(\mathbf{c}_i \cdot \mathbf{u})\mathbf{c}_i}{\rho c_s^4} \right] \cdot \mathbf{F}, \tag{4.10}$$

was examined, but no noticeable difference was observed in simulation results.

Due to the velocity-based approach, additional pressure, $\mathbf{F}_p$, and viscous, $\mathbf{F}_\mu$, forces need to be accounted for in the hydrodynamic forcing term,

$$\mathbf{F} = \mathbf{F}_p + \mathbf{F}_\mu + \mathbf{F}_B + \mathbf{F}_s. \tag{4.11}$$

Here, $\mathbf{F}_B$ represents external body forces on the system and $\mathbf{F}_s$ is taken as per Equation 3.50. A Chapman-Enskog analysis can be used to determine the form of the pressure term as [4, 145],

$$\mathbf{F}_p = -p^* c_s^2 \nabla \rho, \tag{4.12}$$

The viscous term is then given by,

$$\mathbf{F}_\mu = \nu \left[\nabla \mathbf{u} + (\nabla \mathbf{u})^T\right] \cdot \nabla \rho, \tag{4.13}$$

which can be determined locally through the relation of the deviatoric stress tensor to the hydrodynamic distribution function,

$$F_{\mu,\alpha}^{BGK} = \frac{-\nu}{(\tau + 0.5) c_s^2 \delta t} \left[\sum_i c_{i\alpha} c_{i\beta} (g_i - g_i^{eq})\right] \frac{\partial \rho}{\partial x_\beta}, \tag{4.14}$$

$$F_{\mu,\alpha}^{MRT} = \frac{-\nu}{c_s^2 \delta t} \left[\sum_i c_{i\alpha} c_{i\beta} \times \sum_j (\mathbf{M}^{-1}\mathbf{S}\mathbf{M})_{ij} (g_j - g_j^{eq})\right] \frac{\partial \rho}{\partial x_\beta}, \tag{4.15}$$

for the BGK and MRT collision schemes, respectively. For a detailed analysis of obtaining the velocity gradients locally with the LBM, the interested reader is referred to the work of Krüger et al. [148]. In both of these equations, the kinematic viscosity is related to the relaxation time by,

$$\nu = \tau c_s^2 \delta t. \tag{4.16}$$

Given the relation of the relaxation time to the physical fluid properties, there exist multiple options to determine its value from the phase-field. One approach is to use a harmonic interpolation that favours lower values [149],

$$\frac{1}{\tau} = \frac{1}{\tau_l} + (\phi - \phi_l) \left(\frac{1}{\tau_h} - \frac{1}{\tau_l}\right), \tag{4.17}$$

where τ_l and τ_h are the relaxation rates associated with the light and heavy fluids, respectively. The second common method seen in the literature is to take a simple linear interpolation as is conducted with the density and typically favours higher values,

$$\tau = \tau_l + (\phi - \phi_l)(\tau_h - \tau_l). \tag{4.18}$$

This is equivalent to performing a linear interpolation on the kinematic viscosity of the fluid, alternatively, this could also be conducted with the dynamic viscosity,

$$\mu = \mu_l + (\phi - \phi_l)(\mu_h - \mu_l). \tag{4.19}$$

The relaxation parameter can then be calculated as, $\tau = \mu / \rho c_s^2$. These methods are tested in Section 4.2.1, where the linear interpolation in Equation 4.18 is observed to provide a reasonable balance

between stability and accuracy. This was used in the early work of He et al. [128], but the finding here highlights both the benefit and issues around the dynamic viscosity implementation proposed in Ding et al. [150]. The interpolation scheme used for the fluid parameters in the diffuse interface can impact the spurious velocities observed in phase-field models, particularly in the presence of interface curvature. The recent work by Gruszczyński et al. [1] analysed this using a droplet centred in a square domain. The authors found that Equation 4.19 produced larger spurious velocities, on the order of 10^{-6} lattice units in contrast to Equation 4.18 were the currents were on the order 10^{-8} lattice units.

The hydrodynamic model presented here has some subtle, but notable, differences when compared with the work of Zu and He [145]. Firstly, the method of calculating the viscous forcing term was originally that of finite differences, introducing the velocity vector as a nonlocal variable to the computational grid and ultimately impeding on parallel compute ability. In this work, the benefit of the LBM in determining the deviatoric stress tensor is utilised to reduce computational communication costs. A further difference can be observed in the equilibrium function, which is now designed to simplify the collision step. The third difference comes in the calculation of macroscopic parameters; in the model of Zu and He [145] the pressure and velocity calculations are coupled and, consequently, an iterative, predictor-correct scheme is required. Here, a routine collision-streaming sequence can be used and after which the pressure and velocity can be updated independently by,

$$p = \rho c_s^2 \sum_i g_i, \tag{4.20}$$

$$\mathbf{u} = \sum_i g_i \mathbf{c}_i + \frac{\mathbf{F}}{2\rho}\delta t. \tag{4.21}$$

It is worth noting that the pressure is not dependent on the velocity as in the case of Zu and He [145], and the velocity is calculated after the pressure, eliminating the need for a predictor-corrector step.

To reduce the number of variables communicated between computational nodes, the gradients for the density in Equations 4.12 and 4.13 are related to the phase-field,

$$\nabla\rho = (\rho_h - \rho_l)\nabla\phi. \tag{4.22}$$

As a result, the only nonlocal information that is required in the collision stage is the phase-field of the neighbouring nodes. Additionally, the phase gradient is determined with the use of a second-order, isotropic centred difference [151],

$$\nabla\phi = \frac{c}{c_s^2 \delta x} \sum_i \mathbf{c}_i w_i \phi(\mathbf{x} + \mathbf{c}_i \delta t, t), \tag{4.23}$$

avoiding the need for directional derivatives along lattice links as used in phase-field models of, for example, Lee and Liu [149]. Additionally, the Laplacian of the phase-field, which is required to calculate the chemical potential is given by,

$$\nabla^2\phi = \frac{2c^2}{c_s^2(\delta x)^2} \sum_i w_i \left[\phi(\mathbf{x} + \mathbf{c}_i \delta t, t) - \phi(\mathbf{x}, t)\right]. \tag{4.24}$$

4.1.2 LBE for interface dynamics

The Allen-Cahn equation [43] is used to predict the dynamic behaviour of the fluid-fluid interface in this study rather than the commonly used work of Cahn and Hilliard [42]. The Cahn-Hilliard equation is typically used for the conservative properties evident in the scheme, however, the method requires a fourth-order derivative term to be resolved. Special treatment of this high-order term can reduce the numerical efficiency of the model in addition to its inherent complexity. In contrary to this, the Allen-Cahn equation was initially criticised for lossing mass, but when reformulated in a conservative form, allows for only second-order derivative terms while still maintaining mass conservation. In particular, the phase-field model proposed by Sun and Beckermann [152] and reformulated in a conservative form by Chiu and Lin [153] provides the governing equation,

$$\frac{\partial \phi}{\partial t} + \nabla \cdot \phi \mathbf{u} = \nabla \cdot M \left[\left(\nabla \phi - \frac{\nabla \phi}{|\nabla \phi|} \frac{[1-4(\phi-\phi_0)^2]}{W} \right) \right]. \tag{4.25}$$

The equilibrium profile of the phase-field perpendicular to an interface located at, $\mathbf{x}_0$, is assumed to fit a hyperbolic tangent,

$$\phi(\mathbf{x}) = \phi_0 \pm \frac{\phi_h - \phi_l}{2} \tanh\left(\frac{\mathbf{x}-\mathbf{x}_0}{W/2} \right), \tag{4.26}$$

which is typically used to set the initial condition of the phase-field to enhance stability across the domain. A technique that can be applied for complex initialisation shapes is that of smoothing, where no collision procedure is conducted but the populations are allowed to diffuse for a small number of iterations ($O(10)$). This was found to assist with stability in the early stages of simulations.

In order to resolve Equation 4.25 a second distribution function, h_i, is introduced and evolved according to,

$$h_i(\mathbf{x}+\mathbf{c}_i\delta t, t+\delta t) = h_i(\mathbf{x},t) - \frac{h_i(\mathbf{x},t) - \bar{h}_i^{eq}(\mathbf{x},t)}{\tau_h^{\phi} + 1/2} + F_i^{\phi}(\mathbf{x},t), \tag{4.27}$$

where the forcing term is given by,

$$F_i^{\phi}(\mathbf{x},t) = \delta t \frac{[1-4(\phi-\phi_0)^2]}{W} w_i \mathbf{c}_i \cdot \frac{\nabla \phi}{|\nabla \phi| + \varepsilon}, \tag{4.28}$$

where ε is a small parameter used to avoid a divide by zero singularity. The mobility, M, is related to the phase-field relaxation time through,

$$M = \tau_{\phi} c_s^2 \delta t, \tag{4.29}$$

and the equilibrium of the phase-field distribution function is defined as,

$$\bar{h}_i^{eq} = h_i^{eq} - 0.5 F_i^{\phi}, \tag{4.30}$$

where,

$$h_i^{eq} = \phi w_i \left[1 + \frac{\mathbf{c}_i \cdot \mathbf{u}}{c_s^2} + \frac{(\mathbf{c}_i \cdot \mathbf{u})^2}{2c_s^4} - \frac{\mathbf{u} \cdot \mathbf{u}}{2c_s^2} \right]. \tag{4.31}$$

In order to update the value of the phase-field, the zeroth order moment can be determined after the streaming stage,

$$\phi = \sum_i h_i. \tag{4.32}$$

From this, the local density in the domain can be calculated through a linear interpolation,

$$\rho = \rho_l + (\phi - \phi_l)(\rho_h - \rho_l). \tag{4.33}$$

In the phase-field model presented above, a high-order temporal term is neglected to enhance the efficiency and locality of the formulation. Ren *et al.* [144] included this term in a recent phase-field model, however, neglected the nonlinear terms appearing in the equilibrium distribution function. The additional numerical diffusion associated with this may increase the importance of this temporal derivative but for the work conducted here, no significance was observed. In testing, the temporal term is included by taking,

$$F_i^{\phi,\partial_t} = F_i^{\phi} + \frac{w_i \mathbf{c}_i \cdot \partial_t(\phi \mathbf{u})}{c_s^2}. \tag{4.34}$$

Finite differences are applied to the continuous temporal derivative such that it can be consistently applied,

$$F_i^{\phi,\partial_t} = F_i^{\phi} + \frac{w_i \mathbf{c}_i \cdot [(\phi \mathbf{u})|_t - (\phi \mathbf{u})|_{t-1}]}{c_s^2}, \tag{4.35}$$

where the subscript t indicates the current timestep and $t-1$ the previous.

4.2 Model verification

With the proposal of a new method, it is first necessary to show that the model is able to correctly recover the equations that it set out to solve. As such, this section focuses on the layered Poiseuille and Rayleigh-Taylor instability flow cases. These are commonly used benchmarks for multiphase flow models and will be used to show the robustness of the phase-field LBM for a range of parameter values.

4.2.1 Layered Poiseuille flow

The gravity-driven flow of fluids in a rectangular channel has been used as a benchmark for numerous multiphase LB models [154, 155]. This simple test case can be used to compare the accuracy and convergence of formulations as well as give an initial indication towards their ability to handle density and or viscosity contrasts. Figure 4.1 provides a schematic for this benchmark in which the top ($y = L$) and bottom ($y = 0$) are fixed walls created using the bounce-back scheme. The bottom half of the domain is then filled with a light fluid with density, ρ_l, and viscosity, μ_l. The fluid motion is driven

through a body force, $\mathbf{F}_B = \rho g_x$, where g_x is the applied acceleration along the x-axis. With the absence of surface tension effects, the NSE with the conditions stated can be reduced to,

$$\frac{d}{dy}\left(\mu\frac{du}{dy}\right)+\rho g_x = 0, \tag{4.36}$$

where u represents the component of velocity in the x direction. The system is initialised with a diffuse interface, in which the density and viscosity become functions of the vertical height,

$$\rho(y) = 0.5\left[\rho_h+\rho_l-(\rho_h-\rho_l)\tanh\left(\frac{2y-L}{W}\right)\right], \tag{4.37}$$

$$\mu(y) = 0.5\left[\mu_h+\mu_l-(\mu_h-\mu_l)\tanh\left(\frac{2y-L}{W}\right)\right]. \tag{4.38}$$

With a known profile for the density and viscosity, Equation 4.36 can be readily solved using a high-resolution finite difference scheme. The results from this are used to analyse the accuracy of the phase-field model presented in which the measured velocities are normalised through the maximum velocity of the finite difference solution, $\max(u_{FD})$, and the vertical position through the domain height, L. This allows the velocity profiles predicted from the LBM to be compared with a diffuse interface solution to the simplified Navier-Stokes equation and errors quantified through an L_2-norm defined as,

$$||\delta u||_2 = \sqrt{\frac{\sum_y (u_x-u_{x,FD})^2}{\sum_j (u_{x,FD})^2}}\,. \tag{4.39}$$

In addition to this, if one assumes the interface is a discontinuity in which,

$$\mu(y) = \begin{cases}\mu_h, & y\in[0.5L, L]\\ \mu_l, & y\in[0.0L, 0.5L),\end{cases} \tag{4.40}$$

a sharp interface solution can be obtained by applying boundary and interface conditions. Namely, nonslip wall boundaries are imposed at the top and bottom of the domain while continuous shear stress and velocity must be maintained at the interface,

$$u_x|_{y=0} = u_x|_{y=L} = 0, \tag{4.41}$$

$$\mu_h\partial_y u_x|_{y=0.5L} = \mu_l\partial_y u_x|_{y=0.5L}, \tag{4.42}$$

$$u_x|_{y=0.5L+} = u_x|_{y=0.5L-}. \tag{4.43}$$

From this, the analytical solution for the sharp interface is found in which $L/2 = l$ is specified for convenience,

$$u(y) = \begin{cases}\frac{g_x l}{2\mu_h}\left[-\rho_h\frac{y^2}{l^2}-\frac{y}{l}\left(\frac{\mu_h\rho_l-\mu_l\rho_h}{\mu_h+\mu_l}\right)+\mu_h\frac{\rho_h+\rho_l}{\mu_h+\mu_l}\right], & y\in[l, L]\\ \frac{g_x l}{2\mu_l}\left[-\rho_l\frac{y^2}{l^2}-\frac{y}{l}\left(\frac{\mu_h\rho_l-\mu_l\rho_h}{\mu_h+\mu_l}\right)+\mu_l\frac{\rho_h+\rho_l}{\mu_h+\mu_l}\right], & y\in[0, l).\end{cases} \tag{4.44}$$

This is superimposed on the following results, however, note is made that comparison with the finite difference results capturing the diffuse interface resolved in simulations is still used for the L_2-norm.

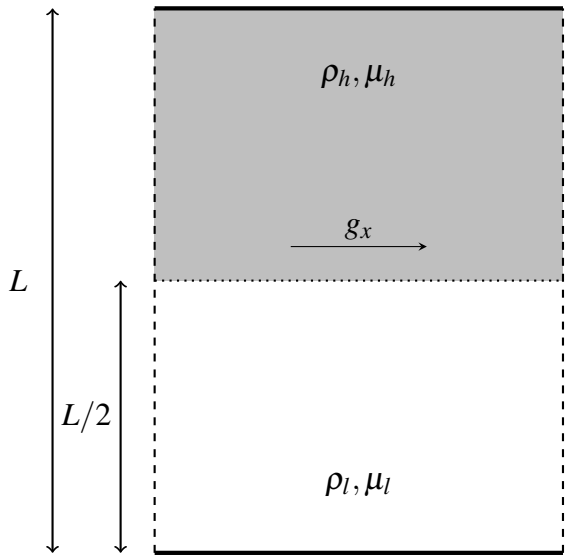

Figure 4.1: Two-phase Poiseuille flow schematic with a light fluid occupying $y = 0$ to $y = L/2$ and a heavy fluid from $y = L/2$ to $y = L$.

With the general flow domain described, it can now be used to analyse the interpolation schemes used in the phase-field LBM to determine the relaxation parameter across the interface. For this, three methods are compared, namely, the harmonic interpolation (Eq. 4.17), the linear interpolation (Eq. 4.18) and interpolation through the dynamic viscosity (Eq. 4.13). Density ratios of one, $\rho^* = 1$, and ten, $\rho^* = 10$, are tested and the domain resolution is specified by setting the height to 64 lattice units, $L = 64$. With the relaxation rate being linked to the fluid viscosity, the dynamic viscosity ratio is specified at 100, $\mu^* = 100$, to exaggerate the effect of the chosen interpolation scheme. The interface width is specified as four lattice units, the mobility is set to 0.02 and the gravitational acceleration in the x-direction is 10^{-6} lattice units.

Figure 4.2(a) reveals that the harmonic interpolation scheme is unable to capture the required behaviour with such a large viscosity contrast. However, for this density matched case both the linear and dynamic viscosity updates provide results consistent with the high resolution finite difference solution. However, from Figure 4.2(b), it is evident that when a density contrast is introduced, only the dynamic viscosity update provides results consistent with the expected velocity profile.

In order to determine the cause of inconsistency in the relaxation parameter interpolation scheme, Figure 4.3 provides the τ-profiles over the domain for the various interpolation schemes. Here, it is clear that in the density matched case the linear and dynamic viscosity updates are consistent while the harmonic interpolation provides too much weight to the lower viscosity in the system. Once the density contrast is introduced, the dynamic update can be seen to provide more weighting to the more viscous fluid, which appears to result in a velocity profile consistent with the high resolution finite difference solution.

With a consistent interpolation scheme found, the model is now compared to two momentum-based phase-field LBMs. The first employs *mixed*, directional derivatives [28, 149] in determining the phase-field gradients and the second uses only *centred*, isotropic differences [120, 156], as used in the current model. The layered Poiseuille domain aligns with that described in the interpolation scheme

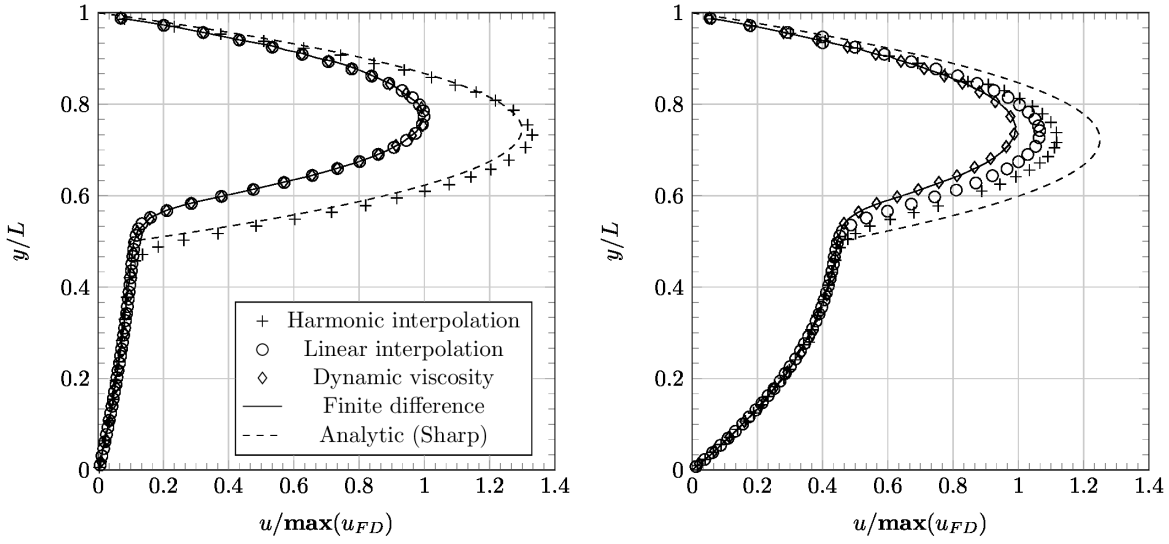

(a) $\rho^* = 1$ (b) $\rho^* = 10$

Figure 4.2: The layered Poiseuille flow test case used in the comparison of interpolation schemes for determining the relaxation parameter, τ.

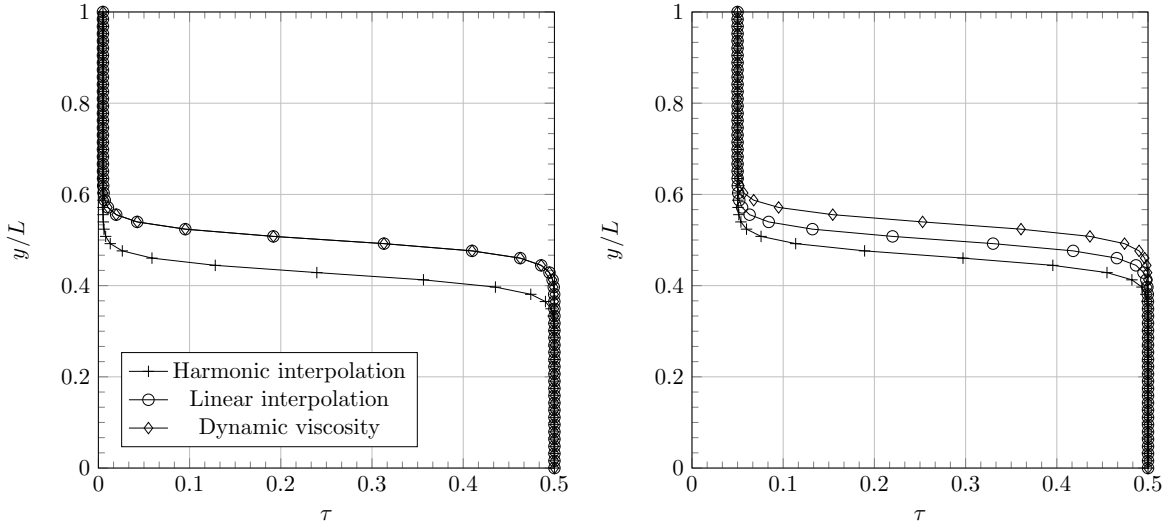

(a) $\rho^* = 1$ (b) $\rho^* = 10$

Figure 4.3: The layered Poiseuille flow test case used in the comparison of interpolation schemes for determining the relaxation parameter, τ.

analysis, however, here the density ratio is specified as 10, 100 and 1000 while the viscosity ratio is fixed at 100. Figure 4.4 presents the velocity profiles found for each of these three cases and allows for a comparison of the model performance. It is evident that all three models are able to consistently capture the expected behaviour for relatively low density ratios (i.e. $\rho^* = 10$). As the contrast increases, the momentum-based LBM with *centred*, isotropic mixed differences fails to mimic the interface behaviour with large and obvious oscillations observed. This is due to the directional gradient term, $\mathbf{c}_i \nabla \phi$, evident in the momentum based LBM (see Equation 3.52). The purpose in using the *centred* difference in place of *mixed* derivatives is the increase in computational locality, allowing for improved run-time performance. However, it can be seen that this approach coupled with a momentum-based

evolution does not recover the governing hydrodynamics. When the LBM is formulated with velocity as the first moment as per the *current* model presented here, it is evident that the isotropic difference is sufficient to recover the desired velocity profile as the directional gradient term listed above is eliminated. Additionally, when analysing the L_2-norm the current model is superior to the previous momentum-based LBMs for this particular flow configuration.

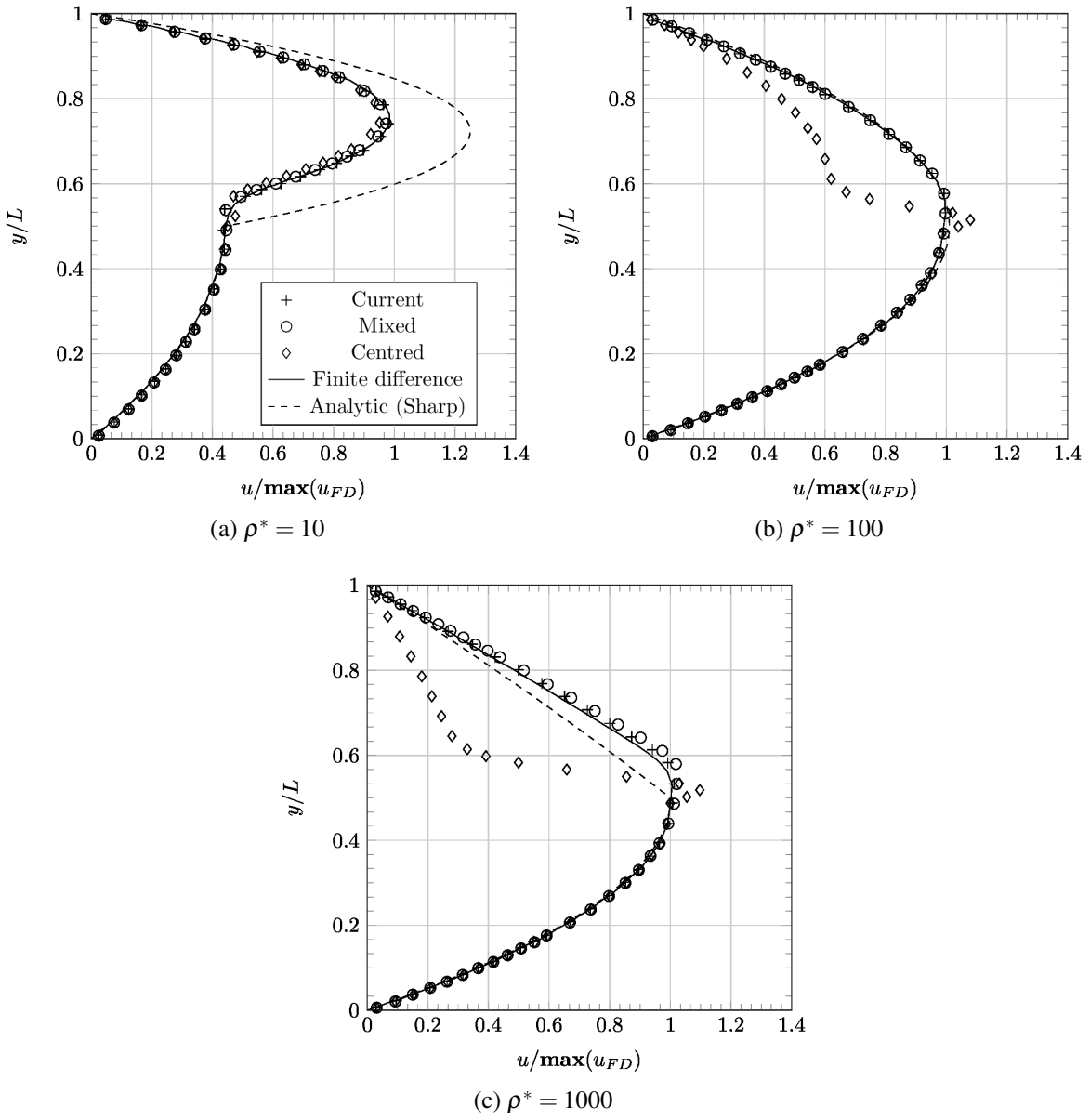

(a) $\rho^* = 10$ (b) $\rho^* = 100$

(c) $\rho^* = 1000$

Figure 4.4: The layered Poiseuille flow test case used to compare various phase-field models including the current model proposed in this Chapter, the model requiring mixed differences by Fakhari *et al.* [28] and the modified version of this using isotropic centred differences by Fakhari and Bolster [120].

Figure 4.5 provides a quantitative comparison of the models as well as their convergence behaviour. The convergence case was conducted with a density ratio of 1000 and a dynamic viscosity ratio of 100. It is noted here that the Cahn number which relates the interface thickness to the domain was held constant, $\mathrm{Cn} = W/L = 3/32$. It can be seen here that the current method produces the lowest error and converges marginally faster than the other models tested. However, it is also observed that no model retains the second-order convergence rate of the single phase LBM [157]. It is speculated that this

could be a result of the viscosity contrast at the top compared to bottom wall. This causes different relaxation rates which may cause the zero velocity point to shift from the halfway location as the mesh is refined [158].

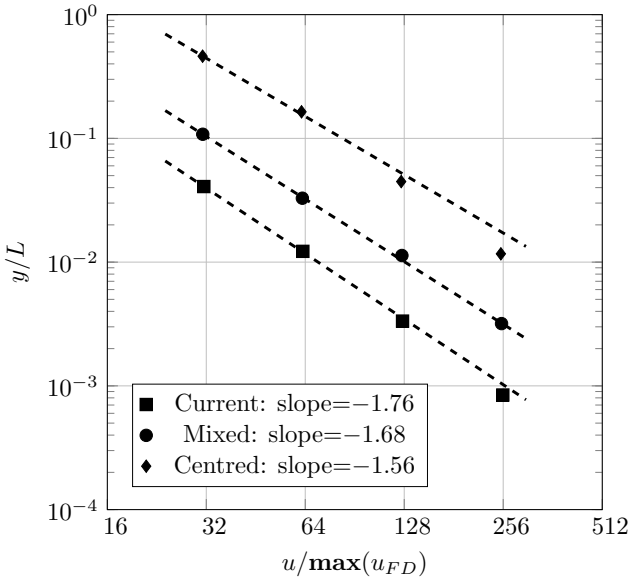

Figure 4.5: Convergence behaviour of the layered Poiseuille flow case for a density ratio of 1000 and viscosity ratio of 100.

4.2.2 Rayleigh-Taylor instability

The instability created when a heavy fluid layer is situated above a lighter fluid within a gravitational field, g, provides another common benchmark problem for multiphase models [103, 144, 145, 159]. To initiate the characteristic dynamics, known as the Rayleigh-Taylor instability, the fluid interface is perturbed and the heavy fluid is observed to penetrate into the lower layer. The initial deviation from planarity drives the instability where sections of fluid situated above the interface mean height experience higher pressure than required for support causing them to rise and displace the heavy fluid. Equivalently, the fluid situated below the mean height requires more than the average pressure for support, and as a result penetrates further into the lower layer [160]. The instability has been widely studied due to its prevalence in both natural occurring phenomena and engineering systems.

The base level setup of this benchmark case has become a de facto standard between authors [103, 144, 145, 159]. Here, a two-dimensional domain of size $[0,L]\times[-2L,2L]$ is initialised with wall boundaries restricting the y-axis and periodic bounds in the x. The top of the domain is filled with a heavy fluid, ρ_h,μ_h, while the light fluid, ρ_l,μ_l, is situated below this. The interface that would currently be lying along $y=0$ is then perturbed by a cosine function such that it is located along,

$$y_0(x) = 0.1L\times\cos(2\pi x/L). \tag{4.45}$$

The phase-field can then be initialised according to,

$$\phi(\mathbf{x}) = \phi_0 + \frac{\phi_h-\phi_l}{2}\tanh\left(\frac{|\mathbf{x}-\mathbf{x}_0|_\perp}{W/2}\right), \tag{4.46}$$

where $\mathbf{x} = (x, y)$, $\mathbf{x}_0$ is the interface location and $|\mathbf{x} - \mathbf{x}_0|_\perp$ is the shortest signed distance from any grid point to the interface location. It should be noted that three additional initialisation schemes were tested with no observable differences. The first method was to simply initialise a sharp interface between the fluids, the second used the displacement in the y-direction from the interface only,

$$\phi(y) = \phi_0 + \frac{\phi_h - \phi_l}{2} \tanh\left(\frac{y - y_0}{W/2}\right), \tag{4.47}$$

and the final method consisted of a sharp interface that was smoothed by performing a stream update without any collision dynamics for $O(10)$ iterations before conducting the normal LBM update. No noticeable difference was observed between these methods, the results shown here were initialised using Equation 4.46.

In order to compare the results of the presented model to others existing in the literature, it is necessary to define a set of dimensionless numbers to define the flow cases tested. Here, the density contrast is reflected by the Atwood number,

$$At = \frac{\rho_l - \rho_g}{\rho_l + \rho_g}, \tag{4.48}$$

a reference velocity scale is defined as, $U_0 = \sqrt{gL}$, allowing the Reynolds number to be specified as,

$$Re = \frac{\rho_l U_0 L}{\mu_l}. \tag{4.49}$$

To uniquely define the remaining physical parameters in the simulation, two additional dimensionless expressions are required, namely the dynamic viscosity ratio, μ^*, and the Capillary number,

$$Ca = \frac{\mu_l U_0}{\sigma}. \tag{4.50}$$

The simulation also requires user inputs for two numerical phase-field parameters for which the interface width is held constant, $W = 5$ lattice units, and the mobility is defined through the Péclet number,

$$Pe = \frac{U_0 L}{M}. \tag{4.51}$$

To verify the model formulation and implementation, computational parameters for the Rayleigh-Taylor benchmark are specified consistently with the work of Ren *et al.* [144]. As such, a reference length of 256 lattice units and a reference time given as $t_0 = \sqrt{L/(g.At)} = 16000$ lattice units is taken. In this work, two cases are conducted, firstly the model is compared with previous works like that of Ren *et al.* [144] in the base case before an extension test is conducted to show the robustness of the model in capturing flow configurations with density ratios and Reynolds numbers beyond previous models [103, 144, 145]. Table 4.1 indicates the relevant parameters for both cases.

Figure 4.6 depicts the time evolution of the Rayleigh-Taylor instability for the base case parameters. Here, the heavy fluid is observed to symmetrically penetrate the lighter fluid. As time progresses, the generation of counter-rotating vortices can be observed and their notable instability as they shed into the wake region behind the liquid front.

Table 4.1: Flow configurations for the base and extension cases of the Rayleigh-Taylor instability.

Parameter	L	t_0	At	Re	μ^*	Ca	Pe	W
Base case	256	16000	0.500	3000	1	0.26	1000	5
Extension case	256	16000	0.998	3000	100	0.44	1000	5

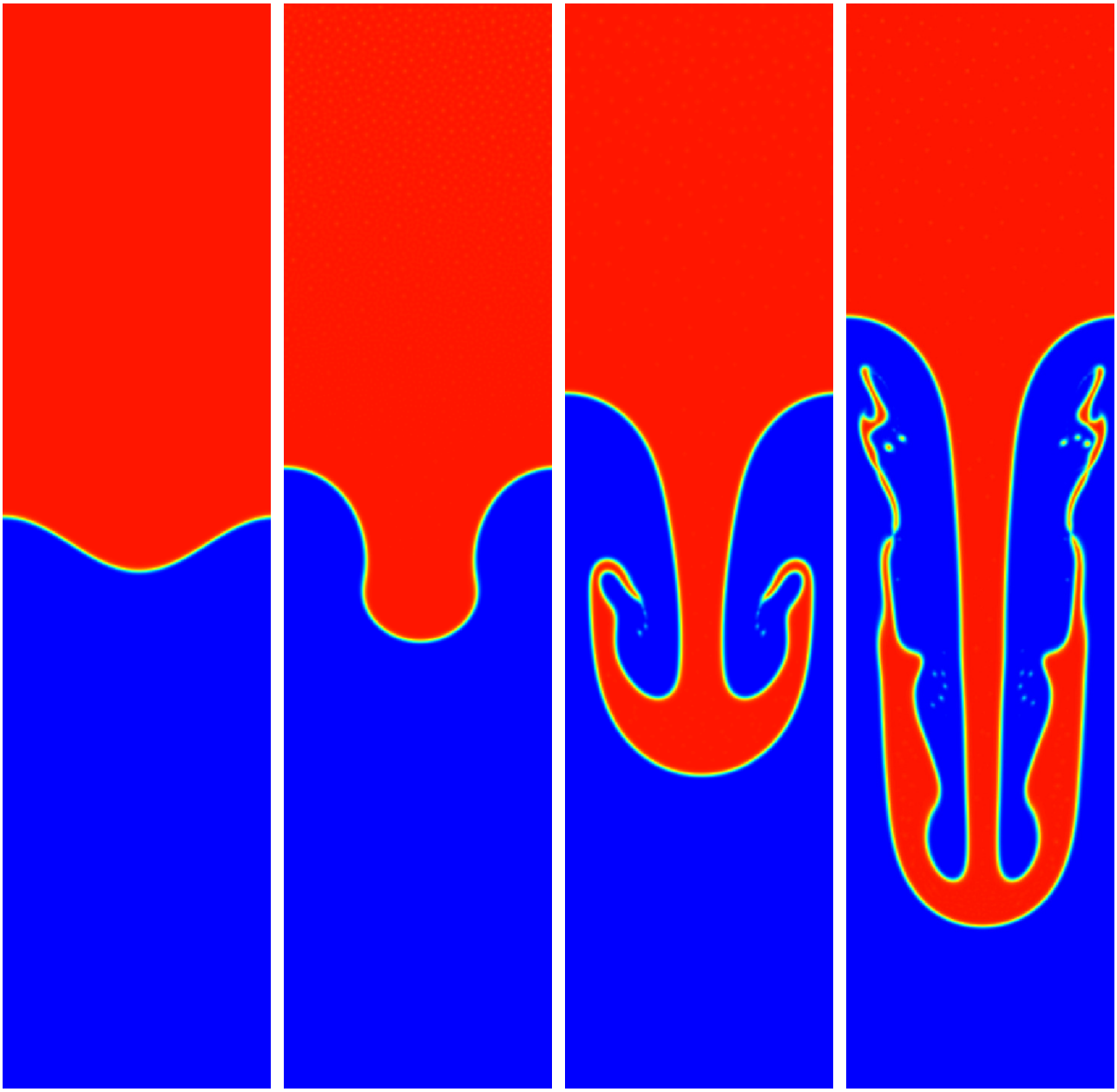

(a) $t^* = 0$ (b) $t^* = 1$ (c) $t^* = 2$ (d) $t^* = 3$

Figure 4.6: The evolution of a single mode Rayleigh-Taylor instability with At $= 0.500$ (i.e. $\rho^* = 3$), Re $= 3000$, $\mu^* = 1$, Ca $= 0.26$ and Pe $= 1000$.

The results of the widely used momentum-based LBM with both an isotropic central [120] and a mixed difference [28] scheme, along with the benchmark data from previous studies [103, 144, 145], are compared with the current model. Figure 4.7 shows the dimensionless position of the bubble and liquid fronts versus the dimensionless time. It is clear that the results obtained using the current model agree well with previously published data. The time evolution of the interface using the momentum-based

lattice Boltzmann schemes are also in close agreement with each other and the data extracted from the literature, suggesting reasonable accuracy for the case where the density ratio is relatively low. This is particularly interesting for the isotropic difference scheme [120], which failed to capture the expected behaviour in the Poiseuille case. On closer inspection, it can be seen that the erroneous velocity in the low density fluid is still exhibited but the correct behaviour for the higher density dominates the dynamics.

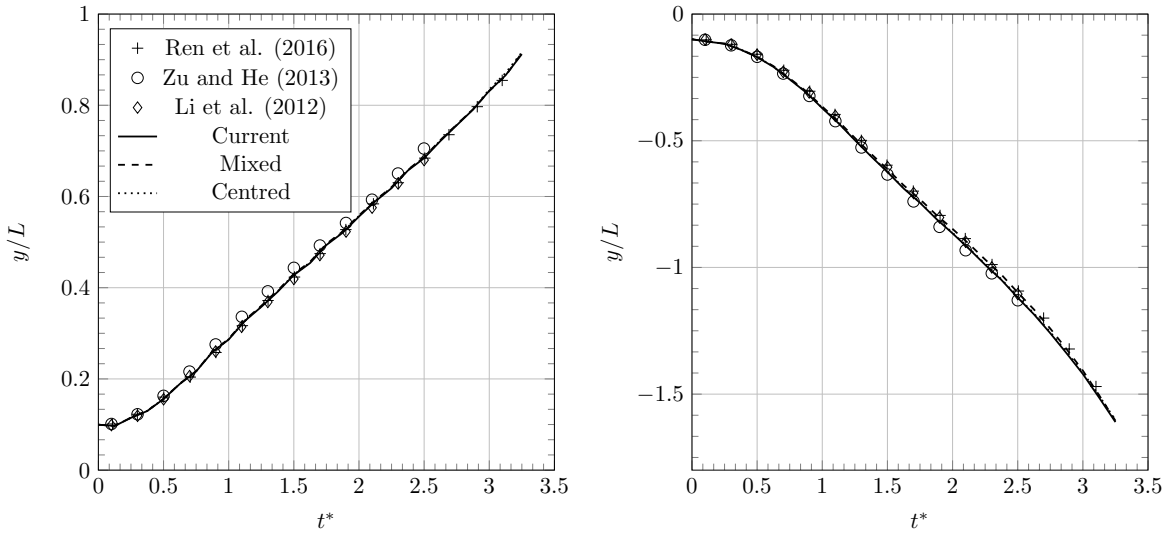

(a) Rising bubble front

(b) Falling liquid front

Figure 4.7: Time evolution of the Rayleigh-Taylor instability at At $= 0.5$, Re $= 3000$, $\mu^* = 1$, Ca $=$ 0.26, and Pe $= 1000$ for (a) the bubble front location along $x = 0$ and (b) the liquid front position along $x = L/2$.

Currently, there exists few studies which analyse the high density ratio Rayleigh-Taylor instability using phase-field theory. Ren *et al.* [144] looked to qualitatively assess this problem for a moderate density ratio at a high Reynolds number ($\rho^* = 99$ and $Re = 3000$), while Shao and Shu [119] presented results for a high density ratio at a moderate Reynolds number ($\rho^* = 1000$ and $Re = 200$). Here, the presented model is used to capture the extension case previously discussed with both a high density ratio and a high Reynolds number flow ($\rho^* = 1000$ and $Re = 3000$). The viscosity ratio for the simulation was taken as 100 to show that it could be applicable to a system such as air and water. Figure 4.8 shows the time evolution where the model is seen to robustly capture the propagation of both the high and low density fronts. This is particularly promising as the model proposed in Ren *et al.* [144] with an MRT collision scheme was reportedly not able to capture the situation investigated here.

4.3 Computational efficiency

For many applications of scientific and industrial relevance, the number of lattice sites in the domain of interest is often substantial. Hence, efficient parallel performance is essential. The previous model, presented in Fakhari and Bolster [120], uses a stencil consisting of a single layer of neighbouring

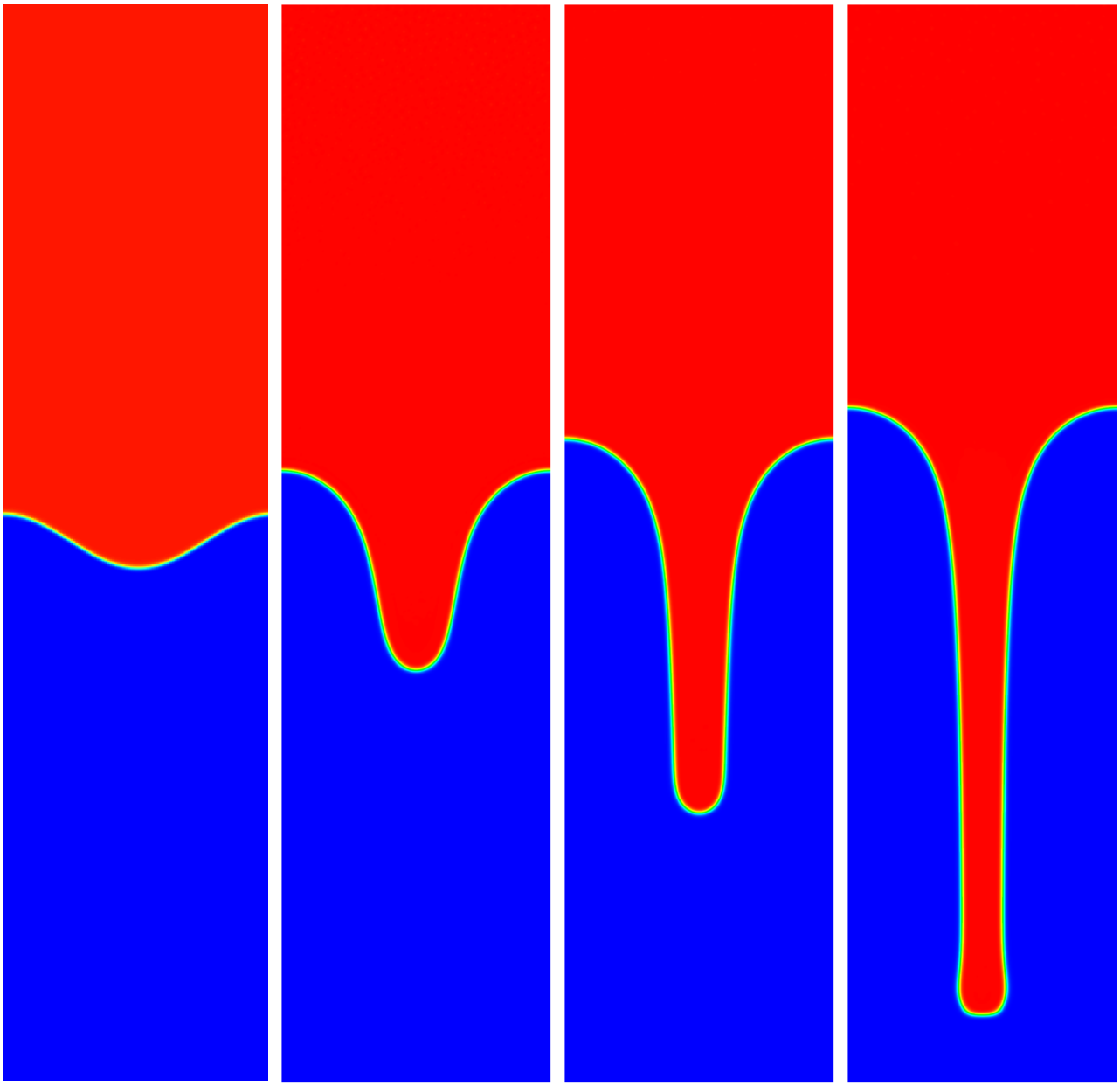

(a) $t^* = 0$ (b) $t^* = 1.0$ (c) $t^* = 1.5$ (d) $t^* = 2.0$

Figure 4.8: The evolution of a single mode Rayleigh-Taylor instability with At $= 0.998$ (i.e. $\rho^* = 1000$), Re $= 3000$, $\mu^* = 100$, Ca $= 0.44$ and Pe $= 1000$.

cells, but is not able to capture the low density flow field if a viscosity or density contrast exists. This was shown using the Poiseuille flow case where the accuracy deteriorated around the interface. In order to capture the interfacial dynamics more accurately, the model in Fakhari *et al.* [28] uses mixed differences, which requires two auxiliary lattice sites (two ghost cells) in each direction. The current model requires only a single stencil and is able to model the flow field at the liquid-gas interface with a high level of accuracy. In the following we aim to probe the computational efficiency of these models.

To investigate the performance of the aforementioned phase-field models, a stationary bubble test on a square domain, $L \times L$, with a bubble radius of $R = L/4$ is conducted. Taking $L = 5120$ lattice units resulted in a test domain of approximately 26 million cells. With this setup, the strong scalability of the methods was analysed, namely, the domain was divided into smaller portions, inducing sublinear

parallelism. This is in contrast to *weak* scaling, where the size of the mesh is kept proportional to the number of processors. The simulations were completed using the open-source TCLB solver [44] on the Prometheus cluster at Cyfronet, Krakow. This is equipped with CPU nodes fitted with two 12-core Intel Xeon E5-2680v3 processors and eight additional GPU nodes with two nVidia Tesla K40 cards on each.

Figure 4.9 shows the performance of the TCLB solver for the various models implemented on a CPU architecture. It is clear that the compared methods have a similar performance, with the speed per node generally decreasing for higher numbers of utilised cores. For the current model, as in all the previous benchmark simulations, the MRT operator was used in the calculation of both the stress tensor and the collision step. In the computational results, it is seen that the MRT formulation of the proposed model increases the computation required per node beyond the memory reduction benefit on the CPU architecture for this simulation domain.

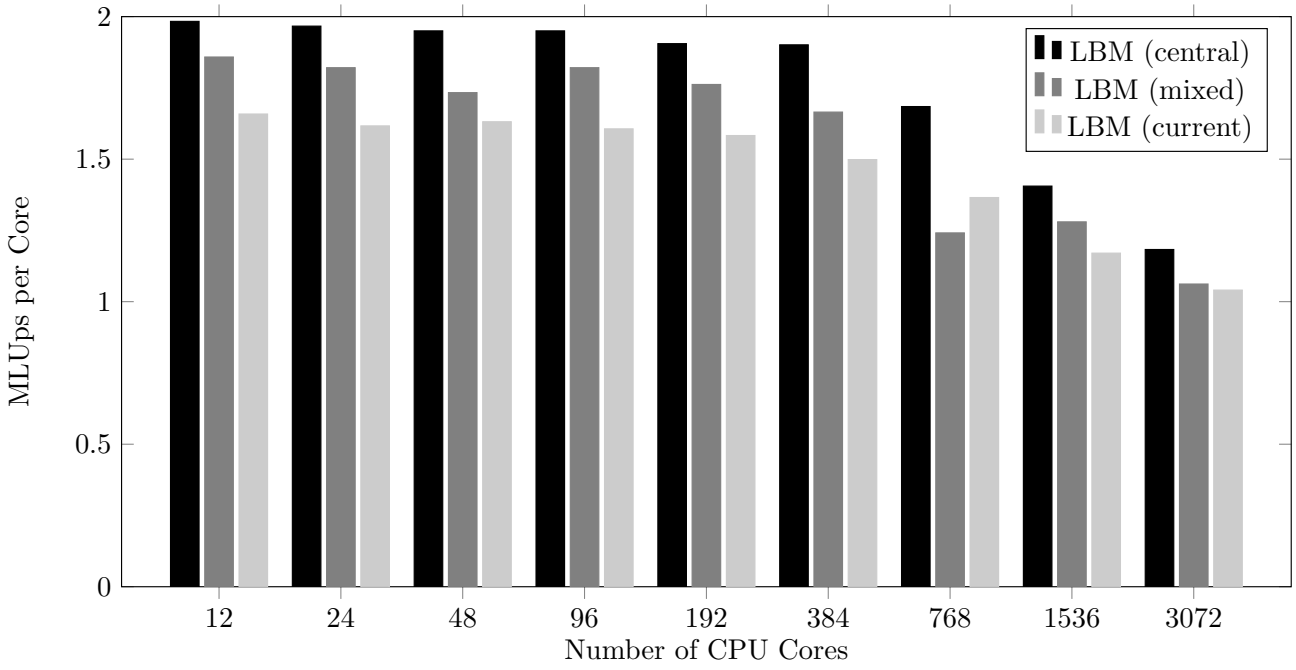

Figure 4.9: The strong scalability of the phase-field models tested using the TCLB solver on CPU cores.

Figure 4.10 shows the scaling of the TCLB code on a GPU architecture for the compared phase-field methods. As expected, the parallel performance can be seen to marginally decrease with core saturation (2880 CUDA cores per nVidia Tesla K40). It is on this parallel architecture that the benefit of the reduced stencil is realised. The difference between the CPU and GPU performances is well explained by the memory access patterns. Here, it is clear that the CPU performance is compute bound, whereas on the parallel architecture the performance is bound by memory. As a result of this, the mixed difference approach, which requires a larger computational stencil than the central difference and current model, sees a significant reduction in computational efficiency. In comparison to the CPU architecture, where the memory access speed is higher, there appears no significant distinction between the models for this simulation domain.

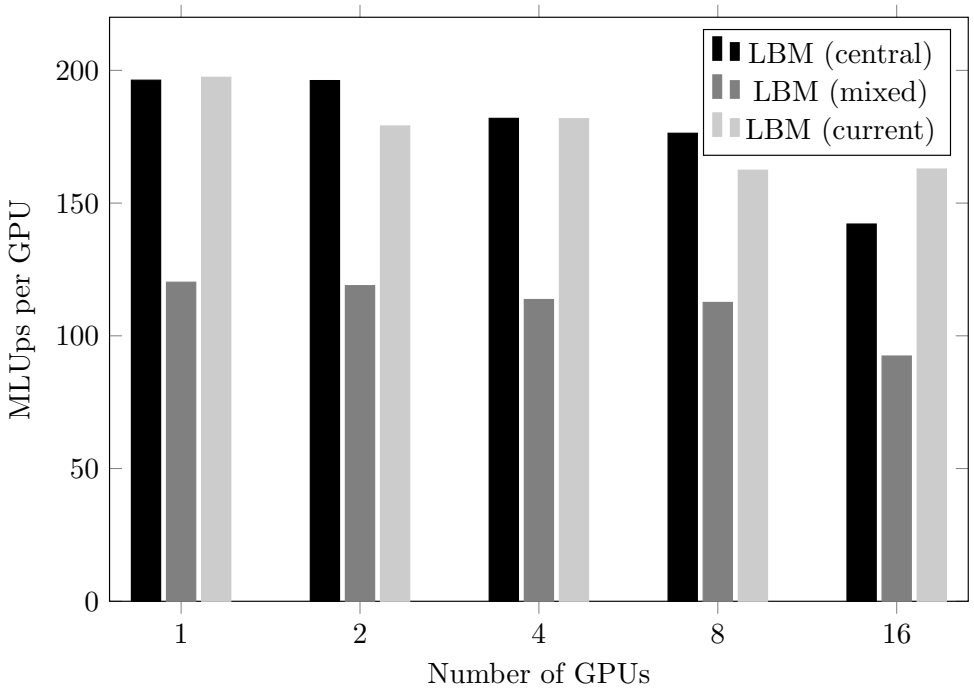

Figure 4.10: The strong scalability of the phase-field models tested using the TCLB solver on GPU cards.

It is often difficult to objectively compare the performance of GPU and CPU codes [161]. In the presented tests, the speed of a single CUDA core is substantially lower than a single CPU core. However, there are 2880 CUDA cores on a single GPU allowing it to vastly outperform a single CPU processor. One technique to compare these computing architectures is to look at the energy efficiency of the computation. The power consumption of a GPU node, consisting of two K40 processors, was measured at 490.5 W. Whereas for a CPU node, with two processors consisting of 24 total cores, the power consumption was 277.0 W. However, this increase in power gives approximately a factor of 4 increase in lattice updates for the proposed model, outweighing the increased energy cost.

4.4 Taylor bubble dynamics

There is significant practical interest in the motion of long bubbles due to their relation to modelling the flow of liquid slugs commonly seen in the oil and gas industry, nuclear reactors, and chemical engineering. As previously discussed, the variable rate of gas flow within a confined geometry such as a pipe or channel can lead to a number of characteristic interface topologies, commonly reported as flow regimes. Here, the focus turns to the slug flow regime in which bubbles have coalesced to a stage where they form an elongated bullet shape due to the wall confinement and are often referred to as Taylor bubbles. The Taylor bubbles are separated by liquid slugs, within which smaller gas bubbles may still be observed.

As a single Taylor bubble rises through a dense fluid, the viscous, inertial, and interfacial forces acting on it can have significant influence on both its shape and its rise velocity. The shape of the Taylor bubble can be characterised by a rounded leading surface followed by an almost cylindrical or

Table 4.2: Planar Taylor bubble results for dimensionless rise velocity (Fr) with negligible surface tension, re-created from the works of Figueroa-Espinoza and Fabre (2011).

Authors	**Result Type**	Fr
Birkhoff & Carter (1957) [35]	Inviscid theory	0.23
Watson (in [35])	Experimental	0.22-0.23
Griffith (in [35])	Experimental	0.23
Collins (1964) [163]	Inviscid theory	0.23
Collins (1964) [163]	Experimental	0.22-0.23
Mao & Dukler (1990) [164]	Numerical	0.22
Ha-Ngoc & Fabre (2004) [165]	Numerical	0.22

rectangular body depending on the flow domain. The trailing edge shape depends strongly on the flow condition and liquid properties with flat, rounded, indented, or jagged profiles reported in the literature. Flow separation in the wake can also be expected for Taylor bubbles at moderate Reynolds numbers, with the transition to separation observed at a Reynolds number between 13.4 and 32.6 for tubular flows [162]. An increasing Reynolds number also indicates a transition to an inertial regime, in which viscous and interfacial forces have a lesser, or in some cases negligible, impact on the flow dynamics

4.4.1 Planar Taylor bubble validation

In this section, the proposed model is used to simulate the rise of a planar Taylor bubble through stagnant fluid in an inertial regime. This case has been studied theoretically [35, 163], numerically [164, 165], and experimentally [163] by a number of authors, and a summary of these works can be found in Figueroa-Espinoza and Fabre [166]. Table 4.2 reproduces the findings of this to present the propagation speeds expected for this benchmark case. Similar to the Rayleigh-Taylor instability, the Froude number is given as,

$$Fr = \frac{u_r}{U_0}, \tag{4.52}$$

where u_r represents the rise velocity of the bubble and $U_0 = \sqrt{gL}$ is the characteristic velocity for the simulation. The results presented in this table are determined under the assumption of small surface tension and a bubble rise Reynolds number,

$$Re_r = \frac{\rho_l u_r L}{\mu_l} \geq 100. \tag{4.53}$$

In addition to the results provided in Table 4.2, Ha-Ngoc and Fabre [165] provided the numerical results for the bubble Froude number as a function of the Eötvös number,

$$Eo = \frac{(\rho_l - \rho_g) g L^2}{\sigma}. \tag{4.54}$$

They were able to conclude that at low surface tensions, the Froude number of the Taylor bubble was independent of the Eötvös number, tending towards $Fr = 0.22$. Additionally, the authors managed to predict the Taylor bubble shapes using the boundary element method for $Eo = 10$, 100, and 1000. In

this section, Ha-Ngoc and Fabre's work is used to compare the predicted interface profile, as well as the bubble rise velocity for the case where $Eo = 100$ from the proposed LBM.

Figure 4.11 provides a schematic of the computational domain used to analyse the planar Taylor bubble. Here, a rectangular gas region with a semi-circular front is initialised and a gravitational acceleration is applied acting against the direction of curvature. The bubble then propagates along the channel, transported by the liquid movement and gravitational effects. The domain size is $10LL$, with L being equal to 256 lattice units and an outer layer of nodes flagged as solid surrounding this with full bounce-back applied. The fluid properties are $\mu^* = 100$ and $\rho^* = 1000$, typical of an air-water system, and the gravitational force, $\mathbf{F}_b = \rho g \hat{\mathbf{x}}$ is applied to the entire fluid. The reference time is defined as per the Rayleigh-Taylor simulations and set to $t_0 = 24000$, such that the dimensionless time is given by, $t^* = t/t_0$, and $20t^*$ iterations are conducted.

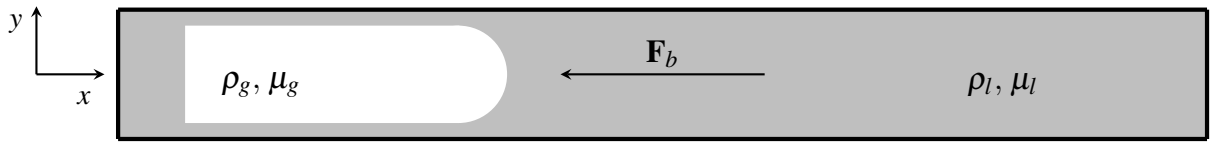

Figure 4.11: Domain schematic of the slug flow tests for the Taylor bubble rise. The fluid domain size is 10L × L, and the initial bubble size is 3L × 4L/5.

Figure 4.12 shows the time evolution of the Taylor bubble with the grey region representing fluid where $\phi = \phi_l = 1$ and the white region where $\phi = \phi_g = 0$. The expansion of the liquid film as it passes the end of the bubble induces a recirculating wake region that causes extension of the trailing edge and is capable of liberating smaller bubbles from the initial gas region. Here, the shearing force from the heavy fluid and the re-circulation of the falling liquid layer was sufficient to cause a continuous breakup and coalescence-type behaviour in the bubble wake. This behaviour in the wake region was observed to have no significant impact on the shape of the Taylor bubble front or the rise velocity.

Five contours of the equilibrium interface profile found at the conclusion of the simulation are displayed in Figure 4.13. Here, the diffuse-interface is highlighted, as such, contours of the phase-field are graphed for comparison with the sharp-interface result in Ha-Ngoc and Fabre [165]. It is seen that the centre of the diffuse interface produces a thinner Taylor bubble, but the curvature of the outer regions of the diffuse layer appear to match quite well with the sharp interface solution.

The steady rise velocity was found by tracking the position of the bubble front, where $\phi = \phi_0 = 0.5$, at intervals of $0.5t_0$ throughout the simulation. A linear regression was then performed using the final five data points with consistency checked against the remainder. This was additionally verified by assessing the average velocity of the entire gas bubble, as well as the instantaneous velocity at the front of the bubble where $\phi = 0.5$. In the test case, a bubble Froude number of 0.217 was measured, which very closely matches the expected range of $0.22 - 0.23$ from Table 4.2.

Overall, the results using the proposed LBM were shown to agree well with those based on the sharp-interface model as well as with experimental data in terms of the planar Taylor bubble's shape and rise velocity. However, an additional finding of this initial validation was that of improved model stability when using the linear interpolation scheme for the relaxation parameter. Here it was observed

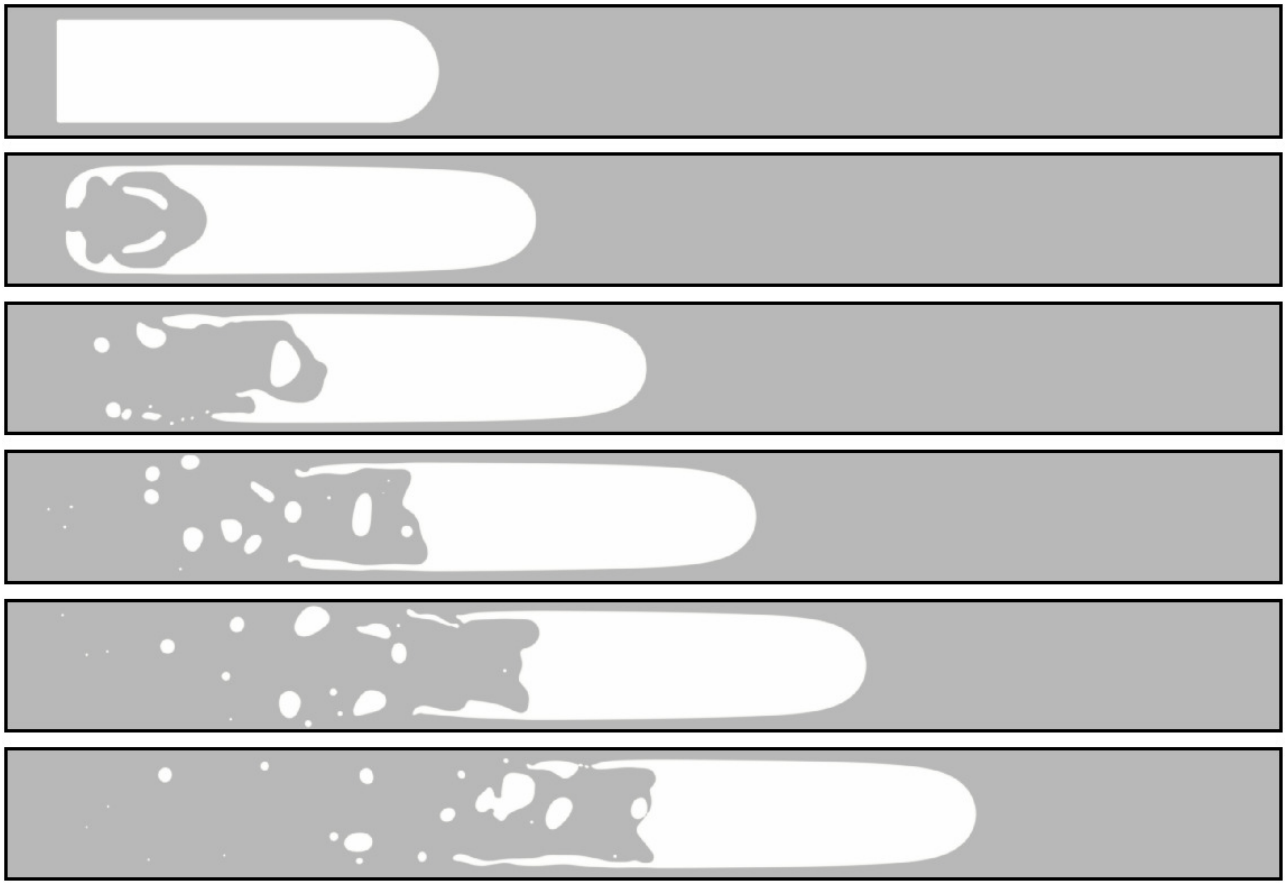

Figure 4.12: The time evolution of the planar Taylor bubble with snapshots taken at $t^* = 0$, 4, 8, 12, 16, 20. The fluid properties are defined by $\rho^* = 1000$ and $\mu^* = 100$, while the flow condition is specified through $Re_r = 200$ and $Eo = 100$.

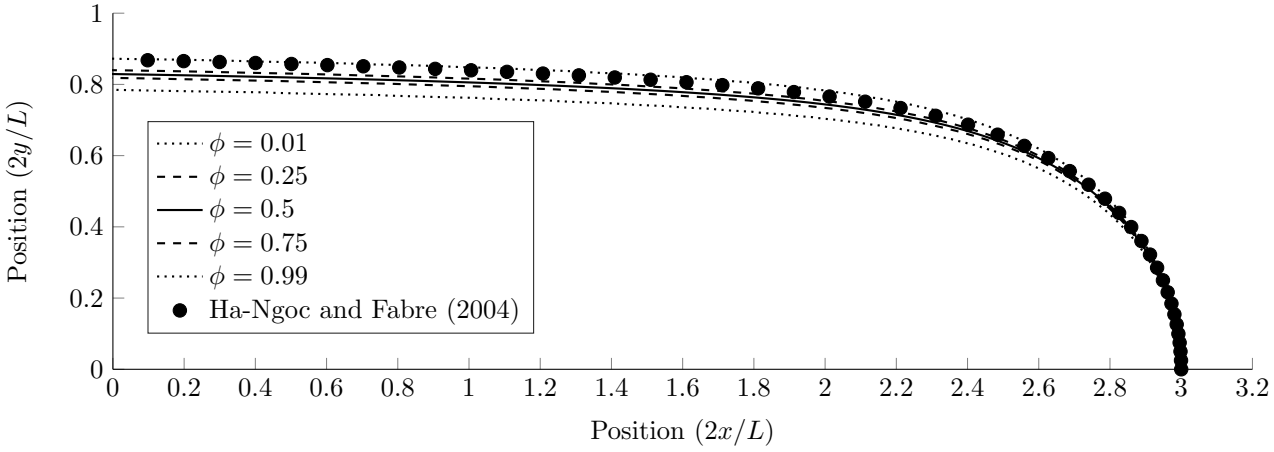

Figure 4.13: Contours of the phase-field for a Taylor bubble at $t^* = 20$ with $Eo = 100$ and $Re_r = 200$. The results from Ha-Ngoc and Fabre [165] were supplied by Dr. J. Fabre allowing for the current LBM outputs to be compared with the profile obtained using the boundary element method. The values x_i and y_i are used to define the interface location with respect to the bubble nose located at (3,0).

that simulations quickly progressed to instability when the diffuse interface was updated via the dynamic viscosity. Thus, there appears a trade off when looking at the methodology in choosing physically relevant parameters within the diffuse interface. Even so, with the model capturing the expected physical behaviour, this Chapter looks to assess the effect surface tension has on the Taylor

bubble rise and then introduce both co- and counter-current fluid flow into the domain.

4.4.2 Effect of Eötvös and Morton number

This section aims to validate the phase field LBM presented over a large parameter space and highlight its applicability to physically-relevant phenomena associated with the multiphase flow of fluids in a confined setting, e.g. the pipe configurations of a wellbore. In this chapter, the model is restricted to a 2D formulation which provides a proof of concept for extension into high resolution 3D simulations as well as a qualitative expectation on the dynamics of the slug flow regime.

The computational domain size length for this section was increased to, $20L \times L$, but the characteristic width was reduced to, $L = 128$ lattice units. Noting certain stability issues at higher Eötvös numbers, various reference times were tested, $t_0 = \{16000, 24000, 32000\}$, with a higher reference time being analogous to a more refined time-step. Similar to the detailed validation test conducted in the previous section, a density and viscosity ratio of 1000 and 100 were used, respectively. The work of Ha-Ngoc and Fabre [165] was used to predict a reference velocity, u_{ref}, so that the Reynolds number could be guaranteed to be in the inertial regime.

Figure 4.14 indicates the measured rise velocity of the planar Taylor bubbles for various Eötvös numbers and reference times. It is observed from this figure, that a reference time of $t_0 = 16000$ was insufficient to capture the expected behaviour of the bubble. However, increasing the temporal resolution to $t_0 = 24000$ and $t_0 = 32000$, it was evident that the results agreed well with the work of Ha-Ngoc and Fabre [165]. This is particularly clear for, $Eo < 100$, where the predicted rise velocity is a function of the surface tension, prior to plateauing at $Fr \approx 0.225$.

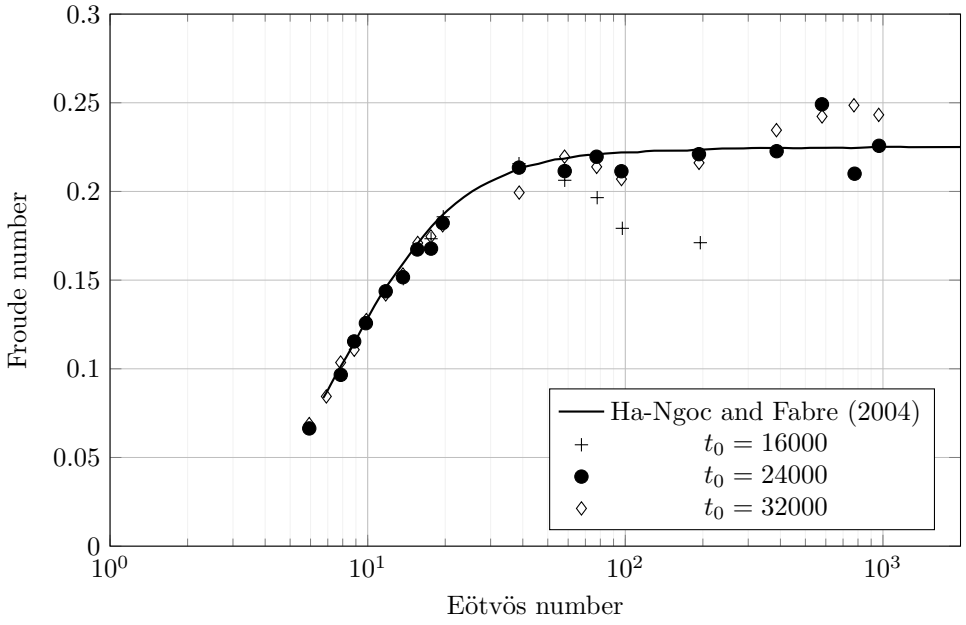

Figure 4.14: The bubble Froude number as a function of the Eötvös number for a planar Taylor bubble in an inertial regime.

The measured rise velocities at higher Eötvös numbers can be seen to deviate slightly from the results of Ha-Ngoc and Fabre [165]. The loss in accuracy for these cases is believed to be a result

of the wake behaviour of the Taylor bubble. Figure 4.15 shows the Taylor bubble and wake region for various Eötvös numbers. Here, as the value increases, namely as the gravitational forces start to dominate surface tension effects, a continuous system of bubble detachment, break-up, coalescence and reattachment in the wake region is formed. The unsteadiness of this behaviour may have contributed to the minor variation from the predicted macroscopic rise velocity in this range.

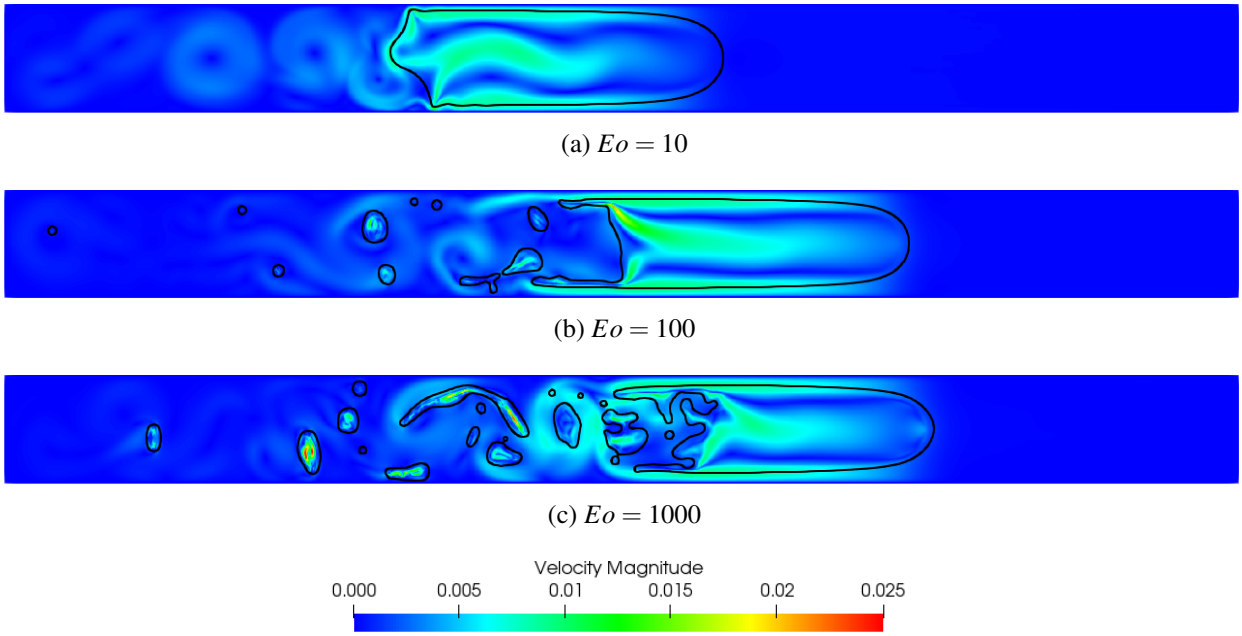

(a) $Eo = 10$

(b) $Eo = 100$

(c) $Eo = 1000$

Figure 4.15: The shape profile of the Taylor bubbles at $t^* = 20$ for (a) $Eo = 10$, (b) $Eo = 100$ and, (c) $Eo = 1000$, displayed on a heat map of the lattice total velocity.

In order to gain further insight into the behaviour of the Taylor bubble wake, simulations were conducted at various Morton numbers. Figure 4.16 indicates the shape profiles of the Taylor bubble, with an initial symmetry observed prior to the wake region progressing to a more chaotic structure. As the simulations approach the inertial regime (decreasing Morton number), it is evident that vortices in the continuous fluid shed from the tail of the Taylor bubble and strongly influence the behaviour of smaller bubbles that have detached into the wake. In Figure 4.16, it is clear that there is a variation in rise velocity for the different Morton numbers. This demonstrates that while not in an inertial regime, the rise velocity of a Taylor bubble with specified density and viscosity ratios, is at the least, a function of both the Eötvös and Morton number, $Fr = Fr(Eo, Mo)$.

The simulations conducted here were conducted with both the MRT formulation described in this dissertation as well as with a cascaded relaxation implemented into the developed TCLB code base for Gruszczyński *et al.*(*accepted*). The cascaded formulation does not fall under the scope of this thesis, as such the detail has been omitted and the simulations results included here were conducted with MRT relaxation. However, it is noted that there was negligible difference in the results of these particular simulations as the lattice velocities are relatively low. When this is the case, the *shift* matrix that transforms the distribution functions into central moment space for the cascaded relaxation tends towards the identity matrix and the scheme returns to an MRT relaxation.

This subsection has demonstrated that the developed phase field LBM is capable of capturing the

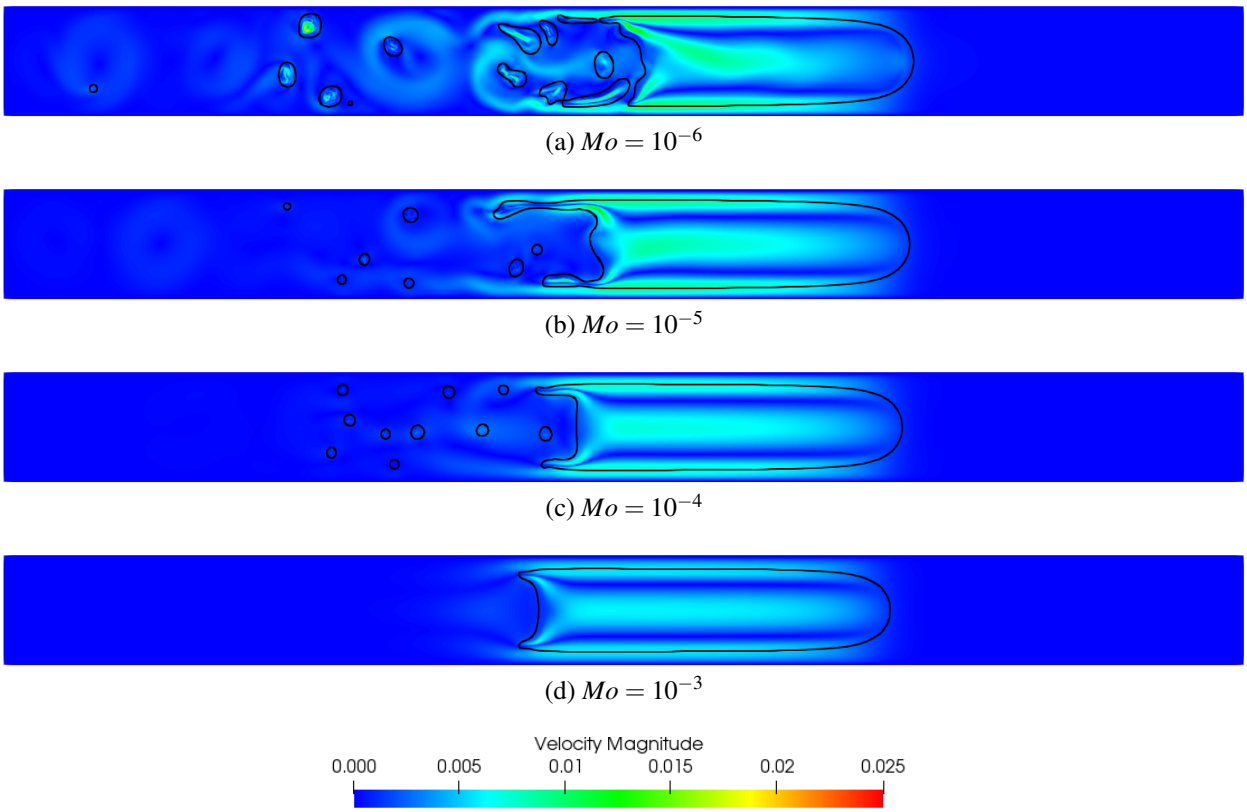

Figure 4.16: The shape profile of the Taylor bubbles at $t^* = 20$ for $Eo = 100$ and (a) $Mo = 10^{-6}$, (b) $Mo = 10^{-5}$, (c) $Mo = 10^{-4}$ and, (d) $Mo = 10^{-3}$, displayed on a heat map of the lattice total velocity.

key dynamics of a Taylor bubble, rising through a stagnant fluid in a scenario with fluid properties similar to a liquid-air system. Furthermore, the highly resolved detail of the simulations allowed the wake behaviour to be qualitatively inspected. It was observed to progress from a symmetric flow field for high Morton numbers ($O(10^{-3})$) to a scenario of vortex shedding prior to the detachment, and in some cases coalescence and re-attachment, of smaller bubbles from the Taylor bubble itself. In addition to this, the model showed accuracy and stability over a wide range of dimensionless parameters, a key feature when considering the range of fluid types that are applicable in coal seam gas extraction, let alone the broader oil and gas industry.

4.4.3 Effect of flowing fluid

To assess the behaviour of a Taylor bubble in flowing fluid, as could be expected in natural gas extraction, a moving reference frame is used. To transform into this frame of reference, velocity boundaries need to be implemented for the incoming and outgoing fluid as well as the channel walls. The formulation for these boundaries is given in the work of Zu and He [145] as well as in Appendix A.1.1, allowing for both co- and counter-current flow conditions to be created. When the continuous phase is flowing, a complex interaction occurs between the liquid force on the bubble and the buoyancy forces present. In order to describe this, the average liquid velocity, u_∞, measured in the far field is weighted by an empirical scaling factor, C_0, and superimposed onto the expected bubble rise velocity

in a stagnant channel, $u_{stagnant}$,

$$u_r = C_0 u_\infty + u_{stagnant}. \tag{4.55}$$

In order to determine $u_{stagnant}$, simulations were run with zero velocity in the channel walls using the Zu and He conditions. These were found to align with the previous simulations that utilised the full-bounce-back boundary condition. This can also be non-dimensionalised in the form of Froude numbers by dividing through by a reference velocity scale similar to that of the Rayleigh-Taylor instability, $U_0 = \sqrt{g_x L}$,

$$Fr_r = C_0 Fr_\infty + Fr_{stagnant}. \tag{4.56}$$

The size of the domain is held constant to the previous section at, $20L \times L$, with $L = 128$ lattice units. However, the bubble is now initialised in the centre of the domain with the front situated at, $x_0 = 10L$. The density and viscosity ratios are again kept at 1000 and 100, respectively while the flow configuration is defined through $t^* = 24000$, $Eo = 100$ and $Mo = 10^{-3}$. These parameters were chosen such that the wake region would have a low-level of bubble detachment, reducing the need for a multiphase outlet in this 2D, proof of concept test.

To simulate the incoming fluid flow, a Poiseuille flow profile (fully developed channel flow) is assumed for the inlet and outlet of the domain. In the moving reference frame, this is given by

$$U_{in/out}(y) = U_{TB} + 6U_\infty \frac{(yD - y^2)}{D^2}. \tag{4.57}$$

With this definition, a negative value of liquid velocity corresponds to counter-current flow while a positive value indicates a co-current configuration. The velocity of the top and bottom walls is prescribed based on the expected rise velocity of the Taylor bubble through the flowing fluid.

Table 4.3 shows the results obtained for the rise velocity of the Taylor bubble in both co- and counter-current flow configurations. Here, one observes a relatively constant value for the empirical coefficient, C_0, which agrees with common assumptions typically taken in the literature. To further validate the co-current dynamics determined in the moving reference frame, the values of C_0 were compared with the previous work of Ha-Ngoc and Fabre [167]. Interestingly, the value obtained for this parameter was found to be approximately constant for both liquid flow configurations.

Figure 4.17 presents the results obtained in comparison to Ha-Ngoc and Fabre [167] as well as the independence of C_0 with respect to the liquid Froude number, Fr_∞, and flow direction. It is highlighted here, that future work will look to incorporate a larger range of pipe configurations (inclination angle, internal obstructions, etc.) to address global correlations of rise velocity to dimensionless flow parameters. This will enable otherwise difficult experiments to be conducted numerically to determine suitable models describing the rise velocity of Taylor bubbles. This is useful, for example, in predicting pressure drops through piping systems, including wellbores, where simplified models are required to describe phase interactions due to the system scales.

This subsection has demonstrated that the phase field LBM can be solved within a moving reference frame allowing the realisation of flowing fluids and Taylor bubble development without the need for

Table 4.3: Resultant Taylor bubble rise velocity and empirical coefficient value in both co- and counter-current flowing configurations where $Fr_\infty = 0$ corresponds to a rise velocity of $Fr_{stagnant} = 0.2085$.

Counter-current					
Fr_∞	-0.25	-0.20	-0.15	-0.10	-0.05
Fr_r	-0.1022	-0.0386	0.0233	0.0856	0.1470
C_0	1.2429	1.2355	1.2350	1.2297	1.2298
Co-current					
Fr_∞	0.05	0.10	0.15	0.20	0.25
Fr_r	0.2714	0.3338	0.3984	0.4656	0.5294
C_0	1.2574	1.2526	1.2656	1.2855	1.2836

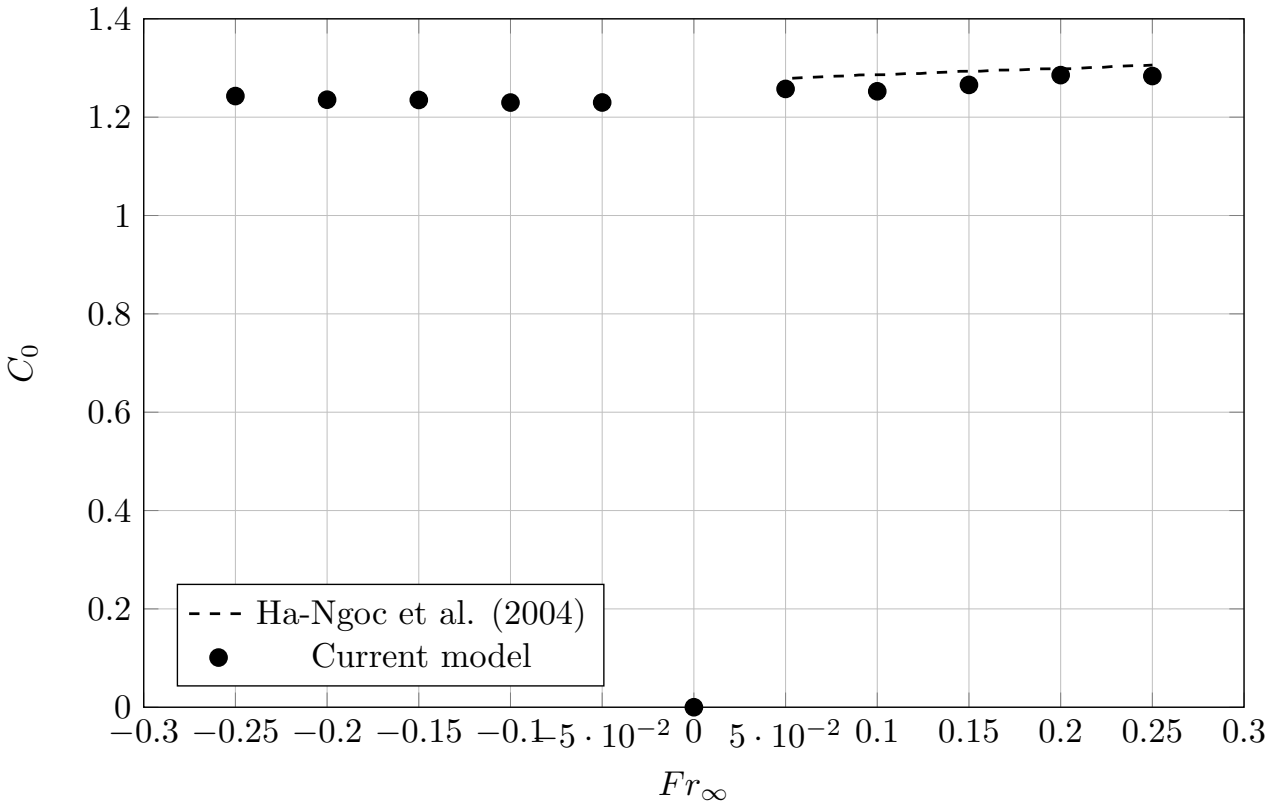

Figure 4.17: Comparison of the value of C_0 for various liquid Froude numbers, F_∞, and the work of Ha-Ngoc and Fabre [167].

excessive domain sizes. When looking to conduct resolved 3D simulations, this is particularly important as domains can quickly exceed computational limits when searching for steady-state behaviours using an explicit numerical scheme. In addition to this, the velocity boundary conditions from Zu and He [145] were validated for the presented, velocity-based LBM.

4.5 Chapter summary

The ability to simulate high density ratio flows over a large range flow conditions defined through dimensionless parameters such as the Eötvös and Morton numbers is essential when looking to produce reduced-order models that are useful in industrial applications. This chapter extended, verified

and validated an improved multiphase lattice Boltzmann model based on phase field theory. The formulation was first presented before benchmark cases including the layered Poiseuille flow and Rayleigh-Taylor instability were investigated. These indicated that the model was able to out-perform the previous state-of-the-art phase field models published in the literature in terms of stability at high density ratios and Reynolds number. Additionally, the computational locality of the model was improved whilst being shown to consistently recover the Navier-Stokes Equation across the interface with only a single layer of neighbouring nodes. This is in comparison to models that use mixed derivatives and require two layers of neighbouring nodes, and those that use isotropic differences, but fail to capture the velocity profile when a density or viscosity contrast exists. A balance was also found with the techniques used to determine the relaxation parameter over the diffuse interface. In this, three methods were tested including a harmonic and linear interpolation of the relaxation parameter as well as an update via a linear interpolation of the dynamic viscosity. It was found that the dynamic viscosity update provided the most accurate result, however, suffered stability issues in complex flows. As such, the linear interpolation was primarily used, managing to outperform the harmonic interpolation scheme.

Following the benchmark cases, the dynamics of a Taylor bubble was investigated due to its importance in modelling the slug flow regime. Initially, a detailed validation case was constructed looking at the elongated bubble propagation through a stagnant fluid in an inertial regime, a scenario previously analysed by numerous authors with the main comparison made with the work of Ha-Ngoc and Fabre [165]. The model was found to perform well, accurately predicting the correct macroscopic rise velocity of the bubble as well as its shape profile. This was done with fluid properties exhibiting density and viscosity contrasts beyond that of water-gas to test the robustness of the model and ensure its applicability to a range of possible scenarios.

With the planar model validated, the effect of surface tension on the rise velocity was investigated. Here, the phase field LBM indicated that the bubble propagation was a function of the surface tension. When non-dimensionalised, it was able to show that the Froude number was a function of the Eötvös number only, when in an inertial flow regime. However, when not in this regime ($Re \lesssim 100$) it was observed that the Morton number was also important. This was a promising result, however, in the transport of hydrocarbons, where both the liquid and gaseous phase are expected to be in motion. As such, the simulation was transformed into a reference frame moving with the bubble and velocity boundaries were implemented to allow for both co- and counter-current flows to be generated. An empirical relation to predict the effect of flowing fluid on the Taylor bubble is tested for co-current flow, aligning closely with the LBM results. The flow configuration was then reversed to explore the dynamics in a counter-current regime. Interestingly, the empirical factor used in the correlation holds relatively constant for both flow directions ranging from 1.2298 to 1.2855 for the Froude numbers tested.

This chapter has provided a detailed description of the developed phase field LBM as well as its verification, validation and application to planar Taylor bubble dynamics. The subsequent chapter extends this work to 3D and discusses the modifications required to retain the robustness displayed in

2D. Following this, it verifies and validates the 3D implementation in flow scenarios applicable to the slug flow regime.

Part of the following publication has been incorporated in Chapter 5.

1. [3] **T. Mitchell**, C. Leonardi, and A. Fakhari, Development of a three-dimensional phase-field lattice Boltzmann method for the study of immiscible fluids at high density ratios, *International Journal of Multiphase Flow* 107, 1–15, 2018.

Contributor	Statement of contribution	%
Travis Mitchell	writing of text	85
	proof-reading	70
	theoretical derivations	75
	numerical calculations	100
	preparation of figures	100
	initial concept	80

Chapter 5

Extension of the Phase-Field Lattice Boltzmann Model

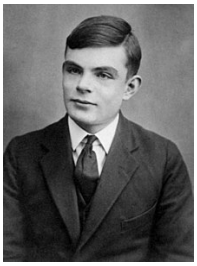

"We can only see a short distance ahead,
but we can see plenty there that needs to be done."
Alan Turing

The work conducted in Chapter 4 was restricted to two-dimensions (2D). This allowed for the formulation to be rigorously tested without the additional computational overhead that is entailed in resolving a three-dimensional (3D) domain. The findings indicated that the proposed LBM improved the computational efficiency on parallel architectures as well as the stability at high density ratios and moderate Reynolds numbers when compared to certain state-of-the-art, phase-field models. Furthermore, an investigation into the rise behaviour of planar Taylor bubbles carried out over a range of flow configurations proved that the governing equations could accurately mimic physically relevant, multiphase systems. However, the 3D nature of multiphase flows in the oil and gas industry limits the applicability of 2D, planar simulations, particularly from a quantitative point of view. At moderate Reynolds numbers it is expected that the symmetry of a confined, multiphase flow will break down reducing the applicability of axisymmetric formulations. As such, this chapter extends the planar implementation described in the previous chapter to handle 3D domains.

Building on Chapter 4, the Navier-Stokes (NSE) and Allen-Cahn (ACE) equations that govern the system dynamics are not repeated here. However, to retain the stability improvements observed in 2D, a weighted-multiple-relaxation-time (WMRT) scheme had to be implemented. The details of this collision operator and how it is included in the model framework provides the starting point for this chapter. Following on from this, the implementation is verified by analysing the deformation of a droplet in a density-matched binary fluid. The results obtained are compared with the work of Leclaire *et al.* [168] to ensure consistency of the model. The 3D Rayleigh-Taylor instability is the second test case investigated, in which the current results are compared with the work of Zu and He [145] and He *et al.* [103] at a low Reynolds number and a small density contrast. The capability of the model is then

shown by simulating the Rayleigh-Taylor instability at a relatively high Reynolds number with fluid properties similar to that of an air-water system. This particular case extends beyond previous literature, indicating the capability of the model as well as supplying data for the testing of new formulations. The model is validated via comparison with the experimental work of Bugg and Saad [169], analysing the rise of a Taylor bubble in a tube filled with olive oil. This experimental case has previously been used to validate finite-volume methods in commercial codes such as ANSYS CFX 5.6 by Ndinisa *et al.* [170] and ASCOMP's TransAT by Lizarraga-Garcia *et al.* [18]. The model is observed to accurately capture the experimental findings, proving its potential applicability to modelling multiphase transport through tubular geometries, e.g. piping networks.

5.1 Improved collision operator

Traditional techniques for computational fluid dynamics were based on the discretisation of the NSE, whereas the LBM finds its roots in kinetic theory [171, 172]. Here, the conservation laws are solved based on linearised kinetic models within which a collision, or relaxation, model is required to close the system. A number of collision kernels have been proposed as part of the LBM framework and they can have significant impact on the model's stability and accuracy. As per the previous chapter, the multiple relaxation time (MRT) methodology is applied here. This consists of performing the advection (or streaming) component of the LBM algorithm in particle velocity space, however, projecting the distribution functions to their velocity moments for collision. The benefit here comes from the fact that a number of these moments are related to macroscopic parameters and as such can be relaxed in a physically meaningful process.

The first description of the MRT consisted of taking moments of the particle velocity which are mutually orthogonal for the specified discrete set, $\{\boldsymbol{c}_i\}$. The issue here arises from an undesirable coupling of conserved hydrodynamic modes and higher-order, non-hydrodynamic modes that is not consistent with the continuous velocity space. In particular, the coupling of the density with the fourth-order moment has been reported to generate numerical instabilities for certain multiphase systems [173]. To mitigate this, it has been proposed by Fakhari *et al.* [173] that a weighted orthogonalisation should be used, for which the inner product for the D3Q27 lattice is defined as,

$$\left\langle \mathbf{m}_i, \mathbf{m}_j \right\rangle = \sum_{k=0}^{26} w_k m_{ik} m_{jk} \delta_{ij}, \tag{5.1}$$

where $\mathbf{m}_i$ is the ith row vector of the collision matrix, M.

The weighted orthogonality stated above is summated based on the use of 27 discrete velocities. This follows from the D3Q27 lattice that is used to recover the NSE in this work. It is noted here that a D3Q15 lattice along with a single-relaxation-time scheme is sufficient for the ACE [174], and the use of the reduced stencil supports the computational efficiency of the algorithm. The discrete velocity set

for the ACE population is given by,

$$\boldsymbol{c}_{15} = \begin{pmatrix} c_x \\ c_y \\ c_z \end{pmatrix} = \begin{pmatrix} 0 & 1 & -1 & 0 & 0 & 0 & 0 & 1 & -1 & 1 & -1 & 1 & -1 & 1 & -1 \\ 0 & 0 & 0 & 1 & -1 & 0 & 0 & 1 & 1 & -1 & -1 & 1 & 1 & -1 & -1 \\ 0 & 0 & 0 & 0 & 0 & 1 & -1 & 1 & 1 & 1 & 1 & -1 & -1 & -1 & -1 \end{pmatrix}. \tag{5.2}$$

and the corresponding lattice weights are,

$$w_i = \frac{1}{72} \begin{cases} 16, & i = 0, \\ 8, & i = 1-6, \\ 1, & i = 7-14. \end{cases} \tag{5.3}$$

As for the discrete velocity set for the D3Q27 lattice used for the hydrodynamics, a slightly unconventional ordering was used to align the first 15 velocity directions with the D3Q15 model,

$$\boldsymbol{c}_{27} = \begin{pmatrix} c_x \\ c_y \\ c_z \end{pmatrix}, \tag{5.4}$$

$$= \begin{pmatrix} c_{0-14,x} & 1 & -1 & 1 & -1 & 1 & -1 & 1 & -1 & 0 & 0 & 0 & 0 \\ c_{0-14,y} & 1 & 1 & -1 & -1 & 0 & 0 & 0 & 0 & 1 & -1 & 1 & -1 \\ c_{0-14,z} & 0 & 0 & 0 & 0 & 1 & 1 & -1 & -1 & 1 & 1 & -1 & -1 \end{pmatrix}. \tag{5.5}$$

The corresponding lattice weights are then given by,

$$w_i = \frac{1}{216} \begin{cases} 64, & i = 0, \\ 16, & i = 1-6, \\ 1, & i = 7-14, \\ 4, & i = 15-26. \end{cases} \tag{5.6}$$

With the lattice velocity and weights defined, the details of the WMRT implemented on the D3Q27 can be formulated. The collision operator can be defined as,

$$\Omega_i^{WMRT} = -(M^{-1}SM)(g_i - \bar{g}_i^{eq}). \tag{5.7}$$

Here, M^{-1} is the inverse of the transformation matrix and S is a diagonal matrix of relaxation rates. Optimisation of these was not necessary or attempted in the simulations presented in this chapter, but this could present an avenue for future studies. Here, the relaxation of the second-order moments, which are related to shear stress, are varied according to the kinematic viscosity of the fluid, while all other modes are relaxed directly to their equilibrium values. It is noted here that one may be able to improve the stability of the collision scheme through optimising the relaxation of higher-order moments through either mapping that stability parameter space [175] or analysing the modes of the linearised lattice Boltzmann equation [176–178]. The matrix used in this works follows from the studies of Fakhari et al. [173], which can be written as,

$$S = \mathrm{diag}(1,1,1,1,s_\nu,s_\nu,s_\nu,s_\nu,s_\nu,1,1,\ldots,1), \tag{5.8}$$

where,

$$s_\nu = \frac{1}{\tau + 1/2}, \tag{5.9}$$

and τ is the relaxation time related to the kinematic viscosity by, $\nu = \tau c_s^2 \delta t$.

The transformation matrix is presented as row vectors up to the sixth-order for a D3Q27 lattice:
Zeroth-order:

$$\mathbf{m}_0 = 1$$

First-order:

$$\mathbf{m}_1 = c_{i,x}$$
$$\mathbf{m}_2 = c_{i,y}$$
$$\mathbf{m}_3 = c_{i,z}$$

Second-order:

$$\mathbf{m}_4 = c_{i,x}c_{i,y}$$
$$\mathbf{m}_5 = c_{i,y}c_{i,z}$$
$$\mathbf{m}_6 = c_{i,z}c_{i,x}$$
$$\mathbf{m}_7 = 3c_{i,x}^2 - |\boldsymbol{c}_i|^2$$
$$\mathbf{m}_8 = c_{i,y}^2 - c_{i,z}^2$$
$$\mathbf{m}_9 = |\boldsymbol{c}_i|^2 - 1$$

Third-order:

$$\mathbf{m}_{10} = c_{i,x}(3|\boldsymbol{c}_i|^2 - 5)$$
$$\mathbf{m}_{11} = c_{i,y}(3|\boldsymbol{c}_i|^2 - 5)$$
$$\mathbf{m}_{12} = c_{i,z}(3|\boldsymbol{c}_i|^2 - 5)$$
$$\mathbf{m}_{13} = c_{i,x}(c_{i,y}^2 - c_{i,z}^2)$$
$$\mathbf{m}_{14} = c_{i,y}(c_{i,z}^2 - c_{i,x}^2)$$
$$\mathbf{m}_{15} = c_{i,z}(c_{i,x}^2 - c_{i,y}^2)$$
$$\mathbf{m}_{16} = c_{i,x}c_{i,y}c_{i,z}$$

Fourth-order:

$$\mathbf{m}_{17} = 0.5(3|\boldsymbol{c}_i|^4 - 7|\boldsymbol{c}_i|^2 + 2)$$
$$\mathbf{m}_{18} = (3|\boldsymbol{c}_i|^2 - 4)(3c_{i,x}^2 - |\boldsymbol{c}_i|^2)$$
$$\mathbf{m}_{19} = (3|\boldsymbol{c}_i|^2 - 4)(c_{i,y}^2 - c_{i,z}^2)$$
$$\mathbf{m}_{20} = c_{i,x}c_{i,y}(3|\boldsymbol{c}_i|^2 - 7)$$

$$\mathbf{m}_{21} = c_{i,y}c_{i,z}(3|\boldsymbol{c}_i|^2 - 7)$$
$$\mathbf{m}_{22} = c_{i,z}c_{i,x}(3|\boldsymbol{c}_i|^2 - 7)$$

Fifth-order:

$$\mathbf{m}_{23} = 0.5c_{i,x}(9|\boldsymbol{c}_i|^4 - 33|\boldsymbol{c}_i|^2 + 26)$$
$$\mathbf{m}_{24} = 0.5c_{i,y}(9|\boldsymbol{c}_i|^4 - 33|\boldsymbol{c}_i|^2 + 26)$$
$$\mathbf{m}_{25} = 0.5c_{i,z}(9|\boldsymbol{c}_i|^4 - 33|\boldsymbol{c}_i|^2 + 26)$$

Sixth-order:

$$\mathbf{m}_{26} = 0.5(9|\boldsymbol{c}_i|^6 - 36|\boldsymbol{c}_i|^4 + 33|\boldsymbol{c}_i|^2 - 2)$$

Using these definitions, the transformation matrix can be created and the phase-field LBM presented in the previous chapter can be extended into 3D while maintaining numerical robustness,

$$\mathbf{M} = \left(\begin{array}{ccccccccccccccccccccccccccc}
1 & 1 & 1 & 1 & 1 & 1 & 1 & 1 & 1 & 1 & 1 & 1 & 1 & 1 & 1 & 1 & 1 & 1 & 1 & 1 & 1 & 1 & 1 & 1 & 1 & 1 & 1 \\
0 & 1 & -1 & 0 & 0 & 0 & 0 & 1 & -1 & 1 & -1 & 1 & -1 & 1 & -1 & 1 & -1 & 1 & -1 & 1 & -1 & 1 & -1 & 0 & 0 & 0 & 0 \\
0 & 0 & 0 & 1 & -1 & 0 & 0 & 1 & 1 & -1 & -1 & 1 & 1 & -1 & -1 & 1 & 1 & -1 & -1 & 0 & 0 & 0 & 0 & 1 & -1 & 1 & -1 \\
0 & 0 & 0 & 0 & 0 & 1 & -1 & 1 & 1 & 1 & 1 & -1 & -1 & -1 & -1 & 0 & 0 & 0 & 0 & 1 & 1 & -1 & -1 & 1 & 1 & -1 & -1 \\
0 & 0 & 0 & 0 & 0 & 0 & 0 & 1 & -1 & -1 & 1 & 1 & -1 & -1 & 1 & 1 & -1 & -1 & 1 & 0 & 0 & 0 & 0 & 0 & 0 & 0 & 0 \\
0 & 0 & 0 & 0 & 0 & 0 & 0 & 1 & 1 & -1 & -1 & -1 & -1 & 1 & 1 & 0 & 0 & 0 & 0 & 0 & 0 & 0 & 0 & 1 & -1 & -1 & 1 \\
0 & 0 & 0 & 0 & 0 & 0 & 0 & 1 & -1 & 1 & -1 & -1 & 1 & -1 & 1 & 0 & 0 & 0 & 0 & 1 & -1 & -1 & 1 & 0 & 0 & 0 & 0 \\
0 & 2 & 2 & -1 & -1 & -1 & -1 & 0 & 0 & 0 & 0 & 0 & 0 & 0 & 0 & 1 & 1 & 1 & 1 & 1 & 1 & 1 & 1 & -2 & -2 & -2 & -2 \\
0 & 0 & 0 & 1 & 1 & -1 & -1 & 0 & 0 & 0 & 0 & 0 & 0 & 0 & 0 & 1 & 1 & 1 & 1 & -1 & -1 & -1 & -1 & 0 & 0 & 0 & 0 \\
-1 & 0 & 0 & 0 & 0 & 0 & 0 & 2 & 2 & 2 & 2 & 2 & 2 & 2 & 2 & 1 & 1 & 1 & 1 & 1 & 1 & 1 & 1 & 1 & 1 & 1 & 1 \\
0 & -2 & 2 & 0 & 0 & 0 & 0 & 4 & -4 & 4 & -4 & 4 & -4 & 4 & -4 & 1 & -1 & 1 & -1 & 1 & -1 & 1 & -1 & 0 & 0 & 0 & 0 \\
0 & 0 & 0 & -2 & 2 & 0 & 0 & 4 & 4 & -4 & -4 & 4 & 4 & -4 & -4 & 1 & 1 & -1 & -1 & 0 & 0 & 0 & 0 & 1 & -1 & 1 & -1 \\
0 & 0 & 0 & 0 & 0 & -2 & 2 & 4 & 4 & 4 & 4 & -4 & -4 & -4 & -4 & 0 & 0 & 0 & 0 & 1 & 1 & -1 & -1 & 1 & 1 & -1 & -1 \\
0 & 0 & 0 & 0 & 0 & 0 & 0 & 0 & 0 & 0 & 0 & 0 & 0 & 0 & 0 & 1 & -1 & 1 & -1 & -1 & 1 & -1 & 1 & 0 & 0 & 0 & 0 \\
0 & 0 & 0 & 0 & 0 & 0 & 0 & 0 & 0 & 0 & 0 & 0 & 0 & 0 & 0 & -1 & -1 & 1 & 1 & 0 & 0 & 0 & 0 & 1 & -1 & 1 & -1 \\
0 & 0 & 0 & 0 & 0 & 0 & 0 & 0 & 0 & 0 & 0 & 0 & 0 & 0 & 0 & 0 & 0 & 0 & 0 & 1 & 1 & -1 & -1 & -1 & -1 & 1 & 1 \\
0 & 0 & 0 & 0 & 0 & 0 & 0 & 1 & -1 & -1 & 1 & -1 & 1 & 1 & -1 & 0 & 0 & 0 & 0 & 0 & 0 & 0 & 0 & 0 & 0 & 0 & 0 \\
1 & -1 & -1 & -1 & -1 & -1 & -1 & 4 & 4 & 4 & 4 & 4 & 4 & 4 & 4 & 0 & 0 & 0 & 0 & 0 & 0 & 0 & 0 & 0 & 0 & 0 & 0 \\
0 & -2 & -2 & 1 & 1 & 1 & 1 & 0 & 0 & 0 & 0 & 0 & 0 & 0 & 0 & 2 & 2 & 2 & 2 & 2 & 2 & 2 & 2 & -4 & -4 & -4 & -4 \\
0 & 0 & 0 & -1 & -1 & 1 & 1 & 0 & 0 & 0 & 0 & 0 & 0 & 0 & 0 & 2 & 2 & 2 & 2 & -2 & -2 & -2 & -2 & 0 & 0 & 0 & 0 \\
0 & 0 & 0 & 0 & 0 & 0 & 0 & 2 & -2 & -2 & 2 & 2 & -2 & -2 & 2 & -1 & 1 & 1 & -1 & 0 & 0 & 0 & 0 & 0 & 0 & 0 & 0 \\
0 & 0 & 0 & 0 & 0 & 0 & 0 & 2 & 2 & -2 & -2 & -2 & -2 & 2 & 2 & 0 & 0 & 0 & 0 & 0 & 0 & 0 & 0 & -1 & 1 & 1 & -1 \\
0 & 0 & 0 & 0 & 0 & 0 & 0 & 2 & -2 & 2 & -2 & -2 & 2 & -2 & 2 & 0 & 0 & 0 & 0 & -1 & 1 & 1 & -1 & 0 & 0 & 0 & 0 \\
0 & 1 & -1 & 0 & 0 & 0 & 0 & 4 & -4 & 4 & -4 & 4 & -4 & 4 & -4 & -2 & 2 & -2 & 2 & -2 & 2 & -2 & 2 & 0 & 0 & 0 & 0 \\
0 & 0 & 0 & 1 & -1 & 0 & 0 & 4 & 4 & -4 & -4 & 4 & 4 & -4 & -4 & -2 & -2 & 2 & 2 & 0 & 0 & 0 & 0 & -2 & 2 & -2 & 2 \\
0 & 0 & 0 & 0 & 0 & 1 & -1 & 4 & 4 & 4 & 4 & -4 & -4 & -4 & -4 & 0 & 0 & 0 & 0 & -2 & -2 & 2 & 2 & -2 & -2 & 2 & 2 \\
-1 & 2 & 2 & 2 & 2 & 2 & 2 & -8 & 8 & 8 & 8 & 8 & 8 & 8 & 8 & -4 & -4 & -4 & -4 & -4 & -4 & -4 & -4 & -4 & -4 & -4 & -4
\end{array}\right).$$

5.2 Verification of the three dimensional implementation

5.2.1 Deformation of a droplet in shear

To start benchmarking the 3D phase-field LBM, the deformation of a droplet placed in a shear flow is first analysed. This test case can be found in numerous works in the literature [179–182], but here particular note is taken of the work by Leclaire *et al.* [168]. The authors sought to compare the colour-gradient and pseudopotential lattice Boltzmann models across numerous test cases. Using a droplet in shear flow they were able to show that both models were capable of reproducing analytical relations in the small Capillary number limit. They noted that the colour-gradient model showed good stability and accuracy for a larger range of parameters than those obtained with the chosen pseudopotential model. The aim of this section is to include a phase-field model into this benchmark case through applying a similar test methodology. As such, a domain, $\mathscr{D}$, is defined consistently with the work of Leclaire *et al.* [168] such that,

$$\mathscr{D} = (x,y,z) \in [0,X] \times [0,Y] \times [0,Z]. \tag{5.10}$$

A spherical droplet with radius, R, is initialised with centroid, $(X/2,Y/2,Z/2)$. To do this, the phase-field is specified by,

$$\phi_{x,y,z} = \frac{1}{2}\left[1 - \tanh\left(\frac{|\mathbf{x}-\mathbf{x_0}|-R}{W/2}\right)\right], \tag{5.11}$$

where $\mathbf{x}$ is the spatial location and $\mathbf{x_0}$ is the centroid of the spherical droplet. For simplicity, the number of dimensionless parameters associated with this problem is reduced by defining the following geometric ratios: $X/Z = 2$, $Y/Z = 1$ and $R/Z = 0.2$ [168]. Additionally, the density and viscosity ratios are both set to unity while the interface width, W, is specified to be three lattice units. With these values, the bubble deformation, D, becomes a function of the Capillary and Reynolds numbers only, defined respectively as

$$\mathrm{Ca} = \frac{\dot{\gamma} R \mu_l}{\sigma}, \tag{5.12}$$

$$\mathrm{Re} = \frac{\dot{\gamma} R^2 \rho_l}{\mu_l}, \tag{5.13}$$

where $\dot{\gamma} = 2U/Z$ is the shear rate due to an imposed velocity, U and $-U$, at the top and bottom of the domain, respectively. To provide results over a range of Ca, the same approach used by Leclaire *et al.* [168] is taken, in which μ_l is held constant and the surface tension, σ, is varied. To characterise the final degree of freedom associated with the diffuse interface model, an interface Péclet number is defined as [183],

$$\mathrm{Pe}_{int} = \frac{\dot{\gamma} R W}{M}. \tag{5.14}$$

This is used to relate the convective and diffusive time scales of the interface. For this study of droplet deformation, the mobility is specified as $M = 0.2$ for all Re and Ca tested. For a detailed analysis

on the effect of Pe_{int}, the interested reader is pointed towards the work of van der Sman and van der Graaf [184] as well as the more recent study by Komrakova *et al.* [183].

With the geometric constraints stated, the original analysis describing the bubble deformation conducted by Taylor [179] breaks down with violation of the assumption that, $R/Z \ll 1$. Since this seminal study, numerous authors have utilised techniques such as perturbation theory to gain further understanding of the system. The work of Shapira and Haber [180], for example, incorporated a corrective term in Taylor's formulation to account for wall effects. The expression for bubble deformation from their analysis was expressed for Stokesian flows ($\mathrm{Re} \ll 1$) and was found to be

$$D = \frac{19\kappa+16}{16\kappa+16}\mathrm{Ca}\left[1+C_{sh}\frac{2.5\kappa+1}{\kappa+1}\left(\frac{R}{Z}\right)^3\right], \tag{5.15}$$

where $\kappa = \mu_l/\mu_g$ and $C_{sh} = 5.6996$ is the corrective wall term for a droplet centred in the domain. It is highlighted that the wall effects incorporated in the analytical works of Shapira and Haber [180] are derived to $O(\mathrm{Ca})$. As such, it is expected that the results will deteriorate progressively with increasing capillary number. In this work, results are reported for Reynolds numbers between 0.05 and 0.2 for capillary numbers ranging between 0.02 and 0.3. If one takes $C_{sh} = 0$, the original form proposed by Taylor [179] is recovered,

$$D = \mathrm{Ca}\frac{19\kappa+16}{16\kappa+16}. \tag{5.16}$$

Taking note from Leclaire *et al.* [168], the grid resolution is specified based on an input parameter, r, and a constant, $N_0 = 50$, such that,

$$N_x = 2rN_0 - 2, \tag{5.17}$$

$$N_y = rN_0, \tag{5.18}$$

$$N_z = rN_0 - 1. \tag{5.19}$$

Here, $N_{x,y,z}$ are the number of nodes in the X, Y, and Z directions, respectively. A node is subtracted from the periodic axis to enforce the geometric requirements of X/Z and Y/Z for the domain extents. For simplicity, velocity boundary conditions on the top and bottom of the domain are implemented by assuming bounce-back of the non-equilibrium parts of the hydrodynamic population, g_i [185].

An alternative approach was taken to analyse the deformation results in comparison with the work of Leclaire *et al.* [168], who formulated the analysis as an optimisation problem. To do this, a contour indicating the centre of the interface was found and an optimisation problem was solved for the shortest and longest distances to the centre of the ellipse (i.e. major and minor axes). The authors then used two additional contours in the interface and performed a similar analysis to determine the angle of rotation. In this work, an ellipsoidal shape is fit to the contour given at $\phi = 0.5$ and then the parameters of the function are utilised to determine the major and minor axes.

Figure 5.1a compares the results of the present phase-field LBM using $r = 1$ with the analytical results of Shapira and Haber [180] and the numerical results of Leclaire *et al.* [168]. It is clear that the phase-field model is in agreement with the results obtained using the colour gradient model. The results

also reinforce the findings of the previous work, where agreement with analytical predictions is seen in the limit of small Ca number. However, at higher Ca, it is evident that the predicted deformation departs significantly from the analytical solution for small Re. This appears contradictory to the formulated correction of Shapira and Haber [180] that is specifically valid for $\mathrm{Re} \ll 1$. In this case, it appears evident that the resolution $r = 1$ is insufficient to capture the flow characteristics for Ca greater than approximately 0.075. This is clear from the increased resolution results in Figure 5.1b, in which results progressively improve for decreasing Re for all Ca tested.

A particular point highlighted by Leclaire *et al.* [168] was the fact that, in contrast to the pseudo-potential LBM, the colour-gradient model was able to achieve a constant interface width across the range of Ca and Re numbers. This is also achieved using the phase-field LBM with direct control given by the interface width parameter, W. What was not investigated however, was the effect of the interface width on the deformation of the droplet. To study this relation, a series of tests were conducted at $\mathrm{Ca} = 0.02$. The interface width was varied from three to nine and Re between 0.05 and 0.20, while the remaining parameters were kept consistent with the previous test. Figure 5.2 displays the deterioration of results with increasing interface thickness, particularly for the resolution of $r = 1$. This behaviour is expected as the simulations tend away from the sharp interface limit. For the results at resolution $r = 2$ a similar, but much less pronounced trend is observed with only a minor deterioration of accuracy observed.

5.2.2 Three dimensional Rayleigh-Taylor instability

To demonstrate the accuracy and stability of the model in 3D, the Rayleigh-Taylor instability represents a common benchmark. This phenomenon occurs when a heavy fluid is situated above a lighter fluid within a gravitational field, and the interface between the two is subject to a perturbation. In this configuration, the heavy fluid is observed to penetrate into the lighter fluid, for which the characteristics of motion have been investigated by many authors [4, 103, 119, 144, 145, 159].

The previous work in Chapter 4 and published in Fakhari *et al.* [4] demonstrated that the proposed model could accurately simulate the Rayleigh-Taylor instability up to high density ratios ($\rho^* = 1000$) and relatively high Reynolds numbers ($\mathrm{Re} = 3000$) in two-dimensions. As such, the instability provides a reasonable test case for which to analyse the three-dimensional extension.

The construction of the flow domain for this case consists of a rectangular prism given by,

$$\mathscr{D} = (x, y, z) \in [-L/2, L/2] \times [-2L, 2L] \times [-L/2, L/2]. \tag{5.20}$$

For the base case, the model parameters were chosen according to the work of Zu and He [145], with $L = 128$ and dimensionless parameters including Atwood number, At, Reynolds number, Re, and Capillary number Ca defined as

$$\mathrm{At} = \frac{\rho_l - \rho_g}{\rho_l + \rho_g} = 0.5, \tag{5.21}$$

$$\mathrm{Re} = \frac{L\sqrt{gL}}{\nu} = 128, \tag{5.22}$$

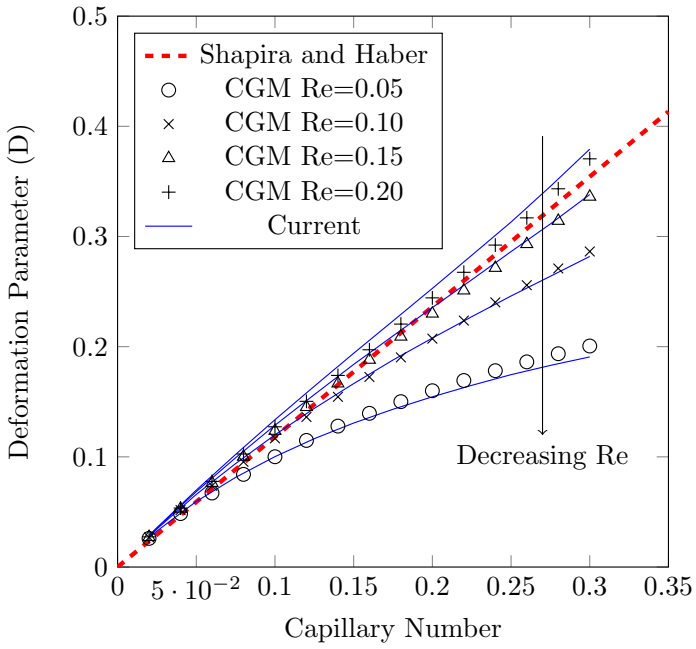

(a) Resolution, $r = 1$

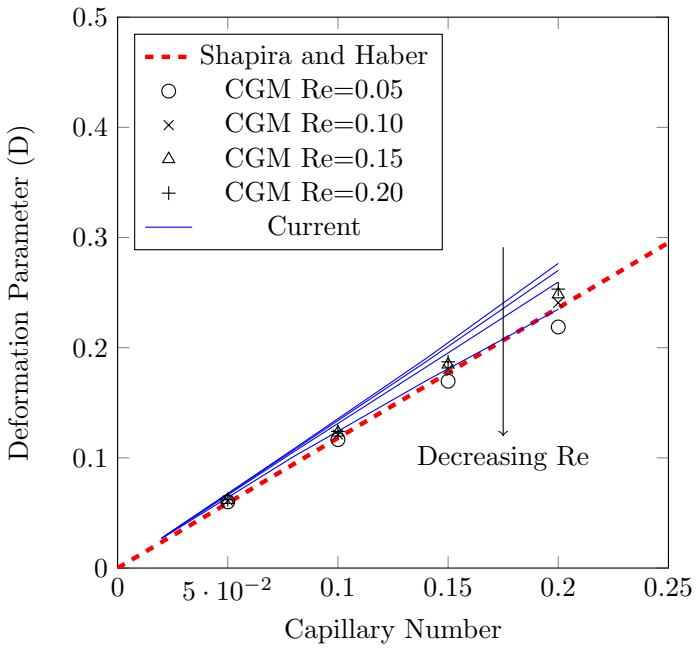

(b) Resolution, $r = 2$

Figure 5.1: Comparison of the colour-gradient model results presented in Leclaire *et al.* [168] (markers) with those from the 3D phase-field LBM proposed in this work (solid lines) with all simulations conducted at a resolution of (a) $r = 1$ and (b) $r = 2$. The arrows indicate the Re for the 'Current' solutions decreasing from 0.2 to 0.05 and the dotted red line is the analytical result of Shapira and Haber [180].

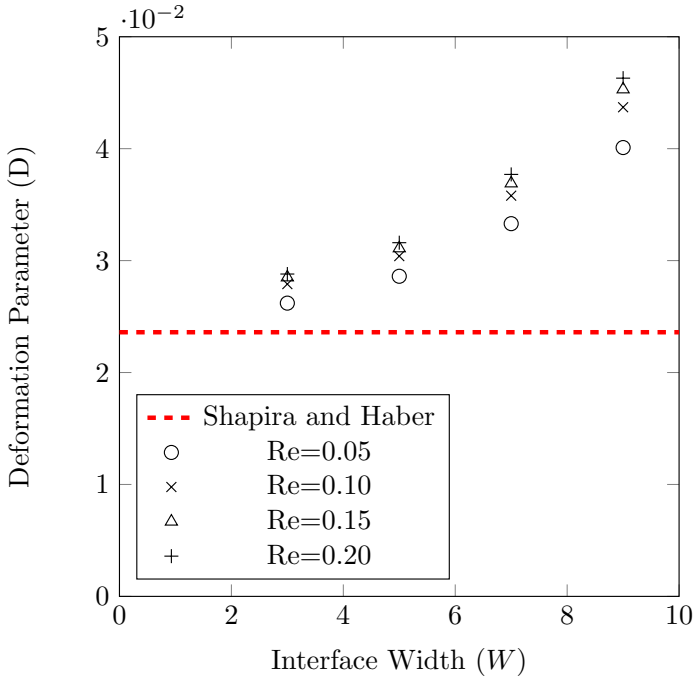

(a) Resolution, $r = 1$

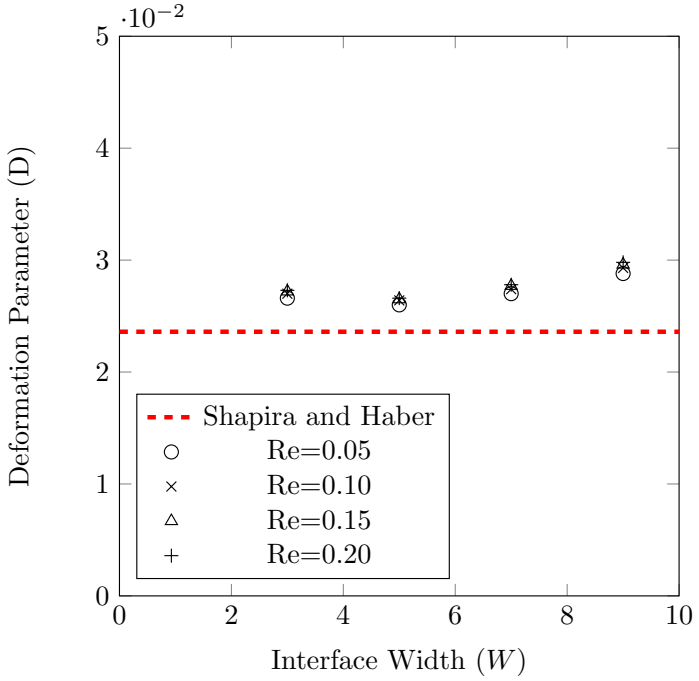

(b) Resolution, $r = 2$

Figure 5.2: Variation of the deformation parameter with interface width for Ca $= 0.02$ with a resolution of (a) $r = 1$ and (b) $r = 2$.

$$\mathrm{Ca} = \frac{\mu_l \sqrt{gL}}{\sigma} = 9.1. \tag{5.23}$$

From the definitions above, it is clear that At describes the density ratio, while the Re indicates the relative effect of gravitational to viscous forces, and the Ca provides the relative effect of viscous forces to surface tension. To close the dimensionless system, the kinematic viscosity of the two fluids is specified to be equal, $\nu^* = 1$, giving a dynamic viscosity ratio of three, $\mu^* = 3$. Additionally, the numerical Péclet number is,

$$\mathrm{Pe} = \frac{L\sqrt{gL}}{M} = 744, \tag{5.24}$$

and the reference time is defined as $t_0 = \sqrt{L/g} = 6000$, such that $t^* = t/t_0$ is the dimensionless time. In order to initiate the Rayleigh-Taylor instability, the interface between the two-fluids is initially perturbed by,

$$y(x,z) = 0.05L \times (\cos(2\pi x/L) + \cos(2\pi z/L)). \tag{5.25}$$

After initialisation, a constant gravitational acceleration applied to the system causes the heavy fluid to penetrate into the lighter fluid. Figure 5.3 shows the evolution of the interface at dimensionless times, $t^* = 1, 2, 3, 4$ and 4.5, with the colour contour based on the local velocity magnitude. The definitions of the points tracked in the simulation are also found on this figure, namely the bubble, spike, and saddle points of the initial perturbation. Qualitatively, similar results to those obtained by Zu and He [145] are observed. The saddle points are the first to display the roll-up like behaviour with the mushroom-like shape forming at the spike shortly after.

A quantitative comparison is performed by tracking the position of the bubble, spike, and saddle points through the simulation in order to compare with the works of Zu and He [145] and He *et al.* [103]. Figure 5.4a shows a close agreement with these studies, showing the accuracy of the 3D model. However, this flow scenario features both a low Reynolds number and low density ratio, with neither of the previous studies extending their analysis beyond this. Therefore, another case with the viscosity and density ratios similar to that found in an air-water system ($\rho^* = 1000$, $\mu^* = 100$) is considered with a Reynolds number of 3000. As per the previous case, the characteristic length scale is taken as $L = 128$. However, the reference time is reduced to $t_0 = 4000$ to maintain a similar capillary number at $\mathrm{Ca} = 8.7$. A density ratio of 1000 implies that the Atwood number for this case is 0.998. The evolution of the bubble, spike, and saddle points for this case are displayed in Fig. 5.4b.

Figure 5.5 shows the time evolution of the interface between the heavy and light fluids. Here the midplane view of the 3D results show qualitative agreement with available 2D data [4, 119, 144]. It is evident that the shear stress parallel to the interface is insufficient to cause the mushroom-like formation of the spike.

Currently, there exist few studies of the Rayleigh-Taylor instability of immiscible fluids with high-density ratios in 2D or 3D [4, 144]. The model presented in this work was not only able to achieve a stable simulation of a high-density ratio flow case, but one with a relatively high Reynolds number as well. This indicates that the solver is sufficiently robust to be applied to practical liquid-gas systems, which is further demonstrated in the following section.

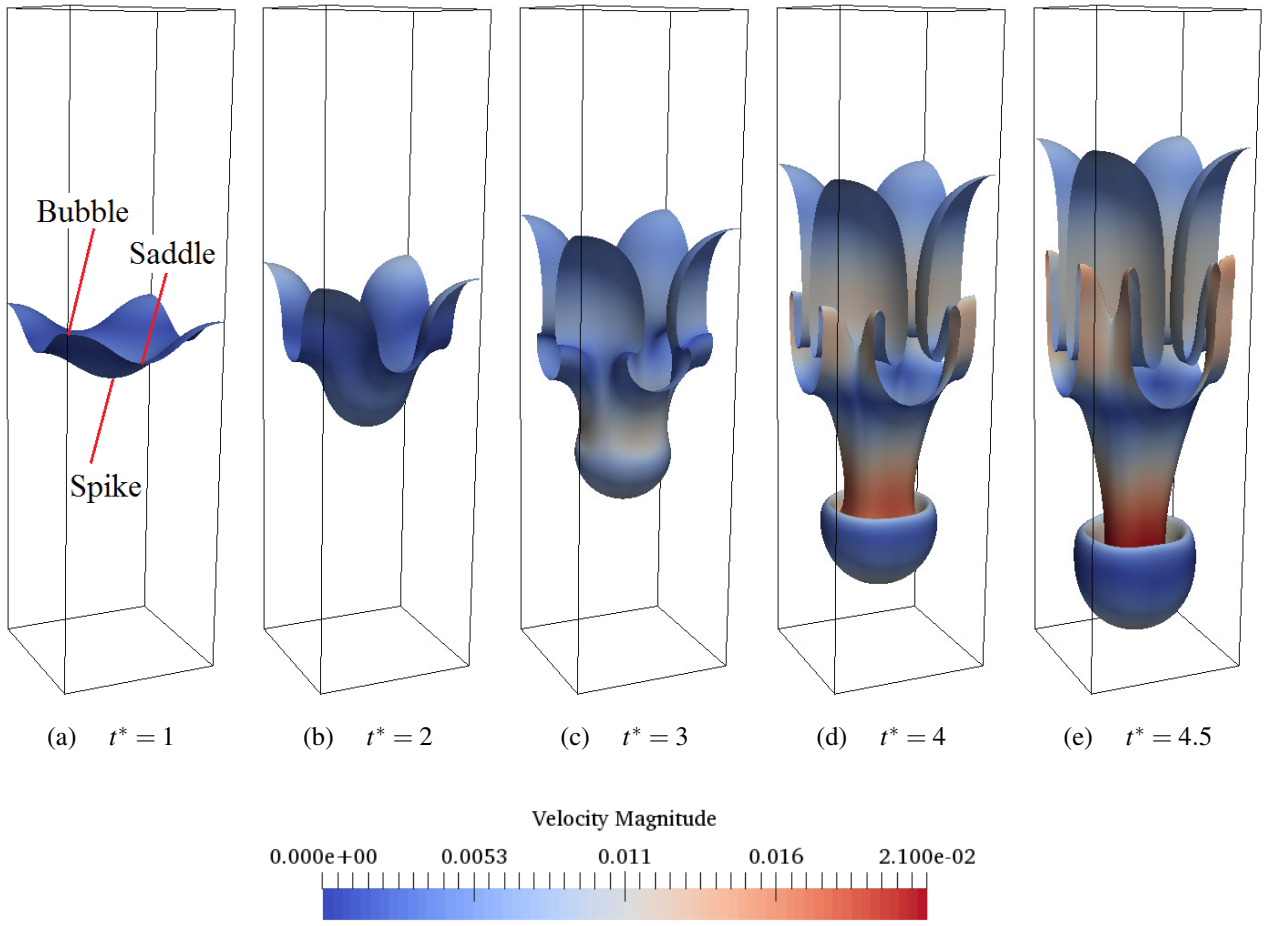

Figure 5.3: The evolution of the three-dimensional Rayleigh-Taylor instability with flow conditions defined by At $= 0.500$, Re $= 128$, $\mu^* = 3$, Ca $= 9.1$, and Pe $= 744$.

5.3 Experimental Taylor bubble validation

The evolution of Taylor bubbles is observed in a wide range of natural and industrial flows. Understanding the associated physics of these flows can provide critical insight into applications such as the concentration polarisation and fouling of membranes [170], and the transportation of hydrocarbons through pipeline systems [18, 169]. It has been reported in the literature that the rise velocity of a Taylor bubble is a key model parameter used in certain mechanistic modelling frameworks in order to predict liquid hold-up and pressure gradients through piping networks. A full review of the literature investigating the motion of rising Taylor bubbles in vertical pipes is not attempted here, and the interested reader is referred to Lizarraga-Garcia *et al.* [18] for an in-depth discussion of the extensive work in this area. The aim of this section is to study the flow features of a Taylor bubble using the three-dimensional phase-field LBM. As such, the macroscopic rise velocity, the local flow field and the interface profile of the bubble will be investigated and compared with experimental work available in the literature [169].

The experimental work of Bugg and Saad [169] has been used by numerous researchers to validate commercial multiphase codes. Lizarraga-Garcia *et al.* [18] recently used this data to validate a level-set

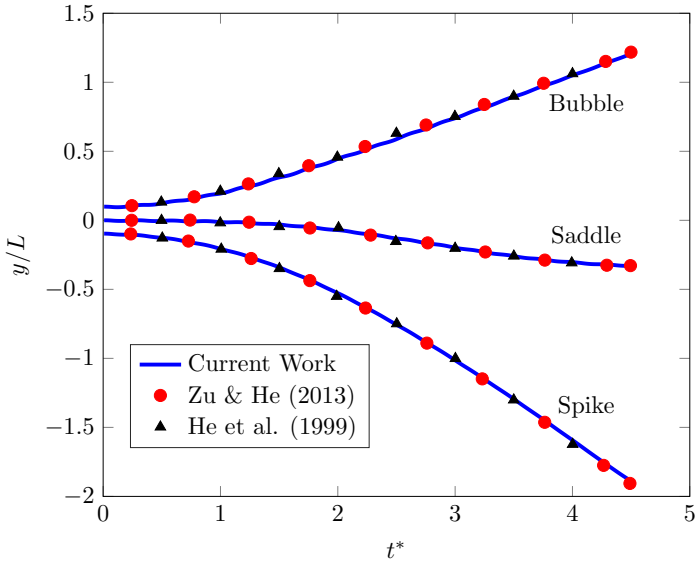

(a) Base Case

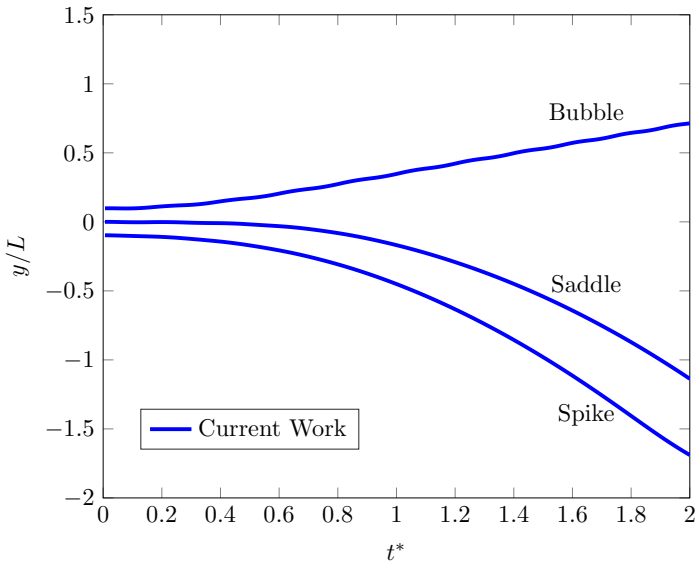

(b) Extension Case

Figure 5.4: Time evolution of the bubble front $(0, y, 0)$, the saddle point $(0, y, 64)$ and the spike $(64, y, 64)$ in the case of the 3D Rayleigh-Taylor instability. The base case (a) indicates the evolution with $\mathrm{At} = 0.500$ and $\mathrm{Re} = 128$ while the extension case (b) presents the results with $\mathrm{At} = 0.998$ and $\mathrm{Re} = 3000$.

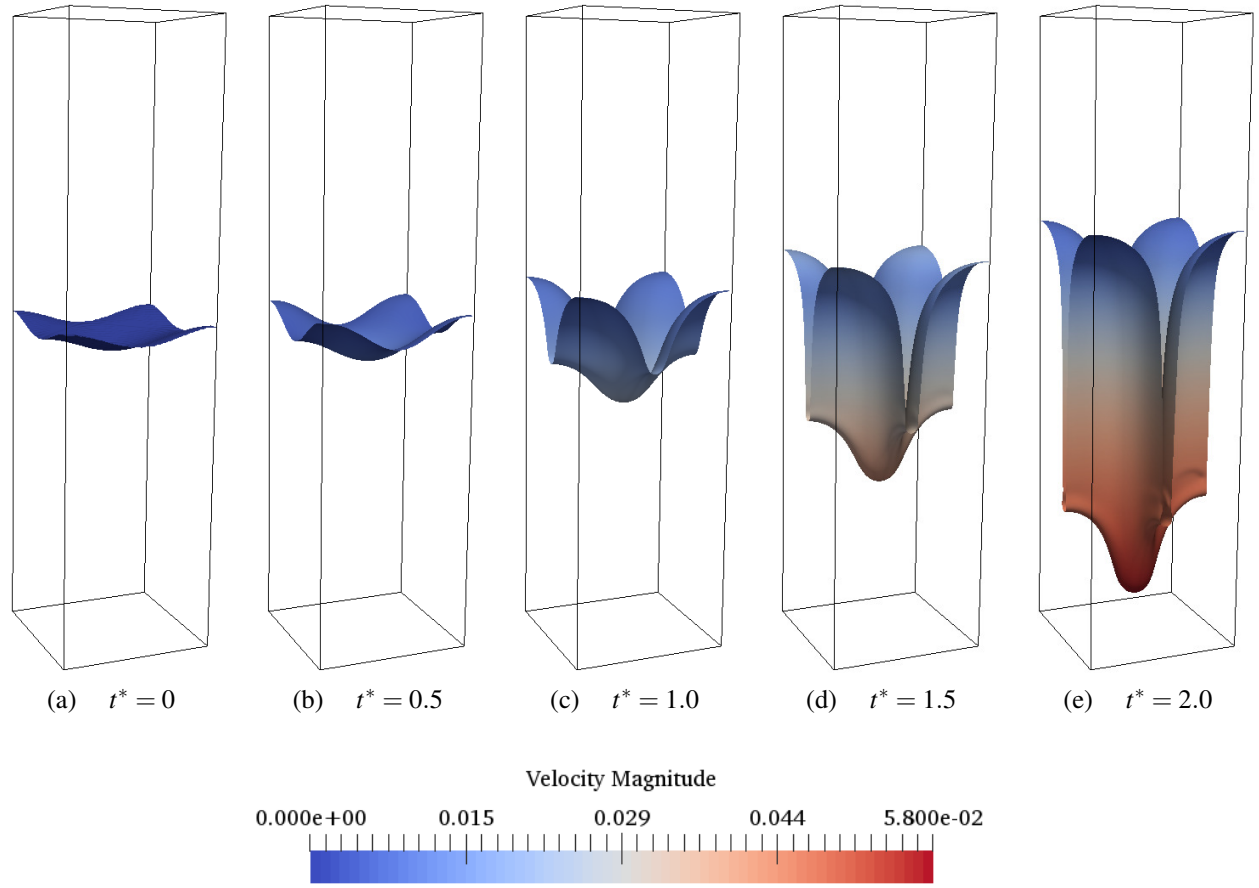

Figure 5.5: The evolution of the three-dimensional Rayleigh-Taylor instability with flow conditions defined by At $= 0.998$, Re $= 3000$, $\mu^* = 100$, and Ca $= 8.7$. The model parameters achieve density and viscosity ratios similar to that of an air-water mixture.

formulation in the TransAT software developed at ASCOMP. Additionally, the work of Ndinisa *et al.* [170] used these experimental results to assess the volume-of-fluid method, two-fluid method, and a combined model available in the CFX 5.6 code from ANSYS. The experimental work was conducted in a vertical tube with the diameter, $D_T = 19\ mm$, filled with olive oil as the working fluid. The relevant dimensionless numbers include the Eötvos number, Eo, which is the ratio of gravitational to interfacial forces, the Morton number, Mo, which assists in defining the expected shape of the bubble, and the Reynolds number, Re_r, based on the terminal rise velocity of the bubble, U_t. These are defined as

$$\mathrm{Eo} = \frac{(\rho_l - \rho_g) g D_T^2}{\sigma} = 100, \tag{5.26}$$

$$\mathrm{Mo} = \frac{g \mu_l^4}{(\rho_l - \rho_g)\sigma^3} = 0.015, \tag{5.27}$$

$$\mathrm{Re}_r = \frac{\rho_l U_t D_T}{\mu_l} = 27. \tag{5.28}$$

For this study, it is assumed that the density and viscosity of the air injected into the olive oil is 1.225 kg/m^3 and $1.983 \times 10^{-5}\ Pa.s$, respectively. This gives a density ratio of 744 and a viscosity ratio of 4236, which when combined with the reported olive oil properties [169], supplies the five π-groups required to define the bubble dynamics.

Particle image velocimetry (PIV) was used by Bugg and Saad [169] in order to obtain results for the liquid flow field surrounding the Taylor bubble. Macroscopically, the results of the experiment found a terminal rise velocity of $U_t = 0.131\ m/s$, which equates to a Froude number of 0.303 ($\mathrm{Fr} = U_t/\sqrt{gD_T}$) and the Reynolds number calculated in Eq. (5.28). The work done in CFX 5.6 by Ndinisa *et al.* [170] was able to provide comparable results to this with terminal velocities of $0.140\ m/s$, $0.119\ m/s$, and $0.110\ m/s$ obtained using the volume-of-fluid (VOF) technique, the two-fluid model (TFM), and a combined model, respectively. Here it can be seen that the order of error is within 8%. However, it was reported that the bubble shape was inadequately captured by the VOF technique and the interfacial transition region was excessive for the TFM. The combined model was thus suggested by Ndinisa *et al.* [170] to match the flow field measured by Bugg and Saad [169], in which large features are captured by the VOF and sub-grid bubbles modelled with the TFM.

In order to capture the system using the phase-field LBM described in this dissertation, one only needs to define a characteristic length (tube diameter) and a time scale in order to derive the remaining simulation parameters from the dimensionless variables stated. Three different resolutions were tested to demonstrate the results were independent of the grid, with similar findings obtained using 64, 128 and 256 cells across the tube diameter. The time scale for these simulations was defined according to the diffusive scaling such that, $t_0 = 2000$, 8000, and 32000, for the different grid resolutions, respectively. A total run time of, $10t_0$, was found to be sufficient for convergence of both shape and rise velocity for these cases. The results using $D_T = 128$ are presented here, with the length of the simulation domain specified as $10D_T$. As in the work of Ndinisa *et al.* [170], the low density region was initialised as a cylinder with a diameter of $0.75D_T$ and a height of $3D_T$. Figure 5.6 shows the time evolution of the bubble, with 3D images showing an iso-plane of $\phi = 0.5$ and a 2D-slice of the phase-field distribution across the pipe diameter. With this simulation the macroscopic bubble rise velocity, the local flow field dynamics about the bubble, and the interface profile in regions of interest can be compared.

5.3.1 Bubble rise velocity

During the simulation, the bubble interface location and interface velocity was recorded to check steady-state convergence. This was approximately achieved at $6-7t_0$ depending on the resolution. The rise velocity was then taken as the average of the local velocity between $9t_0$ and $10t_0$. Table 5.1 provides a comparison of the terminal velocity found in the current study with those from the literature. Here it is seen that the proposed LBM is able to provide a very close match to the experimental data [169] for all the resolutions tested, outperforming the previous numerical results [170].

5.3.2 Flow field analysis

The flow field is assessed in the same manner as in previous works by interrogating the velocity field along the tube centreline in front of the bubble nose as well as along four radial lines at various locations relative to the bubble. The locations for the radial lines of interest are given by $0.111D_T$

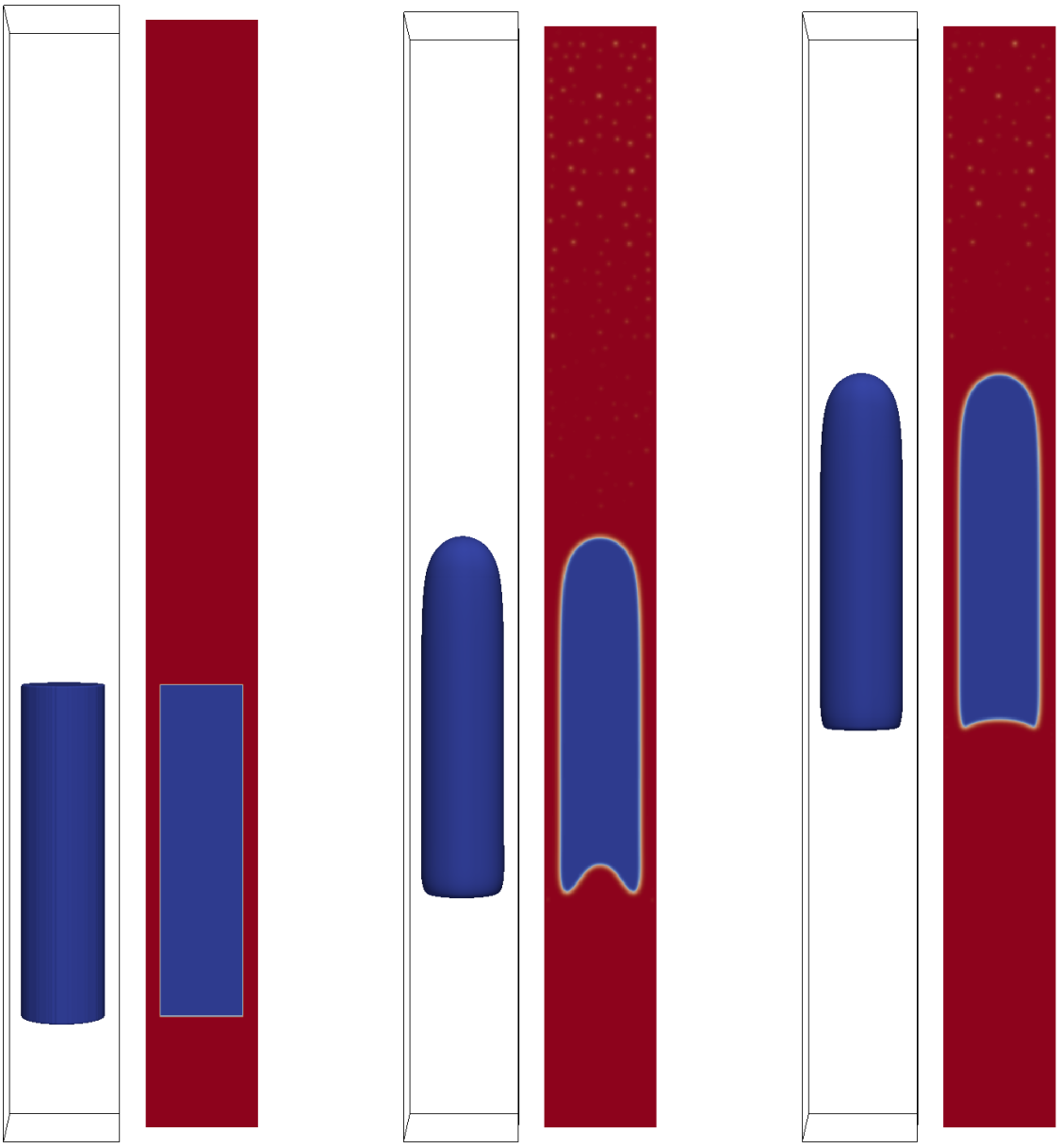

(a) $t^* = 0$ (b) $t^* = 5$ (c) $t^* = 10$

Figure 5.6: The evolution of a three-dimensional Taylor bubble inside of a cylindrical tube is shown at time increments of $5t_0$ from left to right. The flow conditions were specified according to the experimental work of Bugg and Saad [169] with $D_T = 128$, $\rho^* = 744$, $\mathrm{Re}_r \approx 27$, $\mu^* = 4236$, $\mathrm{Mo} = 0.015$, and $\mathrm{Eo} = 100$. In each figure, the right frame indicates the mid-plane view of the simulation domain.

Table 5.1: Reynolds numbers found with varying numerical techniques including VOF, TFM, and the combined TFM-VOF model from Ndinisa et al. [170], as well as the current LBM in comparison to the reference experimental (Exp) study [169].

Study	[170]			[169]	$D_T = 64$	$D_T = 128$	$D_T = 256$
Method	VOF	TFM	Combined	Exp	LBM	LBM	LBM
Re	28.9	24.5	22.7	27	27.98	26.99	26.77

ahead of the bubble nose as well as at $0.504D_T$ and $2D_T$ behind the bubble nose where the liquid film is developing and developed, respectively, and at, $D_T/5$, behind the bubble in the wake region. It is noted here that the flow behaviour in the wake region changes rapidly, thus with only an approximate location given in the experimental work [169], this study provides two additional measurements at $D_T/6$ and $D_T/7$ behind the bubble (measured from the centre-line) for comparison. For clarity, these lines have been superimposed onto the interface contour defined at $\phi = 0.5$ in Fig. 5.7.

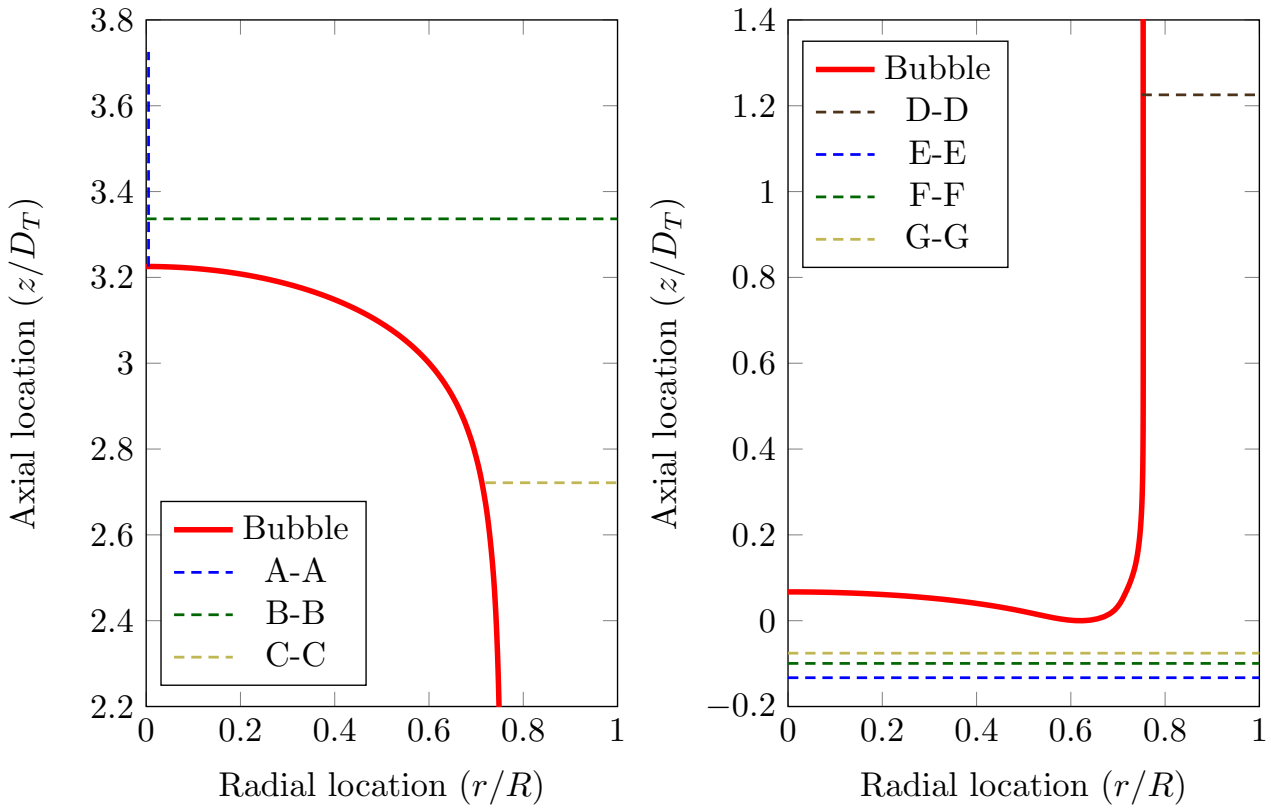

(a) Front of bubble (b) Back of bubble

Figure 5.7: Contour of $\phi = 0.5$ from simulation results with a resolution defined by $D_T = 128$, this is used to indicate the position of flow velocity profile lines in subsequent figures marked out by cut lines A-A through to G-G.

Figure 5.8 shows that the velocity along the tube axis in front of the bubble nose is captured accurately, with the LBM results matching well with both the experimental and numerical findings in the literature. The figure shows that the bubble has limited influence on the liquid ahead of it, with the velocity decaying to near zero at around, $0.3D_T$.

A characteristic of the Taylor bubbles modelled in this regime is the existence of a liquid film between the low density phase and the wall. The development of this film was well reported through the PIV experiments providing a further means of validation for the present 3D LBM. Figure 5.9 provides a comparison with the axial velocity along a radial line $0.111D_T$ in front of the bubble nose. In agreement with the conclusions of Ndinisa *et al.* [170], this figure indicates a transition from upwards to downwards flow of the high density fluid roughly halfway between the tube wall and the central axis. Additionally, the radial profile indicates a strong velocity component above the bubble

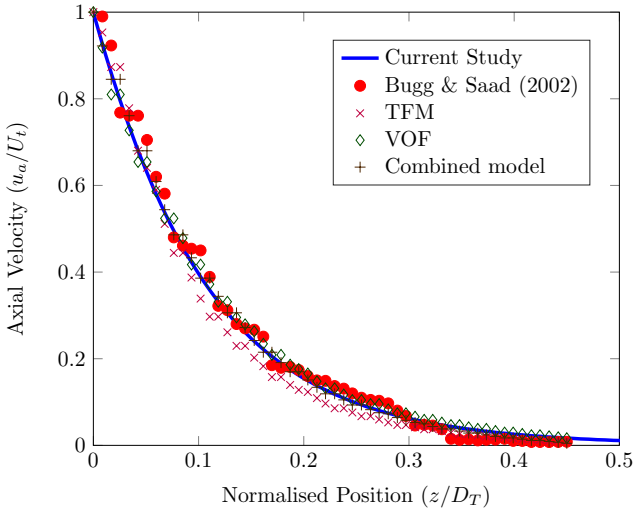

Figure 5.8: The profile of the axial velocity, u_a, directly in front of the Taylor bubble along slice A-A. The comparative numerical results including the TFM, VOF, and the combined TFM-VOF model were supplied by Ndinisa *et al.* [170].

where the fluid is accelerating into the liquid film region near the tube wall. The model presented in the current work performs in a similar fashion to the numerical methods from the literature, closely matching the axial velocity, but unable to capture the premature decay in the radial velocity observed at approximately $0.8D_T$ in the experimental results.

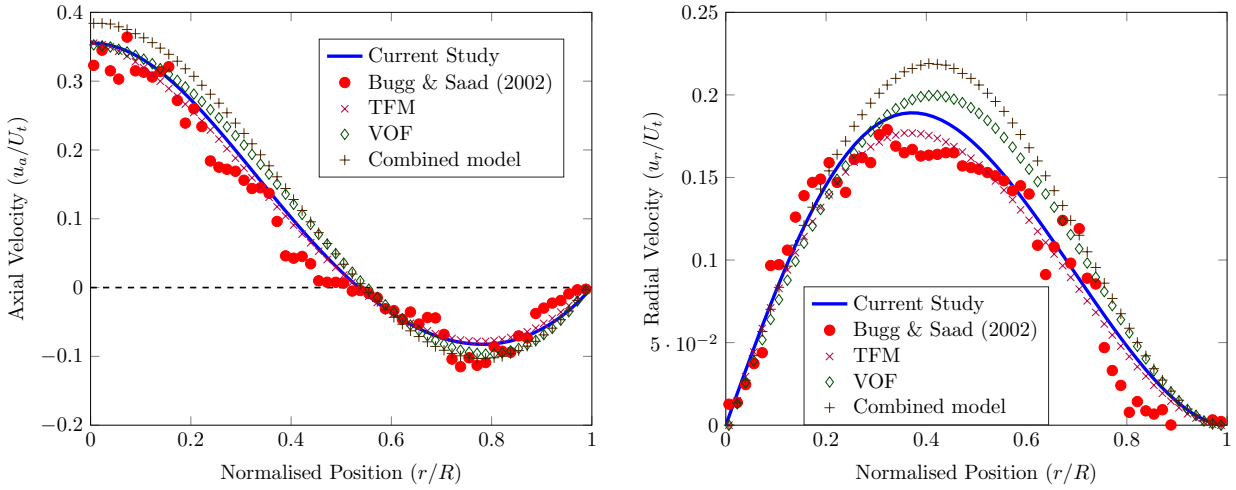

(a) Axial Velocity (b) Radial Velocity

Figure 5.9: The velocity profiles along a radial line positioned $0.111D_T$ above the bubble nose (B-B).

The heavy fluid that is forced towards the tube wall by the rising bubble develops into the liquid film. Figure 5.10 shows the high axial velocity of the heavy fluid as it propagates downwards surrounding the Taylor bubble. At this point, it is evident that there is still a large radial component of velocity, indicating that the film is still developing. The present model is again seen to perform on a similar level of accuracy as the reference numerical methods [170].

As the liquid film moves past the elongated bubble, it tends towards a fully-developed profile with negligible velocity in the radial direction and high velocities in the axial direction of the pipe. At this

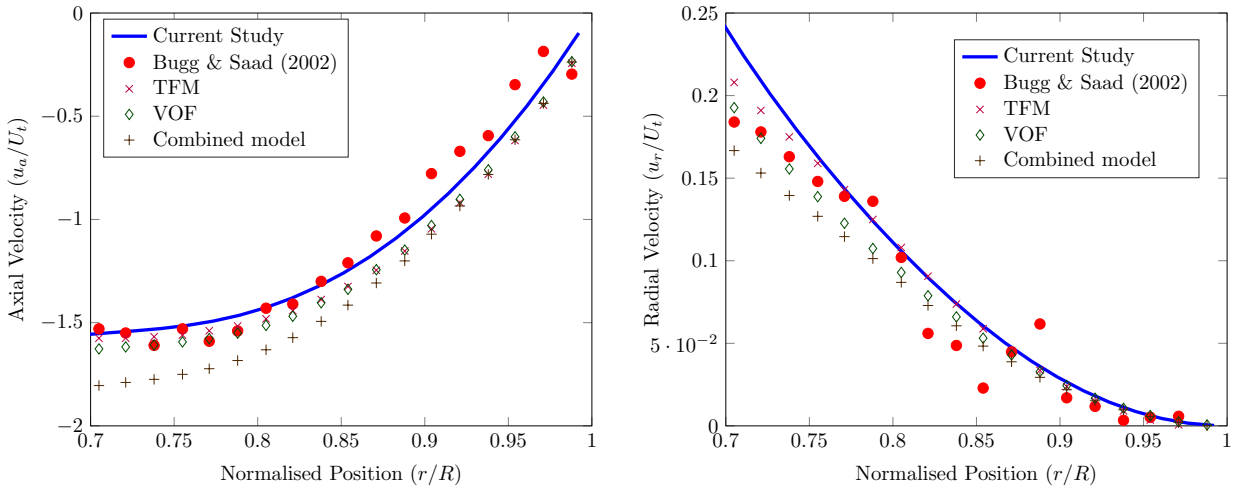

(a) Axial Velocity (b) Radial Velocity

Figure 5.10: The velocity profiles along a radial line positioned $0.504D_T$ behind the bubble nose (C-C).

stage, the shear stress at the wall is capable of supporting the weight of the film with zero velocity at the solid contact, but high velocity near the liquid-gas interface where the shear stress is negligible in comparison [170]. Figure 5.11 shows the axial velocity at this stage where it can be observed that the maximum velocity in the liquid film is over twice that of the bubble propagation speed. This result again shows a close agreement between the LBM simulations conducted in this study and the CFX 5.6 results [170] as well as the experimental findings [169].

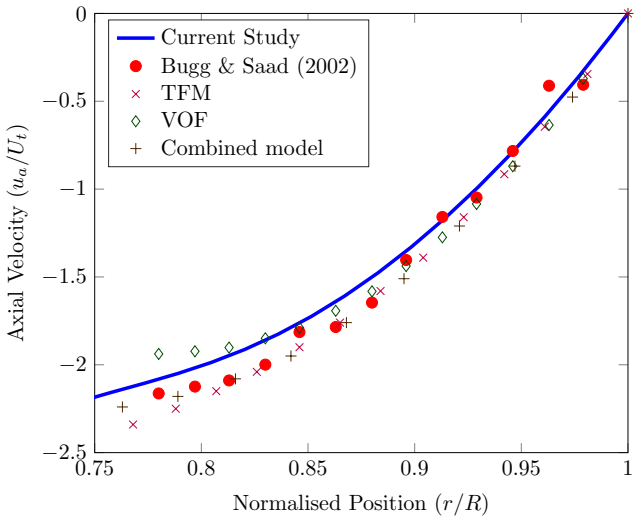

Figure 5.11: The axial velocity profile along a radial line positioned $2D_T$ behind the bubble nose (D-D).

When the liquid film moves past the end of the bubble a significant deceleration is observed as flow expands and recirculates in the wake region. Figure. 5.12 highlights this fact with the axial flow component still downwards in the near wall region, but upwards near the axis of the tube. Additionally, this figure shows that the wake has the region of maximum radial flow as the energy from the liquid film dissipates into the bulk. It is observed that the results measured at $D_T/5$ slightly under predict

the magnitude of axial velocity, but at $D_T/6$ (which is only four computational cells above the $D_T/5$ location) a significantly better match is obtained. This could be a result of either the diffuse-interface modelling approach adopted in the LBM algorithm or an uncertainty in the experimental location measurement. Nonetheless, this deviation seems to denote only a minor error in comparison to experimental results. To identify possible causes of this discrepancy, an analysis of the bubble shape is undertaken.

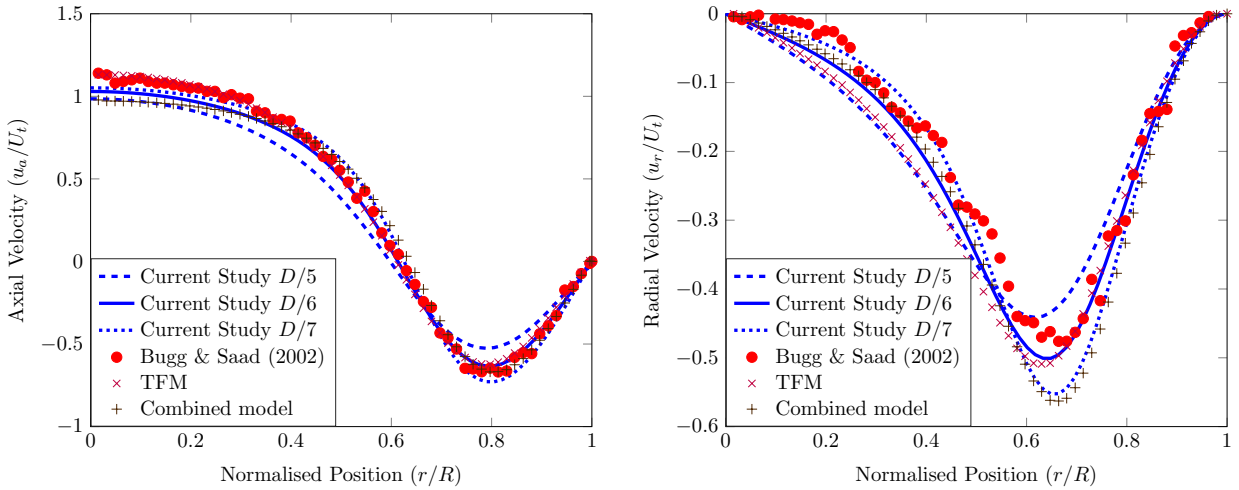

(a) Axial Velocity (b) Radial Velocity

Figure 5.12: The velocity profiles along radial lines positioned behind the bubble (in the wake region) at distances of $D_T/5$ (E-E), $D_T/6$ (F-F), and $D_T/7$ (G-G).

5.3.3 Bubble shape analysis

So far, a detailed comparison of the flow field surrounding the Taylor bubble in relation to experimental [169] and numerical [170] works available in the literature has been shown. In this section, the key features of the bubble profile in the nose and tail regions are analysed. Furthermore, the profile for various simulation resolutions is presented to demonstrate the grid dependency of the results. The purpose of this is to provide a complete validation and analysis of the macroscopic propagation of Taylor bubbles, the local flow field, and the interface topology.

Figure 5.13a gives a comparison of the Taylor bubble nose profile using the current LBM and the reference experimental work [169]. It is noted here that the phase-field model for capturing the interface dynamics is a diffuse interface model, and as such the interface is distributed over a finite distance rather than being a sharp discontinuity. The contour shown represents the iso-line for which $\phi = 0.5$. A good fit can be seen between the works, however a discrepancy is evident about the radial location of $r/R = 0.5$. The grid dependency of the nose profile is evident in the case where the resolution is defined by $D_T = 64$, but is clearly negligible with only minor variation from $D_T = 128$ to $D_T = 256$.

Figure 5.13b provides the profile about the tail of the Taylor bubble for various resolutions. Here the discrepancy between experiment and numerics is more pronounced. Additionally, the grid resolution

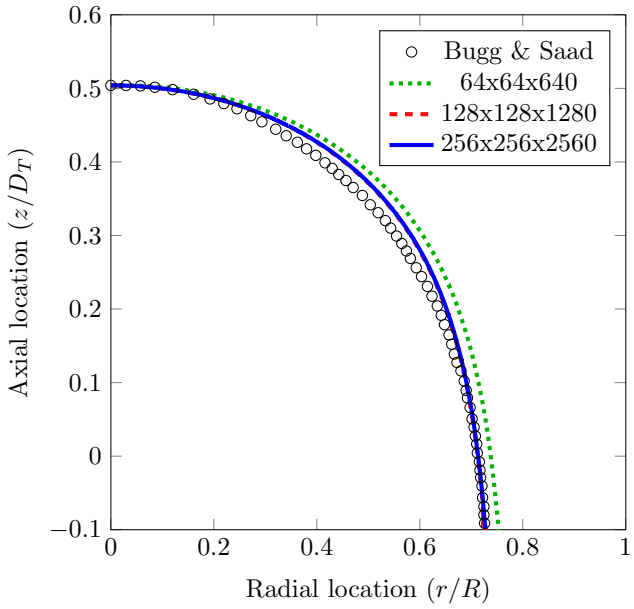

(a) Bubble front profile

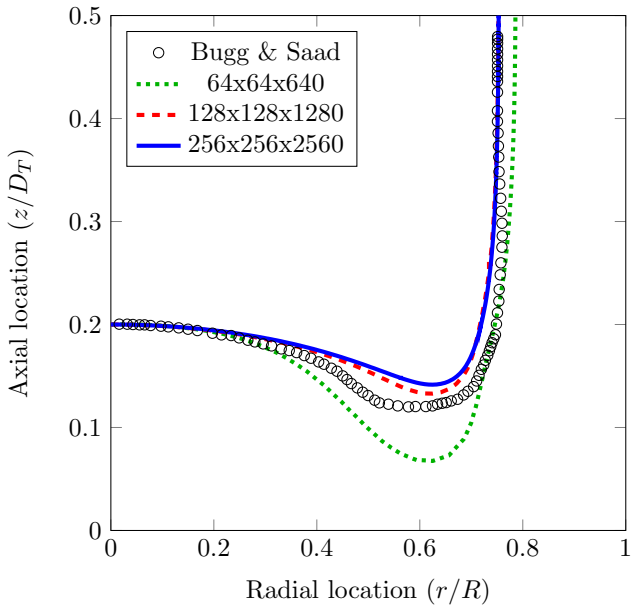

(b) Bubble tail profile

Figure 5.13: The profiles of the Taylor bubble interface are indicated by the contour of $\phi = 0.5$ in the LBM results. Here the vertical location is given with reference to an arbitrary location: (a) the front of the bubble is defined at a dimensionless height of 0.5; (b) the centre line of the interface tail is defined at a dimensionless height of 0.2. The interface profile is compared with the reference PIV experiments [169].

is observed to have a higher influence on the interface topology, particularly for the lowest resolution of $D_T = 64$. The converged shape of the higher resolution tests seemingly do not capture the lower bubble tail observed in experimental measurements, with an error of approximately 20% observed at $r/R \approx 0.52$. The discrepancy in shape is likely the cause of minor deviations observed in the flow field of the wake presented in Fig. 5.12. In particular, the elongation observed in the tail of the experimental bubble could be expected to lead to a greater axial, but lower radial velocity component near the tube centre line. This occurs as a result of the expansion of the liquid film at a location closer to the measurement point ($D/5$ below the central axis of the bubble). This is further verified by the numerical results presented at a location of $D/6$, which provide a close fit to experimental data. Qualitatively, the reduced elongation observed numerically agrees with the findings presented in Fig. 10 of Ndinisa *et al.* [170].

5.3.4 Summary of experimental validation

In this section, it has been shown that the phase-field LBM is able to accurately capture the Taylor bubble rise velocity, the local flow field, and the interface profile in key areas of interest. The rise velocity determined during simulation was observed to more accurately align with experimental results in comparison with previous numerical work in the literature. Furthermore, the local flow field showed only minor discrepancies with the PIV measurements. This finding shows particular promise as the expected rise velocity of a Taylor bubble has a significant effect on the pressure gradient when analysing the slug flow regime in tubular pipes with certain mechanistic models [18].

The convergence of the interface profile was observed at a computational resolution of $D_T = 128$ and agreed closely with experimental images. This, along with the flow field data, indicate that the developed model is able to capture both local and macroscopic details of the flow, correctly resolving the desired level of physics. With this, extrapolation to a wider range of dimensionless numbers to cover an array of pipe sizes and fluid properties will allow existing closure models to be evaluated and updated if required.

5.4 Conclusions

This chapter presented the development, verification and validation of a phase-field LBM in three dimensions. The model was benchmarked and validated against numerical and experimental works. The use of a WMRT collision scheme enhanced the numerical stability of the model, enabling the simulation of high density ratios and high Reynolds numbers. The model itself employs the conservative phase-field LBE designed to simulate immiscible fluids coupled with a velocity-based LBE to recover the system hydrodynamics at high density ratios. The current model contains just one non-local parameter in the LB collision step, offering an improved locality in comparison with other available LB models. The benefit of this was highlighted in 2D in which computational

efficiency on parallel architectures was enhanced; in 3D this would be more noticeable again with more communication required due to an increase in neighbour nodes.

The performance of the model for density matched droplet deformation, a common case used in the benchmarking of certain LB models, was first demonstrated. Here, similar performance to published results using a colour-gradient model was observed, with theoretical results being reasonably well matched in the low capillary number limit. Similarly to the existing LB models, the present LBM upheld useful features such as an easily adjustable surface tension and a consistent interface thickness.

Flow cases where the density contrast of the fluids have a significant impact on the system dynamics were also investigated. This included the Rayleigh-Taylor instability in 3D, in which a slight interface perturbation was introduced causing the heavy fluid to characteristically penetrate into the lighter one. The model was benchmarked against previous literature where a density ratio of three was used and a mushroom-like roll-up of the heavy fluid spike was observed. From here, the model was extended beyond the comparative literature by simulating the Rayleigh-Taylor instability with fluids similar in properties to an air-water system. The model was observed to capture the dynamics of such a system stably up to relatively high Reynolds numbers.

Having verified the model with the previous numerical tests, validation against experimental results investigating the rise of a Taylor bubble in a quiescent fluid was conducted. The experiment injected an air bubble into a tube filled with olive oil and utilised PIV technology to capture high resolution flow field data. The phase-field LBM was not only able to recover the observed rise velocity reported in experiments, but the local flow field data about the bubble was also accurately captured. The steady-state interface profile about the bubble nose and tail was extracted from simulations and compared with that found experimentally. Minor discrepancies were observed, but overall the results were deemed to capture the physical system, providing a detailed validation case for the model presented.

The following chapter will look to investigate the applicability of the phase-field LBM over a large parameter range that is expected to be of interest for oil and gas operations. A tubular pipe geometry is maintained, however, the fluid properties and pipe inclination are varied. Additionally, the effect of flowing fluid is investigated and provides motivation for the development of moving cylindrical boundary conditions.

Part of the following publication has been incorporated as Chapter 6.

1. [2] **T. Mitchell**, C. Leonardi, M. Firouzi, B. Towler, Towards closure relations for the rise velocity of Taylor bubbles in annular piping using phase-field lattice Boltzmann techniques, *21st Australasian Fluid Mechanics Conference*, Adelaide, Australia, 10-13 December, 2018.

Contributor	Statement of contribution	%
Travis Mitchell	writing of text	85
	proof-reading	50
	theoretical derivations	95
	numerical calculations	100
	preparation of figures	100
	initial concept	90

Chapter 6

Taylor Bubble Dynamics in Tubular Pipes

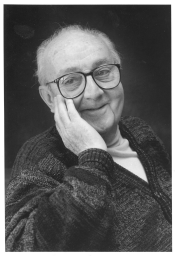

"All models are wrong, but some are useful."
George Box

This chapter uses the phase-field LBM developed in this dissertation to study the dynamics associated with Taylor bubbles in tubular pipes. Up until here, the focus of the work was to formulate the multiphase model, verify that the governing equations were being resolved and validate that the equations were incorporating all the necessary physics to mimic systems of practical relevance. Characterisation of Taylor bubbles and their associated dynamics is closely related to the slug flow regime commonly observed in oil and gas wellbores, gathering networks and major transport pipelines. In order to effectively design and operate artificial lifting equipment as well as to determine surface equipment sizing at a well site, it is essential to understand the flows that can manifest within the confined pipe environment.

As described in Chapter 2, a Taylor bubble is known for its characteristic shape in which an elongated bullet-type profile is observed to occupy almost the entire pipe cross section. In a continuous flow, the Taylor bubbles are often separated by liquid slugs in which additional gas volume may be present in the form of smaller dispersed bubbles. A flowing liquid film forms around the Taylor bubbles separating them from the pipe wall, and can cause detachment and circulation effects as it expands into the liquid slug. This flow regime can occur at a range of superficial gas and liquid velocities as well as in various flow configurations; co-current upwards, downwards and counter-current. Depending on the application, slug flow can be detrimental due to its inherent pulsatile nature causing cyclic/fatigue damage; or beneficial with its ability to carry liquid, for example in gas-lift techniques applied to enhance oil extraction.

Primarily due to the industrial relevance of slug flows, Taylor bubble dynamics has been studied extensively in the literature. Experimental work in this area typically focuses on stagnant, co-current upwards or downwards flows in vertical [6, 169, 186–189], horizontal [190, 191] or inclined pipes

[6, 192–195]. Nevertheless, accurate and non-invasive measurements of gas-liquid flows can be complex and expensive especially when looking to conduct them for a large range of pipe configurations and fluids with varying properties. Numerical simulation provides a means in which one can validate with experiments using simple geometries and safe fluids before extrapolating the parameter range in a computational setting (i.e. substituting methane). For this, it is common for researchers to apply the volume-of-fluid (VOF) [170] or level-set (LS) [18] techniques to resolve interfacial dynamics within a flow field. However, with promising results presented in Chapter 5, phase-field theory provides an alternative to this and will be the basis for this analysis.

With the model validated, its ability to capture a wide parameter range is first tested by varying fluid properties through the Eötvös and Morton numbers, and pipe configurations by analysing the effect of inclination on bubble rise. Following this, the chapter looks to gain insights into the effect of flowing liquid on the propagation of Taylor bubbles, for which boundary conditions are presented and comparisons with pre-existing rise velocity correlations are made.

6.1 Taylor bubble domain setup

For conducting parameter sweeps, it is desirable for the solution algorithm to be as efficient as possible, minimising computational cost. In order to do this, the forcing term seen in Equation 4.3 is updated such that it is applied in moment space. To do this, the update rule for the model is written as,

$$g_i(\mathbf{x}+\mathbf{c_i}\delta t, t+\delta t) = \mathbf{M}^{-1}\left[m_i - (m_i - m_i^{eq} + 0.5F_{m,i})\hat{S}_{i,i} + F_{m,i}\right], \tag{6.1}$$

where $\mathbf{m} = \mathbf{Mg}$ and the forcing term is given by $\mathbf{F}_m = \rho^{-1}(0, F_x, F_y, F_z, 0, \ldots, 0)$. This minor adjustment to the algorithm saw a significant speedup by a factor of approximately two for the Taylor bubble domain simulated in the previous chapter. This increased computational efficiency was primarily due to the ease of calculation of the viscous stress tensor as well as the cancelation observed in the relaxation of higher-order moments to equilibrium in this space [2].

Figure 6.1 provides an image output from Paraview of the initial configuration for the Taylor bubble simulations. For this, a cylindrical gas region is specified with a diameter of $0.75D$ and length of $3D$, where D is the diameter of the solid pipe. The pipe itself has a length of $10D$ and is closed on the top and bottom with the use of the bounce back boundary conditions. A gravitational force, G, is applied in the negative x-direction causing the bubble to propagate in the positive x-direction due to buoyancy effects. For all the cases tested, both experimental and numerical, it was assumed that the gas density and viscosity were negligible in comparison to the liquid and as such a density and viscosity ratio of 1000, $\rho^* = \mu^* = 1000$, is defined in the simulations in this section. As a result of this, the dimensionless numbers that define the flow configurations are given by,

$$Mo = \frac{G\mu_l^4}{\rho_l \sigma^3}, \tag{6.2}$$

$$Eo = \frac{G\rho_l D^2}{\sigma}, \tag{6.3}$$

$$N_f = \frac{\rho_l \sqrt{GD^3}}{\mu_l}, \tag{6.4}$$

$$Fr = \frac{u_{TB}}{\sqrt{GD}}, \tag{6.5}$$

$$Re = \frac{\rho_l u_{TB} D}{\mu_l}, \tag{6.6}$$

$$Pe = \frac{D\sqrt{GD}}{M}, \tag{6.7}$$

$$Ca = \frac{W}{D}, \tag{6.8}$$

where the Peclet number, Pe, and Cahn number, Ca, have been introduced to define the phase-field parameters.

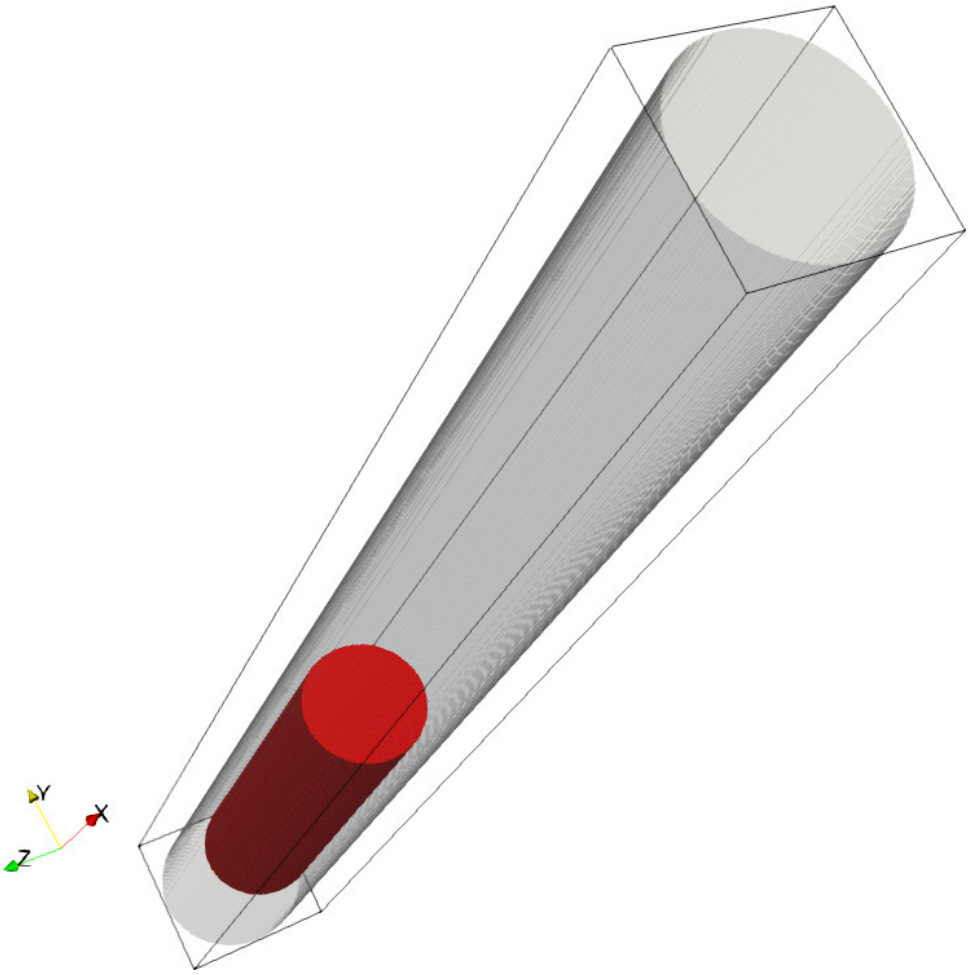

Figure 6.1: The initial configuration for the Taylor bubble simulations where the red contour indicates the liquid-gas interface and the grey contour shows the liquid-solid interface.

Unless otherwise stated, the diameter of the tube in this chapter is 128 lattice units and a reference time,

$$t^* = \sqrt{D/G} = 12000, \tag{6.9}$$

is specified. This defines the gravitational acceleration for each simulation, which along with the required Eötvös and inverse viscosity or Morton number, can be used to define the surface tension and

viscosity, respectively. The phase-field parameters are provided by setting the Peclet number to a value of five and the Cahn number to 0.0391 (corresponding to an interface width of five lattice units).

6.2 Effect of fluid parameters

To investigate how Taylor bubbles behave as well as how the developed model performs for a range of dimensionless numbers, the work of Lizarraga-Garcia *et al.* [196] is used as a benchmark. This consists of a mixture of experimental results as well as correlations provided by the literature for which simulation results can be compared. The test matrix of parameters is graphically presented on the chart of White and Beardmore [6] in Figure 6.2. Here, the x- and y-axis represent the Eo number and the Mo number, respectively. Additionally, the chart displays zoned regions identifying where certain effects have negligible contributions to the Taylor bubble dynamics (i.e. where the motion is independent of inertial, viscous or surface tension effects).

Of the eight cases initially tested, four were constructed from experimental works; Case C was based on the studies of Shosho and Ryan [194]; Case D was from Bugg and Saad [169]; Case F was from Nogueira *et al.* [189]; and Case G was from Jeyachandra *et al.* [195]. To analyse the hydrodynamic characteristics of these Taylor bubbles, both the normalised thickness of the liquid film surrounding the bubble, $h^* = 2h/D$, and the dimensionless rise velocity in the form of the Froude number, Fr, are measured. These parameters give insights into both the motion and shape of the Taylor bubble which can impact predicted pressure gradients in mechanistic models [18].

6.2.1 Modelling of liquid film thickness

Knowledge of the liquid film development, equilibrium state and propagation into the wake region behind a Taylor bubble is fundamentally relevant to the behaviour of both single and consecutive bubbles. The film has impacts on all four regions typically used to describe a Taylor bubble; (1) the hemispherical-like nose, (2) the body section consisting of both the developing and developed film, (3) the tail region that may be convex, flat or concave depending on the system parameters, and (4) the wake [197, 198].

The importance of the liquid film was noted as far back as the 1940s by Dumitrescu [199]. Dumitrescu's analysis of the Taylor bubble assumed a spherical nose along with a potential flow. Thus, by fixing the coordinate system to the bubble, the condition of conserved vorticity allows an approximate solution to be found for a stagnant fluid in this region. A complete picture of the bubble is then obtained by matching this solution with the results of an asymptotic analysis of an inviscid falling film. The asymptotic analysis assumes a thin film, allowing for the curvature of the pipe wall to be neglected [188, 199, 200]. Later, Brown [188] extended this by taking the film to be in an equilibrium state, balancing gravitational forces with the wall shear. The effect of surface tension was incorporated into the analysis procedure of Dumitrescu by Bendiksen [193], but this did not make a significant difference to the result for the parameters tested.

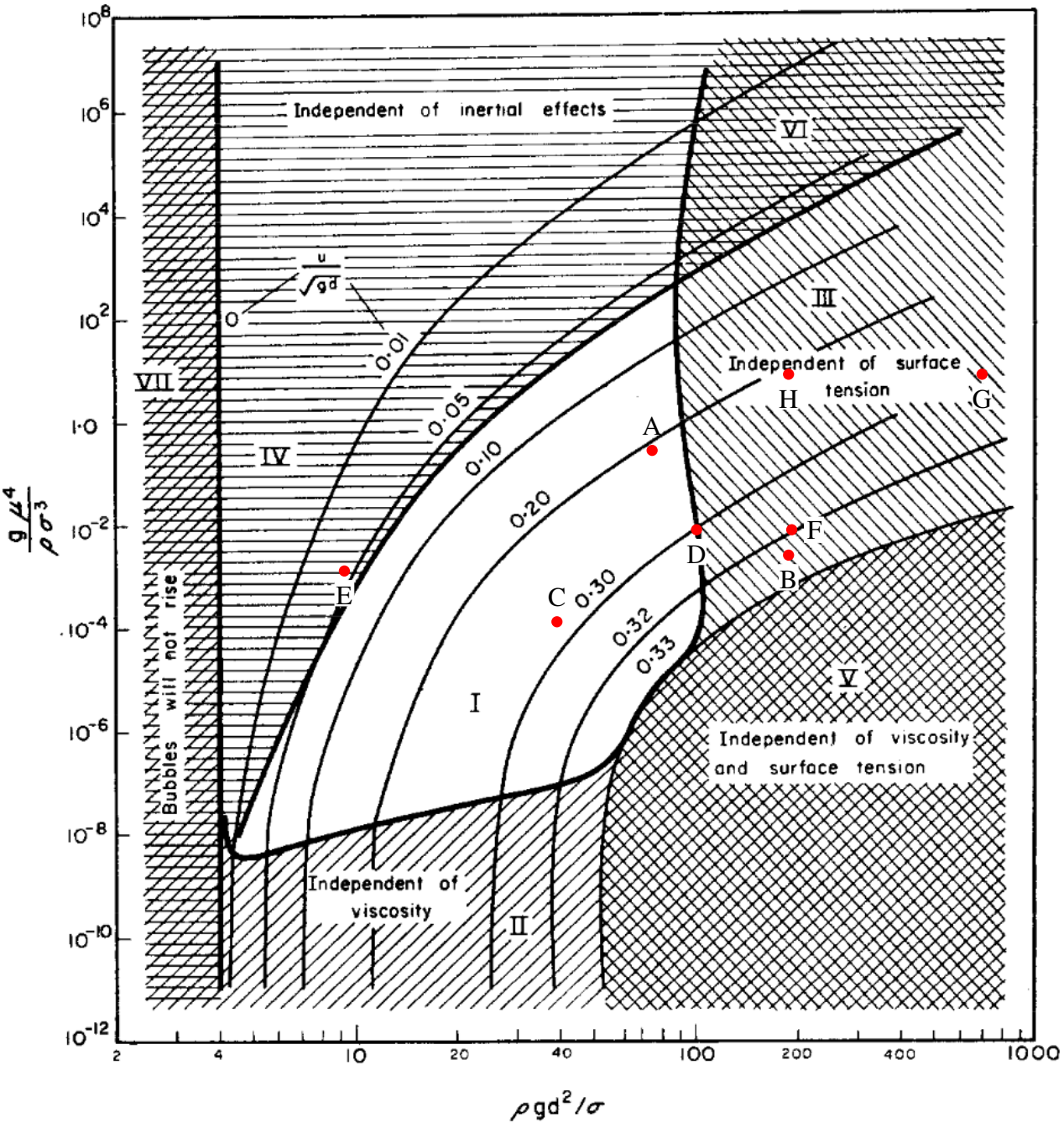

Figure 6.2: The Taylor bubble regime chart of White and Beardmore [6] identifying the test cases used to further validate the multiphase LBM.

Alongside analytical attempts to define the Taylor bubble, significant experimental work has greatly contributed to the understanding of the liquid film. Goldsmith and Mason [200] were amongst the early attempts to characterise the liquid flow in the thin film by tracking aluminium tracer particles through photographs. Nicklin *et al.* [201] were able to visualise velocity profiles around a rising Taylor bubble, and identified the falling film as fully developed when the velocity at the edge of the film matched that of the bubble rise. This constant film thickness is typically used to describe the flow through the film Reynolds number,

$$Re_f = 4\frac{\rho_l u_f h}{\mu_l}, \tag{6.10}$$

where u_f is the film velocity. However, by taking a thin film assumption, where $h \ll D$, Llewellin *et al.* [197] were able to show that the film Reynolds number is equivalent to the bubble Reynolds number previously defined. With this, a number of early correlations written as a function of Re_f could be rewritten based on N_f, Fr, and Re. Notable correlations were proposed by Nusselt [202], Karapantsios and Karabelas [203] and Lel *et al.* [204]. Here, the later work of Llewellin *et al.* [197] is used for comparison.

Llewellin *et al.* [197] studied the falling films surrounding Taylor bubbles from a dimensionless approach and found that the thickness of the film, h, was a function of only the inverse viscosity number. This was then empirically tuned with their own measurements along with the results of Nogueira *et al.* [189]. From this, they concluded the film thickness normalised by the pipe radius, could be predicted by,

$$h^* = 0.204 + 0.123 \tanh(2.66 - 1.15 \log_{10} N_f). \tag{6.11}$$

6.2.2 Modelling of bubble rise velocity

In the doctoral work of Lizarraga-Garcia [63], a sensitivity study of contributions to pressure gradient predictions was conducted using a range of modelled parameters. Lizarraga-Garcia identified the rise velocity of the Taylor bubble as having a significant impact on prediction uncertainties and as such, developed an improved, unified correlation for tubular pipes. The sensitivity study was conducted for a range of existing predictive tools for two-phase flow. Originally, these tools were largely empirical, but have continued to incorporate further physical relevance and are now commonly based on a mixture or mechanistic multi-fluid formulation [18, 205]. The specific models used in the study of Lizarraga-Garcia included the mechanistic models of Orell and Rembrand [206], Ansari *et al.* [72], and Petalas and Aziz [73].

There is extensive literature surrounding the propagation of Taylor bubbles through stagnant liquid in vertical pipes. In addition to the work of Dumitrescu [199] previously discussed, Davies and Taylor [186] also made significant progress from an analytical approach in the limit of negligible surface tension and viscosity. White and Beardmore [6] took an experimental approach and proposed the graph used in Figure 6.2. Initially, it was common for correlations to vary depending on dimensionless parameters, for example the correlation proposed by Wallis [68],

$$u_{TB} = 0.345 \left[1 - \exp\left(\frac{-0.01 N_f}{0.345}\right)\right] \left[1 - \exp\left(\frac{3.37 - Eo}{m}\right)\right] \sqrt{\frac{GD(\rho_l - \rho_g)}{\rho_l}}, \tag{6.12}$$

$$m = \begin{cases} 10, & \text{if } N_f \geq 350 \\ 69 N_f^{-0.35}, & \text{if } 350 > N_f > 18. \\ 25, & \text{if } N_f \leq 18 \end{cases} \tag{6.13}$$

Viana *et al.* [207] collected data from 255 experiments from the literature and conducted seven of their own in an attempt to improve upon previous rise velocity correlations. In doing this, they were able to define the rise velocity through the Froude number as $Fr = Fr(Eo, N_f)$. The curves obtained by

Viana *et al.* [207] gave rise to two separate power laws when graphed against Eo for small ($N_f < 10$) and large ($N_f > 200$) inverse viscosity numbers. A universal correlation was derived using logistic dose curves to fit the transition region leading to,

$$Fr = \frac{0.34}{(1+(14.793/Eo)^{3.06})^{0.58}} \Bigg/ \left(1+\left(\frac{N_f}{31.08(1+(29.868/Eo)^{1.96})^{0.49}}\right)^{a}\right)^{b} \tag{6.14}$$

$$a = -1.45(1+(24.867/Eo)^{9.93})^{0.094} \tag{6.15}$$

$$b = -1.0295/a \tag{6.16}$$

Lizarraga-Garcia *et al.* [196] was not the first to look at the dynamics of a Taylor bubble with interface-resolved computational fluid dynamics, however they were one of the few groups to use a 3D domain. Ndinisa *et al.* [170] used axisymmetric formulations of the volume-of-fluid and two-fluid models in ANSYS Fluent to determine the characteristics of a Taylor bubble in olive oil. Araùjo *et al.* [208, 209] also used ANSYS Fluent to study both single and consecutive Taylor bubbles using a volume-of-fluid technique in an axisymmetric domain. Taha and Cui [97] extended a 2D analysis to 3D resolved simulations and were able to conclude that the symmetry of the Taylor bubble breaks down for $N_f > 500$. From the numerical database created by Lizarraga-Garcia *et al.* [18], the vertical rise prediction given by Equation 6.14 was found to be suitable, as such this is used for comparison when experimental results are not available.

6.2.3 Comparison of results

As previously mentioned, the setup for cases C, D, E and F were from experimental work, of which, cases D and F reported on film thickness as well as bubble rise velocity. For the remaining tests, comparisons were made using Equation 6.14 for the rise velocity and Equation 6.11 for the film thickness. Table 6.1 provides the dimensionless numbers describing the flow system as well as the simulation results.

Table 6.1: Summary of Taylor bubble rise and film thickness over a range of Eo and N_f numbers in comparison with literature and the finite volume method (FVM) simulations of Lizarraga-Garcia *et al.* [196]. Experimental results are highlighted by a *.

Case	Mo	Eo	Nf	Fr (lit.)	Fr (FVM)	Fr (LBM)	h^* (lit.)	h^* (FVM)	h^* (LBM)
A	0.328	76.5	34.2	0.210	0.212	0.209	0.295	0.288	0.289
B	4.03e-3	187	201	0.324	0.306	0.322	0.198	0.189	0.197
C	1.17e-4	38.6	149	0.276*	0.295	0.292	0.212	0.234	0.209
D	1.52e-2	98.4	89.0	0.303*	0.291	0.293	0.246*	0.238	0.242
E	1.50e-3	9.88	82.3	0.0411	0.0458	0.048	0.192	0.189	0.194
F	4.75e-2	192	111	0.336*	0.322	0.308	0.235*	0.218	0.230
G	8.38	747	84.0	0.289*	0.299	0.301	0.250	0.261	0.247
H	8.38	181	29.0	0.199	0.216	0.206	0.306	0.295	0.301

Here, it is evident that the results found using the phase-field lattice Boltzmann method are able to accurately capture both the Froude number and the film thickness for all tested cases. The average

error for the rise velocity was 5.4%, which aligned closely with the accuracy of Lizarraga-Garcia *et al.* [196] at 5.6%. For the film thickness, the phase-field method appears superior to the level-set methods employed in the previous study with an average error of only 1.4% compared to 4.7%.

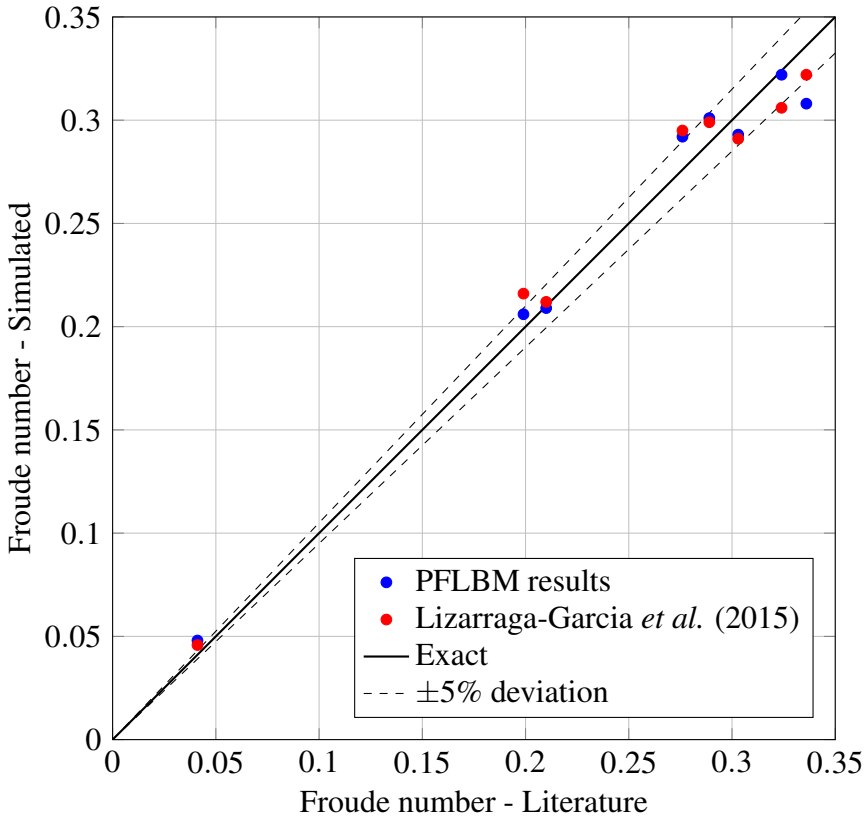

Figure 6.3: Comparison of the Froude number simulated with the phase-field LBM (PFLBM) compared to the work of Lizarraga-Garcia *et al.* [196] and to correlated/experimental results.

Figures 6.3 and 6.4 further indicate the comparison of the lattice Boltzmann results compared to the level set-finite volume method used by Lizarraga-Garcia *et al.* [196] as well as reported literature values. These simulations further validate the performance of the proposed model and provide insight into the accuracy of correlations formulated for Taylor bubble characteristics in vertical tubular pipes. However, it is noted here that the viscosity values that correspond to the tested Morton numbers is more similar to that of heavy oil rather than brine, as may be expected in a coal seam gas wellbore. The stability of Taylor bubbles propagating in low viscosity liquid (or equivalently liquid with a high inverse viscosity number, N_f) can introduce additional modelling complexities. As previously stated, Taha and Cui [97] found that the symmetry of Taylor bubbles breaks down for N_f over 500 which significantly increases the computational cost through the need for 3D simulations. Due to this, Section 6.2.4 extends the parameter range tested by Lizarraga-Garcia [63] to Morton numbers more applicable for an air-water system,

$$Mo = \frac{G\mu_l^4}{\rho_l \sigma^3} = \frac{9.81 \times 0.001002^4}{998 \times 0.07286^3} = 2.5618e-11. \tag{6.17}$$

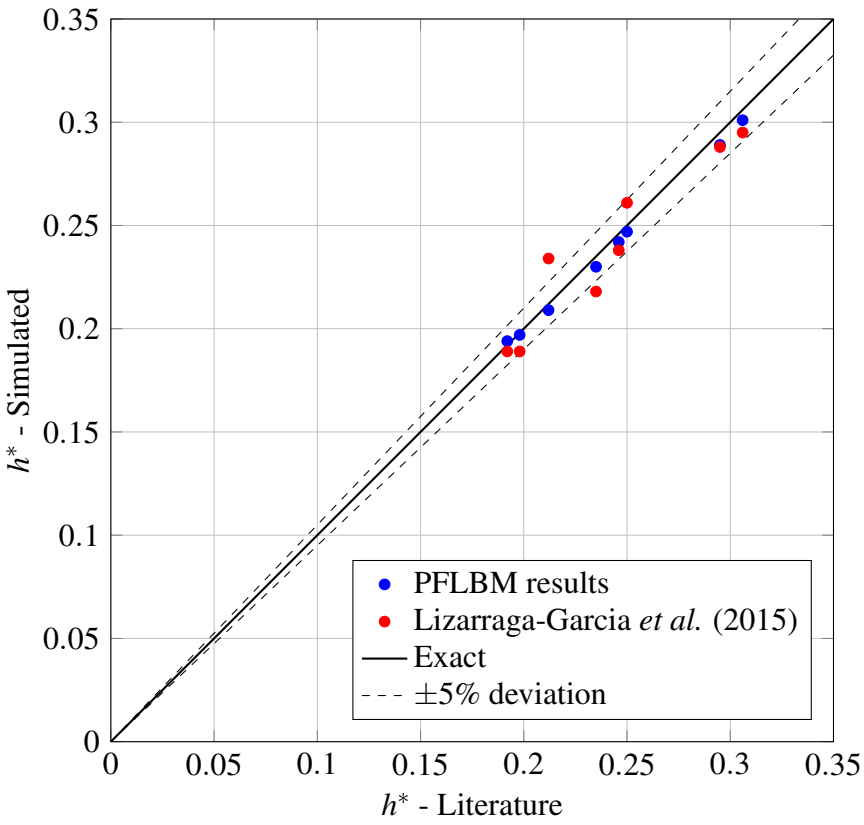

Figure 6.4: Comparison of the normalised film thickness simulated with the PFLBM compared to the work of Lizarraga-Garcia *et al.* [196] and to correlated/experimental results.

6.2.4 Extension of parameter space

Having validated the proposed phase-field LBM's applicability to high viscosity liquids (e.g. heavy oils), the stability is now tested by extending the parameter sweep to lower viscosity values. Figure 6.5 indicates in blue the proposed test area in which natural gas wells producing from coal seams may be expected to operate, while in red is shown the primary area of interest for Lizarraga-Garcia [63]. The specific test set used here can be defined by,

$$Mo \in \{10^{-3}, 10^{-5}, 10^{-7}, 10^{-9}, 10^{-11}\}, \tag{6.18}$$

$$Eo \in \{10, 20, 40, 100, 200, 400, 1000\}. \tag{6.19}$$

Initially, the reference time was set to $t^* = 20000$ to produce favourable lattice values of viscosity and surface tension. The primary aim of this subsection is to identify methods for enhancing stability of certain dimensionless parameter ranges. Lessons learned from this will be taken forward into Chapter 7 in which annular piping configurations will be investigated. From these tests, Figure 6.6 indicates the stable regions for the initial test suite. Here, it can be seen that there is a clear strip of stability for the specified reference time, t^*. It is evident in the regions of high Eötvös number (low surface tension) and low Morton number (low viscosity), instabilities appear to be initiated from the deformability of the interface under such conditions. Further testing will be conducted into this area, but first the correlation used by Lizarraga-Garcia *et al.* [18] and developed by Viana *et al.* [207] is assessed for the completed simulations.

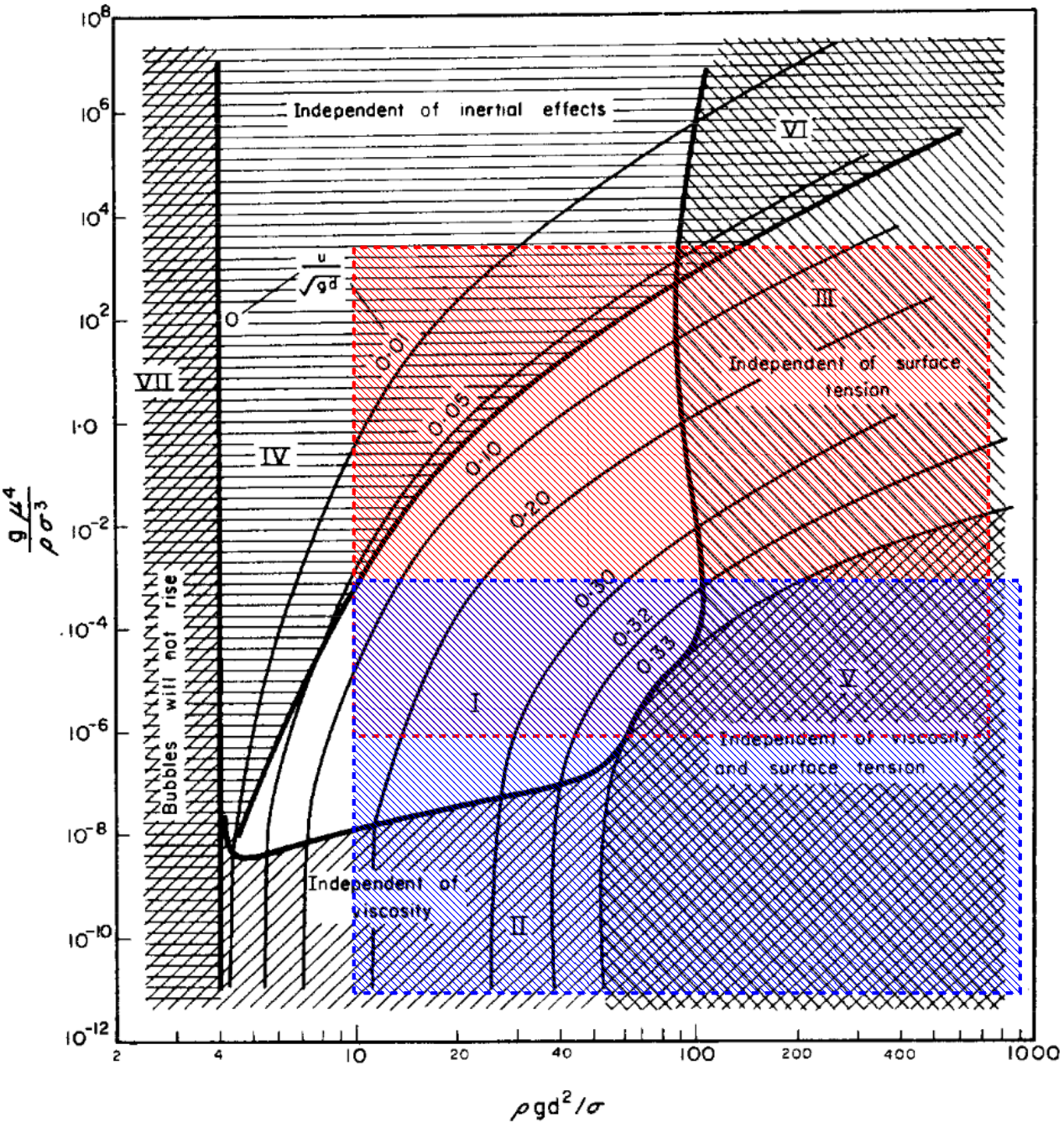

Figure 6.5: The Taylor bubble regime chart of White and Beardmore [6] indicating the area of interest (red) for the study by Lizarraga-Garcia [63] compared to that explored in this section (blue).

Table 6.2 presents the comparison for each stable simulation with Equation 6.14. The level of accuracy here is clear, with an average error percentage of only 2.900%. This indicates the correlation is sufficient as the multiphase system progresses into a viscosity independent regime. However, with both the independence of viscosity and surface tension, the deformation of the bubble wake caused instabilities in the lattice Boltzmann simulations to arise. Figure 6.7 indicates the variation in bubble profile as the Morton number is reduced for a fixed Eötvös number, while Figure 6.8 presents the effect of increasing Eötvös number for a fixed Morton number.

To assess if this limitation could be relaxed, the reference time was the first 'user-specified' parameter to be adjusted in the workflow. Initially, the value had been set to, $t^* = 20000$, as this

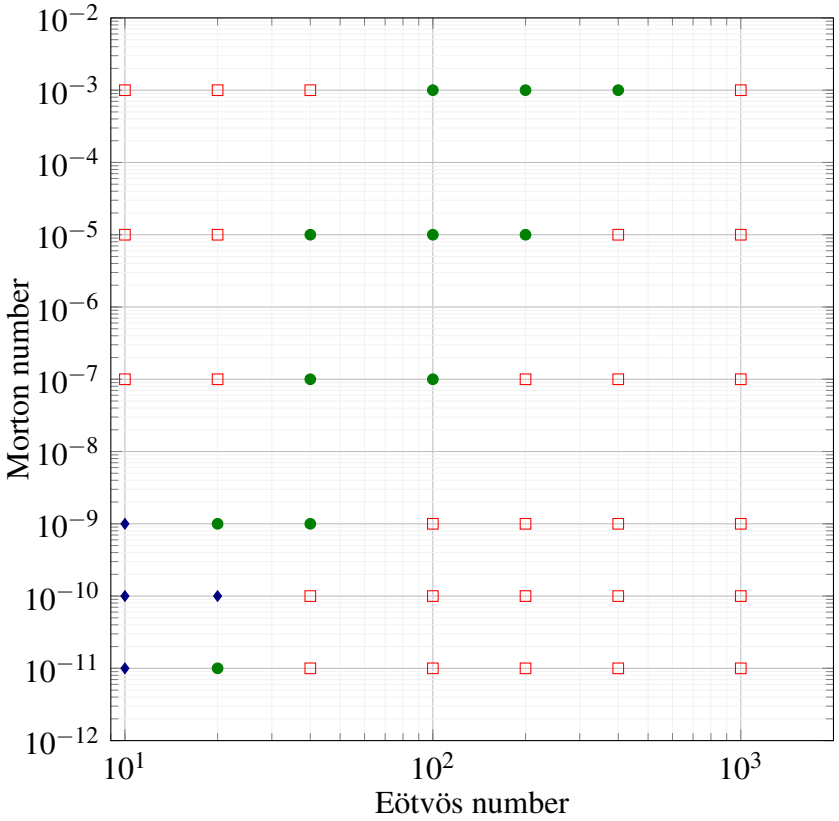

Figure 6.6: Stability zone for preliminary parameter sweep to explore lower viscosity fluids applicable to natural gas extraction. Hollow red dots indicate that numerical instability was detected during the running of the simulation, while green filled circles indicate the completion to a steady rise condition. The blue filled diamonds represent the additional stability gained from setting $t^* = 30000$.

Table 6.2: Results obtained for the stable rise of Taylor bubbles in a vertical, tubular pipe in comparison with the correlation presented in Equation 6.14.

Mo	10^{-9}	10^{-11}	10^{-5}	10^{-7}	10^{-9}	10^{-3}	10^{-5}	10^{-7}	10^{-3}	10^{-5}	10^{-3}
Eo	20	20	40	40	40	100	100	100	200	200	400
Fr (Corr.)	0.280	0.280	0.318	0.329	0.331	0.320	0.336	0.339	0.331	0.338	0.336
Fr (LBM)	0.274	0.284	0.300	0.318	0.327	0.310	0.327	0.360	0.320	0.338	0.324
Error (%)	1.995	1.305	5.794	3.097	0.927	3.276	2.501	6.159	3.184	0.017	3.634

resulted in what appeared to be a suitable balance between the numerical viscosity, surface tension and gravitational acceleration for the majority of flow cases. To investigate its effect on stability, the reference time was first increased to, $t^* = 30000$, for a subset of, $Mo \in \{10^{-9}, 10^{-10}, 10^{-11}\}$, and $Eo \in \{10, 20, 40, 100\}$ numbers. Testing these improved the stability, with previous successful simulations unaltered, but additionally allowing for the $Eo = 10$ cases to be computed, with the results reported in Table 6.3 and shown graphically in Figure 6.6.

The next set of tests assessed the effect of numerical viscosity and surface tension, for which, Figure 6.6 was analysed as the respective ν_l and σ values. This indicated a potentially stable region for values for ν_l and σ which could be used along with the desired dimensionless parameters to specify t^* and D in simulations. However, it was observed that as the Morton number decreased and Eötvös number increased, the size of the reference time and domain quickly became impractical to test on the

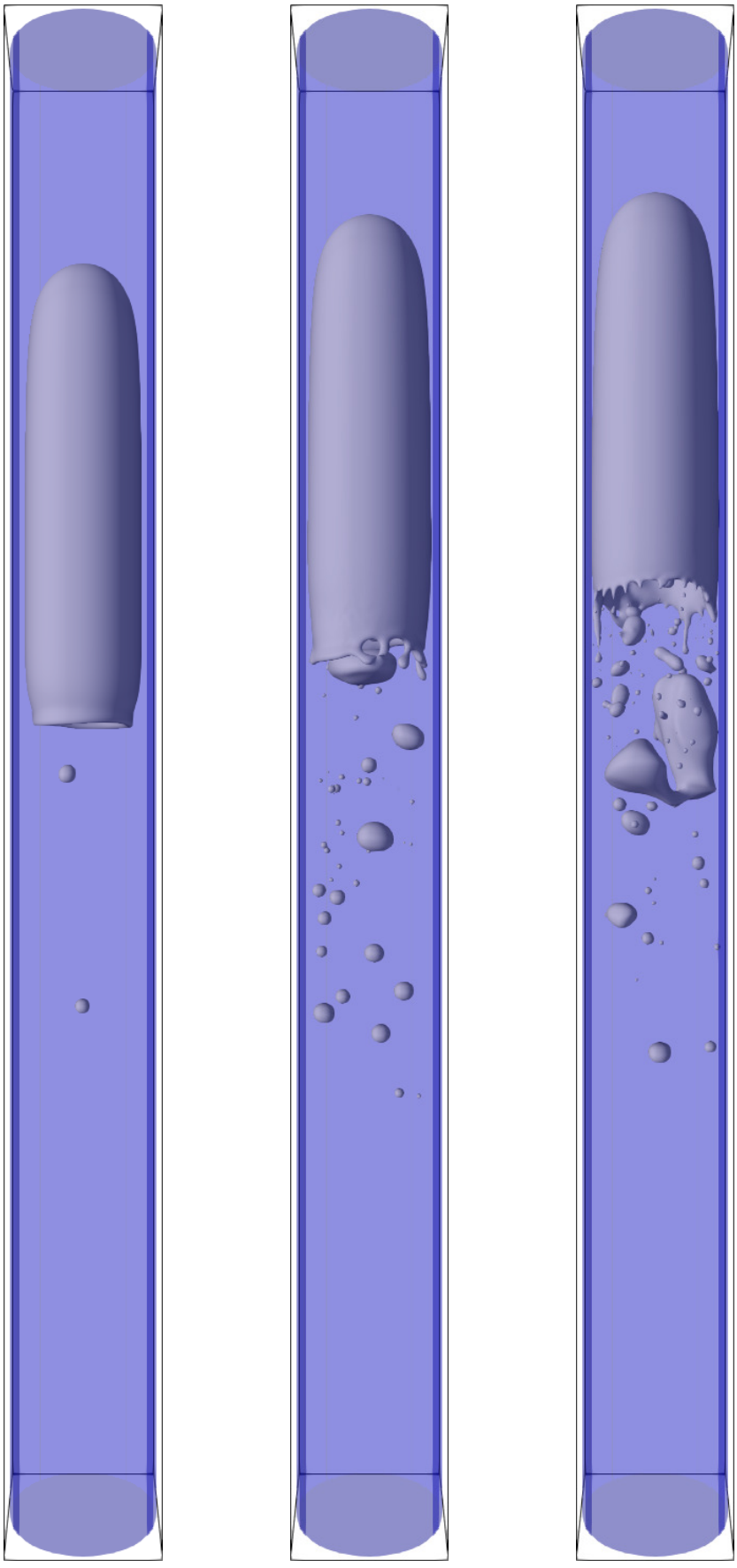

(a) $Mo = 10^{-3}$ (b) $Mo = 10^{-5}$ (c) $Mo = 10^{-7}$

Figure 6.7: Taylor bubble profiles at $t^* = 15t_0$ with an Eötvös number of 100 and Morton numbers; (a) $Mo = 10^{-3}$, (b) $Mo = 10^{-5}$, (c) $Mo = 10^{-7}$.

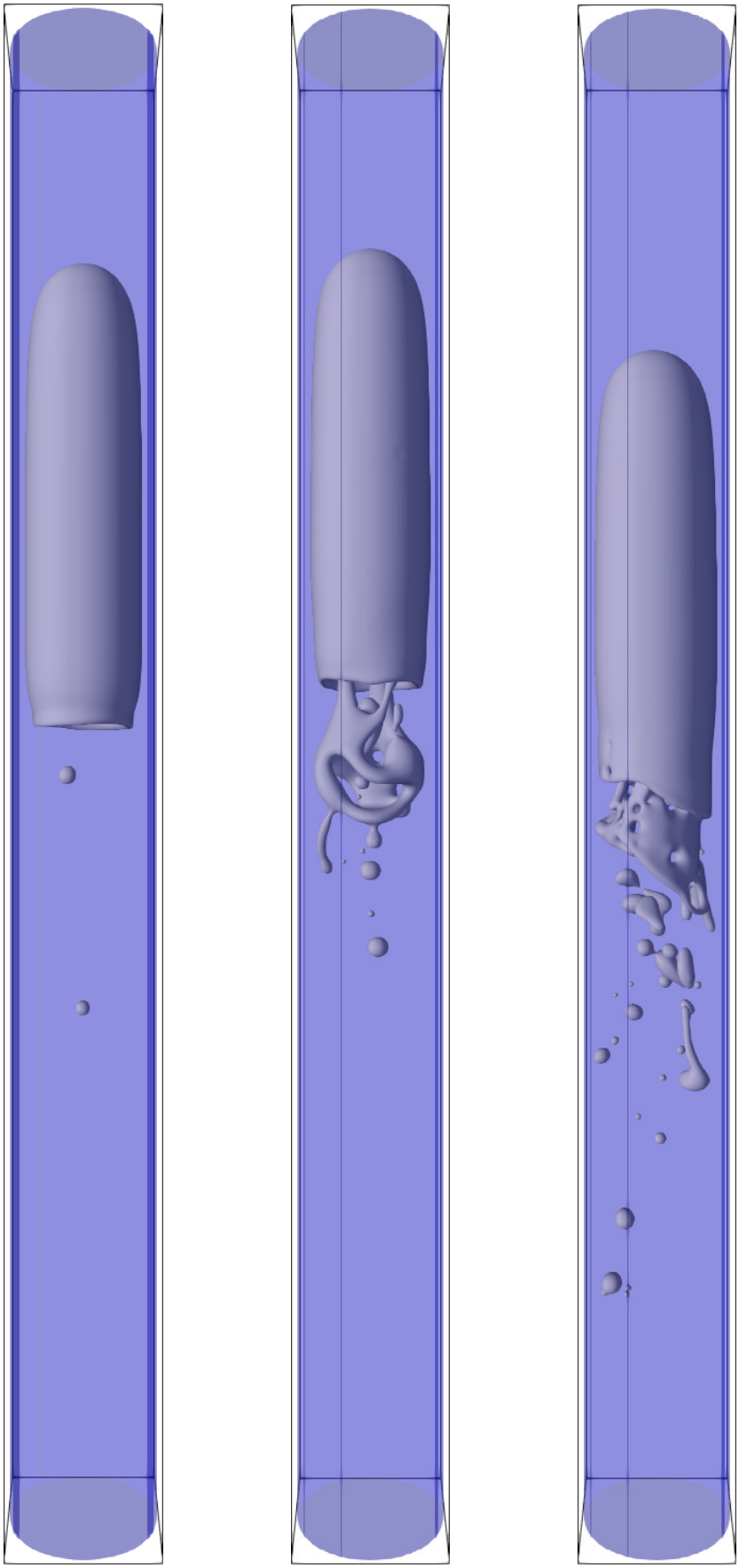

(a) $Eo = 100$ (b) $Eo = 200$ (c) $Eo = 400$

Figure 6.8: Taylor bubble profiles at $t^* = 15t_0$ with an Morton number of 10^{-3} and Eötvös numbers; (a) $Eo = 100$, (b) $Eo = 200$, (c) $Eo = 400$.

Table 6.3: Results obtained for the stable rise of Taylor bubbles in a vertical, tubular pipe in comparison with the correlation presented in Equation 6.14.

Mo	10^{-9}	10^{-10}	10^{-11}
Eo	10	10	10
Fr (Corr.)	0.146	0.146	0.146
Fr (LBM)	0.158	0.161	0.163
Error (%)	8.486	10.827	11.863

available architectures. It is also expected that this stability band would be influenced by the dynamics of the simulated system, in which the large interfacial curvatures and complex bubble breakup and coalescence behaviours, may result in instabilities within the numerics. Incorporation of an adaptive mesh refinement algorithm could assist with this problem, however, this is placed out of the scope of works in the current study and is instead recommended for future work. The interested reader is pointed towards the work of Fakhari *et al.* [28, 157, 173] for literature on adaptive grids and their implementation with multiphase LBM.

One potential technique for improving stability in the numerical simulations, while still gaining an insight into the system dynamics, is to reduce the gradients through a reduction in the density ratio. The work of Hua and Lou [210] as well as Amaya-Bower and Lee [211] indicated variations in the rise velocity of a spherical bubble to be on the order of 10% with density ratios examined between $\rho^* \in \{10, \ldots, 1000\}$. Hua and Lou concluded that for a density ratio larger than 50, little effect could be seen on the terminal shape and rise velocity of the spherically initialised bubble. As such, the subset of simulations conducted for $t^* = 30000$ were analysed with $\rho^* = 100$ and the original reference time of $t^* = 20000$. The new stability plot can be seen in Figure 6.9, in which it is evident that the lower density ratio improved the stability of simulations for increasing Eötvös and decreasing Morton numbers. Figure 6.10 compares the simulation results with the correlation of Viana *et al.* [207] for the rise velocity of a Taylor bubble, the average variation here was found to be 6.2%. Note that this is ignoring the outliers evident in Figure 6.10 obtained with $Eo = 400$, which appears to be at the limit of stability for this current configuration. This aligns with the order of error observed by Hua and Lou [210] and Amaya-Bower and Lee [211], however, it is interesting to note that the simulation with a reduced density ratio measured a rise velocity greater than the prediction from Viana *et al.* [207].

From the work conducted in this section, it is clear that the phase-field LBM is able to accurately capture the bubble dynamics of high-viscosity fluids as well as low viscosity fluids, if restricted to smaller pipe sizes (i.e. lower Eötvös numbers) or certain simplifications are accepted. In addition to this, an avenue of future work is evident for the proposed model, in which it could be coupled with an adaptive mesh refinement scheme to assist with instabilities arising from the complex interfacial deformations evident in low viscosity, liquid-gas systems. Following on from this, the next section highlights the benefits of numerical modelling by investigating pipe inclination effects. The costs to conduct tests like this experimentally can be quite high as they require significant spatial clearances and a dynamic setup allowing for the pipe system to be adjusted between runs. In comparison to this, one may simply adjust the gravitational datum in the numerical framework such that both vertical and

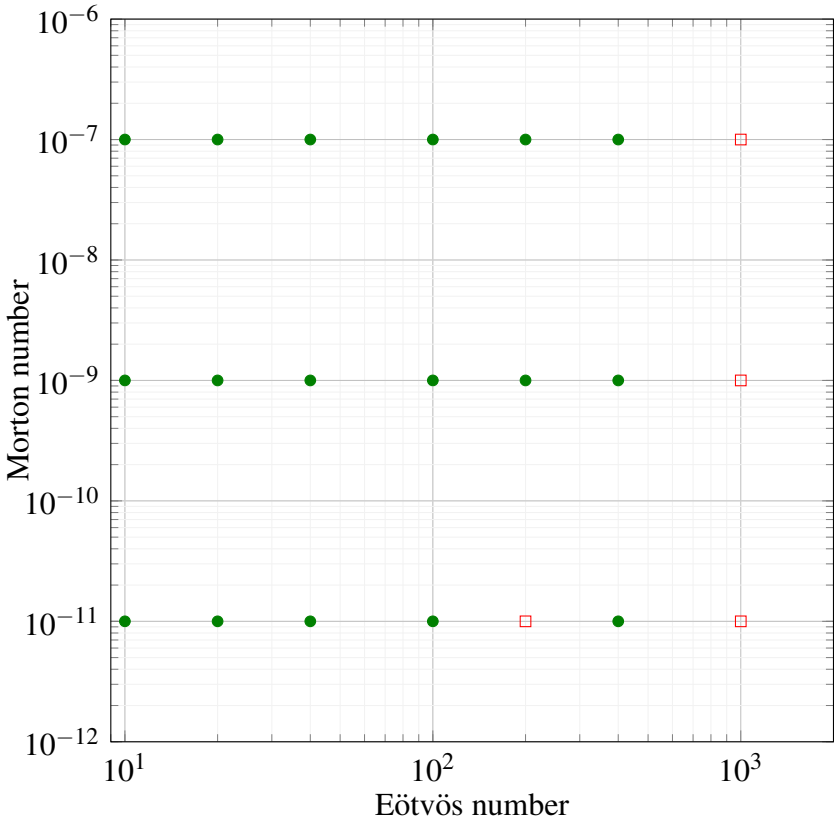

Figure 6.9: Stability zone for preliminary parameter sweep to explore lower viscosity fluids applicable to natural gas extraction. Hollow red dots indicate that numerical instability was detected during the running of the simulation, while green filled circles indicate the completion to a steady rise condition.

horizontal components are applied onto the pipe, mimicking the effects of inclining the system.

6.3 Effect of pipe inclination

6.3.1 Rise velocity correlations

Inclined pipe dynamics have been widely studied in the literature, with the first elongated bubble propagation speed correlation proposed by Bendiksen [193]. This was formulated based on a combination of the velocity predicted for a Taylor bubble through a stagnant fluid in a vertical and horizontal tube, commonly referred to as its *drift velocity*,

$$v_d^v = 0.351\sqrt{GD}\,, \tag{6.20}$$

$$v_d^h = 0.542\sqrt{GD}\,, \tag{6.21}$$

respectively. From this, Bendiksen predicted the Taylor bubble velocity in an inclined tube would be given by,

$$u_{TB} = v_d^h \cos\theta + v_d^v \sin\theta. \tag{6.22}$$

This was further developed by Weber *et al.* [212] following an experimental campaign that included Eötvös numbers in the range [4.9, 490] and Morton numbers between $[2.2\times10^{-11}, 1.5\times10^{4}]$. From

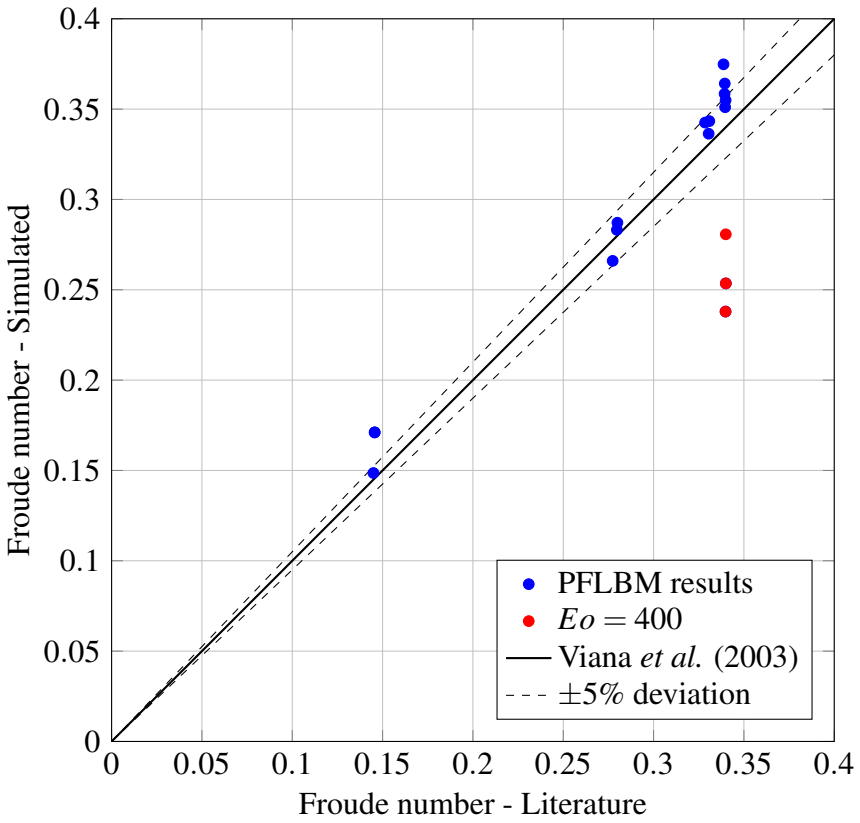

Figure 6.10: Comparison of the Froude number simulated with the phase-field LBM (PFLBM) compared to the correlation proposed by Viana *et al.* [207]. Highlighted in red are the results observed with an $Eo = 400$ that indicate the edge of stability in the current configuration.

the experimental findings, vertical (Fr_d^v) and horizontal (Fr_d^h) dimensionless velocities were extracted and a correction term included in the correlation of Bendiksen such that,

$$Fr_{TB} = Fr_d^h \cos\theta + Fr_d^v \sin\theta + Q, \tag{6.23}$$

$$Q = \begin{cases} 1.37(\delta Fr_d)^{2/3} \sin\theta(1-\theta), & \text{if } \delta Fr_d > 0, \\ 0, & \text{if } \delta Fr_d \leq 0, \end{cases} \tag{6.24}$$

where $\delta Fr_d = Fr_d^v - Fr_d^h$. Other researchers, particularly when looking at angles far from horizontal, simplified their analysis by assuming the horizontal drift component was negligible, $v_d^h \approx 0$. Using this, Hasan and Kabir [213] proposed,

$$u_{TB} = v_d^v \sqrt{\sin\theta}\,(1+\cos\theta)^{1.2} \tag{6.25}$$

$$v_d^v = 0.35\sqrt{GD}\,, \tag{6.26}$$

from their experimental work, in which angles from 58 degrees to vertical were explored. Later, Petalas and Aziz [73] built on the work of Bendiksen [193], Wallis [68] and Zukoski [192] to formulate,

$$u_{TB} = f_m(v_d^h \cos\theta + v_d^v \sin\theta), \tag{6.27}$$

$$\text{where } v_d^h = \left[0.54\frac{1.76}{Eo^{0.56}}\right]\sqrt{\frac{GD(\rho_l - \rho_g)}{\rho_l}}\,, \tag{6.28}$$

$$v_d^v = 0.345(1 - e^{-Eo \cdot \exp(3.278 - 1.424 \ln Eo)}) \sqrt{\frac{GD(\rho_l - \rho_g)}{\rho_l}}, \tag{6.29}$$

and f_m is the minimum of unity and $0.316\sqrt{\rho_l v_d^v D/2\mu_l}$.

A number of other notable works have been undertaken in this area. Here, the studies of Shosho and Ryan [194] and Jeyanchandra *et al.* [195] are highlighted as they are used for comparison of simulation results. Shosho and Ryan investigated the behaviour of Taylor bubbles in both Newtonian and non-Newtonian fluids while Jeyachandra proposed a new correlation for the horizontal drift velocity based on experimental works. They coupled this with a correlation from Joseph [214] to obtain,

$$Fr_{TB} = Fr_d^h \cos\theta + Fr_d^v \sin\theta, \tag{6.30}$$

$$\text{where } Fr_d^h = 0.53 \exp(-13.7 N_f^{0.46} Eo^{-0.1}), \tag{6.31}$$

$$Fr_d^v = -\frac{1}{3}\left(8N_f^{-1} - \sqrt{\frac{2\rho_l}{\rho_l - \rho_g} + 64N_f^{-2}}\right). \tag{6.32}$$

Lizarraga-Garcia *et al.* [18] performed computational experiments with the commercial multiphase simulation code TransAT. This was used to generate a numerical database from which a unified bubble velocity correlation was formulated. Initially, an attempt was made to fit the data with an expression based on a balance between buoyancy and drag forces, but poor results were obtained for low angles of inclination as well as for high Morton numbers and low Eötvös numbers. Due to this, it was proposed that the velocity could be found from an expression of the form,

$$Fr = Fr_v(1 - \exp(-b\theta))(1 + c \cdot \sin 2\theta), \tag{6.33}$$

where, Fr_v, is given by Equation 6.14 and the coefficients $b = b(Eo, Mo)$ and $c = c(Eo, Mo)$ are chosen to fit the simulated results. After analysing the database, the best fit was obtained with,

$$b(Eo, Mo) = 47.06 Fr_v + 4, \tag{6.34}$$

$$c(Eo, Mo) = -0.9118 Fr_v + 0.67 - \frac{0.0148(\log_{10} Mo)^2 - 0.125 \log_{10} Mo - 0.9118 Fr_v - 1.118}{[1 + (0.05Eo)^8]^8}, \tag{6.35}$$

in which c is a logistic dose-response curve which allows a unified correlation which can describe the transitions in governing behaviours.

6.3.2 Numerical experiments

To determine the effect of pipe inclination, the test cases investigated by Lizarraga-Garcia *et al.* [196] were studied for a wider range of rotations. Cases A, C, G and H were analysed at inclinations of $\theta = (5, 15, 30, 45, ..., 90)$ degrees from horizontal, for which experimental work is used for comparison with cases C [194] and G [195]. In this section, three dimensional computational fluid dynamics results of Lizarraga-Garcia *et al.* [196] as well as correlations from Hasan and Kabir [213], Jeyanchandra *et*

al. [195] and Petalas *et al.* [73] are included to determine the suitability of existing correlations for inclined pipe flow. From here, the unified correlation proposed by Lizarraga-Garcia *et al.* [18] is tested against a low Morton number case, similar to that of an air-water system.

The construction of the numerical domain for the inclined pipes follows from the vertical pipe tests. The variation comes with the introduction of gravitational components in both the horizontal, y, and vertical, x, directions such that,

$$g_x = G\sin\theta, \tag{6.36}$$

$$g_y = G\cos\theta. \tag{6.37}$$

The reference time is specified as per originally stated, $t^* = 12000$, to maintain a practical number of iterations expected until convergence to a steady-state rise velocity and interface profile is reached. For convenience, the non-dimensional parameters for the test cases are re-stated in Table 6.4.

Table 6.4: Summary of non-dimensional parameters used for inclined pipe tests and the vertical Taylor bubble rise velocities previously obtained. Experimental results are highlighted by a *.

Case	Mo	Eo	Nf	Fr (lit.)	Fr (FVM)	Fr (LBM)
A	0.328	76.5	34.2	0.210	0.212	0.209
C	1.17e-4	38.6	149	0.276*	0.295	0.292
G	8.38	747	84.0	0.289*	0.299	0.301
H	8.38	181	29.0	0.199	0.216	0.206

Figure 6.11 provides a visualisation of the inclination angle effects for $\theta \in \{15, 30, \ldots, 75\}$. As the phase-field method provides a diffuse interface in simulations, it can be seen that there is a minor interaction with the walls of the pipe as the inclination approaches horizontal. To cater for this, the three phase contact interactions described by Fakhari and Bolster [120] were implemented on a stairwise approximation of the pipe wall. The details for implementing this can be found in Appendix A.1.2. It is highlighted here that other methods exist for imposing a desired contact angle, in the current approach the value of the phase field is determined geometrically. Other methods such as that by Connington and Lee [215] look to build in the free energy of the solid boundary into the free energy functional when deriving the flow model. These methods show promising results, but can require complex treatment of phase gradients. When implementing the three-phase contact dynamics a suitable contact angle needs to be specified, for an air-water contact, literature values of 22 degrees was taken in this work. Furthermore, this figure indicates the maximum propagation distance occurs at a pipe inclination angle of 45 degrees, which agrees with reports in the literature.

Figures 6.12 to 6.15 present the relationship found between angle of inclination and bubble rise velocity for the cases introduced. It can be seen here that the maximum velocity occurs at an inclination of 45 degrees for all cases. This is a result of the competing forces, namely, the drag force which reduces with lower inclination angles due to the reduction in bubble cross-sectional area and the effect of buoyancy which, as expected, increases as the pipe tends towards vertical. Figure 6.12 shows excellent agreement between the LBM findings in this study and the available range of numerical results from Lizarraga-Garcia *et al.* [196]. However, it can be observed that the correlations existing

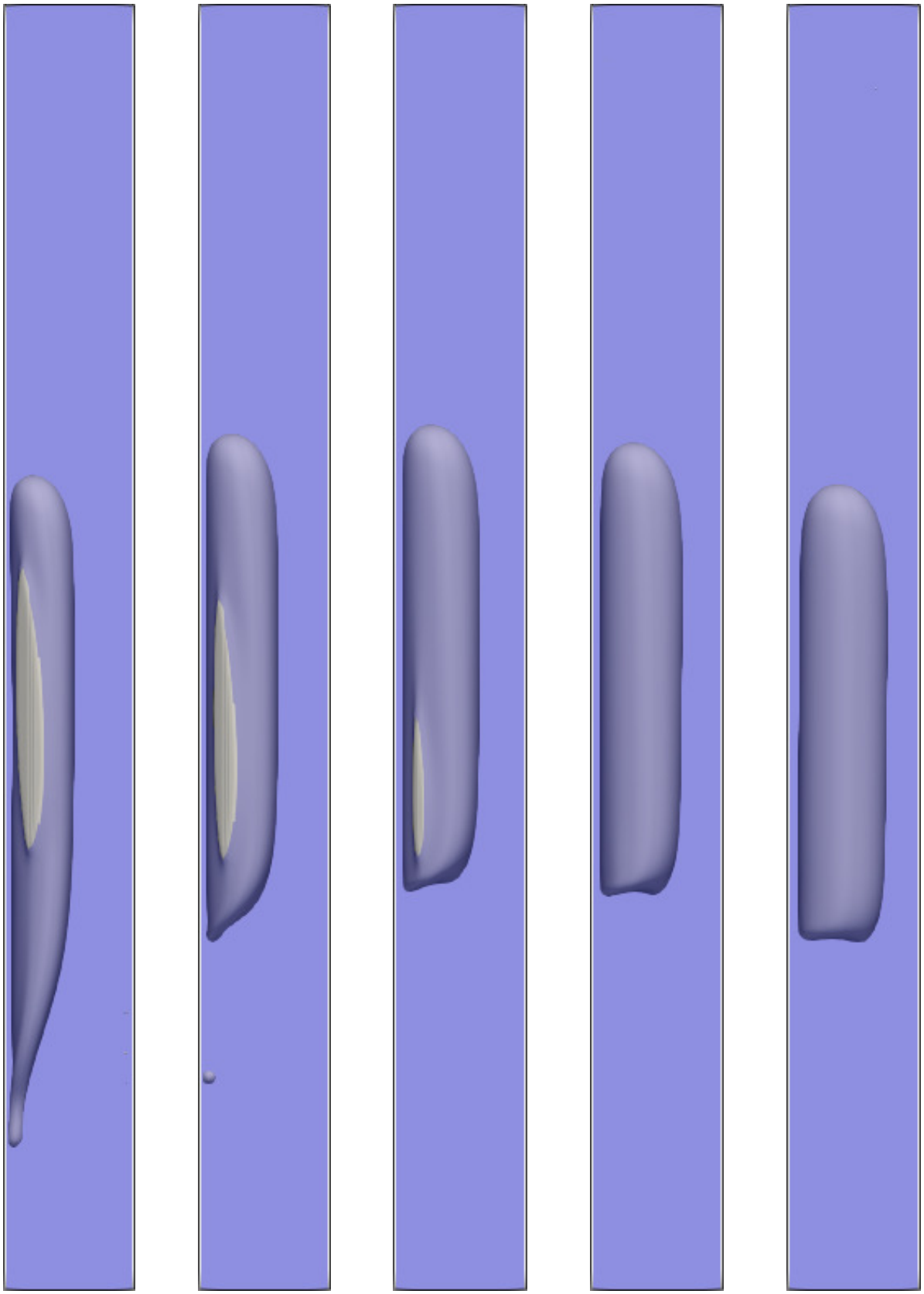

(a) $\theta = 15$ (b) $\theta = 30$ (c) $\theta = 45$ (d) $\theta = 60$ (e) $\theta = 75$

Figure 6.11: Taylor bubble profiles at $t^* = 10t_0$ with fluid parameters according to Case A (Mo=0.328, Eo=76.5) and for pipe inclination angles of (a) $\theta = 15$, (b) $\theta = 30$, (c) $\theta = 45$, (d) $\theta = 60$, (e) $\theta = 75$.

from the literature vary significantly from the numerical simulations. The method from Hasan and Kabir [213] provided the only close match with the high-fidelity simulations conducted for Case A, agreeing well for vertical and near horizontal pipe, but over-predicting the propagation speed for intermediary inclinations.

The difference between both the simulation and correlations as well as the correlations themselves is further displayed in Figure 6.13. The Hasan and Kabir [213] correlation again performs relatively well for vertical and near horizontal pipe configurations. Case C had experimental data from Shosho *et al.* [194] that agreed well with simulations from 15 degrees until vertical. However, there appears to have been additional wall interactions in the experimental case that slowed the propagation of bubbles at near (5 degrees) horizontal pipe inclinations. It is clear in this figure that the correlations for Taylor bubble propagation at intermediary pipe inclination are inadequate, deviating from both the simulated and experimental results.

The results from Case G are presented in Figure 6.14, with both experimental and correlated data to compare with. For this case, the PFLBM results agree very accurately with the experimental measurements of Jeyanchandra *et al.* [195] and the simulation results from Lizarraga-Garcia *et al.* [196]. This provides confidence in both the governing equations being resolved and the numerical method applied to do this. The final case analysed from the literature can be seen in Figure 6.15, in which the correlation of Hasan and Kabir [213] again appears the most accurate of the literature correlations tested. The same trend as previous cases is observed in which near vertical and horizontal pipe configurations are accurately determined by the correlation, but intermediary inclinations are over-predicted.

The results of inclination tests imply serious limitations and poor predictive capability of Taylor bubble velocity models. This observation agrees with the recent work of Livinus et al. [216] where correlation errors of over 20% were common, even for their proposed model. The reason for such large uncertainty when predicting the velocity of these elongated bubbles comes from two primary sources. The first of which comes down to the cost and time required to undertake an experimental study often resulting in a parameter range too narrow for correlations to be extended. The second cause can be related to the formulation of the correlation itself in which its form may not be suited for describing the physical characteristics of the Taylor bubble.

Using data such as that presented, Lizarraga-Garcia *et al.* [18] formulated a unified bubble rise velocity correlation. However, this was completed with a database primarily focused on high-viscosity oils rather than fluids such as brine, which are expected in CSG extraction. As such, the following test builds on the confidence in the PFLBM created from the previous simulations to determine the applicability of this closure to low viscosity flows. Table 6.5 provides a comparison of the simulated bubble rise velocity for a tubular pipe flow in which, $Eo = 20$, and, $Mo = 10^{-11}$, with that predicted by Lizarraga-Garcia *et al.* [18].

Figure 6.16 presents Table 6.5 in graphical form, indicating the over-prediction of rise velocities. Here, it is clear that the accuracy of the correlation deteriorates for intermediary inclination angles, as was observed with correlations compared in the higher viscosity simulations previously conducted.

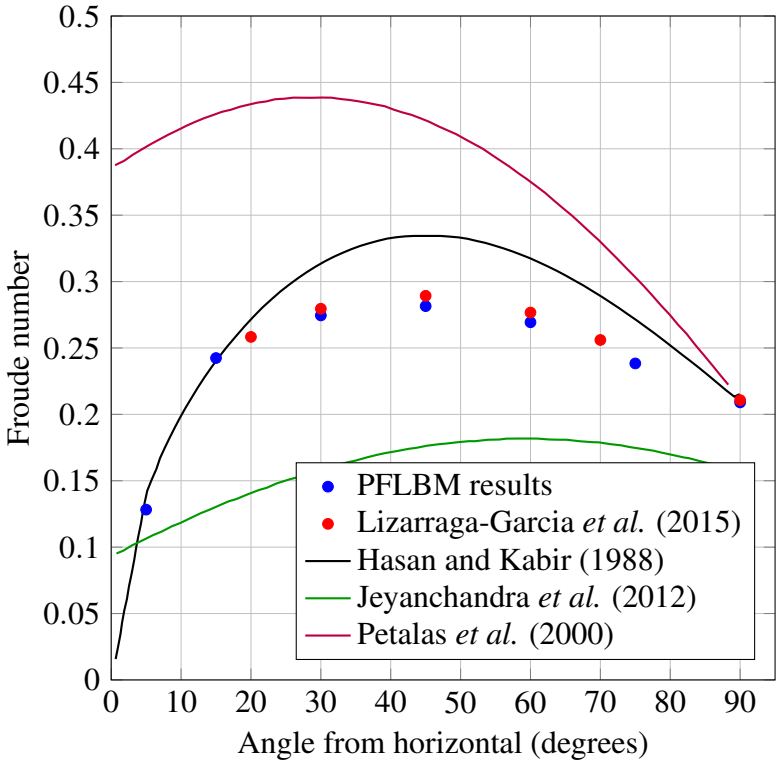

Figure 6.12: Comparison of simulated results for Case A with the numerical results of Lizarraga-Garcia *et al.* [196] and the correlations of Hasan and Kabir [213], Jeyanchandra *et al.* [195] and Petalas *et al.* [73].

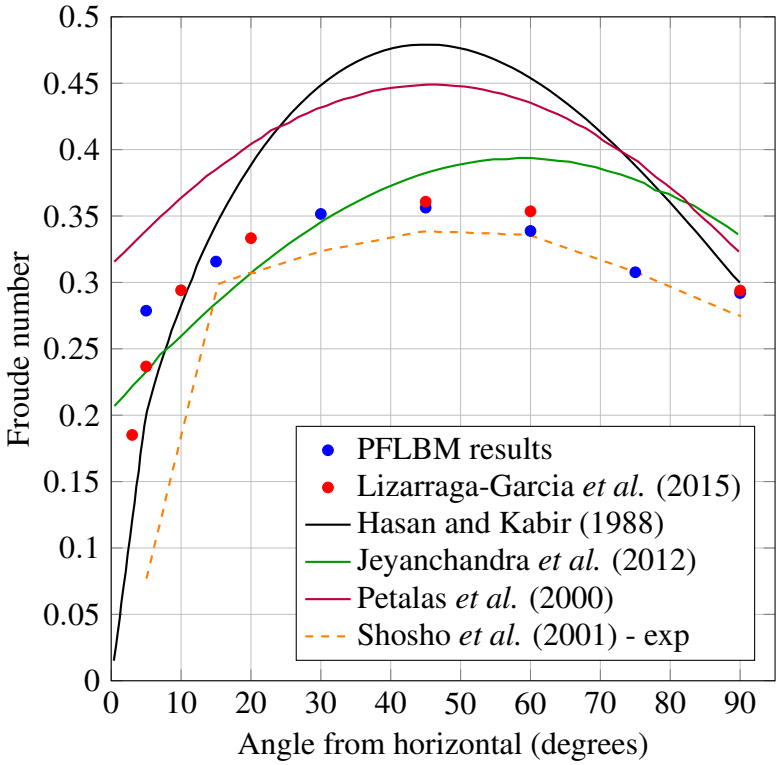

Figure 6.13: Comparison of simulated results for Case C with the numerical results of Lizarraga-Garcia *et al.* [196], the correlations of Hasan and Kabir [213], Jeyanchandra *et al.* [195] and Petalas *et al.* [73] as well as the experimental work of Shosho *et al.* [194].

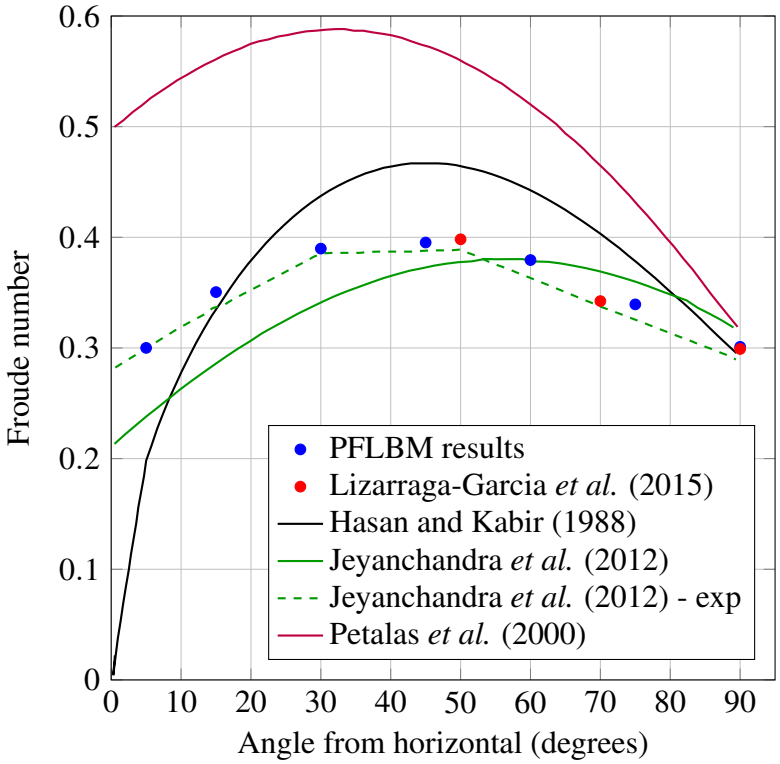

Figure 6.14: Comparison of simulated results for Case G with the numerical results of Lizarraga-Garcia *et al.* [196], the correlations of Hasan and Kabir [213], Jeyanchandra *et al.* [195] and Petalas *et al.* [73] as well as the experimental work of Jeyanchandra *et al.* [194].

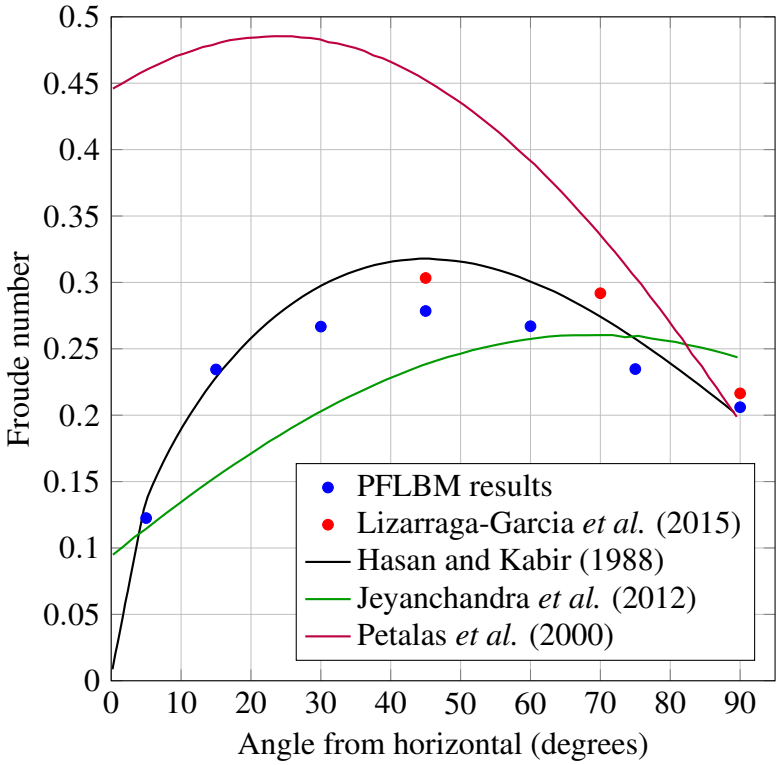

Figure 6.15: Comparison of simulated results for Case H with the numerical results of Lizarraga-Garcia *et al.* [196] and the correlations of Hasan and Kabir [213], Jeyanchandra *et al.* [195] and Petalas *et al.* [73].

Table 6.5: Measured Froude number using the phase-field LBM in comparison to the correlation proposed by Lizarraga-Garcia *et al.* [18].

Inclination Angle (θ)	Mo	Eo	Fr [18]	Fr (LBM)	Variation (%)
5	10^{-11}	20	0.2328	0.2478	6.44
15	10^{-11}	20	0.3333	0.3074	7.77
30	10^{-11}	20	0.3788	0.3255	14.07
45	10^{-11}	20	0.3941	0.3431	12.94
60	10^{-11}	20	0.3788	0.3265	13.81
75	10^{-11}	20	0.3371	0.2936	12.90
90	10^{-11}	20	0.2800	0.2740	2.14

Additionally, the bubble profiles at $t^* = 15t_0$ are presented in Figure 6.17. These differ substantially from the high viscosity case displayed in Figure 6.11, with significant shedding of small, dispersed bubbles into the wake region for higher angles of inclination. The reduction in viscous drag results in less elongation of the gas region in the axial pipe direction and provides less protection in terms of bubble interaction with the pipe walls.

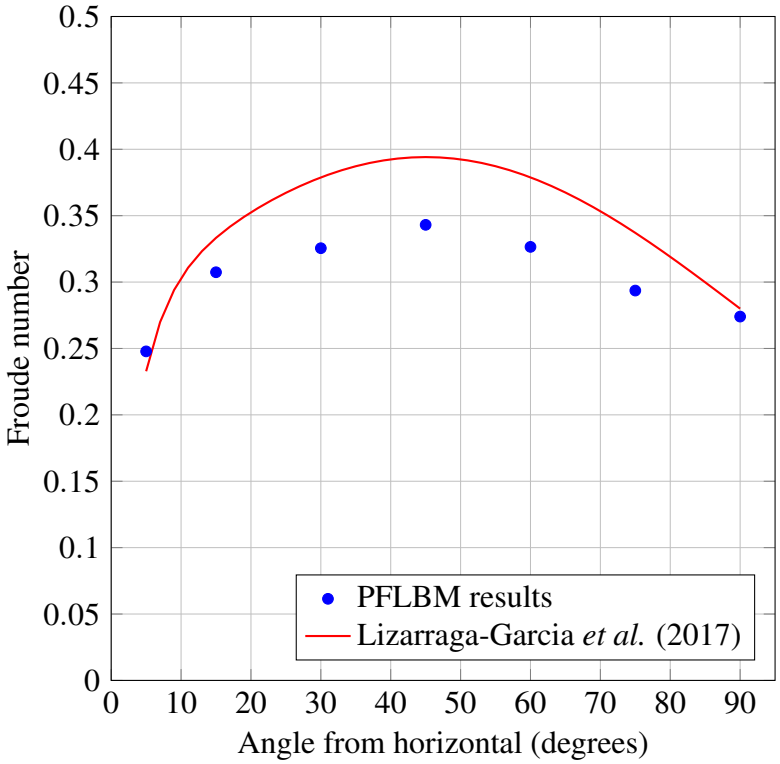

Figure 6.16: Comparison of simulated predicted bubble velocity in tubular pipes at various inclinations with the unified correlation proposed by Lizarraga-Garcia *et al.* [18].

From the simulations conducted in this study, it appears that a unified correlation applicable across not only a broad range of fluid parameters, but pipe dimensions and inclinations is yet to be formulated. However, with the model developed and simulation methodology presented, the phase-field LBM is shown to be an invaluable tool for determining the applicability of correlations for desired circumstances. Furthermore, a future direction of work with this model is apparent in modelling pipe inclination effects in tubular pipes with the potential of contributing towards the accuracy of a unified

velocity rise correlation, particularly at intermediary angles, $\theta \in \{15, \ldots, 75\}$. This is placed out the scope of work in this dissertation with interest focused on annular piping configurations.

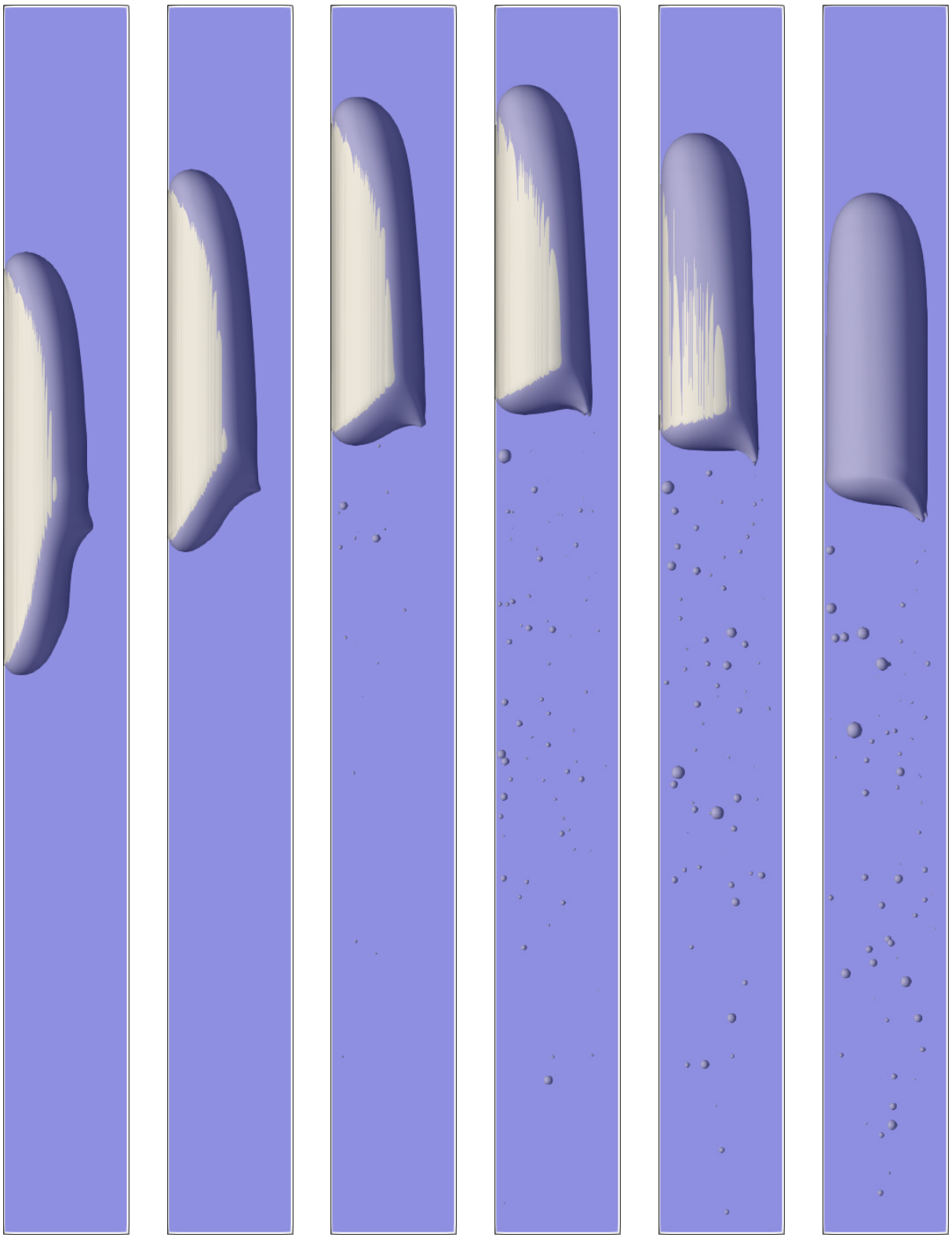

(a) $\theta = 5$ (b) $\theta = 15$ (c) $\theta = 30$ (d) $\theta = 45$ (e) $\theta = 60$ (f) $\theta = 75$

Figure 6.17: Taylor bubble profiles mimicking an air-water system in a small pipe at $t^* = 15t_0$ with Mo=10^{-11}, Eo=20 and pipe inclination angles of (a) $\theta = 5$, (b) $\theta = 15$, (c) $\theta = 30$, (d) $\theta = 45$, (e) $\theta = 60$, (e) $\theta = 75$ degrees.

6.4 Effect of flowing fluid

In practical scenarios relating to the extraction of hydrocarbons from the subsurface environment, it is expected that gas may rise through upward (co-current), downward (counter-current) as well as stagnant fluid, depending on the stage of production. Understanding how this flowing fluid alters the behaviour of Taylor bubbles is critical in predicting the dynamics associated with the slug flow regime. In general, the propagation rate of the bubble, u_{TB}, in a flowing fluid is considered to be a function of the drift velocity, u_d of an elongated bubble in a stagnant fluid and the velocity of the liquid phase, u_l,

$$u_{TB} = C_0 u_l + u_d. \tag{6.38}$$

The approach for this was first proposed by Nicklin *et al.* [201], where the coefficient, C_0, was used to capture effects associated with nonuniform flow and void concentration profiles [63, 217]. The drift velocity, u_d, of the Taylor bubble may be determined through any of the correlations previously discussed to determine the rise velocity through stagnant fluid. The introduction of this method highlighted the importance of the liquid flow in front of a Taylor bubble, with the value of $C_0 u_l$ often assumed to be equal to the maximum local velocity in this region [218]. Early in the literature, values were typically taken as $C_0 \approx 1.2$ for turbulent and $C_0 = 2$ for fully developed laminar flows. This has proved to be a reasonable engineering approximation, and is still common place in industry and research studies [63]. Polonsky *et al.* [217] showed that the value of the coefficient was a function of flow velocity presenting results where it decreased from a value of, $C_0 = 1.86$, for a liquid velocity of, $u_l = 0.87$ m/s, to $C_0 = 1.16$, for a liquid velocity of, 25.5 m/s. Additionally, Polonsky *et al.* investigated the developing behaviours of a Taylor bubble in liquid flow from which they were able to suggest physical models for understanding undeveloped slug flow.

Bendiksen [193] further tested this correlation in inclined pipes and found reasonable agreement with the previously proposed 'engineering' values for, C_0. Soon after Bendiksen [219] proposed correlations for this coefficient based on potential flow theory and vertical pipe flow experiments,

$$C_0 = \begin{cases} 2.29\left(1 - \frac{20}{Eo}(1 - e^{-0.0125Eo})\right), & \text{laminar flow and } Eo > 40, \\ \frac{\log Re_l + 0.309}{\log Re_l - 0.743}\left(1 - \frac{2}{Eo}(3 - e^{-0.025Eo}\log Re_l)\right), & \text{turbulent flow.} \end{cases} \tag{6.39}$$

Here, it can be seen that the liquid Reynolds number, $\rho_l u_l D/\mu_l$, and the Eötvös number are used to approximate the effects of liquid motion and surface tension. Developments on this are still evident today with additional terms being introduced, for example, to cater for varying fluid viscosity ratios [220]. Around a similar time to the work conducted by Bendiksen, Fréchou [221] proposed a correlation for upward liquid flow based on the liquid Reynolds number only,

$$C_0 = 1.2 + \frac{0.8}{1 + 10^{-8} Re_l^{2.55}}. \tag{6.40}$$

Tomiyama *et al.* [222] used air-water experiments to correlate the coefficient to the Eötvös number in laminar flows and to the liquid Reynolds number in the transitional/turbulent regime,

$$C_0 = \begin{cases} 1.5 - 0.5e^{-4\cdot 10^{-4} Eo^{2.36}}, & Re_l < 2000, \\ 1.18 + 0.32e^{1.7\cdot 10^{-3}(2300 - Re_l)}, & Re_l > 2300. \end{cases} \tag{6.41}$$

With the variance in behaviour observed from the onset of turbulence, it is critical to understand where this transition point occurs. Pinto *et al.* [223] conducted an experimental study to this end in tubular pipes with internal diameters of 22 mm, 32 mm and 52 mm. The authors reported that the transition towards turbulence initiated at a liquid Reynolds number of 2100, however, the value of the coefficient, C_0, varied prior to this indicating dependence on additional dimensionless parameters even in the laminar regime. Based on their experimental work, Pinto *et al.* [223] were able to establish a correlation for rise velocity as a function of the liquid Reynolds number, the ratio of liquid to Taylor bubble drift velocity and the Weber number defined as, $We_{u_d} = \rho_l D u_d^2/\sigma$. To present their correlation, the parameter,

$$c_1 = Re_l We_{u_d}^{0.21} \left(\frac{u_l}{u_d}\right)^{0.28}, \tag{6.42}$$

is introduced such that,

$$C_0 = \begin{cases} 2.0 \pm 0.1, & c_1 < 1000, \\ 2.08 - 1.38 \cdot 10^{-4} c_1, & 1000 \leq c_1 < 6000, \\ 1.2 \pm 0.1, & c_1 > 6000. \end{cases} \tag{6.43}$$

In addition to combining potential flow theory and experimental findings to formulate these correlations, recent studies have seen the use of numerical simulations to verify these or at least assess their bounds of validity. Taha and Cui [97] used a 2D axisymmetric volume of fluid formulation and fully 3D simulations to analyse the behaviour of air and water inside a 20 mm diameter pipe with stagnant and flowing fluids. They obtained favourable comparisons with published experimental results for the velocity of the bubble and the local wall shear. Lu and Prosperetti [224] also performed 2D simulations with a volume of fluid technique finding reasonable agreement with measurable quantities available in the experimental literature. Lizarraga-Garcia *et al.* [18] performed a numerical survey with fully 3D simulations using the level-set method to determine interfacial interactions. They concluded that additional work is still required to determine the effect of pipe inclination angle and Eötvös number on the coefficient, C_0. In this section, the flowing fluid configuration is used to validate the performance of velocity boundaries in the proposed phase-field LBM as well as to assess the selection of C_0 in co- and counter-current scenarios.

6.4.1 Simulation details

In order to simulate co- and counter-current flows, a similar methodology to Chapter 4 is used. Therefore, boundary conditions need to be specified to allow for the cylindrical pipe walls to propagate at the expected rise velocity for the instantiated Taylor bubble. The unknown lattice populations incoming to the pipe wall vary with azimuthal position, and so a generalised boundary condition that caters for an arbitrary wall normal is required. By assessing any motion of the Taylor bubble in relation to the moving reference frame, the value of C_0 can be determined.

Velocity boundaries for arbitrary normal directions

For a defined velocity, $\mathbf{u}$, on a boundary located at $\mathbf{x}_b$, the probability distribution functions for the velocity-based LBM must satisfy momentum conservation, namely,

$$\sum_i g_i(\mathbf{x}_b)\mathbf{c}_i = \sum_i g_i^{eq}(\mathbf{x}_b)\mathbf{c}_i = \mathbf{u}. \tag{6.44}$$

In addition to this, taking the normal approach of performing the bounce-back scheme for the nonequilibrium component of the distribution functions gives,

$$g_i(\mathbf{x}_b) - g_i^{eq}(\mathbf{x}_b) = g_{\bar{i}}(\mathbf{x}_b) - g_{\bar{i}}^{eq}(\mathbf{x}_b), \tag{6.45}$$

where $\bar{i}$ indicates the opposing lattice direction to i. This satisfies conservation of momentum in the normal direction, however, an excess of momentum can be observed tangentially along the boundary. This is where the set of tangential directions are identified through the known normal, $\Pi = \{i|\mathbf{c}_i \cdot \mathbf{n} = 0\}$. Therefore, the excess momentum can be found through,

$$\mathbf{M}_g(\mathbf{x}_b) = \sum_{i\in\Pi} \mathbf{c}_i \left[g_i(\mathbf{x}_b) - g_i^{eq}(\mathbf{x}_b)\right]. \tag{6.46}$$

This is then distributed over the N unknown distributions as discussed by Zu and He [145], but proposed as far back as Zou and He [137],

$$g_i(\mathbf{x}_b) = g_{\bar{i}}(\mathbf{x}_b) + \left[g_i^{eq}(\mathbf{x}_b) - g_{\bar{i}}^{eq}(\mathbf{x}_b)\right] - \frac{1}{Nc^2}\mathbf{c}_i \cdot \mathbf{M}_g(\mathbf{x}_b). \tag{6.47}$$

A similar methodology can be applied to the distribution used to resolve the Allen-Cahn equation. Here, the moving boundary generally has a known value of phase, ϕ, that is being applied and as such, the distribution functions should satisfy mass conservation [145],

$$\sum_i h_i(\mathbf{x}_b) = \sum_i h_i^{eq}(\mathbf{x}_b) = \phi. \tag{6.48}$$

The nonequilibrium component of the distribution can be written as,

$$h_i(\mathbf{x}_b) - h_i^{eq}(\mathbf{x}_b) = -\left[h_{\bar{i}}(\mathbf{x}_b) - h_{\bar{i}}^{eq}(\mathbf{x}_b)\right], \tag{6.49}$$

which results in an excess of density according to [145],

$$\mathrm{M}_h(\mathbf{x}_b) = \sum_{i\in\Pi} \left[h_i(\mathbf{x}_b) - h_i^{eq}(\mathbf{x}_b)\right]. \tag{6.50}$$

This is distributed over the unknown distributions allowing the boundary to be resolved,

$$h_i(\mathbf{x}_b) = \begin{cases} h_i(\mathbf{x}_b) - \left[h_{\bar{i}}(\mathbf{x}_b) - h_{\bar{i}}^{eq}(\mathbf{x}_b)\right], & \text{if } \mathbf{c}_i \cdot \mathbf{n} = 0 \\ h_i(\mathbf{x}_b) - \left[h_{\bar{i}}(\mathbf{x}_b) - h_{\bar{i}}^{eq}(\mathbf{x}_b)\right] - \frac{\mathrm{M}_h(\mathbf{x}_b)}{N}, & \text{if } \mathbf{c}_i \cdot \mathbf{n} \neq 0. \end{cases} \tag{6.51}$$

Therefore, it can be seen from the above formulation, that if the normal to the boundary is known, conditions can be specified to determine the unknown distribution functions required to specify a desired velocity and phase. This is used for the cylindrical pipe walls as well as for the inlet and outlet of the domain in this section. It is noted here that three phase interactions are not expected to be significant, but if required, the method from Fakhari *et al.* [120] is used to determine the value of phase to be set.

Case configuration and simulation setup

To validate that the moving reference frame configuration can capture the Taylor bubble rise behaviour in stagnant, co- and counter-current regimes, two cases are taken from Lizarraga-Garcia [63]. In addition to this, a third case is conducted with dimensionless quantities progressing towards fluids relevant in the extraction of natural gas from coal seams. The important quantities for these cases are specified in Table 6.6 along with the predicted Taylor bubble drift velocity from Equation 6.14 and that found with the phase-field LBM in the moving reference frame. With the first two cases providing support for the model accuracy, the third will be used to assess the validity of the closure relations previously discussed and determine the variation in hydrodynamic response between co- and counter-current configurations.

Table 6.6: Summary of non-dimensional parameters used for inclined pipe tests and the vertical Taylor bubble rise velocities determined with the phase-field LBM and the correlation proposed by Viana *et al.* [207].

Case	Mo	Eo	Nf	Fr_d Eqn. 6.14	Fr_d LBM	Variation (%)
A	7.1e-2	29	24	0.1341	0.1326	1.1523
B	7.1e-2	240	120	0.3086	0.3079	0.2422
C	1.0e-5	20	168	0.2605	0.2512	3.5825

In order to determine the empirical coefficient, C_0, for the flow cases described by Table 6.6 the domain constructed for the stagnant fluid simulations is transformed into a moving reference frame. Therefore, the domain resolution is specified as $\{x \times y \times z\} = \{10D \times D \times D\}$, where $D = 128$. At the centre of this domain, a cylindrical, low density region is initialised with a length of $3D$ and diameter of $0.75D$. The initial Taylor bubble shape is finalised with the addition of a hemisphere on the front of the cylinder as indicated in Figure 6.18. The moving reference frame is created through the velocity boundary condition previously discussed. It is used to set all boundary velocities to oppose the drift velocity of the Taylor bubble, $-u_d$. Therefore, the buoyancy force acts to propagate the bubble in the positive x-direction, but is counteracted by the imposed velocity at the boundary walls. To incorporate co- and counter-current flow into this setup, a fully developed pipe flow condition is superimposed at the top and bottom of the domain,

$$u_x(0,y,z) = u_x(10D,y,z) = u_d + 2u_l(1 - \left[(y-R)^2 + (z-R)^2\right]/R^2), \tag{6.52}$$

where $R = 0.5D$ is the radius of the pipe.

To assess the performance of the phase-field LBM for flowing fluid simulations, liquid Reynolds numbers were tested for $Re_l = \{-10,-1,0,1,10\}$. The motion of the bubble could then be used to determine C_0 in comparison to existing correlations from the literature, namely, Equations 6.39 6.40, 6.41 and 6.43 by Bendiksen [219], Fréchou [221], Tomiyama *et al.* [222] and Pinto *et al.* [223], respectively.

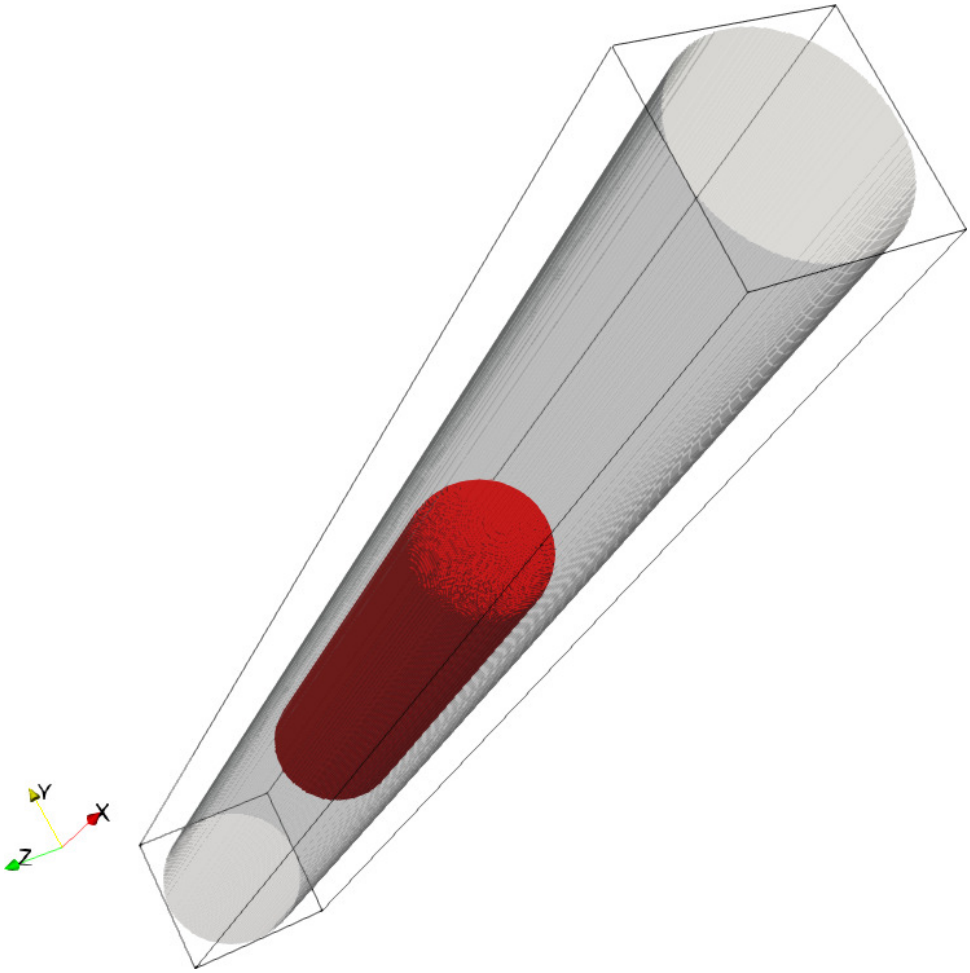

Figure 6.18: The initial configuration for the Taylor bubble simulations with a moving reference frame where the red contour indicates the liquid-gas interface and the grey contour shows the liquid-solid interface.

6.4.2 Results

Table 6.7 provides the coefficients determined using the proposed multiphase LBM in a moving reference frame in comparison to the correlations discussed in the previous section. Here, it is evident that the correlations predict a constant value of, C_0, for each case. This was not found to be consistent with the simulation results in which the value of the coefficient decreased as the absolute rate of liquid flow increased. In the work of Lizarraga-Garcia [63], it was evident that the Taylor bubble Froude numbers were not a linear function of the liquid velocity, indicating that $C_0 = C_0(Eo, Re_l)$ at the least. This is observed in the current results and formulating an improved coefficient based on simulation results highlights a potential avenue for future work using the model proposed in this dissertation.

When considering the value of the coefficient chosen, it is important to understand the effect it has on the actual rise velocity of the Taylor bubble. Figure 6.19 shows the measured Froude number for the simulated bubbles in comparison to the correlations previously introduced. The formulation by Bendiksen [219] proves very effective in predicting the bubble behaviour, even considering the limitation on Eötvös number is not strictly met. This appears to be the case as the coefficient determined matches relatively well at higher fluid velocities, where its effect compared to the drift velocity of the

Table 6.7: The values obtained for the distribution parameter, C_0, using the phase-field LBM in comparison to existing correlations by Bendiksen [219], Fréchou [221], Tomiyama *et al.* [222] and Pinto *et al.* [223].

Case	Re_l	C_0 Eqn. 6.39	C_0 Eqn. 6.40	C_0 Eqn. 6.41	C_0 Eqn. 6.43	C_0 LBM
A	-10	1.8098	n/a	1.3386	n/a	1.8500
A	-1	1.8098	n/a	1.3386	n/a	2.2285
A	1	1.8098	2.0000	1.3386	2.0 ± 0.1	2.0253
A	10	1.8098	2.0000	1.3386	2.0 ± 0.1	1.7019
B	-10	2.1087	n/a	1.5000	n/a	1.9487
B	-1	2.1087	n/a	1.5000	n/a	2.0544
B	1	2.1087	2.0000	1.5000	2.0 ± 0.1	1.9829
B	10	2.1087	2.0000	1.5000	2.0 ± 0.1	1.6206
C	-10	1.7835	n/a	1.1876	n/a	1.4213
C	-1	1.7835	n/a	1.1876	n/a	1.4222
C	1	1.7835	2.0000	1.1876	2.0 ± 0.1	1.4125
C	10	1.7835	2.0000	1.1876	2.0 ± 0.1	1.4121

Taylor bubble is more apparent. This results in the deviation at low flow rates to have a negligible impact on predicted rise velocity. An additional point of note from Figure 6.19 is the breakdown of bubble rise at a liquid Reynolds number of approximately two, where the entrainment of the Taylor bubble is observed. Here, the Taylor bubble no long rises but is entrapped by the moving liquid phase creating a co-current downward flow.

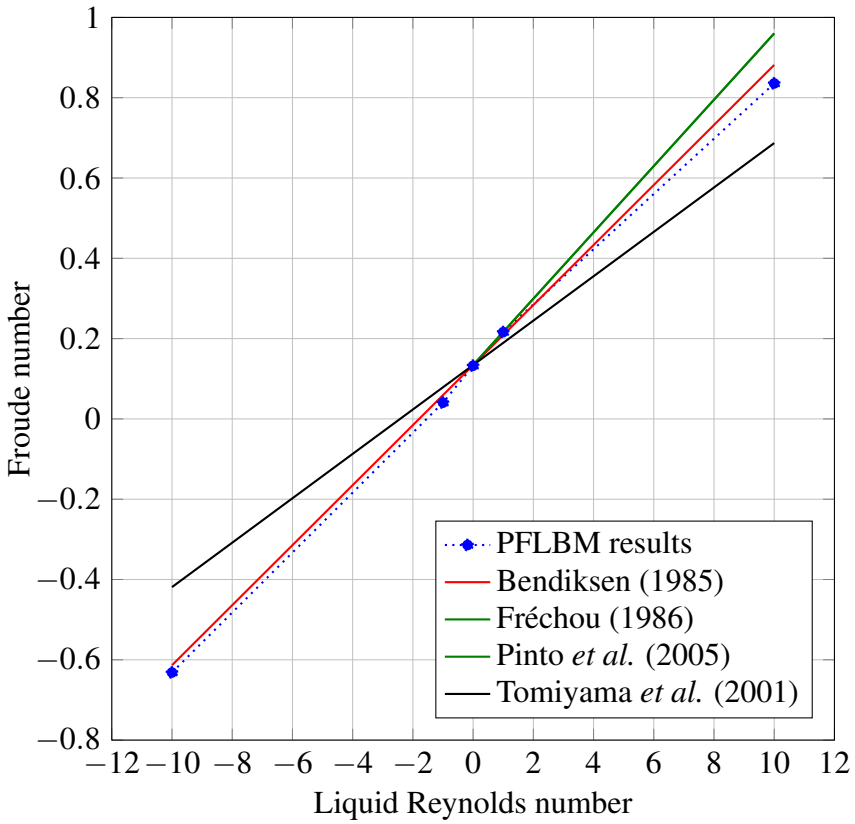

Figure 6.19: Effect of liquid motion on the bubble rise velocity with fluid parameters from Case A. Note that in this regime, the correlations of Fréchou (1986) and Pinto *et al.* (2005) are equivalent.

Increasing the Eötvös number for Case B results in a deterioration of correlation accuracy when compared with the simulated results. Figure 6.20 shows the decrease in linearity of the bubble Froude number versus liquid flow as the surface tension effects are reduced. In this figure, the gradient of the simulated velocity varies quite significantly between co- and counter-current flow. The results for co-current matching reasonably with the correlation of Tomiyama *et al.* [222] and counter-current with that of Bendiksen [219], however, further testing would be required to verify this conclusion. In Case B, the effect of surface tension is reduced as a result of the higher Eötvös number which results in elongation of the bubble and a larger annular film through which the liquid can propagate, without reversing the bubble rise direction.

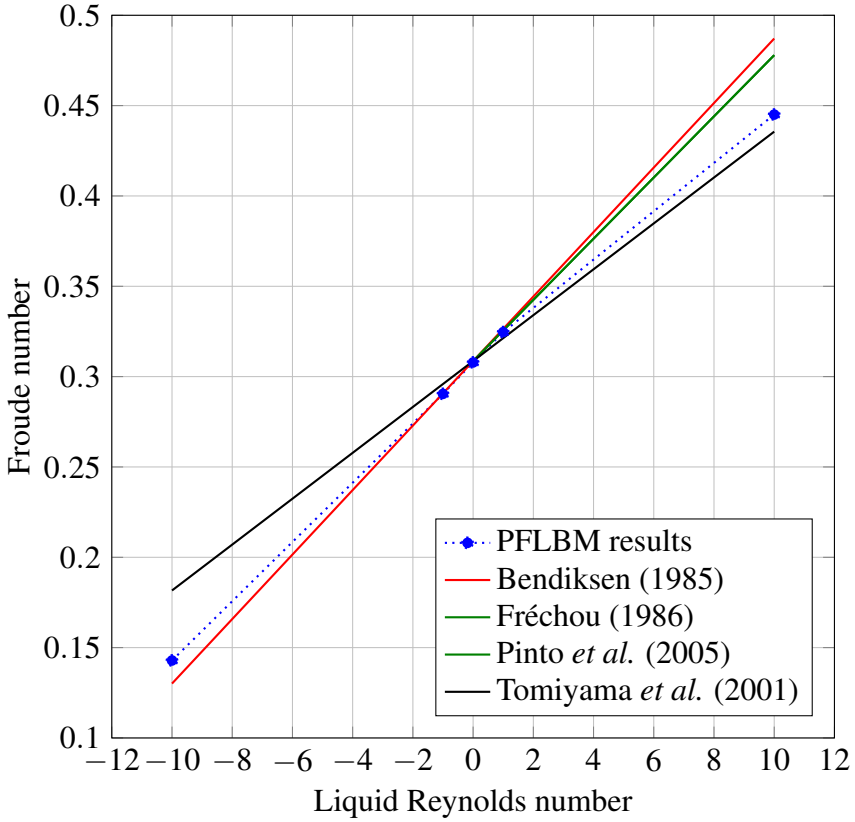

Figure 6.20: Effect of liquid motion on the bubble rise velocity with fluid parameters from Case B. Note that in this regime, the correlations of Fréchou (1986) and Pinto *et al.* (2005) are equivalent.

The rise velocity results for the simulations of Case C are displayed in Figure 6.21. The purpose of this case is to observe the effects of decreasing the Mo number in the tubular pipe configuration when liquid flow is present. Here, the value of the empirical coefficient, C_0, is observed to be almost independent of liquid velocity. This is expected from the correlations proposed in the literature, however, understanding why this is observed here and not for Case A and B is important. Considering the physical meaning of a lower Morton number, namely a lower liquid viscosity for this configuration, one can reason the independence of C_0. The rise velocity of the bubble is effectively determined from a balance of the viscous drag and buoyancy forces, as such, the lower viscosity reduces the influence of the liquid on the Taylor bubble and leads towards an inertially dominated system. The inverse viscosity number, N_f, appears to be correlated with this, taking into account effects of both viscosity

and surface tension. This is further observed by the lower value of C_0 obtained for increasing N_f in all simulations within this section. For Case C in particular, the empirical coefficient did not match well with correlations, determined to be in between the predictions of Bendiksen [219] and Tomiyama *et al.* [222].

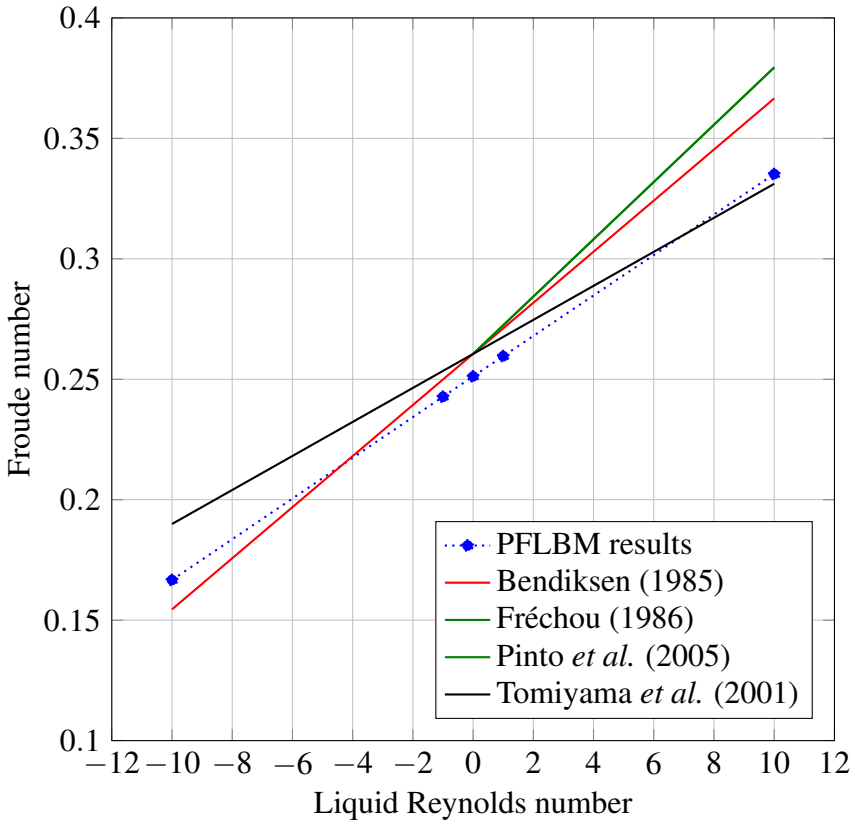

Figure 6.21: Effect of liquid motion on the bubble rise velocity with fluid parameters from Case C. Note that in this regime, the correlations of Fréchou (1986) and Pinto *et al.* (2005) are equivalent.

In this section, Taylor bubbles have been simulated in stagnant, co- and counter-current flow for various dimensionless parameters. From these simulations, it is clear that further work is required for a unified relation between liquid flow and Taylor bubble rise for both co- and counter-current configurations. The correlation by Bendiksen [219] performed the best for a low inverse viscosity number, but deteriorated in accuracy as the flow became more inertially dominated. However, in this regime, the results seemed to be bounded by the predictions of Bendiksen [219] and Tomiyama *et al.* [222]. The simulations performed here provide a methodology for which one could build a database of relations between the relevant dimensionless parameters and the empirical coefficient, C_0, in order to determine a universal model for the rise of an elongated bubble in stagnant and flowing liquid.

6.5 Conclusions

In this chapter, the proposed phase-field LBM was used to investigate the behaviour of elongated bubbles within tubular pipes for a range of different configurations. This highlighted numerous shortcomings in the current literature, with limited accuracy observed for existing correlations when

predicting the rise velocity of Taylor bubbles for intermediate pipe inclinations as well as when there is bulk liquid motion. Initially, fluids with relatively high Morton numbers were investigated so as to compare to previous works by the likes of Lizarraga-Garcia *et al.* [18], further developing confidence in the developed model. From here the parameter range was increased to capture liquid-gas systems that could be expected in the extraction of natural gas from coal seams. Here, the stability of the phase-field LBM was tested and the limit of the current implementation reached. It is believed that coupling the method with an adaptive mesh refinement algorithm would significantly extend the capability of the model for flows that can be practically simulated on modern architectures. A further possibility for improving the model stability is to investigate the use of recent LBM collision operators, for example, using cascaded, cumulant or entropic relaxation. Having analysed Taylor bubble flow for a range of fluid properties, the piping configuration was tested through an imposed angle of inclination. These tests indicated the benefits of numerical modelling to investigate scenarios that would present design issues (e.g. spatial and financial requirements) for experimental studies. Limited applicability was found for correlations describing the dynamics of a Taylor bubble in pipes with intermediary inclination angles, however, accurate predictions were observed in near vertical and horizontal systems. In coal seam gas extraction, typically the bulk liquid phase is also extracted from the wellbore creating co- or counter-current liquid-gas flows at various stages of a well's life cycle. As such, understanding the effect of a flowing liquid phase on a Taylor bubble is essential for determining the pressure gradient and void fraction in the slug flow regime. Testing of various liquid flow rates indicated inaccuracies in the values currently chosen for the empirical coefficient, C_0. The results of simulations performed show dependence of C_0 on the liquid flow rate at low inverse viscosity numbers. The simulation of more cases is recommended to extract a quantitative relation for C_0 to ensure accurate prediction of bubble behaviours. Additionally, the work in this chapter validated the phase-field model for complex, practical flows and the implementation of velocity wall, inlet and outlet boundary conditions. The lessons learnt in regards to stability and the model developments made are taken into the following chapter in which annular piping configurations are studied.

Part of the following publication has been incorporated as Chapter 7.

1. [2] **T. Mitchell**, C. Leonardi, M. Firouzi, Towards closure relations for the rise velocity of Taylor bubbles in annular piping using phase-field lattice Boltzmann techniques, *21st Australasian Fluid Mechanics Conference*, Adelaide, Australia, 10-13 December, 2018.

Contributor	Statement of contribution	%
Travis Mitchell	writing of text	85
	proof-reading	50
	theoretical derivations	95
	numerical calculations	100
	preparation of figures	100
	initial concept	90

Chapter 7

Taylor Bubble Dynamics in Annular Piping

"An approximate answer to the right problem is worth a good deal more than an exact answer to an approximate problem."
John Tukey

Following on from Chapter 6, in which the dynamics of elongated bubbles in tubular pipes was investigated, the effect of annular piping configurations is analysed. Applications for this can be found in numerous areas from double pipe heat exchangers to nuclear reactors with the presence of catalyst rods creating an annular flow condition. However, the primary motivation for this work comes from the extraction techniques associated with coal seam gas (CSG). As previously discussed, the wellbore designed to transport fluids from the reservoir to the surface uses an annular configuration such that water can be removed through the central tubing string to alleviate reservoir pressure at the early stages of production. Additionally, the use of artificial lifting equipment may be required at later stages of a well's life, namely, when the energy of the reservoir is insufficient to facilitate fluid flow to the surface.

Due to the unconventional well configuration and operation, various flow conditions from gas flow through a stagnant liquid column to co- and counter-current liquid-gas flow can be expected in the production annulus. In addition to this, it is rare for CSG wells to be drilled completely vertical, thus, an understanding of how pipe inclination can alter the associated fluid dynamics is also important. A rich array of fluid behaviours can be observed in multiphase flows through annular conduits that are not apparent in the tubular analogue. For example, Taylor bubbles that are characteristic of the slug flow regime, evolve asymmetrically about the cylindrical insert forming an open sectorial wrap. The nose of the bubble in this form takes on an ellipsoidal shape, unlike the spherical cap seen in a tubular pipe for a fully developed Taylor bubble.

In this chapter, the focus is again placed on the slug flow regime with a detailed analysis of annular Taylor bubbles. This starts with a review of previous work conducted in the literature. Following from this, the experimental cases investigated by Das *et al.* [225] are reproduced with the phase-field LBM (PFLBM). With confidence that the expected annular behaviour can be naturally captured in the

simulations, the effect of pipe inclination is studied. Finally, liquid flow is introduced into the annular geometry to assess if existing rise velocity correlations are valid for conditions expected in CSG wells.

7.1 Annular Taylor bubbles

In comparison to the body of literature available on Taylor bubbles in tubular conduits, research into the dynamics associated with flow in an annulus is limited [226, 227]. The primary variation between the two flow confinements comes from the shape of the bubble nose that develops and the breakdown of symmetry observed in the annular configuration. As was discussed in Chapter 6, a Taylor bubble in a tube has an almost hemispherical cap region which leads to a liquid film that continues at a constant thickness around a cylindrical gas volume. In comparison, the nose of an annular Taylor bubble is elliptic when the major axis is orientated vertically and progresses into a region of inner and outer liquid films. Additionally, the symmetry of the bubble is lost with an incomplete wrapping of the central pipe creating a liquid bridge through which fluid is accelerated into the wake region. Figure 7.1 indicates the variation of the commonly observed topology of Taylor bubbles in a tubular versus annular pipe geometry. Here it can be seen that the cross section of a tubular bubble is broken into two regions, namely the Taylor bubble and the liquid film, whereas for the annular pipe, Das *et al.* [225] defined four regions in an attempt to understand the bubble's dynamics.

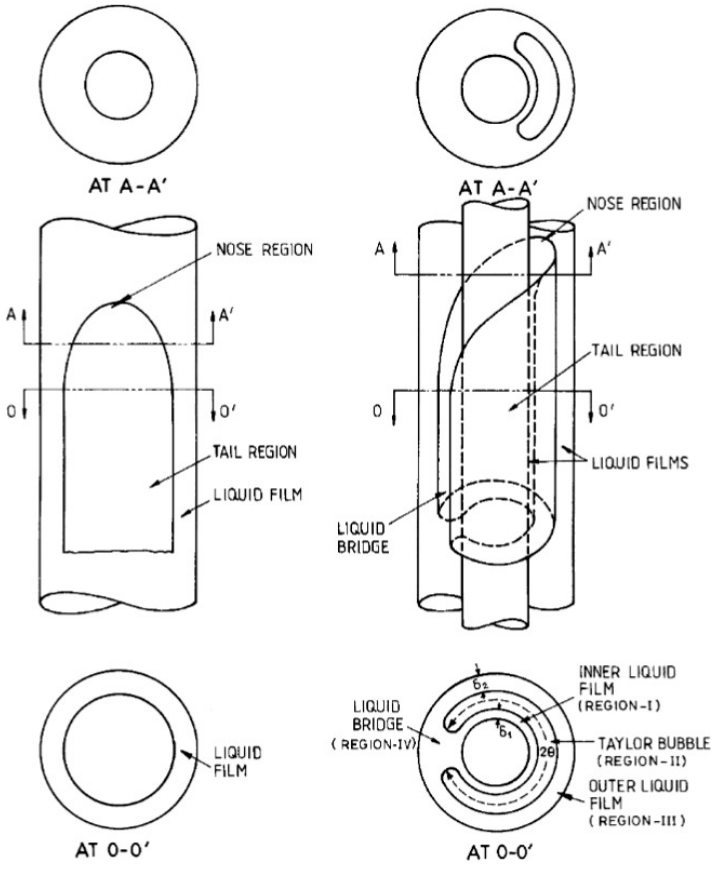

Figure 7.1: Schematic of a tubular Taylor bubble compared with one rising through a concentric annular configuration. This image has been reproduced from Das *et al.* [225]

In the axial direction, the bubble is differentiated into the nose region in which the thickness of the surrounding fluid varies, and the tail region where it has a constant thickness. As the liquid film expands past the tail of the bubble, it creates a vortex which can cause the dissociation of small bubbles into the liquid slug. According to Das *et al.* [225] these bubbles have negligible impact on the macroscale rise behaviour of the Taylor bubble itself. The definition of the nose region in the annular bubble is slightly more complex with the need to define the thickness of the inner film, δ_1, and the outer, δ_2, in addition to the wrap angle of the inner pipe, 2θ. In the nose region, these parameters are all functions of the axial distance from the bubble tip, whereas they remain constant through the tail region. This asymmetric shape caused by the incomplete wrapping is a unique feature of bubbles rising through annular configurations which is not evident when a bubble rises either in a tubular pipe or encompasses a tubular pipe in an infinite pool. Previous researchers have explained this by picturing the channel flow that would be formed by cutting the cross-section of the annulus and opening it. This channel would have two parallel walls with lengths equal to the circumference of the inner and outer tubes and a thickness equal to the size of the annular gap [225, 228]. If a large gas bubble was then situated in this channel, it would evolve with liquid films about all sides due to the surface tension at the walls. When transforming this back to a circular restriction, the liquid film on the thinner sides could be seen to coalesce forming the liquid bridge that restricts the full closure of the annular wrap. Due to the potential flow techniques employed in the early stages of Taylor bubble analysis, understanding the shape and governing forces in these different bubble regions became critical to the analysis. A limited number of studies look to investigate this problem in detail, with recent investigations by the likes of Rohilla and Das [227], finding novel conclusions about the nature of the annular Taylor bubble shape. From the previous chapter, it is clear that high resolution data is obtainable with the proposed PFLBM, and as such the aim of this chapter is to demonstrate the capability of the model and present a methodology for which the behaviour of Taylor bubbles can be further understood.

7.2 Propagation in a stagnant fluid

Griffith [229] presented one of the earliest investigations into the dynamics of bubbles inside an annulus in order to predict boiling behaviours in heated conduits. In their work, a velocity correlation was proposed in which the inner diameter of the outside pipe, D_2, was used as the characteristic length,

$$u_{TB} = K\sqrt{gD_2}\,, \tag{7.1}$$

and the tuning parameter, $K = K(D_1/D_2)$, was taken as a weak function of the inner pipe, D_1, to outer pipe diameter ratio. Continuing on from the work of Griffith, Sadatomi *et al.* [230] studied liquid-gas flows in conduits with various cross-sectional shapes. When looking at the slug flow regime, they recognised the dependence of the Taylor bubble rise on the periphery diameter, $D_1 + D_2$. Then matching this with their own data and that of Griffith [229] obtained,

$$u_{TB} = 0.345\sqrt{g(D_1 + D_2)}\,. \tag{7.2}$$

This finding was later supported by the work of Caetano *et al.* [60, 61]. Caetano's group additionally investigated the effect of eccentricity and concluded that the maximum velocity was observed in a concentric annulus. This correlation has seen application in mechanistic models for counter-current annular flow, such as that proposed by Firouzi *et al.* [16].

Barnea and Shemer [231] took a different approach assuming the Taylor bubble to be an open annular ring with negligible film thickness, and then relating the characteristic dimension to the curvature of the cap bubble obtained,

$$u_{TB} = K\sqrt{gD_e}\,, \tag{7.3}$$

$$D_e = \frac{D_2}{4}\left((\pi+1)+(\pi-1)\frac{D_1}{D_2}\right). \tag{7.4}$$

Hasan and Kabir [62] used the data of Barnea and Shemer along with the theory proposed by Griffith to formulate an expression of their own. They found K to be weakly related to the ratio of pipe diameters through,

$$u_{TB} = (0.345 + 0.1D_1/D_2)\sqrt{gD_2}\,. \tag{7.5}$$

Later, Das *et al.* [225] produced a detailed study on the dynamics of Taylor bubbles in air-water flow for a range of annular gap sizes. They were able to determine correction terms for small, $D_2 \leq 0.0254$ m, and large, $D_2 \geq 0.247$ m, pipe configurations, with which accurate predictions were obtained for their own and existing experimental data in the literature. From this study, the rise velocity of a Taylor bubble in pipe sizing applicable to natural gas wells can be predicted as,

$$u_{TB} = \begin{cases} u_{TB} = 0.322 \times 0.765\sqrt{g(D_1+D_2)}\,, & D_2 \leq 0.0254 \text{ m} \\ u_{TB} = 0.323\sqrt{g(D_1+D_2)}\,, & 0.0254 \text{ m} < D_2 < 0.247 \text{ m}. \end{cases} \tag{7.6}$$

This correlation was further validated by Agarwal *et al.* [228], where it was used to make conclusions about the practicality of extending the analysis from a circular annulus to a square shaped conduit. Rohilla and Das [227] more recently made use of it when analysing the effects of eccentricity as well as investigating the transition from a tubular to annular Taylor bubble as it passed over a cylindrical insert. These few findings represent the main body of research existing for annular Taylor bubbles, "despite being a widely observed phenomenon" [227]. To further develop understanding of annular Taylor bubbles, the experimental test cases from Das *et al.* [225] were recreated with computational fluid dynamics. Following on from the experimental validation, pipe inclination and liquid flow were introduced into the system to observe the effects on the annular Taylor bubble. This investigation provides a *proof-of-concept* study from which the methodology presented could be extended to formulate a unified bubble rise model.

7.2.1 Simulation details

Three test cases were initially simulated with the PFLBM in order to compare to both experimental results and correlations existing in the literature. The relevant dimensionless numbers and physical

annuli dimensions are presented in Table 7.1, along with the measured experimental Froude number and correlations from Das *et al.* [225], Sadatomi *et al.* [230] and Hasan and Kabir [62]. It is noted here that the correlation of Das *et al.* [225] was tuned using these experimental works and as such, it is not a surprise that it provides the most accurate prediction of rise velocity.

With the change in piping configuration, the definitions of the relevant dimensionless parameters are adjusted slightly from Chapter 6. Here, the reference time, Eötvös, Morton, inverse viscosity and Froude numbers are defined as,

$$t^* = \sqrt{\frac{D_2 - D_1}{G}}, \tag{7.7}$$

$$Eo = \frac{(\rho_l - \rho_g) G (D_2 - D_1)^2}{\sigma}, \tag{7.8}$$

$$Mo = \frac{(\rho_l - \rho_g) G \mu^4}{\rho_l^2 \sigma^3}, \tag{7.9}$$

$$N_f = \frac{\sqrt{(\rho_l - \rho_g)\rho_l G (D_2 - D_1)^3}}{\mu_l}, \tag{7.10}$$

$$Fr = \frac{u_{TB}}{\sqrt{G(D_2 + D_1)}}, \tag{7.11}$$

respectively. In addition to these, the ratios of density, $\rho^* = \rho_l/\rho_g$, viscosity, $\mu^* = \mu_l/\mu_g$, and pipe diameter, $D^* = D_2/D_1$, are used to define each flow case. The experimental work carried out by Das *et al.* [225] was conducted with air and water, as such the density and viscosity ratios are taken as,

$$\rho^* = \frac{998}{1.2047} = 828.4220, \tag{7.12}$$

$$\mu^* = \frac{1.0020 \times 10^{-3}}{1.8205 \times 10^{-5}} = 55.0398. \tag{7.13}$$

Table 7.1: Summary of annular experimental geometry and flow cases from Das *et al.* [225]. Predictions of the dimensionless rise velocity are provided by Das *et al.* [225], Sadatomi *et al.* [230] and Hasan and Kabir [62].

Case	D_2 [m]	D_1 [m]	Eo	Mo	N_f	Fr (Exp.)	Fr [225]	Fr [230]	Fr [62]
1	0.0508	0.0254	86.587	2.559e-11	12620	0.334	0.324	0.345	0.323
2	0.0381	0.0127	86.587	2.559e-11	12620	0.338	0.326	0.345	0.328
3	0.0254	0.0127	21.647	2.559e-11	4462	0.277	0.260	0.345	0.323

To discretise the annular piping system, the outer tube diameter, D_2, is set to 128 lattice units (lu) and the reference time is fixed to, $t^* = 12000$ lu. From here, all fluid parameters and the pipe geometry can be determined using the dimensionless numbers stated in Table 7.1. To initialise the system, one can take the naive analogue of the simulations conducted in Chapter 6, and initialise an axi-symmetric, toroidal bubble that encapsulates the entire inner tube. To do this, first the pipe is assumed to align parallel with the x-axis and as such, the surface of the liquid-gas interface can be specified,

$$x_{int}^2 = r_1^2 - \left(r_2 - \sqrt{(y - y_c)^2 + (z - z_c)^2} \right)^2, \tag{7.14}$$

where r_1 is the radius of the toroidal tube, r_2 is the distance from the axis of the annular pipe to the centre of the toroidal tube and the subscript, c, specifies the location of the annular pipe axis. From here, a dilation factor, d_f, is applied to extend the cross-section of the toroid into an elliptical form,

$$x_{int} = d_f \sqrt{r_1^2 - \left(r_2 - \sqrt{(y-y_c)^2 + (z-z_c)^2} \right)^2}. \tag{7.15}$$

Using this shape is suitable for capturing the behaviour of an annular Taylor bubble with simulations naturally evolving into the asymmetrical shape observed in Figure 7.1. However, to reduce the time to steady-state it is favourable to initialise the Taylor bubble in a shape closer to that expected from experiments reported in the literature. To do this, an angle, α, from the y-axis in the $y-z$ plane is specified as,

$$\alpha = tan^{-1}\left(\frac{z-z_c}{y-y_c} \right). \tag{7.16}$$

From here, the phase-field in the domain is defined as,

$$\phi(x,y,z) = \begin{cases} 1.0, & x \leq x_0 - x_{int} \\ 0.0, & x_0 - x_{int} < x < x_0 + x_{int} sin(\alpha/2) \\ 1.0, & x \geq x_0 + x_{int} sin(\alpha/2), \end{cases} \tag{7.17}$$

where, x_0, is the location of the bubble centre along the pipe axis. The resultant initialisation shape is shown in Figure 7.2, for which $y_c = z_c = D_2/2$, $r_1 = (D_2 - D_1)/6$, $r_2 = (D_2 + D_1)/4$, $d_f = 0.1D_2$ and $x_0 = 2D_2$.

7.2.2 Results

In this section, the attempts to simulate the experimental cases of Das *et al.* [225] are described and the findings presented. These are then compared with existing correlations developed by Das *et al.* [225], Sadatomi *et al.* [230] and Hasan and Kabir [62]. The initial attempt to simulate the flow cases described in Section 7.2.1 with the specified discretisation led to instabilities in Case 1 and 2 while Case 3 progressed to a steady-state rise velocity. According to the combination of Morton and Eötvös numbers for these flows, this stability behaviour aligns with the findings presented in Figure 6.6. In order to alleviate the instability present in the simulations, the density ratio was reduced by a factor of 10 for Case 1 and 2. In Chapter 6, when the density ratio was reduced by a factor of 10, there did not prove to be a significant impact on the rise velocity results of the Taylor bubble, with $\rho_g \ll \rho_l$ still evident.

To determine the bubble rise velocity from simulations, the axial velocity of gas cells in the Taylor bubble was tracked during the simulation. The average of the local gas velocity corresponds to the bubble propagation speed. Simulations are run for $15t^*$ and the velocity is averaged over the final t^*, before being converted into the bubble Froude number as per Equation 7.11. Table 7.2 shows the results obtained for this in comparison to the experimental measurements and correlated predictions.

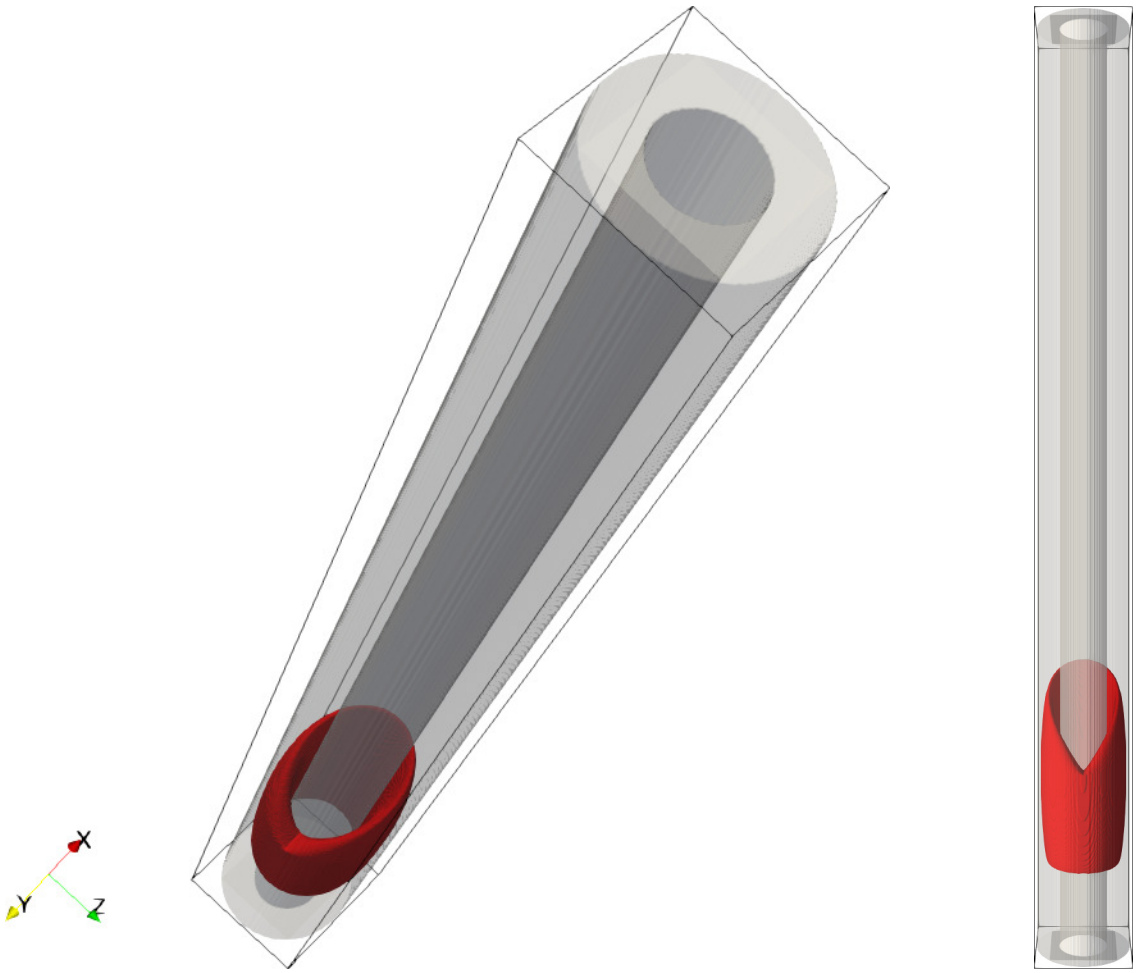

(a) (b)

Figure 7.2: Initialisation shape for annular Taylor bubbles; (a) isometric-style view, (b) $x-z$ plane.

For Cases 1 and 2, it is evident that the CFD results underpredict the experimental measurements due to the reduced effect of buoyancy at the lower density ratio specified. However, the results for these still show good agreement with the experimental measurements and the correlated predictions of Das *et al.* [225]. For Case 3, the experimental conditions were replicated and the accuracy of the CFD findings in comparison to the measured experimental result is clear, with a variation of only 2.3%.

Table 7.2: Summary of vertical annular simulation results for the experimental flow cases from Das *et al.* [225]. Comparisons can be drawn between experimental measurements as well as the correlations of Das *et al.* [225], Sadatomi *et al.* [230] and Hasan and Kabir [62].

Case	ρ^*	Fr (LBM)	Fr (Exp.)	Error (%)	Fr [225]	Fr [230]	Fr [62]
1	82.8422	0.316	0.334	-5.33	0.324	0.345	0.323
2	82.8422	0.317	0.338	-6.08	0.326	0.345	0.328
3	828.4220	0.283	0.277	2.31	0.260	0.345	0.323

Figure 7.3 plots the progression of the Taylor bubble described by Case 3, from initialisation through to a steady rise velocity and nose shape. Additionally, the vorticity of the flow has been contoured to allow the progression of the liquid bridge to be observed. It is noted that the steady state shape forms even if a cylindrical initialisation of the gas region is used, however, the required

number of iterations increases. The use of the vorticity field provides a means in which the length of influence from the Taylor bubble can be assessed. With this, it is possible to gain insight on the length of the liquid slug propagating behind a single annular Taylor bubble, another factor that influences mechanistic pressure drop predictions discussed in this dissertation. For vertical pipes, a rule of thumb of approximately 16 times the pipe diameter is used for the size of the liquid slug [29]. The simulations here do not provide sufficient pipe length to interrogate the accuracy of this for vertical pipe flow, but this presents another future avenue of work with the model developed. The methodology applied for these three simulations provides a means with which one can analyse Taylor bubble dynamics in vertical annular pipes. This could replace the use of physical experiments in correlating dimensionless flow parameters with the bubble rise behaviour, and as such gives a potential method for developing a unified rise velocity correlation.

7.3 Effect of pipe inclination

With the limited literature available on the flow of Taylor bubbles in annular piping [226, 227], it is not surprising that their flow in inclined annuli is also remiss. The general problem of two-phase flow in a deviated annulus has seen more focused research interest in the past than the particulars of the slug flow regime. Johnson and Cooper [232] used a polymer mud, in addition to water, to test various fluids in both pipes and annuli. In their work, they concluded that the slip velocity remained effectively constant from vertical to 45 degrees. Hasan and Kabir [62] conducted an experimental study in small diameter pipes and annuli using air and water as the working fluids. They observed a reduction in curvature as the bubble nose sharpened for inclined conduits. This initially resulted in a reduction of drag and as such, an increase in bubble rise velocity. However, as the conduit inclination progressed below 45 degrees to the horizontal, the buoyancy reduction offsets the drag and the bubble propagation speed reduces. From their experiments, and a balance of buoyancy to drag forces, they proposed the velocity in inclined flows, u_θ, to be,

$$u_\theta = u_{TB}\sqrt{\sin\theta}\,(1+\cos\theta)^{1.2}. \tag{7.18}$$

The drift velocity, u_{TB}, of the Taylor bubble in a vertical annulus was taken as,

$$u_{TB} = (0.345 + 0.1(D_1/D_2))\sqrt{GD_2(\rho_l-\rho_g)/\rho_l}\,. \tag{7.19}$$

This correlation has seen use in mechanistic models by the likes of Yu *et al.* [233], which follows a similar process to the tubular mechanistic model of Zhang *et al.* [234].

In addition to comparing with the correlation of Hasan and Kabir [62], this section examines the validity of the unified tubular correlation proposed by Lizarraga-Garcia *et al.* [18] for annular pipes. To do this, the characteristic diameter is taken as the hydraulic diameter, $D_h = D_2 - D_1$, for dimensionless parameters, and the rise velocity is determined as per Equations 6.33 to 6.35. The choice of hydraulic diameter is commonly used by researchers, for an example in the a recent correlation by Ibarra and

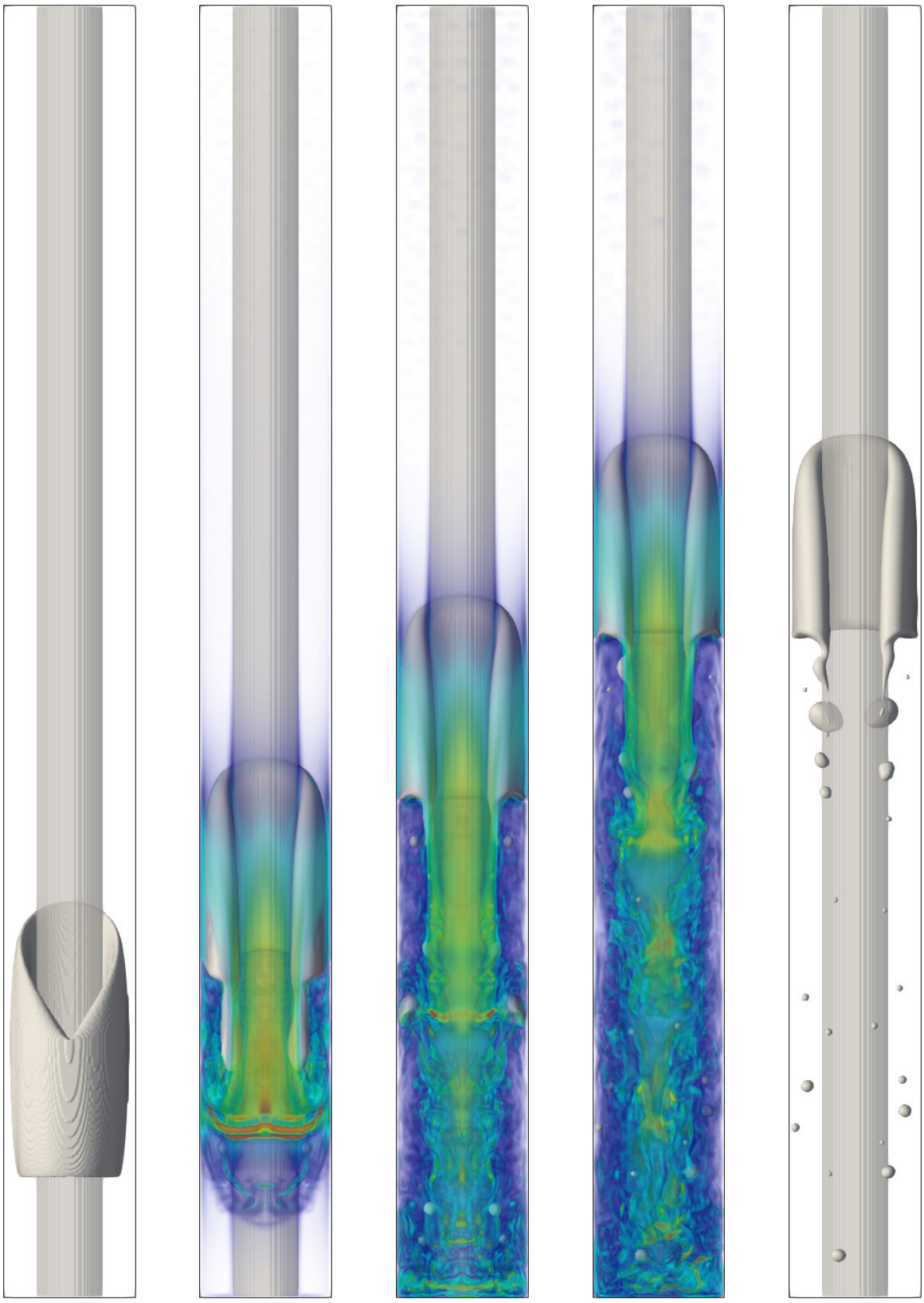

(a) $t^* = 0$ (b) $t^* = 5$ (c) $t^* = 10$ (d) $t^* = 15$ (e) $t^* = 15$

Figure 7.3: Taylor bubble profiles through time (a) $t^* = 0$, (b) $t^* = 5$, (c) $t^* = 10$, (d) $t^* = 15$, (e) $t^* = 15$, for Case 3 (Mo=2.5587e-11, Eo=21.65). The vorticity of the flow has been superimposed to show the development of the liquid bridge through which liquid is transported into the wake region.

Nossen [226],

$$u_\theta = (Fr_v \sin\theta + Fr_h \cos\theta)\sqrt{GD_h(1-\rho_g/\rho_l)}\,. \tag{7.20}$$

For the vertical and horizontal dimensionless rise velocities, Dumitrescu [199] found $Fr_v = 0.351$ and Benjamin [235] found $Fr_h = 0.542$, respectively. This was used later by Ibarra *et al.* [236] for horizontal and low-inclination annuli, in which the models developed agreed well with their experimental work later presented in [237].

7.3.1 Simulation details

As per Chapter 6, the ease of transition from a vertical to inclined annuli highlights the benefits associated with numerical modelling. Case 3 is used for further analysis in this section due to the accuracy and stability observed in the vertical case. To test the correlations introduced, inclination angles of $\theta \in \{10, 20, 30, 40, 45, 50, 60, 70, 80\}$ are specified allowing for the gravitational forces to be determined as,

$$g_x = -G\sin\theta, \tag{7.21}$$

$$g_y = G\cos\theta. \tag{7.22}$$

As per the previous simulations conducted, the axis of the annular pipes aligns with the x-axis of the computational domain. Thus, the initialisation of the domain can be seen in Figure 7.2 in which the buoyancy of the gaseous phase drives the Taylor bubble in the positive x-direction and negative y-direction.

Table 7.3: Summary of annular experimental geometry and fluid parameters for Case 3 from Das *et al.* [225].

Case	D_2 [m]	D_1 [m]	Eo	Mo	N_f	ρ^*	Fr (Exp.)	Fr (LBM)
3	0.0254	0.0127	21.647	2.559e-11	4462	828.422	0.277	0.283

For convenience, the relevant numerical parameters are displayed in Table 7.3. The simulations are run with a reference time of $t_0 = 12000$ for a total of $20t_0$. The numerical parameters for the phase-field population are specified as $M = 0.05$ for the interface mobility and $W = 5$ for the diffuse interface width. This value of mobility was used in validation tests, in which the experimental data was accurately captured by the phase field model. Selection of the mobility using scaling arguments as specified by Jacqmin [39] or methods discussed by Donaldson et al. [238] could also be used to determine an appropriate value. The simulation domain is defined as $(10D_2 \times D_2 \times D_2)$ with $D_2 = 128$ lu.

7.3.2 Results

Figures 7.4 and 7.5 indicate the final state of the Taylor bubbles from the simulations conducted. These depictions have the vorticity field superimposed to indicate areas of fluid motion, in particular, the

wake region. The void fraction in the wake can be observed to increase with pipe inclination as the effect of the liquid jet causes shedding of smaller bubbles from the Taylor bubble. As the inclination of the pipe tends towards vertical, a higher gravitational force in the direction of the wake and a reduction in the buoyancy force towards the upper wall of the annulus is evident. This results in an expansion of the wake region length as well as an increase in the wrap angle of the bubble around the annular pipe.

The rise velocity determined from simulations along with those predicted by correlations from Lizarraga-Garcia *et al.* [18], Hasan and Kabir [62] and Ibarra and Nossen [226] are presented in Table 7.4. To remain consistent in this comparison with the varied methods for non-dimensionalising the rise velocity, each correlation was used to determine u_θ in lattice units before being normalised such that the Froude number displayed in the table is given by,

$$Fr = \frac{u_\theta}{\sqrt{G(D_1 + D_2)}}. \tag{7.23}$$

Additionally, as the drift velocity in a vertical pipe used in the correlation of Lizarraga-Garcia *et al.* [18] is based on tubular flow, a further comparison was made in which the experimentally measured rise velocity from Das *et al.* [225] was coupled with the inclination closure. This is displayed in Table 7.4 by the Froude number, Fr_{exp}.

Table 7.4: Summary of inclined annular pipe simulations results comparing the measured velocity in the LBM simulations with the correlations of Lizarraga-Garcia *et al.* [18], Hasan and Kabir [62] and Ibarra and Nossen [226].

Inclination	Fr (LBM)	Fr_{exp} [18]	Fr [18]	Fr [62]	Fr [226]
10^o	0.329	0.300	0.315	0.328	0.343
20^o	0.356	0.350	0.365	0.447	0.363
30^o	0.373	0.377	0.392	0.516	0.372
40^o	0.380	0.391	0.406	0.548	0.370
45^o	0.380	0.393	0.408	0.552	0.364
50^o	0.381	0.391	0.406	0.548	0.356
60^o	0.368	0.377	0.392	0.523	0.332
70^o	0.350	0.351	0.366	0.477	0.297
80^o	0.322	0.317	0.331	0.415	0.254
90^o	0.283	0.277	0.290	0.345	0.203

Figure 7.6 plots the data in Table 7.4, and shows that the correlation extrapolated from tubular pipe configurations performs the best, closely aligning with the simulated results. Here, the results from Lizarraga-Garcia *et al.* [18] capture the inclination effect on the bubble more accurately than correlations currently applied to annular piping configurations. The correlation is further improved with the use of the Taylor bubble rise velocity measured in an annulus. From this, it is recommended that the rise velocity correlation from Das *et al.* [225] to determine the velocity of the Taylor bubble in a vertical annulus be coupled with the inclination effects from Lizarraga-Garcia *et al.* [18]. However, this cannot be universally concluded from the results of a single test and as such, future work consists of generating a database of relations between inclination angle, fluid parameters and the Froude number.

In order to highlight that multiple possibilities exist when formulating closure relations, a minor tuning was performed on the correlation of Ibarra and Nossen [226]. Here, it is noted that this was

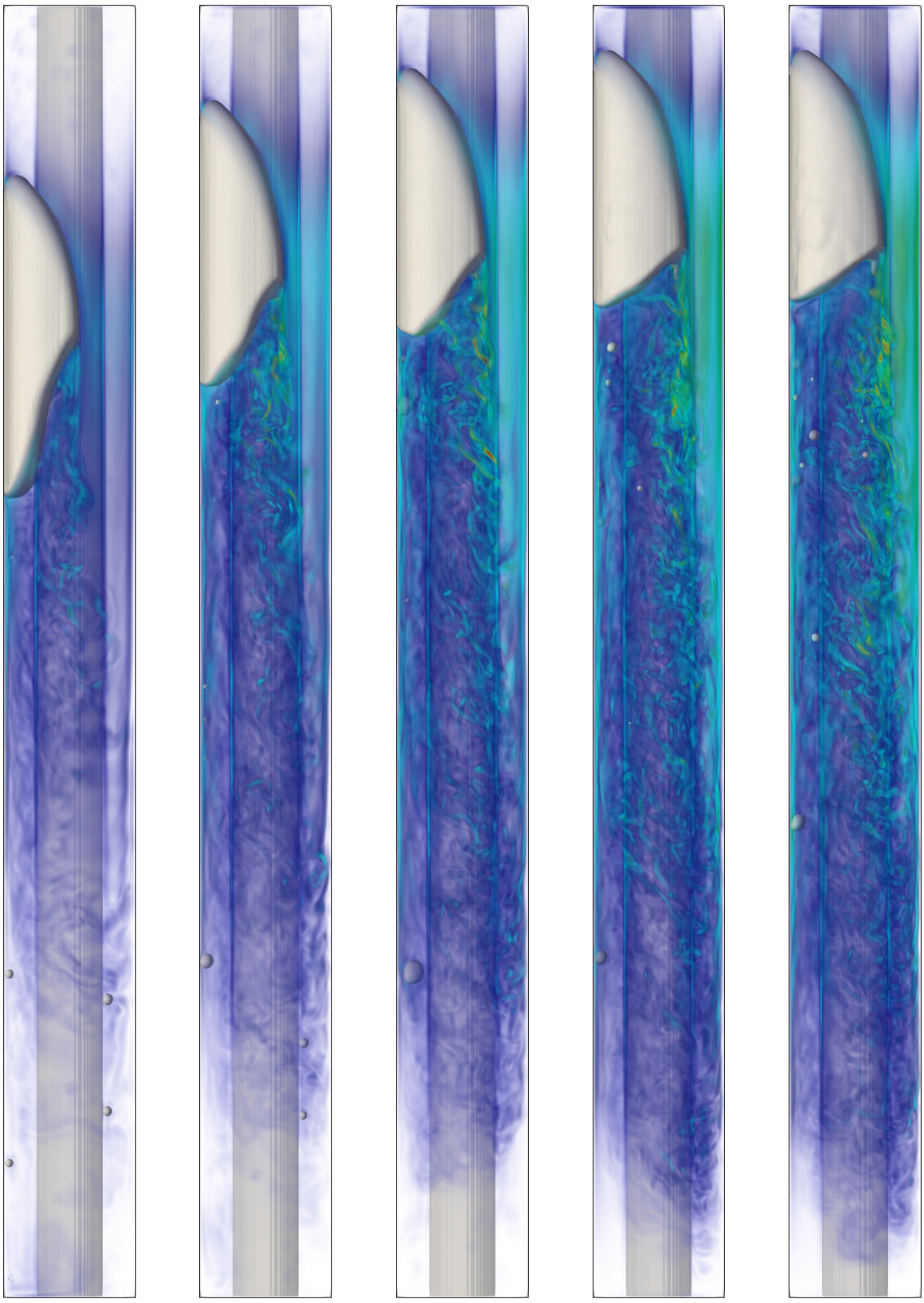

(a) $\theta = 10^o$ (b) $\theta = 20^o$ (c) $\theta = 30^o$ (d) $\theta = 40^o$ (e) $\theta = 45^o$

Figure 7.4: Taylor bubble profiles at $t^* = 20t_0$ with fluid parameters according to Case 3 (Mo=2.56e-11, Eo=21.65) and for pipe inclination angles (a) $\theta = 10$, (b) $\theta = 20$, (c) $\theta = 30$, (d) $\theta = 40$, (e) $\theta = 45$ degrees.

(a) $\theta = 45^o$ (b) $\theta = 50^o$ (c) $\theta = 60^o$ (d) $\theta = 70^o$ (e) $\theta = 80^o$

Figure 7.5: Taylor bubble profiles at $t^* = 20t_0$ with fluid parameters according to Case 3 (Mo=2.56e-11, Eo=21.65) and for pipe inclination angles (a) $\theta = 45$, (b) $\theta = 50$, (c) $\theta = 60$, (d) $\theta = 70$, (e) $\theta = 80$ degrees.

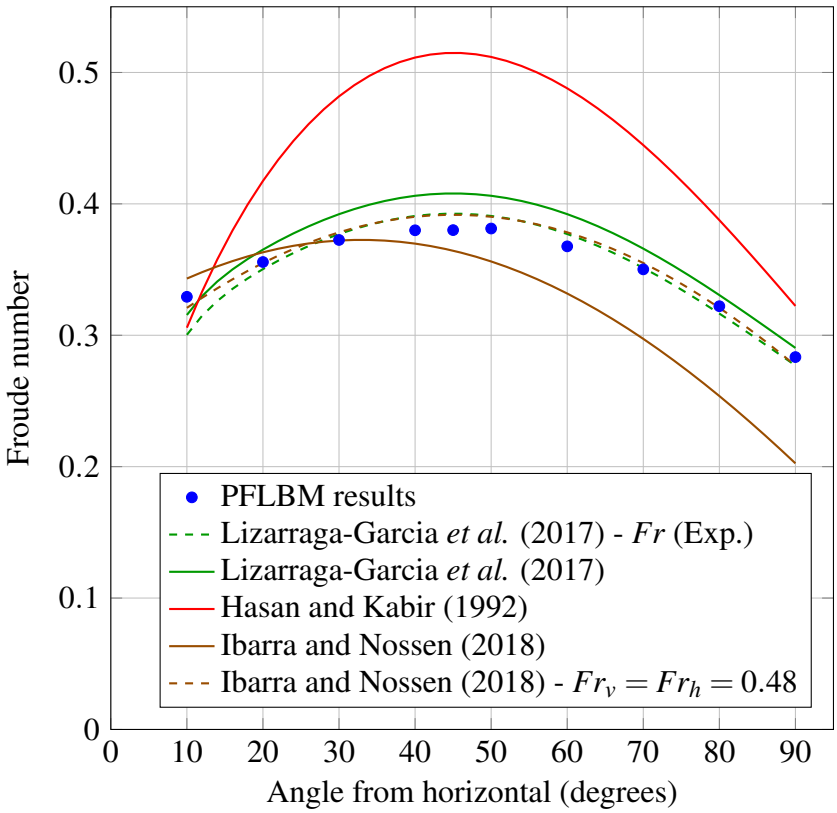

Figure 7.6: Comparison of simulated predicted bubble velocity in tubular pipes at various inclinations with the unified correlation proposed by Lizarraga-Garcia *et al.* [18].

initially formulated for horizontal and near-horizontal annuli, which is where it is observed to be most accurate. This is based on a competition between the drift velocity of a Taylor bubble in horizontal, Fr_h, and vertical, Fr_v, annuli along with a dependence on the hydraulic diameter. In Figure 7.6 it is evident that specifying these two parameters at a value of 0.48, (arbitrarily chosen to optimise the fit) allows the dynamics of the full inclination range to be predicted.

This section has indicated that the current methods employed to determine the rise velocity of a Taylor bubble in an inclined annulus lack accuracy, however, this appears rectifiable by extending tubular pipe models and or tuning model parameters. It further indicates the need for the creation of a database relating dimensionless parameters describing the geometry and fluid properties of a Taylor bubble in an annulus to its rise velocity. In this section, two potential formulations were shown for the Taylor bubble rise in inclined pipes. The first was based on extrapolating the tubular model from Lizarraga-Garcia *et al.* [18] by coupling it with a vertical rise model for bubbles in annular pipes. The second was determined through tuning of the closure model originally proposed by Ibarra and Nossen [226] for horizontal and near-horizontal pipes.

7.4 Propagation in a flowing fluid

In terms of predicting the effect of liquid flow on the dynamics of an annular Taylor bubble, previous investigators have taken a similar approach to that of tubular pipes. In this sense, the interaction between the phases is superimposed onto the drift velocity of the Taylor bubble with an empirical

distribution parameter, C_0,

$$u_{TB} = C_0 u_l + u_d, \tag{7.24}$$

as per Equation 6.38. It was concluded by Bendiksen [193] and Zhang *et al.* [234] that a value of $C_0 = 2.0$ should be used in laminar flow and $C_0 = 1.3$ in turbulent flows. This was used in the mechanistic model for vertical upward flows in an annulus by Yu *et al.* [233] along with a simple linear interpolation in the transitional region ($2000 < Re < 4000$),

$$C_0 = 2.0 - 0.7(Re - 2000)/2000. \tag{7.25}$$

Yu *et al.* [233] coupled this model with the drift velocity correlation of Hasan and Kabir [62], however, did not include the effect of inclination.

A similar form of Equation 6.38 was also used by Firouzi *et al.* [16], however, the drift velocity was determined by the model from Caetano *et al.* [61] and formulated with the superficial liquid, u_{SL}, and gas, u_{SG}, velocities,

$$u_{TB} = C_0(u_{SG} - u_{SL}) + u_d, \tag{7.26}$$

$$= C_0(u_{SG} - u_{SL}) + 0.345\sqrt{g(D_1 + D_2)}\,. \tag{7.27}$$

There is no gas phase injection into the simulations in this chapter, as such, $u_{SG} = 0$. Also, it is noted here that the form is presented as per the works of Firouzi *et al.* [16], in which the negative corresponds to the counter-current flow imposed. The values for the flow distribution parameter, C_0, were referred to by the works of Martin [239] in which it was reported to be less than unity for completely downward flows in moderate and large diameter pipes, and,

$$C_0 = \begin{cases} 1.0, & \text{stagnant fluid,} \\ 1.2, & \text{upward flowing fluid.} \end{cases} \tag{7.28}$$

For downward flows in small pipes, namely with a low Eötvös number, it was reported that the value of C_0 may be greater than one. In particular, in a pipe of diameter, $D_2 = 2.6$ cm, the average value was determined to be 1.14 by three investigators [239].

As can be seen, inconsistency exists in the conclusions that have been drawn in the early works studying the dynamics of a Taylor bubble within annular pipes. Not only are there limited published results, but there is a disconnect between authors that take tubular pipe values for coefficients such as the distribution parameter and those that use values tailored for annular pipe. Findings from mechanistic models are often reported using a certain closure relation for the rise behaviour of the gaseous phase without a description of the inaccuracies that it could entail. In this section, the methodology for conducting flowing fluid simulations with the phase-field LBM is provided along with results that show a *proof-of-concept* for which these correlations could be improved.

7.4.1 Simulation details

In order to impose a flowing fluid on the computational domain, the reference frame was shifted from stationary to one moving with the expected drift velocity of a Taylor bubble in an annulus. In order to

do this, the velocity boundary condition described in Chapter 6 was applied to both the extents of the computational domain as well as the pipe walls. This is used to set the velocity of the outer and inner tubing to the drift velocity, u_d. The inlet and outlet at the top and bottom of the system, are specified as a fully developed single phase flow in an annulus. In order to derive this, one can consider the steady-state, incompressible Navier-Stokes equation as,

$$0 = -\rho \partial_x p + \mu \partial_r \left(r \partial_r u_x \right), \tag{7.29}$$

where cylindrical co-ordinates, (x, r), are used. For simplicity, one can apply zero-velocity boundary conditions at the inner, r_i, and outer, r_o, pipe walls. Using this, the equation can be integrated to give,

$$u_x = \frac{-r_o^2 \partial_x p}{4\mu} \left(1 - (r/r_o)^2 + \frac{1 - (r_i/r_o)^2}{\ln(r_o/r_i)} \ln(r/r_o) \right). \tag{7.30}$$

Here, it can be seen that the term in front of the main bracket corresponds to the maximum velocity, $u_{tube,0}$, that would be observed in a tubular pipe of radius, r_o. To write this in terms of an average velocity, one can integrate u_x for the flow rate and divide by the cross-sectional area to obtain,

$$u_{avg} = 0.5 u_{tube,0} \left(1 + (r_i/r_o)^2 - \frac{1 - (r_i/r_o)^2}{\ln(r_o/r_i)} \right). \tag{7.31}$$

Thus, in order to define the liquid flow conditions in this section, a liquid Reynolds number,

$$Re_l = \frac{2 u_{avg} (r_o - r_i)}{\nu}, \tag{7.32}$$

is specified. From here, the average velocity can be determined and used to calculate, $u_{tube,0}$. With the value of this found, the velocity at the inlet and outlet can be specified in the moving frame of reference as,

$$u_{inlet/outlet}(r) = u_d + u_{tube,0} \left(1 - (r/r_o)^2 + \frac{1 - (r_i/r_o)^2}{\ln(r_o/r_i)} \ln(r/r_o) \right). \tag{7.33}$$

It is noted here, that one can also apply a constant velocity, u_{avg}, to the entire inlet and outlet region as long as sufficient separation exists between the bubble and the domain extents. Both of these configurations were tested without significant variation observed in the results. In this section, the results are presented in which the inlet and outlet are specified as fully developed flow.

The domain used in this section is consistent with that presented for the analysis of Taylor bubble propagation through stagnant liquid in vertical and inclined annuli, with the minor modification of shifting the bubble centre to align with that of the annular pipe. Therefore, the reference time is $t^* = 12000$ with simulations run for a total of $10t^*$ to reach a steady state rise velocity. The diameter of the outer annulus is again discretised such that $D_2 = 128$ lu. For the diffuse interface parameters, the mobility is held constant at $M = 0.05$ and the interface width at $W = 5$ lu. Table 7.5 provides the relevant dimensionless numbers for the three test cases used to investigate the effect of flowing fluid. The Froude number presented here is determined using the hydraulic diameter and the rise velocity correlation of Viana *et al.* [207] given in Equation 6.14.

Table 7.5: Summary of annular experimental test cases for investigating the effects of flowing liquid on a Taylor bubble's dynamics.

Case	D_2 [lu]	D_1 [lu]	Eo	Mo	N_f	Fr [207]	Re_l
A	128	64	21.647	2.559e-3	45	0.175	$\{-10,-1,0,1,10\}$
B	128	64	21.647	2.728e-4	78	0.226	$\{-10,-1,0,1,10\}$
C	128	64	21.647	6.550e-5	112	0.250	$\{-10,-1,0,1,10\}$

7.4.2 Results

Table 7.6 provides the dimensionless rise velocity of the bubble in the form of the Froude number and the corresponding distribution parameter, C_0, that were extracted from simulations. Here, it is evident that the value of C_0 remains relatively constant for the tests conducted, effectively being independent of the liquid Reynolds number, Morton number and inverse viscosity number. As the liquid velocity has been specified based on the Reynolds number, more viscous fluids (lower value of N_F) have a larger fluid velocity to balance the inertial and viscous forces. This corresponds to a larger variation in bubble rise velocity, however, the distribution parameter describing the liquid contribution remains almost constant.

Table 7.6: Summary of the bubble rise behaviour incorporating the effect of flowing liquid through annular piping.

Case	Re_l	Fr_l	Eo	Mo	N_f	Fr [LBM]	C_0
A	-10	0.1293	21.6478	2.5587e-3	45	0.0566	1.1552
	-1	0.0129				0.1910	1.1612
	0	0.0000				0.2060	-
	1	-0.0129				0.2210	1.1625
	10	-0.1293				0.3544	1.1479
B	-10	0.0259	21.6478	2.7281e-4	78	0.1579	1.2076
	-1	0.0026				0.2382	1.2082
	0	0.0000				0.2471	-
	1	-0.0026				0.2560	1.2050
	10	-0.0259				0.3360	1.2029
C	-10	0.0517	21.6478	6.5502e-5	112	0.1980	1.1800
	-1	0.0052				0.2530	1.1695
	0	0.0000				0.2590	-
	1	-0.0052				0.2652	1.1821
	10	-0.0517				0.3199	1.1766

The results presented in Table 7.6 are displayed graphically in Figure 7.7. This confirms the linear relation between liquid velocity and bubble rise that is observed by the constant value of C_0. The average value found for this coefficient in the three test cases was,

$$\bar{C}_{0,case-A} = 1.16, \tag{7.34}$$

$$\bar{C}_{0,case-B} = 1.21, \tag{7.35}$$

$$\bar{C}_{0,case-C} = 1.18. \tag{7.36}$$

These agree very closely with the findings of Martin [239], that were used in the recent mechanistic model proposed by Firouzi *et al.* [16].

The Eötvös number used here corresponds to a relatively small pipe size, and as a result, it could be expected that the co- and counter-current flow simulations retain a similar value for C_0. However, for larger pipe sizes and or higher flow rates, it has been reported that the eccentricity of the Taylor bubble can increase for downward flowing liquid. This results in the bubble rising in a region with less velocity than the cross-sectional average and thus, a lower expected value for C_0 [239]. The methodology used in this section could be extended to investigate the critical diameter at which the concentricity of the bubble degrades. This is not attempted in this dissertation, however, is recommended for future work as it could potentially provide a correlation for C_0 in the counter-current flow regime that does not currently have sufficient data to make accurate predictions.

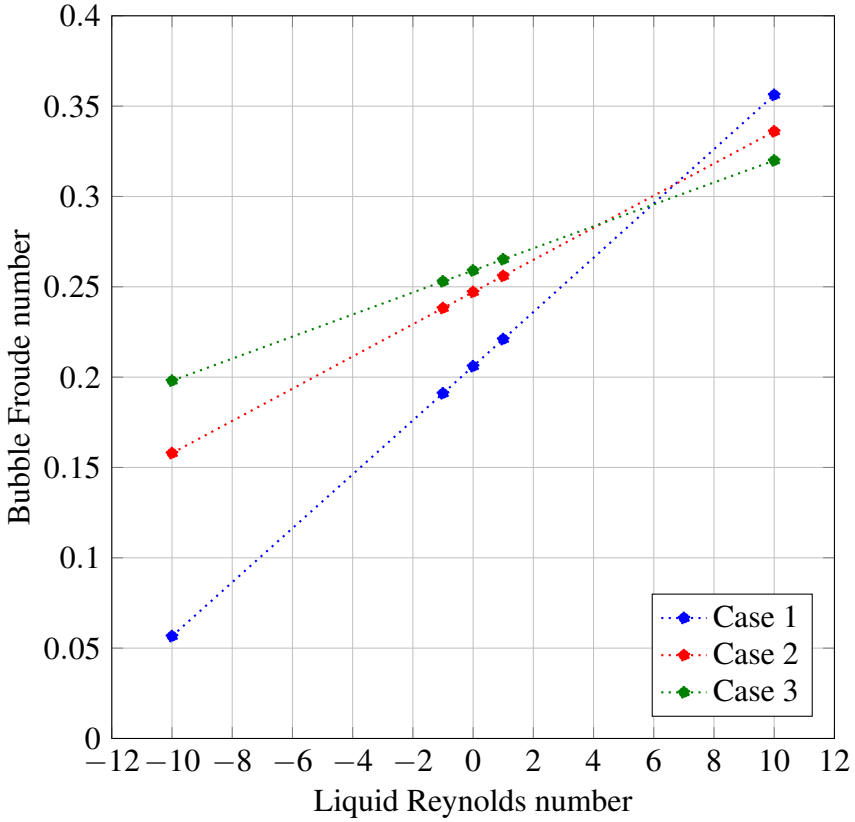

Figure 7.7: The relationship between the bubble Froude number and the liquid Reynolds number indicating the linear relationship that the liquid flow has on the bubble rise.

Figure 7.8 provides a visualisation of Case A in which the Taylor bubble propagates through the annular gap between two pipes with liquid motion imposed. Comparing these qualitatively to the experimental cases recreated from the work of Das *et al.* [225], it can be observed that the bubbles are more elongated and the radial wrap of the inner tubing has reduced. Here, it is noted that with the velocity boundary conditions presented, the model was unable to reach a numerical viscosity low enough to recreate the experimental case in the moving reference frame. As such, the simulations conducted here have a higher viscosity, which can be seen to result in a larger liquid bridge as well as the elongation of the Taylor bubble.

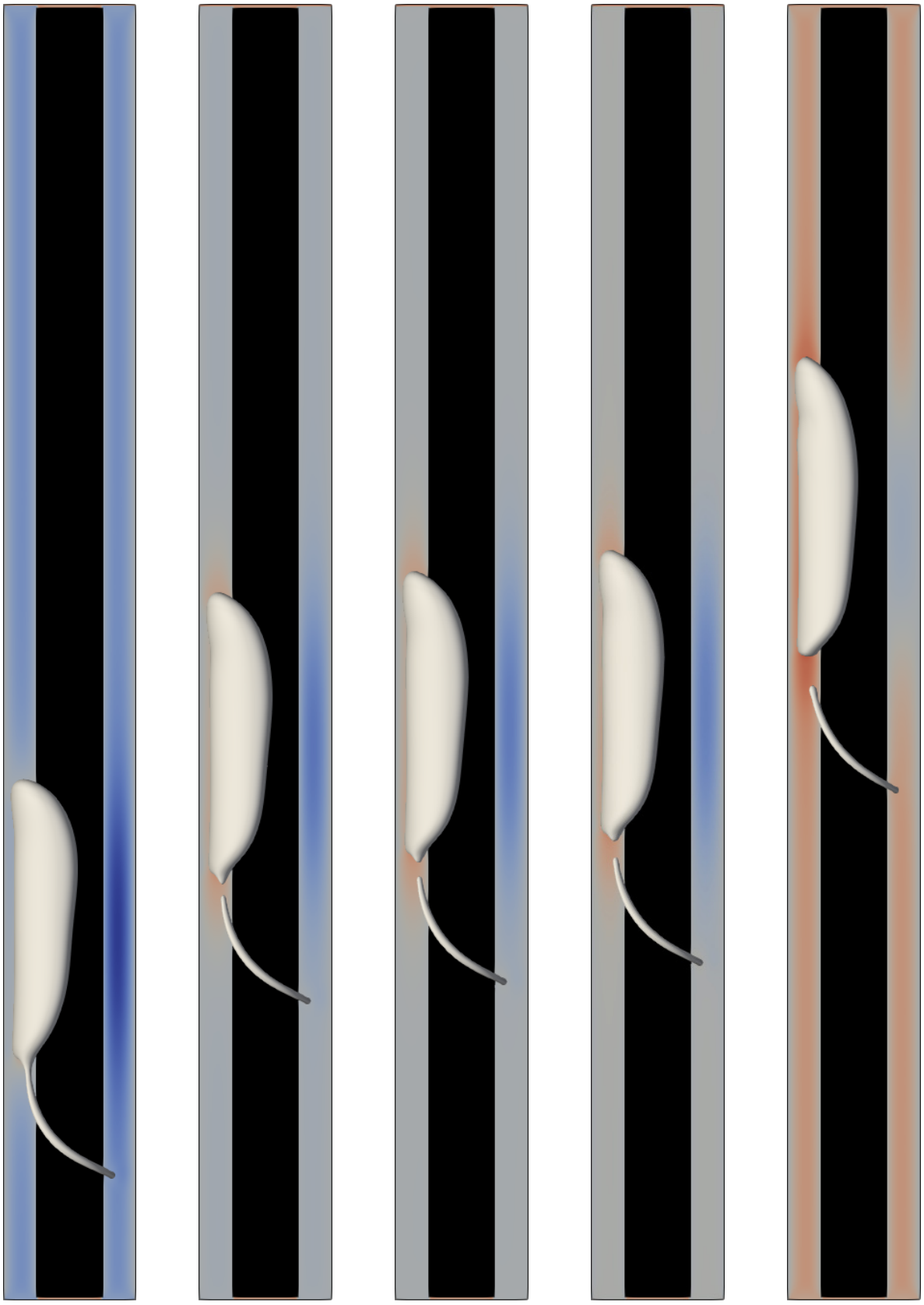

(a) $Re_l = -10$ (b) $Re_l = -1$ (c) $Re_l = 0$ (d) $Re_l = 1$ (e) $Re_l = 10$

Figure 7.8: Case A simulation results for a Taylor bubbles propagating through an annulus after $10t^*$ iterations, with liquid flowing at: (a) $Re_l = -10$; (b) $Re_l = -1$; (c) $Re_l = 0$; (d) $Re_l = 1$; (e) $Re_l = 10$. The colour in the annulus represents the velocity of the liquid with red and blue indicating upwards and downwards flow, respectively.

In this section, the effect of flowing liquid on the propagation rate of a Taylor bubble in an annular gap was investigated. It was found that for small pipes, the coefficient proposed by Nicklin [201] and Martin [239] to model the phase interaction was the most accurate. The application of this to counter-current flow in large pipes, however, is debatable and requires further investigation. As such, it is recommended for future work, that the methodology applied here is used to study and propose a model for C_0 in both large pipe and high flow rate cases. In additional to this, further assessment of the effects of fluid properties is required to confirm the accuracy in small pipes, particularly under various conditions.

7.5 Conclusions

This chapter presented an investigation into the dynamics of Taylor bubbles within annular piping configurations. This highlighted the limited work currently in existence as well as established a method through which further studies could be conducted. Initially, the work analysed the experimental test cases reported by Das *et al.* [225], validating the capability of the model to capture relevant flow cases. This indicated that the axi-symmetric shape of Taylor bubbles observed in tubular pipes breaks down in the annular analogue. Here, a liquid bridge formed (whether artificially initiated or not), which allowed the downward transportation of the liquid into the wake region of the bubble. The size of the liquid bridge, or equivalently, the angle of wrap observed for the Taylor bubble about the inner tube, was qualitatively seen to depend on the inclination angle of the pipe as well as the viscosity of the liquid phase.

The effect of pipe inclination on the rise of the Taylor bubble proved to be another gap in the literature. Here, the recent work of Ibarra and Nossen [226] was shown to reasonably predict the rise behaviour in horizontal and low pipe inclinations, but quickly deteriorated in accuracy as the annular pipe approached vertical. Additionally, the correlation of Hasan and Kabir [62] failed to capture the bubble velocity at intermediary inclination angles, with smaller errors observed at near horizontal and near vertical flow configurations. Looking to resolve the inaccuracies of these models, the correlation proposed by Lizarraga-Garcia *et al.* [18] for tubular pipes was coupled with the hydraulic diameter and the drift velocity correlation proposed by Das *et al.* [225]. This provided a very accurate prediction of the rise velocity for all inclination angles. Further to this, it was noted that the form of the model by Ibarra and Nossen [226] balanced the horizontal and vertical drift velocity for a Taylor bubble. Using these two values as tuning parameters, another possible model was presented that could capture the rise behaviour with reasonable accuracy at all inclination angles tested. This provided a *proof-of-concept* for correlating the Taylor bubble dynamics in inclined annuli, however, it is recommended as future work that the parameter range be increased so as unified models can be proposed.

Finally, liquid flow was introduced into the domain to assess the competing behaviours of buoyancy and viscous drag. In this area, there appeared to be a lack of rigorously tested closure correlations to describe the propagation rate of the Taylor bubble, which can significantly affect the accuracy of pressure gradient predictions [63]. Simulations were conducted in relatively small pipe and it was

found that the value for the distribution parameter, C_0, agreed well with the conclusions made by Martin [239]. The work in this section provided a methodology through which the proposed LBM could be applied to generate a database of dimensionless flow parameter relations. This could be used in place of experimental works and ultimately lead to the formulation of a unified rise velocity model for Taylor bubbles in a range of piping configurations and flow conditions.

Chapter 8

Conclusions and directions for future study

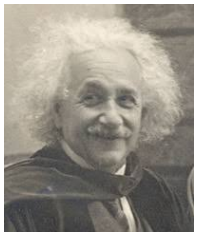

"Imagination is more important than knowledge.
Knowledge is limited. Imagination encircles the world."
Albert Einstein

The transportation of hydrocarbons through piping networks is a critical component of the oil and gas production life cycle. In particular, it is evident in linking the subsurface environment to the wellhead and the wellhead to delivery points. In the wellbore there exists both production liquids and gases that can inhibit the accurate calculation of pressure gradients which are required for operational processes.

To further the current understanding of these multiphase systems, this work defined two primary aims:

(1) develop a fully resolved computational model capable of simulating two phase flows with high density and viscosity ratios, and to
(2) use this modelling capability to gain key insights into the counter-current flow that occurs in the process of extracting natural gas from coal seams.

To this end, a computational multi-fluid dynamics model was developed within the lattice Boltzmann framework and was shown to robustly resolve flows with density and viscosity contrasts, mimicking liquid-gas systems. After verification and validation, the model was applied to investigate the behaviour of Taylor bubbles in annular piping, a flow configuration similar to the slug flow regime observed in unconventional gas extraction. This provided insights into the effects of fluid properties through varying dimensionless quantities such as the Morton and Eötvös numbers of the simulated flow as well as inducing bulk motion of the liquid phase. Additionally, pipe configurations were varied to include inclination angles, increasing the relevance to practical wells, and internal obstructions, such as the production tubing in a coal seam gas wellbore. This not only gave key insights into the accuracy and applicability of pre-existing correlations, but provided a methodology through which they could be improved and or extended to new flow configurations.

8.1 Major contributions and summary of works

The major contributions of this work can be summarised as:

- Verification and validation of a two-dimensional, multiphase lattice Boltzmann model that is capable of simulating flows with high density and viscosity contrasts. The initial form of the model was developed by Dr. Fakhari in collaboration with the author to extend on the existing work in the literature by enhancing the locality of the algorithm. Additionally, the proposed model was seen to improve stability, highlighted by the simulation of relatively high Reynolds number flows with fluid properties similar to that of an air-water system reportedly out of reach for other models.

- Extension of the two-dimensional model to three-dimensions along with the proposed methods required to retain its stability. This involved the implementation of the *weighted*-orthogonalisation of the transformation matrix [173] from particle-distribution to moment space. The weighting allowed for de-coupling of moments that had been seen to degrade the model stability. This indicated the first coupling of the relaxation method with a velocity-based LBM and provided a correction for higher-order moments listed in Fakhari et al. [173].

- Verification and validation of the 3D model with existing benchmarks as well as the extension of these (e.g. results for the Rayleigh-Taylor instability with high density ratio and Reynolds number) to provide data for the testing of models developed for 'real' liquid-gas systems.

- Investigation of confined, multiphase flows relevant to the transport of hydrocarbons in both conventional and unconventional wells. This included the effects of pipe inclination on the multiphase dynamics as well as the behaviour of elongated bubbles in the presence of internal obstructions, similar to the central tubing used in the extraction of coal seam gas. Furthermore, the study was able to conclude the behaviour of Taylor bubbles in a counter-current flow could be captured with the distribution parameter from co-current flow.

This clearly outlines the stages of the work, in which the initial focus was on the development of capability and its extension beyond what was available in the literature. From here, a rigorous process of verification and validation was undertaken to test the limits of the proposed model. With this understood, the thesis entered the investigation stage in which flows relevant to the oil and gas industry were interrogated. Finally, the work outlined the methodology used, highlighting its ability to replace physical experiments in the development of closure correlations. This was shown in particular for the rise velocity of a Taylor bubble which is used in determining the pressure gradient and liquid hold-up in a well when the slug flow regime is evident.

The initial development of the phase field lattice Boltzmann model was outlined in Chapter 4. Here, the model was proposed in two-dimensions and tested against the layered Poiseuille flow and Rayleigh-Taylor instability as benchmarks. In testing the layered Poiseuille flow, the method of determining fluid properties in the diffuse interface was investigated. Ultimately, this was used to determine the relaxation

rate for the collision operation in the hydrodynamic Boltzmann update. From this investigation it was concluded that updating the relaxation rate by first using a linear interpolation of the dynamic viscosity with respect to the phase parameter gave the most accurate result. However, when a density contrast was imposed this method suffered from stability issues and as such, directly interpolating the relaxation rate with the phase parameter supplied the best balance of accuracy and stability from the methods tested. Comparing to reported results of the Rayleigh-Taylor instability provided verification of the implementation for a flow system exhibiting significant interface deformation. This benchmark was extended to a system with a large density contrast and a high Reynolds number, in a case that was reportedly out of reach for certain existing phase field models. Following the model verification, planar Taylor bubbles were analysed in stagnant and flowing fluids. Here, the model was able to recreate the relation between surface tension and rise velocity for Taylor bubbles in an inertial regime ($Re > 100$). To impose liquid flow on the system, the model was coupled with the boundary conditions presented by Zu and He [145], allowing the simulation domain to move with the propagating Taylor bubble. From this investigation it could be concluded that the empirical scaling factor used to assess the impact of liquid velocity on bubble rise was almost constant for both co- and counter-current flow, with an average value of 1.2518 across the planar simulations.

In Chapter 5, the model was extended to three-dimensions making use of a D3Q27 lattice for the hydrodynamics and a D3Q15 lattice for the interfacial dynamics of the system. Apart from the extension of the velocity space, a *weighted*-multiple relaxation scheme was also required to retain the stability properties observed in two-dimensions. The implementation was benchmarked against a colour-gradient lattice Boltzmann model through the analysis of bubble deformation in a shear flow. Here, no density contrast was imposed and as such similar results were obtained for both models. A three-dimensional Rayleigh-Taylor instability allowed further testing, where again, the proposed model was able to extend on the density ratio - Reynolds number combination existing in the literature. The experimental work of Bugg and Saad [169] was then used for a thorough validation using the rise of a Taylor bubble in olive oil. Their experimental study was conducted with PIV measurements allowing both local flow velocities and macroscopic bubble dynamics to be captured, all of which were used for comparison with the simulated results. This investigation highlighted the model's ability to capture the physical flow of elongated bubbles in pipes, a regime closely related to the system of interest.

With the model validated against a single experiment, it was desirable to test its range of stability by performing a parameter sweep across a variety of experimental and numerical results reported on by Lizarraga-Garcia *et al.* [196]. This proved that the model was able to capture the bubble propagation and shape for a range of fluid properties, however, more so relevant to oils. On the contrary, liquids extracted from coal seam gas operations are expected to be similar to water in terms of density and viscosity, as such, a lower viscous drag could be expected on the elongated bubbles. To investigate this, the dimensionless parameter range was extended from the later works of Lizarraga-Garcia [63] to, $10^{-7} \leq Mo \leq 10^{-11}$, and, $10 \leq Eo \leq 1000$. In doing this, the current stability limit of the implemented model was found. From the results that were obtained, it could be concluded that the correlation proposed by Viana *et al.* [207] is sufficient for describing Taylor bubble rise in vertical, tubular pipes.

Following on, the practicality of a computational multi-fluid dynamics model was shown through the ease in which pipe inclination effects can be incorporated. The results of this agreed very well with experimental measurements, however, indicated that the current correlations do not predict the bubble rise velocity with sufficient accuracy at intermediary inclination angles. The final component of this chapter assessed the influence of liquid velocity on the Taylor bubble dynamics. To do this, the constant velocity boundary conditions were implemented in three-dimensions and used to create a reference frame that moved with the expected drift velocity of the bubble. Here, the empirical tuning factor was determined for three different cases in which the accuracy of existing correlations varied significantly. This indicates the possibility of a weak dependence of the coefficient on fluid properties that is not currently captured correctly in the literature.

The primary motivation of this work came from the coal seam gas sector in which annular piping configurations are required for the construction of the wellbore. As such, a central tubing string was introduced into simulations to improve the understanding of multiphase flows in annular systems. The initial stages of this chapter investigated three air-water flows experimentally studied by Das *et al.* [225]. In this, the model was able to capture the evolution of the Taylor bubble to the asymmetric shape expected from experimental observations. The macroscopic rise properties agreed closely with those measured, however, the larger pipe diameters challenged the stability of the model and the numerical density ratio had to be reduced to obtain meaningful results. From here, inclination was introduced and the rise behaviour was compared with existing correlations for tubular and annular pipes. It was found that the tubular correlation of Lizarraga-Garcia *et al.* [18] was the most accurate when coupled with the hydraulic diameter of the system and the drift velocity correlation of Das *et al.* [225]. However, it was shown that tuning of other model types, like that of [226], could also provide reasonable accuracy for the case simulated. From here, the effect of flowing liquid was studied following a similar methodology to Chapter 6. The drift velocity of the annular Taylor bubble was applied to the inner and outer tubing while a fully developed annular flow was superimposed on the drift velocity at the inlet and outlet of the annulus. The three cases studied were found to have an approximately constant value for the flow distribution parameter, agreeing well with the work of Martin [239]. The average value obtained was $C_0 \approx 1.18$ for small annular pipes, irrespective of flow direction.

8.2 Avenues for future work

A number of potential avenues for further study can be identified from the research conducted in this dissertation. These relate both to the multiphase flow in annular tubing as well as the continued development of the phase field lattice Boltzmann model. Here, a non-exhaustive list has been compiled of potential opportunities:

- **Taylor bubble rise in inclined annular pipes:** in Chapter 7 a modification on the existing correlations was shown, however, this was for just one case. Extension of this would involve a systematic parameter sweep, determining the rise behaviour of bubbles for various Morton and

Eötvös numbers. From here, model fitting could be used to define a unified model for Taylor bubble velocity in annular pipes.

- **Inclined annular pipes with flowing fluid:** this was not discussed in the current work, but combines the uncertainties of both inclined and flowing fluid correlations. As such a systematic parameter sweep would significantly enhance the accuracy of models currently employed to predict the propagation of a Taylor bubble in this system.

- **Breakdown of Taylor bubbles - flow regime transition:** apart from determining the pressure gradients within flow regimes, the onset of regime transition is another critical component of modelling confined multiphase flows. Directly resolving the interaction of multiple Taylor bubbles and or Taylor bubbles in the transition regions could provide high resolution data on the processes involved with the transition from slug to churn flow.

- **Two-fluid model correlations:** the closure relations studied in this dissertation were primarily for one-dimensional mechanistic models, however, the two-fluid model requires methods to determine mass and momentum exchanges between phases that could be examined with the proposed phase field lattice Boltzmann model.

- **Improved collision operator:** the stability of lattice Boltzmann schemes can be very dependent on the collision operator employed for the relaxation of the distribution functions. Work on this was required in this thesis when extending the model to three-dimensions, however, it was not the focus. As such, coupling the model with the cascaded, cumulant or entropic relaxation schemes has the potential to provide additional stability.

- **Adaptive mesh refinement:** this avenue comes with possibly the strongest recommendation from the author, in terms of improving the model applicability. With diffuse interface approaches, high resolution is desirable around the interface such that its size is significantly less than the characteristic dimension of the domain. However, when working on a fixed, Cartesian grid this level of resolution is applied throughout the domain. As such, simulations can often become computationally expensive and even impractical without supercomputing facilities. It was found that to counter this, a very low numerical viscosity was required in simulations to achieve the desired dimensionless parameters for realistic air-water flows of interest in this work.

- **Three-phase contact behaviour:** the model used here was applied to the flow in the connection between a natural gas reservoir and the wellhead. However, the extension of no-slip boundaries to cater for variable contact angles would open up the possibility of simulating multiphase flow in the reservoir as well.

- **Three-phase flow model:** often in oil and gas operations, it can be expected that oil, gas and a water or brine type fluid will be extracted. There currently exists phase field models capable of this three-phase flow, and introducing this to the current solver would further the applications that could be investigated.

- **Non-Newtonian flow model:** for certain unconventional resources to be feasibly extracted, stimulation techniques such as hydraulic fracturing may be required. In hydraulic fracturing, non-Newtonian fluids can be used to enhance the transport of proppant into the reservoir. These interact with the Newtonian fluids present in the reservoir. With the phase field model, it would be possible to include a Newtonian and non-Newtonian phase in the multifluid framework allowing this interaction to be examined. Further to this, coupling in a discrete-element solver would allow the proppant itself to be included in this analysis.

Bibliography

[1] G. Gruszcynski, T. Mitchell, C. Leonardi, L. Łaniewski-Wołłk, and T. Barber. A cascaded phase-field lattice Boltzmann model for the simulation of incompressible, immiscible fluids with high density contrast. *Computers and Mathematics with Applications*, In Press, 2019.

[2] T. Mitchell, C. Leonardi, M. Firouzi, and B. Towler. Towards closure relations for the rise velocity of Taylor bubbles in annular piping using phase-field lattice Boltzmann techniques. *21st Australasian Fluid Mechanics Conference*, Adelaide, Australia: 10–13 December, 2018.

[3] T. Mitchell, C. Leonardi, and A. Fakhari. Development of a three-dimensional phase-field lattice Boltzmann method for the study of immiscible fluids at high density ratios. *International Journal of Multiphase Flow*, 107:1–15, 2018.

[4] A. Fakhari, T. Mitchell, C. Leonardi, and D. Bolster. Improved locality of the phase-field lattice-Boltzmann model for immiscible fluids at high density ratios. *Physical Review E*, 96:053301, 2017.

[5] B. Wu, M. Firouzi, T. Mitchell, T. Rufford, C. Leonardi, and B. Towler. A critical review of flow maps for gas-liquid flows in vertical pipes and annuli. *Chemical Engineering Journal*, 326:350–377, 2017.

[6] E. White and R. Beardmore. The velocity of rise of single cylindrical air bubbles through liquids contained in vertical tubes. *Chemical Engineering Science*, 17(5):351–361, 1962.

[7] Australian Pipelines & Gas Association and APPEA and Energy Networks Association. Australia's Bright Gas Future - Competitive, Clean and Reliable. Technical report, 2015.

[8] R. Hotinski. Stabilization Wedges: A Concept & Game. Technical report, Carbon Mitigation Initiative and Princeton Environmental Institute, Princeton University, 2015.

[9] Department of the Environment and Energy. Australian energy update 2017. Technical report, Australian Government, 2017.

[10] MagentaGreen (Wikimedia Commons). (Non) Conventional Deposits. `https://commons.wikimedia.org/wiki/File:(Non)_Conventional_Deposits.svg`, 2014.

[11] B. Towler, M. Firouzi, J. Underschultz, W. Rifkin, A. Garnett, H. Schultz, J. Esterle, S. Tyson, and K. Witt. An overview of the coal seam gas developments in Queensland. *Journal of Natural Gas Science and Engineering*, 31:249–271, 2016.

[12] S. Bikbulatov, M. Khasanov, and A. Zagurenko. Flowing bottomhole pressure calculation for a pumped well under multiphase flow, 2005.

[13] E. Osman, M. Ayoub, and M. Aggour. An artificial neural network model for predicting bottomhole flowing pressure in vertical multiphase flow. *Society of Petroleum Engineers*, page 93632, 2005.

[14] X. Zhang, X. Wu, W. Liang, C. Zhou, and D. Wu. Prediction of producing pressure drop for two-phase coalbed methane wells. *International Journal of Advancements in Computing Technology*, 4(17):540–548, 2012.

[15] P. Nurafza and J. Fernagu. Estimation of static bottom hole pressure from well-head shut-in pressure for a supercritical fluid in a depleted HP/HT reservoir. *Society of Petroleum Engineers*, page 124578, 2009.

[16] M. Firouzi, B. Towler, and T. Rufford. Developing new mechanistic models for predicting pressure gradient in coal bed methane wells. *Journal of Natural Gas Science and Engineering*, 33:961–972, 2016.

[17] M. Ramdin and R. Henkes. Computational fluid dynamics modeling of Benjamin and Taylor bubbles in two-phase flow in pipes. *Journal of Fluids Engineering*, 134(4):041303–041303, 2012.

[18] E. Lizarraga-Garcia, J. Buongiorno, E. Al-Safran, and D. Lakehal. A broadly-applicable unified closure relation for Taylor bubble rise velcity in pipes with stagnant fluid. *International Journal of Multiphase Flow*, 89:345–358, 2017.

[19] J. Grace, R. Clift, and M. Weber. *Bubbles, Drops and Particles*. Academic Press, New York, first edition edition, 1978.

[20] G. Tryggvason and A. Prosperetti. *Computational methods for multiphase flow*. Cambridge University Press, Cambridge, UK, 2007.

[21] S. M. A. Safi. *Efficient Computations for Multiphase Flow Problems Using Coupled Lattice Boltzmann-Level Set Methods*. PhD thesis, Technical University of Dortmund, 2016.

[22] X. Shan and H. Chen. Lattice Boltzmann model for simulating flows with multiple phases and components. *Physical Review E*, 47(3):1815–1819, 1993.

[23] S. Chen and G. Doolen. Lattice Boltzmann method for fluid flows. *Annual Review of Fluid Mechanics*, 30(1):329–364, 1998.

[24] X. He, X. Shan, and G. D. Doolen. Discrete Boltzmann equation model for nonideal gases. *Physical Review E*, 57(1):R13–R16, 1998.

[25] T. Lee and C.-L. Lin. A stable discretization of the lattice Boltzmann equation for simulation of incompressible two-phase flows at high density ratio. *Journal of Computational Physics*, 206(1):16–47, 2005.

[26] P. Yuan and L. Schaefer. Equations of state in a lattice Boltzmann model. *Physics of Fluids*, 18(4):042101, 2006.

[27] D. Lycett-Brown and K. Luo. Improved forcing scheme in pseudopotential lattice Boltzmann methods for multiphase flow at arbitrarily high density ratios. *Physical Review E*, 91(2):023305, 2015.

[28] A. Fakhari, M. Geier, and T. Lee. A mass-conserving lattice Boltzmann method with dynamic grid refinement for immiscible two-phase flows. *Journal of Computational Physics*, 315:434–457, 2016.

[29] M. Firouzi, B. F. Towler, and T. E. Rufford. Mechanistic modelling of counter-current slug flows in vertical annuli. *Society of Petroleum Engineers - SPE Asia Pacific Unconventional Resources Conference and Exhibition*, 2015.

[30] Heriot Watt University. Production technology, 2013.

[31] CSIRO. What is coal seam gas? `https://gisera.csiro.au/more-information/frequently-asked-questions/what-is-coal-seam-gas/`, 2018.

[32] S. Evje and K. K. Fjelde. Relaxation schemes for the calculation of two-phase flow in pipes. *Mathematical and Computer Modelling*, 36:535–567, 2002.

[33] H. Shi, J. A. Holmes, L. J. Durlofsky, K. Aziz, L. Diaz, B. Alkaya, and G. Oddie. Drift-flux modeling of two-phase flow in wellbores. *SPE Journal*, 10:24–33, 2005.

[34] F. Harlow and J. Welch. Numerical calculation of time-dependent viscous incompressible flow of fluid with free surface. *The Physics of Fluids*, 8(12):2182–2189, 1965.

[35] G. Birkhoff. Taylor instability and laminar mixing. Technical Report LA-1862, Los Alamos Scientific Lab., 1954.

[36] C. Hirt and B. Nichols. Volume of fluid (VOF) method for the dynamics of free boundaries. *Journal of Computational Physics*, 39(1):201 – 225, 1981.

[37] S. O. Unverdi and G. Tryggvason. A front-tracking method for viscous, incompressible, multi-fluid flows. *Journal of Computational Physics*, 100:25–37, 1992.

[38] S. Osher and J. Sethian. Fronts propagating with curvature-dependent speed: Algorithms based on Hamilton-Jacobi formulations. *Journal of Computational Physics*, 79(1):12–49, 1988.

[39] D. Jacqmin. Calculation of two-phase Navier-Stokes flows using phase-field modeling. *Journal of Computational Physics*, 155(1):96–127, 1999.

[40] D. Rothman and J. Keller. Immiscible cellular-automaton fluids. *Journal of Statistical Physics*, 52(3-4):1119–1127, 1988.

[41] X. Shan and H. Chen. Simulation of nonideal gases and liquid-gas phase transitions by the lattice Boltzmann equation. *Physical Review E*, 49(4):2941–2948, 1994.

[42] J. W. Cahn and J. E. Hilliard. Free energy of a nonuniform system. I. Interfacial free energy. *The Journal of Chemical Physics*, 28:258–267, 1958.

[43] S. M. Allen and J. W. Cahn. Mechanisms of phase transformations within the miscibility gap of Fe-rich Fe-Al alloys. *Acta Metallurgica*, 24:425, 1976.

[44] L. Łaniewski-Wołłk and J. Rokicki. Adjoint lattice Boltzmann for topology optimization on multi-GPU architecture. *Computers & Mathematics with Applications*, 71(3):833 – 848, 2016.

[45] E. Michaelides. *Particles, Bubbles & Drops*. World Scientific Publishing Co. Pte. Ltd., 2006.

[46] S. Martin and J. Williams. *Multiphase flow research*. Hauppauge, NY: Nove Science Publishers, 2009.

[47] A.-K. Tornberg. *Interface Tracking Methods with Application to Multiphase Flows*. PhD thesis, Department of Numerical Analysis and Computing Science, Royal Institute of Technology, Stockholm, 2000.

[48] C. Peskin. Numerical analysis of blood flow in the heart. *Journal of Computational Physics*, 25(3):220–252, 1977.

[49] J. Brackbill, D. Kothe, and C. Zemach. A continuum method for modeling surface tension. *Journal of Computational Physics*, 100(2):335–354, 1992.

[50] F. Boyer. A theoretical and numerical model for the study of incompressible mixture flows. *Computer and Fluids*, 31(1):41–68, 2002.

[51] J. Kim. A continuous surface tension force formulation for diffuse-interface models. *Journal of Computational Physics*, 204:784–804, 2005.

[52] S. Quan. Co-current flow effects on a rising Taylor bubble. *International Journal of Multiphase Flow*, 37(8):888–897, 2011.

[53] M. Awad. *An Overview of Heat Transfer Phenomena*, chapter Two-phase flow, pages 251–340. InTech, 2012.

[54] D. Lakehal, M. Labois, and C. Narayanan. Advances in the Large-Eddy and Interface Simulation (LEIS) of interfacial multiphase flows in pipes. *Progress in Computational Fluid Dynamics an International Journal*, 12(2-3):153–163, 2012.

[55] A. Hagedorn and K. Brown. Experimental study of pressure gradients occurring during continuous two-phase flow in small-diameter vertical conduits. *Journal of Petroleum Technology*, 17:475–484, 1965.

[56] J. Orkiszewski. Predicting two-phase pressure drops in vertical pipe. *Society of Petroleum Engineers*, 19(6):1546, 1967.

[57] H. Beggs and B. J. A study of two-phase flow in inclined pipes. *Society of Petroleum Engineers*, 25(05):4007, 1973.

[58] Y. Taitel, D. Bornea, and A. Dukler. Modeling flow pattern transitions for steady upward gas-liquid flow in vertical tubes. *AIChE Journal*, 26(3):345–354, 1980.

[59] D. Barnea. A unified model for predicting flow-pattern transitions for the whole range of pipe inclinations. *International Journal of Multiphase Flow*, 13(1):1–12, 1987.

[60] E. Caetano, O. Shoham, and J. Brill. Upward vertical two-phase flow through an annulus - Part I: single-phase friction factor, Taylor bubble rise velocity, and flow pattern prediction. *Journal of Energy Resources Technology*, 114:1–13, 1992.

[61] E. Caetano, O. Shoham, and J. Brill. Upward vertical two-phase flow through an annulus - Part II: Modeling bubble, slug, and annular flow. *Journal of Energy Resources Technology*, 114:14–30, 1992.

[62] A. Hasan and C. Kabir. Two-phase flow in vertical and inclined annuli. *International Journal of Multiphase Flow*, 18(2):279–293, 1992.

[63] E. Lizarraga-Garcia. *A Study of Taylor Bubbles in Vertical and Inclined Slug Flow using Multiphase CFD with Level Set*. PhD thesis, Department of Mechanical Engineering, MIT, 2016.

[64] Y. Taitel and D. Barnea. Counter current gas-liquid vertical flow, model for flow pattern and pressure drop. *International Journal of Multiphase Flow*, 9:637–647, 1983.

[65] K. Yamaguchi and Y. Yamazaki. Characteristics of counter current gas-liquid two-phase flow in vertical tubes. *Journal of Nuclear Science and Technology*, 19(12):985–996, 1982.

[66] E. Caetano. *Upward vertical two-phase flow through an annulus*. PhD thesis, University of Tulsa, 1986.

[67] T. Harmathy. Velocity of large drops and bubbles in media of infinite or restricted extent. *AlChE Journal*, 6:281–288, 1960.

[68] G. Wallis. *One-Dimensional Two-Phase Flow*. McGraw-Hill, New York, 1969.

[69] K. Mishima and M. Ishii. Flow regime transition criteria for upward two-phase flow in vertical tubes. *International Journal of Heat and Mass Transfer*, 27(5):723–737, 1984.

[70] H. Duns and N. Ros. Vertical flow of gas and liquid mixtures in wells. In *6th World Petroleum Congress*, pages 451–456, 1963.

[71] H. Mukherjee and J.P. Brill. Pressure drop correlation for inclined two-phase flow. *Journal of Energy Resources Technology*, 107:549–554, 1985.

[72] A. Ansari, N. Sylvester, C. Sarica, O. Shoham, and J. Brill. A comprehensive mechanistic model for upward two-phase flow in wellbores. *SPE Production & Facilities*, 9(2):143–151, 1994.

[73] N. Petalas and K. Aziz. A mechanistic model for multiphase flow in pipes. *Petroleum Society of Canada*, 39(6):43–55, 2000.

[74] G. Abdul-Majeed and A. Al-Mashat. A mechanistic model for vertical and inclined two-phase slug flow. *Journal of Petroleum Science and Engineering*, 27:59–67, 2000.

[75] D. Barnea and N. Brauner. Holdup of the liquid slug in two phase intermittent flow. *International Journal of Multiphase Flow*, 11:43–49, 1985.

[76] Y. Taitel and D. Barnea. A consistent approach for calculating pressure drop in inclined slug flow. *Chemical Engineering Science*, 45:1199–1206, 1990.

[77] A. Hasan and C. Kabir. A simple model for annular two-phase flow in wellbores. *SPE Production & Operations*, 22(2):168–175, 2007.

[78] D. Lakehal. LEIS for the prediction of turbulent multifluid flows applied to thermal-hydraulics applications. *Nuclear Engineering and Design*, 240(9):2096–2106, 2010. Experiments and CFD Code Applications to Nuclear Reactor Safety (XCFD4NRS).

[79] G. Govier and K. Aziz. Flow of complex mixtures in pipe. *Van Nostrant-Feinhold Co., New York*, 1972.

[80] M. Ishii and K. Mishima. Two-fluid model and hydrodynamic constitutive relations. *Nucl. Eng. Des.*, (82):107–126, 1984.

[81] M. Jerez-Carrizales, J. Jaramillo, and D. Fuentes. Prediction of multiphase flow in pipelines: Literature review. *Ingeniera y Ciencia — ing.cienc.*, 11(22):213–233, 2015.

[82] D. Lakehal. Advanced simulation of transient multiphase flow & flow assurance in the oil & gas industry. *The Canadian Journal of Chemical Engineering*, 91(7):1201–1214, 2013.

[83] A. Prosperetti and G. Tryggvason. *Computational Methods for Multiphase Flow*. Cambridge University Press, 2007.

[84] H. Anglart and O. Nylund. CFD application to prediction of void distribution in two-phase bubbly flows in rod bundles. *Nuclear Engineering and Design*, 163(1):81–98, 1996.

[85] M. Pang, J. Wei, and B. Yu. Numerical study of bubbly upflows in a vertical channel using the Euler-Lagrange two-way model. *Chemical Engineering Science*, 65(23):6215–6228, 2010.

[86] S. Yamoah, R. Marinez-Cuenca, G. Monros, S. Chiva, and R. Macian-Juan. Numerical investigation of models for drag, lift, wall lubrication and turbulent dispersion forces for the simulation of gas-liquid two-phase flow. *Chemical Engineering Research and Design*, 98:17–35, 2015.

[87] R. Sungkorn, J. Derksen, and J. Khinast. Modeling of turbulent gas-liquid bubbly flows using stochastic Lagrangian model and lattice-Boltzmann scheme. *Chemical Engineering Science*, 66(12):2745–2757, 2011.

[88] S. Lo. Application of the MUSIG model to bubbly flows. *AEA Technology*, AEAT-1096, 1996.

[89] D. Lucas, E. Krepper, and H. Prasser. Development of co-current air-water flow in vertical pipe. *Internation Journal of Multiphase Flow*, 31(12):1304–1328, 2005.

[90] E. Krepper, D. Lucas, and H. Prasser. On the modelling of bubbly flow in vertical pipes. *Nuclear Engineering and Design*, 235:597–611, 2005.

[91] A. Parvareh, M. Rahimi, A. Alizadehdakhel, and A. Alsairafi. CFD and ERT investigations on two-phase flow regimes in vertical and horizontal tubes. *International Communications in Heat and Mass Transfer*, 37:304–311, 2010.

[92] D. Dakshinamoorthy, Y. Dai, and M. Agrawal. CFD modeling of bubbly, slug and annular flow regimes in vertical pipelines. *Offshore Technology Conference, 6-9 May, Houston, Texas, USA*, OTC-24245-MS, 2013.

[93] A. Tomiyama, I. Zun, A. Sou, and T. Sakaguchi. Numerical analysis of bubble motion with the VOF method. *Nuclear Engineering and Design*, 141:169–182, 1993.

[94] K. Sankaranarayanan, X. Shan, I. Kevrekidis, and S. Sundaresan. Analysis of drag and virtual mass forces in bubbly suspensions using an implicit formulation of the lattice Boltzmann method. *Journal of Fluid Mechanics*, 452:61–96, 2002.

[95] R. Rzehak and E. Krepper. Closure models for turbulent bubbly flows: A CFD Study. *Nuclear Engineering and Design*, 265:701–711, 2013.

[96] A. Das and D. P.K. Modelling bubbly flow and its transitions in vertical annuli using population balance technique. *International Journal of Heat and Fluid Flow*, 31:101–114, 2009.

[97] T. Taha and Z. Cui. CFD modelling of slug flow in vertical tubes. *Chemical Engineering Science*, 61(2):676–687, 2006.

[98] E. D. Riva and D. D. Col. Numerical simulation of churn flow in a vertical pipe. *Chemical Engineering Science*, 64(17):3753–3765, 2009.

[99] G. Montoya, D. Lucas, E. Baglietto, and Y. Liao. A review on mechanisms and models for the churn-turbulent flow regime. *Chemical Engineering Science*, 141:186–103, 2015.

[100] Y. Liu, J. Cui, and W. Li. A two-phase, two-component model for vertical upward gas-liquid annular flow. *International Journal of Heat and Fluid Flow*, 32(34):796–804, 2011.

[101] A. K. Gunstensen, D. H. Rothman, S. Zaleski, and G. Zanetti. Lattice Boltzmann model of immiscible fluids. *Physical Review A*, 43(8):4320–4327, 1991.

[102] M. R. Swift, W. R. Osborn, and J. M. Yeomans. Lattice Boltzmann simulation of non-ideal fluids. *Physical Review Letters*, 75(5):830–833, 1995.

[103] X. He, S. Chen, and R. Zhang. A Lattice Boltzmann Scheme for Incompressible Multiphase Flow and Its Application in Simulation of Rayleigh-Taylor Instability. *Journal of Computational Physics*, 152(2):642–663, 1999.

[104] D. Grunau, S. Chen, and K. Eggert. A lattice Boltzmann model for multiphase fluid flows. *Physics of Fluids*, 5(10):2557–2562, 1993.

[105] J. Tolke. Lattice Boltzmann simulations of binary fluid flow through porous media. *Philosophical Transactions of the Royal Society of London A. Mathematical, Physical and Engineering Sciences*, 360(1792):535–545, 2002.

[106] F. Jiang and C. Hu. Numerical simulation of a rising CO2 droplet in the initial accelerating stage by a multiphase lattice Boltzmann method. *Applied Ocean Research*, 45:1–9, 2014.

[107] X. He and G. Doolen. Thermodynamic foundations of kinetic theory and lattice Boltzmann models for multiphase flows. *Journal of Statistical Physics*, 107(1):309–328, 2002.

[108] L. Chen, Q. Kang, Y. Mu, Y. He, and W. Tao. A critical review of the pseudopotential multiphase lattice Boltzmann model: Methods and applications. *International Journal of Heat and Mass Transfer*, 76:210–236, 2014.

[109] K. Sankaranarayanan, I. Kevrekidis, S. Sundaresan, J. Lu, and G. Tryggvason. A comparative study of lattice Boltzmann and front-tracking finite-difference methods for bubble simulations. *International Journal of Multiphase Flow*, 29(1):109–116, 2003.

[110] M. R. Kamali and H. E. A. Van den Akker. Simulating gas-liquid flows by means of a pseudopotential lattice Boltzmann method. *Industrial & Engineering Chemistry Research*, 52(33):11365–11377, 2013.

[111] M. Ngachin, R. G. Galdamez, S. Gokaltun, and M. C. Sukop. Lattice Boltzmann simulation of rising bubble dynamics using an effective buoyancy method. *International Journal of Modern Physics C*, 26(03):1550031, 2015.

[112] X. Shan. Analysis and reduction of the spurious current in a class of multiphase lattice Boltzmann models. *Physical Review E*, 73(4):047701, 2006.

[113] A. Kupershtokh, D. Medvedev, and D. Karpov. On equations of state in a lattice Boltzmann method. *Computers & Mathematics with Applications*, 58(5):965–974, 2009. Mesoscopic Methods in Engineering and Science.

[114] M. R. Swift, E. Orlandini, W. R. Osborn, and J. M. Yeomans. Lattice Boltzmann simulations of liquid-gas and binary fluid systems. *Physical Review E*, 54(5):5041–5052, 1996.

[115] D. J. Holdych, D. Rovas, J. G. Georgiadis, and R. O. Buckius. An improved hydrodynamics formulation for multiphase flow lattice-Boltzmann models. *International Journal of Modern Physics C*, 09(08):1393–1404, 1998.

[116] N. Takada, M. Misawa, A. Tomiyama, and S. Hosokawa. Simulation of bubble motion under gravity by lattice Boltzmann method. *Journal of Nuclear Science and Technology*, 38(5):330–341, 2001.

[117] C. Denniston, E. Orlandini, and J. M. Yeomans. Lattice Boltzmann simulations of liquid crystal hydrodynamics. *Physical Review E*, 63:056702, 2001.

[118] H. W. Zheng, C. Shu, and Y. T. Chew. A lattice Boltzmann model for multiphase flows with large density ratio. *Journal of Computational Physics*, 218(1):353–371, 2006.

[119] J. Y. Shao, C. Shu, H. B. Huang, and Y. T. Chew. Free-energy-based lattice Boltzmann model for the simulation of multiphase flows with density contrast. *Physical Review E*, 89:033309, 2014.

[120] A. Fakhari and D. Bolster. Diffuse interface modeling of three-phase contact line dynamics on curved boundaries: A lattice Boltzmann model for large density and viscosity ratios. *Journal of Computational Physics*, 334:620–638, 2017.

[121] Y. Yu, L. Chen, J. Lu, and G. Hou. A coupled lattice Boltzmann and particle level set method for free-surface flows. *ScienceAsia*, 40:238–247, 2014.

[122] G. Thommes, J. Becker, M. Junk, A. Vaikuntam, D. Kehrwald, A. Klar, K. Steiner, and A. Wiegmann. A lattice Boltzmann method for immiscible multiphase flow simulations using the level set method. *Journal of Computational Physics*, 228(4):1139–1156, 2009.

[123] C. Korner, M. Thies, T. Hofmann, N. Thurey, and U. Rude. Lattice Boltzmann model for free surface flow for modeling foaming. *Journal of Statistical Physics*, 121(112):179–196, 2005.

[124] N. Delbosc. *Real-time simulation of indoor air flow using the lattice Boltzmann method on graphics processing unit*. PhD thesis, School of Mechanical Engineering, University of Leeds, 2015.

[125] P. L. Bhatnagar. A model for collision processes in gases. I. Small amplitude processes in charged and neutral one-component systems. *Physical Review*, 94(3):511–525, 1954.

[126] S. Chapman and T. Cowling. *The Mathematical Theory of Non-Uniform Gases*. Cambridge University Press, 1953.

[127] L.-S. Luo. Unified theory of lattice Boltzmann models for nonideal gases. *Physical Review Letters*, 81(8):1618–1621, 1998.

[128] X. He, Q. Zou, L.-S. Luo, and M. Dembo. Analytic solutions of simple flows and analysis of nonslip boundary conditions for the lattice Boltzmann BGK model. *Journal of Statistical Physics*, 87(1-2):115–136, 1997.

[129] U. Frisch, B. Hasslacher, and Y. Pomeau. Lattice-gas automata for the Navier-Stokes equation. *Physical Review Letters*, 56:1505–1508, 1986.

[130] M. Geier. *Ab initio derivation of the cascaded lattice Boltzmann automaton*. PhD thesis, University of Freiburg, 2006.

[131] S. Ansumali and I. V. Karlin. Single relaxation time model for entropic lattice Boltzmann methods. *Physical Review E*, 65:056312, 2002.

[132] M. Geier, A. Greiner, and J. G. Korvink. Cascaded digital lattice Boltzmann automata for high Reynolds number flow. *Physical Review E*, 73:066705, 2006.

[133] M. Geier, M. Schönherr, A. Pasquali, and M. Krafczyk. The cumulant lattice Boltzmann equation in three dimensions: Theory and validation. *Computers & Mathematics with Applications*, 70(4):507–547, 2015.

[134] D. d'Humieres. Generalized lattice Boltzmann equations. In B. Shizgal and D. Weaver, editors, *Progress in Astronautics and Aeronautics*, volume Rarefied gas dynamics: Theory and simulations. American Institute of Aeronautics and Astronautics, 1992.

[135] P. Lallemand and L. Luo. Theory of the lattice Boltzmann method: Dispersion, dissipation, isotropy, Galilean invariance, and stability. *Physical Review E*, 61(6):6546–6562, 2000.

[136] C. Leonardi. *Development of a computational framework coupling the non-Newtonian lattice Boltzmann method and the discrete element method with application to block caving*. PhD thesis, School of Engineering, Swansea University, 2009.

[137] Q. Zou and X. He. On pressure and velocity flow boundary conditions and bounceback for the lattice Boltzmann BGK model. *Physics of Fluids*, 1996.

[138] C. Ho, C. Chang, K. Lin, and C. Lin. Consistent boundary conditions for 2D and 3D lattice Boltzmann simulations. *Computer Modeling in Engineering and Sciences*, 44(2):137–155, 2009.

[139] Z. Guo and C. Shu. *LBE for multiphase and multi-component flows*, chapter 7, pages 239–285. World Scientific, 2013.

[140] H. Huang, M. Sukop, and Z. Lu. *Single-component multiphase Shan-Chen-type model*, chapter 2, pages 18–70. John Wiley & Sons, Ltd, 2015.

[141] M. Sbragaglia, R. Benzi, L. Biferale, S. Succi, K. Sugiyama, and F. Toschi. Generalized lattice Boltzmann method with multirange pseudopotential. *Physical Review E*, 75:026702, 2007.

[142] H. Liu, K. Qinjun, C. Leonardi, S. Schmieschek, A. Narvaez, B. Jones, J. Willimas, A. Valocchi, and J. Harting. Multiphase lattice Boltzmann simulations for porous media applications. *Computational Geosciences*, 20(4):777–805, 2016.

[143] H. Huang, M. C. Sukop, and X.-Y. Lu. *Free-energy-based multiphase Lattice Boltzmann model*, pages 136–166. John Wiley & Sons, Ltd, 2015.

[144] F. Ren, B. Song, and M. Sukop. Terminal shape and velocity of a rising bubble by phase-field-based incompressible Lattice Boltzmann model. *Advances in Water Resources*, 97:100–109, 2016.

[145] Y. Q. Zu and S. He. Phase-field-based lattice Boltzmann model for incompressible binary fluid systems with density and viscosity contrasts. *Physical Review E*, 87:043301, 2013.

[146] A. Fakhari and T. Lee. Multiple-relaxation-time lattice Boltzmann method for immiscible fluids at high Reynolds numbers. *Physical Review E*, 87:023304, 2013.

[147] Z. Guo, C. Zheng, and B. Shi. Discrete lattice effects on the forcing term in the lattice Boltzmann method. *Physical Review E*, 65:046308, 2002.

[148] T. Kruger, F. Varnik, and D. Raabe. Shear stress in lattice Boltzmann simulations. *Physical Review E*, 79:046704, 2009.

[149] T. Lee and L. Liu. Lattice Boltzmann simulations of micron-scale drop impact on dry surfaces. *Journal of Computational Physics*, 229(20):8045–8063, 2010.

[150] H. Ding, P. Spelt, and C. Shu. Diffuse interface model for incompressible two-phase flows with large density ratios. *Journal of Computational Physics*, 226:2078–2095, 2007.

[151] A. Kumar. Isotropic finite-differences. *Journal of Computational Physics*, 201(1):109–118, 2004.

[152] Y. Sun and C. Beckermann. Sharp interface tracking using the phase-field equation. *Journal of Computational Physics*, 220(2):626–653, 2007.

[153] P. Chiu and Y. Lin. A conservative phase field method for solving incompressible two-phase flows. *Journal of Computational Physics*, 230(1):185–204, 2011.

[154] Y. Ba, H. Liu, Q. Li, Q. Kang, and J. Sun. Multiple-relaxation-time color-gradient lattice Boltzmann model for simulating two-phase flows with high density ratio. *Physical Review E*, 94:023310, 2016.

[155] S. Leclaire, N. Pellerin, M. Reggio, and J.-Y. Trépanier. A multiphase lattice Boltzmann method for simulating immiscible liquid-liquid interface dynamics. *Applied Mathematical Modelling*, 40(13):6376–6394, 2016.

[156] A. Fakhari and M. H. Rahimian. Phase-field modeling by the method of lattice Boltzmann equations. *Physical Review E*, 81:036707, 2010.

[157] A. Fakhari and T. Lee. Numerics of the lattice Boltzmann method on nonuniform grids: Standard LBM and finite-difference LBM. *Computers & Fluids*, 107:205–213, 2015.

[158] I. Ginzburg and D. d'Humières. Multireflection boundary conditions for lattice Boltzmann models. *Physical Review E*, 68:066614, 2003.

[159] Q. Li, K. H. Luo, Y. J. Gao, and Y. L. He. Additional interfacial force in lattice boltzmann models for incompressible multiphase flows. *Phys. Rev. E*, 85:026704, 2012.

[160] D. Sharp. An overview of Rayleigh-Taylor instability. *Physica D: Nonlinear Phenomena*, 12(1):3–18, 1984.

[161] M. Schönherr, K. Kucher, M. Geier, M. Stiebler, S. Freudiger, and M. Krafczyk. Multi-thread implementations of the lattice Boltzmann method on non-uniform grids for CPUs and GPUs. *Computers & Mathematics with Applications*, 61(12):3730–3743, 2011.

[162] C.-W. Kang, S. Quan, and J. Lou. Numerical study of a Taylor bubble rising in stagnant liquids. *Physical Review E*, 81:066308, 2010.

[163] R. Collins. A simple model of the plane gas bubble in a finite liquid. *Journal of Fluid Mechanics*, 22(4):763771, 1965.

[164] Z. Mao and A. Dukler. The motion of Taylor bubbles in vertical tubes. I. A numerical simulation for the shape and rise velocity of Taylor bubbles in stagnant and flowing liquid. *Journal of Computational Physics*, 91(1):132–160, 1990.

[165] H. Ha-Ngoc and J. Fabre. Test-case no 29A: The velocity and shape of 2D long bubbles in inclined channels or in vertical tubes (PA, PN) Part I: In a stagnant liquid. *Multiphase Science and Technology*, 16(1-3):177–189, 2004.

[166] B. Figueroa-Espinoza and J. Fabre. Taylor bubble moving in a flowing liquid in vertical channel: transition from symmetric to asymmetric shape. *Journal of Fluid Mechanics*, 679:432454, 2011.

[167] H. Ha-Ngoc and J. Fabre. Test-case no 29B: The velocity and shape of 2D long bubbles in inclined channels or in vertical tubes (PA,PN) - Part II: In a flowing liquid. *Multiphase Science and Technology*, 16:189–204, 2004.

[168] S. Leclaire, A. Parmigiani, B. Chopard, and J. Latt. Three-dimensional lattice Boltzmann method benchmarks between color-gradient and pseudo-potential immiscible multi-component models. *International Journal of Modern Physics C*, 28(07):1750085, 2017.

[169] J. Bugg and G. Saad. The velocity field around a Taylor bubble rising in a stagnant viscous fluid: Numerical and experimental results. *International Journal of Multiphase Flow*, 28(5):791–803, 2002.

[170] N. Ndinisa, D. Wiley, and D. Fletcher. Computational fluid dynamics simulations of Taylor bubbles in tubular membranes: Model validation and application to laminar flow systems. *Chemical Engineering Research and Design*, 83(A1):40 – 49, 2005.

[171] X. He and L. Luo. A priori derivation of the lattice Boltzmann equation. *Physical Review E*, 55:R6333–R6336, 1997.

[172] X. He and L. Luo. Theory of the lattice Boltzmann method: From the Boltzmann equation to the lattice Boltzmann equation. *Physical Review E*, 56:6811–6817, 1997.

[173] A. Fakhari, D. Bolster, and L.-S. Luo. A weighted multiple-relaxation-time lattice Boltzmann method for multiphase flows and its application to partial coalescence cascades. *Journal of Computational Physics*, 341:22–43, 2017.

[174] A. Fakhari, M. Geier, and D. Bolster. A simple phase-field model for interface tracking in three dimensions. *Computers & Mathematics with Applications*, 78:1154–1165, 2019.

[175] K. Suga, Y. Kuwata, K. Takashima, and R. Chikasue. A D3Q27 multiple-relaxation-time lattice Boltzmann method for turbulent flows. *Computers & Mathematics with Applications*, 69:518–529, 2015.

[176] F. Dubois and P. Lallemand. Quartic parameters for acoustic applications of lattice Boltzmann scheme. *Computers & Mathematics with Applications*, 61:3404–3416, 2011.

[177] A. Augier, F. Dubois, B. Graille, and P. Lallemand. On rotational invariance of lattice Boltzmann schemes. *Computers & Mathematics with Applications*, 67:239–255, 2014.

[178] P. Dellar. Lattice boltzmann algorithms without cubic defects in galilean invariance on standard lattices. *Journal of Computational Physics*, 259:270–283, 2014.

[179] G. I. Taylor. The formation of emulsions in definable fields of flow. *Proceedings of the Royal Society A - Mathematical, Physical and Engineering Sciences*, 146:501–523, 1934.

[180] M. Shapira and S. Haber. Low Reynolds number motion of a droplet in shear flow including wall effects. *International Journal of Multiphase Flow*, 16(2):305–321, 1990.

[181] H. Xi and C. Duncan. Lattice Boltzmann simulations of three-dimensional single droplet deformation and breakup under simple shear flow. *Physical Review E*, 59(3):3022, 1999.

[182] T. Inamuro, R. Tomita, and F. Ogino. Lattice Boltzmann simulations of drop deformation and breakup in shear flows. *International Journal of Modern Physics B*, 17(1 & 2):21–26, 2002.

[183] A. Komrakova, O. Shardt, D. Eskin, and J. Derksen. Lattice Boltzmann simulations of drop deformation and breakup in shear flow. *International Journal of Multiphase Flow*, 59:24–43, 2014.

[184] R. van der Sman and S. van der Graaf. Emulsion droplet deformation and breakup with Lattice Boltzmann model. *Computer Physics Communications*, 178:492–504, 2008.

[185] M. Hecht and J. Harting. Implementation of on-site velocity boundary conditions for D3Q19 lattice Boltzmann. *Journal of Statistical Mechanics: Theory and Experiment*, 2010:P01018, 2010.

[186] R. M. Davies and G. I. Taylor. The mechanics of large bubbles rising through extended liquids and through liquids in tubes. *Proceedings of the Royal Society of London. Series A. Mathematical and Physical Sciences*, 200(1062):375–390, 1950.

[187] F. Bretherton. The motion of long bubbles in tubes. *Journal of Fluid Mechanics*, 10:166–188, 1961.

[188] R. Brown. The mechanics of large gas bubbles in tubes: I. Bubble velocities in stagnant liquids. *The Canadian Journal of Chemical Engineering*, 43(5):217–223, 1965.

[189] S. Nogueira, M. Riethmuller, J. Campos, and A. Pinto. Flow patterns in the wake of a Taylor bubble rising through vertical columns of stagnant and flowing Newtonian liquids: An experimental study. *Chemical Engineering Science*, 61(22):7199–7212, 2006.

[190] G. Taylor. Deposition of a viscous fluid on the wall of a tube. *Journal of Fluid Mechanics*, 10:161–165, 1961.

[191] N. Heywood and J. Richardson. Slug flow of air-water mixtures in a horizontal pipe: Determination of liquid holdup by gamma-ray absorption. *Chemical Engineering Science*, 34(1):17–30, 1979.

[192] E. E. Zukoski. Influence of viscosity, surface tension, and inclination angle on motion of long bubbles in closed tubes. *Journal of Fluid Mechanics*, 25(4):821837, 1966.

[193] K. H. Bendiksen. An experimental investigation of the motion of long bubbles in inclined tubes. *International Journal of Multiphase Flow*, 10(4):467–483, 1984.

[194] C. E. Shosho and M. E. Ryan. An experimental study of the motion of long bubbles in inclined tubes. *Chemical Engineering Science*, 56(6):2191–2204, 2001.

[195] B. C. Jeyachandra, B. Gokcal, A. Al-Sarkhi, C. Sarica, and A. Sharma. Drift-velocity closure relationships for slug two-phase high-viscosity oil flow in pipes. *Society of Petroleum Engineers*, 17:593–601, 2012.

[196] E. Lizarraga-Garcia, J. Buongiorno, E. Al-Safran, and D. Lakehal. Development of a New CFD-Based Unified Closure Relation for Taylor Bubble Velocity in Two-Phase Slug Flow in Pipes. *BHR Group*, 2015.

[197] E. W. Llewellin, E. D. Bello, J. Taddeucci, P. Scarlato, and S. J. Lane. The thickness of the falling film of liquid around a Taylor bubble. *Proceedings of the Royal Society A: Mathematical, Physical and Engineering Sciences*, 468(2140):1041–1064, 2012.

[198] M. B. de Azevedo, D. dos Santos, J. L. Faccini, and J. Su. Experimental study of the falling film of liquid around a Taylor bubble. *International Journal of Multiphase Flow*, 88:133 – 141, 2017.

[199] D. Dumitrescu. Strömung an einer Luftblase im senkrechten Rohr. *Z. angew. Math. Mech.*, 23:139–149, 1943.

[200] H. Goldsmith and S. Mason. The movement of single large bubbles in closed vertical tubes. *Journal of Fluid Mechanics*, 14:42–58, 1962.

[201] D. Nicklin, J. Wilkes, and J. Davidson. Two-phase flow in vertical tubes. *Transactions of the Institution of Chemical Engineers*, 40:61–68, 1962.

[202] W. Nusselt. Die oberflachenkondesantion des wasserdamphes. *Zeitschrift des Vereines Deutschem Ingenieure*, 60:541–546, 1916.

[203] T. Karapantsios and A. Karabelas. Longitudinal characteristics of wavy falling films. *International Journal of Multiphase Flow*, 21:119–127, 1995.

[204] V. Lel, F. Al-Sibai, A. Leefken, and U. Renz. Local thickness and wave velocity measurement of wavy films with a chromatic confocal imaging method and a fluorescence intensity technique. *Experiments in Fluids*, 39(5):856–864, 2005.

[205] A. Eissa and J. Brill. *Applied Multiphase Flow in Pipes and Flow Assurance: Oil and Gas Production*. Society of Petroleum Engineers, 2017.

[206] A. Orell and R. Rembrand. A model for gas-liquid slug flow in a vertical tube. *Industrial & Engineering Chemistry Fundamentals*, 25(2):196–206, 1986.

[207] F. Viana and R. Pardo and R. Yánez and J. Trallero and D. Joseph. Universal correlation for the rise velocity of long gas bubbles in round pipes. *Journal of Fluid Mechanics*, 494:379–398, 2003.

[208] J. Araùjo, J. Miranda, A. Pinto, and J. Campos. Wide-ranging survey on the laminar flow of individual Taylor bubbles rising through stagnant Newtonian liquids. *International Journal of Multiphase Flow*, 43:131–148, 2012.

[209] J. Araùjo, J. Miranda, and J. Campos. Flow of two consecutive Taylor bubbles through a vertical column of stagnant liquid: A CFD study about the influence of the leading bubble on the hydrodynamics of the trailing one. *Chemical Engineering Science*, 97:16–33, 2013.

[210] J. Hua and J. Lou. Numerical simulation of bubble rising in viscous liquid. *Journal of Computational Physics*, 222(2):769–795, 2007.

[211] L. Amaya-Bower and T. Lee. Single bubble rising dynamics for moderate Reynolds number using lattice Boltzmann method. *Computers & Fluids*, 39(7):1191–1207, 2010.

[212] M. Weber, A. Alarie, and M. Ryan. Velocities of extended bubbles in inclined tubes. *Chemical Engineering Science*, 41(9):2235–2240, 1986.

[213] A. Hasan and C. Kabir. A study of multiphase flow behavior in vertical wells. *SPE Production Engineering*, 3(2):263–272, 1988.

[214] D. Joseph. Rise velocity of a spherical cap bubble. *Journal of Fluid Mechanics*, 488:213–223, 2003.

[215] K. Connington and T. Lee. Lattice Boltzmann simulations of forced wetting transitions of drops on superhydrophobic surfaces. *Journal of Computational Physics*, 250:601–615, 2013.

[216] A. Livinus, P. Verdin, L. Lao, J. Nossen, M. Langsholt, and H. Sleipnaes. Simplified generalised drift velocity correlation for elongated bubbles in liquid in pipes. *Journal of Petroleum Science and Engineering*, 160:106–118, 2018.

[217] S. Polonsky, D. Barnea, and L. Shemer. Averaged and time-dependent characteristics of the motion of an elongated bubble in a vertical pipe. *International Journal of Multiphase Flow*, 25:795–812, 1999.

[218] R. Collins, F. D. Moraes, J. Davidson, and D. Harrison. The motion of a large gas bubble rising through liquid flowing in a tube. *Journal of Fluid Mechanics*, 89(3):497–514, 1978.

[219] K. Bendiksen. On the motion of long bubbles in vertical tubes. *International Journal of Multiphase Flow*, 11(6):797–812, 1985.

[220] F. Direito, J. Campos, and J. Miranda. A Taylor drop rising in a liquid co-current flow. *International Journal of Multiphase Flow*, 96:134–143, 2017.

[221] D. Fréchou. Etude de L'ecoulement ascendant á trois fluides en conduite verticale. *Thése Inst Natl Polythech, Toulouse, France*, 1986.

[222] A. Tomiyama, Y. Nakahara, and G. Morita. Rising velocities and shapes of single bubbles in vertical pipes. *4th International Conference on Multiphase Flow*, pages 1–12, 2001.

[223] A. Pinto, M. C. Pinheiro, S. Nogueira, V. Ferreira, and J. Campos. Experimental study on the transition in the velocity of indiviudal Taylor bubbles in vertical upward co-current liquid flow. *Chemical Engineering Research and Design*, 83(A9):1103–1110, 2005.

[224] X. Lu and A. Prosperetti. A numerical study of Taylor bubbles. *Industrial & Engineering Chemistry Research*, 48(1):242–252, 2009.

[225] G. Das, P. K. Das, N. K. Purohit, and A. K. Mitra. Rise velocity of a Taylor bubble through concentric annulus. *Chemical Engineering Science*, 53(5):977–993, 1998.

[226] R. Ibarra and J. Nossen. Bubble velocity in horizontal and low-inclination upward slug flow inconcentric and fully eccentric annuli. *Chemical Engineering Science*, 192:774–787, 2018.

[227] L. Rohilla and A. K. Das. Experimental study on the interfacial evolution of Taylor bubble at inception of an annulus. *Industrial & Engineering Chemistry Research*, 58(6):2356–2369, 2019.

[228] V. Agarwal, A. K. Jana, G. Das, and P. K. Das. Taylor bubbles in liquid filled annuli: Some new observations. *Physics of Fluids*, 19(10):108105, 2007.

[229] P. Griffith. The prediction of low-quality boiling voids. *Journal of Heat Transfer*, 86(3):327–333, 1964.

[230] M. Sadatomi, Y. Sato, and S. Saruwatari. Two phase flow in vertical non-curcular channels. *International Journal of Multiphase Flow*, 6:641–655, 1982.

[231] D. Barnea and L. Shemer. Rise velocity of large bubbles in stagnant liquid in non-circular ducts. *International Journal of Multiphase Flow*, 12(6):1025–1027, 1986.

[232] A. Johnson and S. Cooper. Gas migration velocities during gas kicks in deviated wells. *68th Annual Technical Conference and Exibition of the Society of Petroleum Engineers*, SPE 26331:177–185, 1993.

[233] T. Yu, H. Zhang, M. Li, and C. Sarica. A mechanistic model for gas/liquid flow in upward vertical annuli. *SPE Production & Operations*, 25(3):124181, 2010.

[234] H. Zhang, Q. Wang, C. Sarica, and J. Brill. Unified model for gas-liquid pipe flow via slug dynamics - Part 1: Model development. *ASME. Journal of Energy Resources Technology*, 125(4):266–273, 2003.

[235] T. Benjamin. Gravity currents and related phenomen. *Journal of Fluid Mechanics*, 21:209–248, 1968.

[236] R. Ibarra, J. Nossen, and M. Tutkun. Two-phase gas-liquid flow in concentric and fully eccentric annuli. Part II: Model development, flow regime transition algorithm and pressure gradient. *Chemical Engineering Science*, 203:501–510, 2019.

[237] R. Ibarra, J. Nossen, and M. Tutkun. Two-phase gas-liquid flow in concentric and fully eccentric annuli. Part I: Flow patterns, holdup, slip ratio and pressure gradient. *Chemical Engineering Science*, 203(489):500, 2019.

[238] A. Donaldson, D. Kirpalani, and A. Macchi. Diffuse interface tracking of immiscible fluids: Improving phase continuity through free energy density selection. *International Journal of Multiphase Flow*, 37:777–787, 2011.

[239] C. Martin. Vertical downward two-phase slug flow. *Journal of Fluids Engineering*, ASME 98:715–722, 1974.

Appendix A

Details of LBM Processes

A.1 Boundary conditions for the phase field LBM

A.1.1 Velocity boundary condition

To construct the Taylor bubble simulation domains in this work for stagnant fluid flow, zero-velocity conditions were set on the pipe walls. In the lattice Boltzmann method, this is commonly conducted with the bounce-back boundary condition, but advanced methods also exist. These allow imposed non-zero velocity conditions to be specified (in addition to zero velocity). This appendix presents the boundary conditions from the work of Zu and He [145] that were used in this study. For a defined velocity, $\mathbf{u}$, on a boundary located at $\mathbf{x}_b$, the probability distribution functions for the velocity-based lattice Boltzmann method must satisfy momentum conservation, namely,

$$\sum_{\alpha} g_{\alpha}(\mathbf{x}_b)\mathbf{c} = \sum_{\alpha} g_{\alpha}^{eq}(\mathbf{x}_b)\mathbf{c} = \mathbf{u}. \tag{A.1}$$

In addition to this, taking the normal approach of performing the bounce-back scheme for the nonequilibrium component of the distribution functions gives,

$$g_{\alpha}(\mathbf{x}_b) - g_{\alpha}^{eq}(\mathbf{x}_b) = g_{\bar{\alpha}}(\mathbf{x}_b) - g_{\bar{\alpha}}^{eq}(\mathbf{x}_b), \tag{A.2}$$

where $\bar{\alpha}$ indicates the opposing lattice direction to α. This satisfies conservation of momentum in the normal direction, however, an excess of momentum can be observed tangentially along the boundary. This is where the set of tangential directions are identified through the known normal, $\Pi = \{\alpha | \mathbf{c} \cdot \mathbf{n}_b = 0\}$. Therefore, the excess momentum can be found through,

$$\mathbf{M}_g(\mathbf{x}_b) = \sum_{\alpha \in \Pi} \mathbf{c} \left[g_{\alpha}(\mathbf{x}_b) - g_{\alpha}^{eq}(\mathbf{x}_b) \right]. \tag{A.3}$$

This is then distributed over the N unknown distributions as discussed by [145], but proposed as far back as [137],

$$g_{\alpha}(\mathbf{x}_b) = g_{\bar{\alpha}}(\mathbf{x}_b) + \left[g_{\alpha}^{eq}(\mathbf{x}_b) - g_{\bar{\alpha}}^{eq}(\mathbf{x}_b) \right] - \frac{1}{Nc^2} \mathbf{c} \cdot \mathbf{M}_g(\mathbf{x}_b). \tag{A.4}$$

A similar methodology can be applied to the distribution used to resolve the Allen-Cahn equation. Here, the moving boundary generally has a known value of phase, ϕ, that is being applied and as such, the distribution functions should satisfy mass conservation [145],

$$\sum_{\alpha} h_{\alpha}(\mathbf{x}_b) = \sum_{\alpha} h^{eq}_{\alpha}(\mathbf{x}_b) = \phi. \tag{A.5}$$

The nonequilibrium component of the distribution can be written as,

$$h_{\alpha}(\mathbf{x}_b) - h^{eq}_{\alpha}(\mathbf{x}_b) = -\left[h_{\bar{\alpha}}(\mathbf{x}_b) - h^{eq}_{\bar{\alpha}}(\mathbf{x}_b)\right], \tag{A.6}$$

which results in an excess of density according to [145],

$$\mathrm{M}_h(\mathbf{x}_b) = \sum_{\alpha \in \Pi} \left[h_{\alpha}(\mathbf{x}_b) - h^{eq}_{\alpha}(\mathbf{x}_b)\right]. \tag{A.7}$$

This is distributed over the unknown distributions allowing the boundary to be resolved,

$$h_{\alpha}(\mathbf{x}_b) = \begin{cases} h_{\alpha}(\mathbf{x}_b) - \left[h_{\bar{\alpha}}(\mathbf{x}_b) - h^{eq}_{\bar{\alpha}}(\mathbf{x}_b)\right], & \text{if } \mathbf{c}\cdot\mathbf{n}_b = 0 \\ h_{\alpha}(\mathbf{x}_b) - \left[h_{\bar{\alpha}}(\mathbf{x}_b) - h^{eq}_{\bar{\alpha}}(\mathbf{x}_b)\right] - \frac{\mathrm{M}_h(\mathbf{x}_b)}{N}, & \text{if } \mathbf{c}\cdot\mathbf{n}_b \neq 0. \end{cases} \tag{A.8}$$

Therefore, it can be seen from the above formulation, that if the normal to the boundary is known, conditions can be specified to determine the unknown distribution functions required to specify a desired velocity and phase.

A.1.2 Three-phase contact treatment

The three-phase contact interaction in this work was modelled based on a stairwise implementation of the work of Fakhari et al. [120]. In order to do this, one needs to determine the normal of the solid boundary, $\mathbf{n}_w$, as well as the halfway distance, h, between the solid node and the next fluid node in the normal direction. With these details, the desired contact angle, θ, can be achieved by imposing [120],

$$\mathbf{n}_w \cdot \nabla\phi|_{\mathbf{x}_w} = \Theta\phi_w(1-\phi_w), \tag{A.9}$$

where $\mathbf{x}_w$ is the position of the wall, ϕ_w is the value of the phase at the solid boundary location and

$$\Theta = \frac{4}{W}\cos\theta. \tag{A.10}$$

From here, a central difference is used such that,

$$\mathbf{n}_w \cdot \nabla\phi|_{\mathbf{x}_w} = \frac{\partial\phi}{\partial n_w}|_{\mathbf{x}_w}, \tag{A.11}$$

$$= \frac{\phi_m - \phi_{i,j}}{2h}, \tag{A.12}$$

where ϕ_m is the phase value of the next fluid node in the normal direction and $\phi_{i,j}$ is the phase in the solid node that needs to be determined. The value of the phase at the wall is then eliminated from the

equations by assuming, $\phi_w = 0.5(\phi_m + \phi_{i,j})$. Substituting this into the initial equation and rearranging gives,

$$\phi_{i,j} = \frac{(1+a-\left[(1+a)^2 - 4a\phi_m\right]^{0.5})}{a+\varepsilon} - \phi_m, \tag{A.13}$$

$$a = -h\Theta. \tag{A.14}$$

Here, ε has been included as a small parameter that eliminates the possibility of a divide by zero error.

A.2 Transformation from density to pressure evolution

Starting from,

$$D_t f_i = \frac{\partial f_i}{\partial t} + \mathbf{e}_i \cdot \nabla f_i = -\Lambda(f_i - f_i^{eq}) + \frac{(\mathbf{c}_i - \mathbf{u}) \cdot \mathbf{F}}{c_s^2}\Gamma_i \tag{A.15}$$

$$\text{where} \qquad \Gamma_i = w_i \left[1 + \frac{\mathbf{c}_i \cdot \mathbf{u}}{c_s^2} + \frac{(\mathbf{c}_i \cdot \mathbf{u})^2}{2c_s^4} - \frac{\mathbf{u} \cdot \mathbf{u}}{2c_s^2}\right], \tag{A.16}$$

we want to perform the transformation,

$$g_i = f_i c_s^2 + w_i(p - \rho c_s^2) \tag{A.17}$$

$$g_i^{eq} = f_i^{eq} c_s^2 + w_i(p - \rho c_s^2) \tag{A.18}$$

with a forcing term of the form,

$$\mathbf{F} = -\nabla(p - \rho c_s^2) + \mathbf{F}_B + \mu_\phi \nabla \phi. \tag{A.19}$$

Performing the transformation on the term within the collision operator and the right hand side of A.15 gives,

$$f_i - f_i^{eq} = \frac{1}{c_s^2}\left[(g_i - w_i(p - \rho c_s^2)) - (g_i^{eq} - w_i(p - \rho c_s^2))\right] \tag{A.20}$$

$$= \frac{1}{c_s^2}\left[g_i - g_i^{eq}\right] \tag{A.21}$$

$$D_t f_i = \frac{1}{c_s^2}\left[D_t g_i - w_i(D_t p - D_t \rho c_s^2)\right]. \tag{A.22}$$

From here one must look to simplify the material derivatives of p and ρc_s^2. To do this we note the law of continuity and chain rule for derivatives

$$\frac{\partial \rho}{\partial t} + \nabla \cdot \rho \mathbf{u} = 0 \qquad \Longrightarrow \qquad \frac{\partial \rho c_s^2}{\partial t} = -\nabla \cdot \rho c_s^2 \mathbf{u} \tag{A.23}$$

$$\frac{\partial p}{\partial t} = \frac{\partial p}{\partial \rho}\frac{\partial \rho}{\partial t} \qquad \Longrightarrow \qquad \frac{\partial p}{\partial t} = -\frac{\partial p}{\partial \rho}(\nabla \cdot \rho \mathbf{u}). \tag{A.24}$$

The incompressibility constraint is then applied to this giving

$$\frac{\partial \rho c_s^2}{\partial t} = -\left[\mathbf{u} \cdot \nabla \rho c_s^2 + \rho c_s^2 \cdot \cancelto{0}{\nabla \mathbf{u}}\right] \tag{A.25}$$

$$\begin{aligned} \frac{\partial p}{\partial t} &= -\frac{\partial p}{\partial \rho}(\mathbf{u} \cdot \nabla \rho) \\ &= -\mathbf{u} \cdot \frac{\partial p}{\partial \rho}\frac{\partial \rho}{\partial x_i} \\ &= -\mathbf{u} \cdot \nabla p \end{aligned} \tag{A.26}$$

Now applying Equations A.25 and A.26 to Equation A.22

$$D_t f_i = \frac{1}{c_s^2}\left[D_t g_i - w_i((\mathbf{c}_i - \mathbf{u}) \cdot \nabla p - (\mathbf{c}_i - \mathbf{u}) \cdot \nabla \rho c_s^2)\right] \tag{A.27}$$

With this, Equation A.15 can now be expressed in terms of the new distribution function as

$$D_t g_i = -\Lambda(g_i - g_i^{eq}) + \left[w_i((\mathbf{c}_i - \mathbf{u}) \cdot \nabla p - (\mathbf{c}_i - \mathbf{u}) \cdot \nabla \rho c_s^2)\right] + (\mathbf{c}_i - \mathbf{u}) \cdot (-\nabla(p - \rho c_s^2) - \mu_\phi \nabla \phi + \mathbf{F_b})\Gamma_i \tag{A.28}$$

To remove the dependence on the gradient of the density field, the relation between density and the phase field parameter is used

$$\nabla \rho = \frac{\partial \rho}{\partial \phi} \frac{\partial \phi}{\partial x_i} = (\rho_h - \rho_l) \nabla \phi. \tag{A.29}$$

This gives the result for the discrete update equation for g_i

$$D_t g_i = -\Lambda(g_i - g_i^{eq}) - (\Gamma_i - w_i)(\mathbf{c}_i - \mathbf{u}) \cdot \nabla p + \left[(\Gamma_i - w_i)(\rho_h - \rho_l)c_s^2 + \Gamma_i \mu_\phi\right](\mathbf{c}_i - \mathbf{u}) \cdot \nabla \phi + (\mathbf{c}_i - \mathbf{u}) \cdot \mathbf{F_b} \Gamma_i \tag{A.30}$$

According to [25] this expression can be further simplified by using the low Mach number assumption used in lattice Boltzmann simulations. At this asymptotic limit the pressure can be split into the thermodynamic and hydrodynamic pressures. From which the "thermodynamic pressure is assumed uniform in space [25]," giving the resultant gradient dependent on the change in hydrodynamic pressure. From dimensional analysis it is evident that $\nabla p \sim O(Ma^2)$, which means

$$(\Gamma_i - w_i)(\mathbf{c}_i - \mathbf{u}) \cdot \nabla p \sim O(Ma^3) \tag{A.31}$$

which is omitted in line with the second order terms retained in the usual Chapman-Enskog expansion of Equation A.15.

Forever blowing bubbles.

Ed Hay,
Office Chats